Friction and Wear Behavior of Thermally Sprayed Oxide Coatings

Amit Roy

A Dissertation
In the Department of
Department of Mechanical, Industrial and Aerospace Engineering

Presented in Partial Fulfillment of the Requirements
For the Degree of
Doctor of Philosophy (Mechanical Engineering) at
Concordia University
Montréal, Québec, Canada

July 2023

CONCORDIA UNIVERSITY
SCHOOL OF GRADUATE STUDIES

This is to certify that the dissertation prepared

By : **Amit Roy**

Entitled: **Friction and Wear Behavior of Thermally Sprayed Oxide Coatings**

and submitted in partial fulfilment of the requirements for the degree of

DOCTOR OF PHILOSOPHY (Mechanical Engineering)

complies with the regulations of the University and meets the accepted standards with respect to originality and quality.

Signed by the final examining committee:

_____ Chair
Dr. Andrea Schiffauerova

_____ External Examiner
Dr. Katherine Faber

_____ External to Program
Dr. Ali Dolatabadi

_____ Examiner
Dr. Rolf Wuthrich

_____ Examiner
Dr. Martin Pugh

_____ Thesis Co-supervisor
Dr. Richard Chromik

_____ Thesis Co-supervisor
Dr. Pantcho Stoyanov

_____ Thesis Co-supervisor
Dr. Christian Moreau

Approved by: _____

Dr. Muthukumaran Packirisamy, Graduate Program Director

September 05, 2023

_____
Dr. Mourad Debbabi, Dean
Gina Cody School of Engineering and Computer Science

Abstract

Friction and Wear Behavior of Thermally Sprayed Oxide Coatings

Amit Roy, PhD
Concordia University, 2023

Conventional alloys and composites are widely used as coating materials in various contacting interfaces within gas turbine engines. These alloys form *in-situ* lubricious oxides during sliding at high temperatures, which help to reduce friction and wear. However, the formation of an oxide film on the contact zones requires time and depends on the chemical nature of the materials as well as the contact conditions and environment. In most cases, the running-in period for traditional alloys or composites is relatively long, which ultimately causes an overall increase in wear. Since the lubricious oxide is responsible for low wear and steady-state friction coefficient at high temperatures, it could be beneficial to replace the conventional alloys/composites and use such oxides instead. Based on prior work, ionic potential, and interaction parameters, which emphasis the lubricity at high temperatures, examples of such oxides include CuO, Ta_2O_5, CoO, NiO, Co-Ni-O.

In this dissertation, CuO, Ta_2O_5, CoO, NiO, Co-Ni-O oxides were sprayed to produce thick coatings with dense, homogeneous microstructures using Suspension Plasma Spray (SPS) and High Velocity Oxygen Fuel (HVOF). The effects of spray parameters on the composition and microstructure of the coatings were investigated. The CuO and NiO coatings produced by SPS partially reduced to Cu_2O, Cu and Ni, respectively. On the other hand, CoO, Ta_2O_5, and Co-Ni-O coatings remained single phase.

The thermally sprayed coatings were tested on a ball vs flat tribometer with dry sliding reciprocating condition at various temperatures (i.e., 25°C, and 450°C) against an alumina counterface. CuO and CoO were found to have low coefficients of friction at high temperatures compared to other oxides (i.e., Ta_2O_5, NiO, Co-Ni-O). On the other hand, CoO and $Co_{0.75}Ni_{0.25}O$ were found to be superior in terms of wear resistance at high temperatures.

Scanning electron microscopy (SEM), electron channeling contrast imaging (ECCI), X-ray photoelectron spectroscopy (XPS), X-ray diffraction (XRD), Raman analysis, and focused ion beam (FIB) were used to characterize the coatings and the corresponding wear tracks to determine the dominant wear mechanisms. In general, brittle fracture, cracking, and

tribofilm delamination were found to be the main wear mechanisms leading to high wear of the oxides at room temperature. In contrast, the formation of a relatively ductile, smeared tribofilm, grain refinement, and amorphous layer closer to the wear track surface contributed to friction and wear reduction at high temperatures.

In addition, a low interaction parameter of the oxides, regardless of the microstructure of the oxide coatings, led to the low friction. Such a correlation was not observed with the high interaction parameter and ionic potential. Furthermore, the high sintering ability or diffusion coefficient of the oxides could play a role in reducing friction and wear at high temperature.

Résumé

Les alliages et composites conventionnels sont largement utilisés comme matériaux de revêtement dans diverses interfaces de contact dans les moteurs à turbine à gaz. Ces alliages forment des oxydes lubrifiants in situ lors du glissement à haute température, ce qui contribue à réduire le frottement et l'usure. Cependant, la formation d'un film d'oxyde sur les zones de contact nécessite un certain temps qui dépend du comportement chimique des matériaux ainsi que des conditions de contact et de l'environnement. Dans la plupart des cas, les alliages ou composites traditionnels entraînent une longue période de rodage, ce qui engendre finalement une augmentation progressive des frottements et de l'usure. Étant donné que l'oxyde lubrifiant est responsable d'une faible usure et d'un faible coefficient de frottement en régime permanent à des températures élevées, il est proposé de remplacer les alliages/composites conventionnels par de tels oxydes. Sur la base des travaux antérieurs, du potentiel ionique et des paramètres d'interaction qui mettent l'accent sur le pouvoir lubrifiant à haute température, des exemples de tels oxydes comprennent CuO, Ta_2O_5, CoO, NiO, Co-Ni-O.

Dans cette thèse, les oxydes de CuO, Ta_2O_5, CoO, NiO, Co-Ni-O ont été projetés pour produire des revêtements épais, denses et homogènes en utilisant le procédés projection par plasma de suspension (Suspension Plasma Spray, SPS) et High Velocity Oxygen Fuel (HVOF). Les effets des paramètres de projection sur la composition et la microstructure des revêtements ont été étudiés. Les revêtements CuO et NiO produits par SPS ont été réduits partiellement respectivement en Cu_2O, Cu et Ni. En revanche, les revêtements de CoO, Ta_2O_5 et Co-Ni-O sont restés monophasés.

Les revêtements préparés ont été testés avec une bille à mouvement alternatif glissant à sec sur un tribomètre plat à différentes températures (c'est-à-dire 25°C et 450°C) contre une contre-face en alumine. Les revêtements de CuO et CoO se sont avérés avoir de faibles coefficients de frottement à haute température par rapport à d'autres oxydes (c'est-à-dire Ta_2O_5, NiO, Co-Ni-O). D'autre part, CoO et $Co_{0.75}Ni_{0.25}O$ se sont avérés supérieurs en termes de résistance à l'usure à haute température.

La microscopie électronique à balayage (SEM), l'imagerie de contraste par canalisation d'électrons (ECCI), la spectroscopie photoélectronique à rayons X (XPS), la diffraction des rayons X (XRD), l'analyse Raman et le faisceau d'ions focalisé (FIB) ont été utilisés pour caractériser les revêtements et les traces d'usure correspondantes pour déterminer les mécanismes d'usure dominants. En général, la rupture fragile, la fissuration et le délaminage

du tribofilm se sont avérés être les principaux mécanismes d'usure produisant une usure élevée des oxydes à température ambiante. En revanche, la formation de tribofilm relativement ductile et déforme, le raffinement de grain et la couche amorphe plus proche de la surface de la piste d'usure ont contribué au frottement et à la réduction de l'usure à des températures élevées.

De plus, un faible paramètre d'interaction des oxydes, quelle que soit la microstructure des oxydes, conduit à un faible frottement contrainement au paramètre d'interaction élevé et au potentiel ionique. La grande capacité de frittage ou coefficient de diffusion élevé des oxydes pourrait jouer un rôle dans la réduction du frottement et de l'usure à haute température.

Acknowledgements

The author would like to thank his supervisors Prof. Christian Moreau, Prof. Pantcho Stoyanov, and Prof. Richard Chromik, for giving him the opportunity to work on this interesting and challenging topic. The author is also grateful to the supervisors for their suggestions, encouragement, motivation, and patience during the Ph.D. program.

The work was carried out in collaboration between the "Thermal Spray and Multiphase Flow Laboratory", Concordia University and the "McGill Surface Engineering and Coating Tribology Laboratory", McGill University. The authors sincerely thank all the members of these laboratories and in particular Dr. Fadhel Ben Ettouil for the help with the spray parameters and the deposition of the coatings. The author thanks Dr. Ali Nozari (Concordia), Dr. Dmytro Kevorkov (Concordia), Dr. Lise Guichaoua (McGill), Stéphanie Bessette (McGill) for their technical assistance with instruments. Furthermore, the authors special thanks go to Dr. Masiar Rahman, Dr. Vamsi Munagala, Dr. Sima Alidokht, Dr. Bruno, Camilo (Chemical Dept., Concordia) for their enormous support during the study. The author would also like to thank the Natural Sciences and Engineering Research Council (NSERC) project number CRDPJ 530409-18 and the Consortium for Research and Innovation in Aerospace in Québec (CRIAQ) project number MANU-1719 for their financial support. Half of this work was also supported by the Natural Sciences and Engineering Research Council of Canada (NSERC) through the Strategic Program (STPGP/494283-2016), Prima Quebec (grant R13-13-001), Metal7 and Kingston Process Metallurgy. This support extended to NSERC Discovery Grant - Pantcho Stoyanov. The author gratefully acknowledges their financial support.

The author would like to thank his parents, brothers, and sisters-in-law for their sacrifices, endless love, and prayers. The author also expresses his gratitude to his parents-in-law, brother-in-law for their endless support especially during his higher studies abroad. The author extends his gratitude to his beloved wife Mousumi Paul for all her sacrifices, unconditional help, moral support, and encouragement. Last but not the least, the author would like to thank his beautiful daughter Aritri Roy for her innocent love.

Dedication

This dissertation is dedicated to my brother **Dinesh Roy** and sister-in-law **Jayanti Roy**.
For their endless support and encouragement.

Contribution to authors

This dissertation is a manuscript based. Chapters 1, and 8 are the introduction, and conclusion of the dissertation, respectively. The other chapters are reprints from published papers, prepared manuscripts or papers submitted to peer-reviewed journals.

All papers have been published or submitted for publication with the advisor, Prof. Christian Moreau, Prof. Pantcho Stoyanov, and Prof. Richard Chromik as co-authors. The supervisor assisted the author of this dissertation in writing the manuscripts and provided supervision and advice for the experiments and analysis of the results.

The co-authors (i.e., Payank Patel, Navid Sharifi, V.N.V. Munagala, SA. Alidokht) for Chapters 3 and 4 helped in some part of experiments, planning, manuscript organization and review process.

Other authors of the manuscripts in this thesis (i.e., Chapters 5 and 6) include Vahid Jalilvand, Saeed Mohammadkhani who developed the CoO, NiO, Co-Ni-O coatings using thermal spray process, and prepared the Co-Ni-O powders for spraying using HVOF process. Prof. Ali Dolatabadi, Prof. Lionel Roue, Prof. Daniel Guay, and Prof. Christian Moreau were involved in this project. These professors also helped in reviewing the manuscripts.

The author of this dissertation was responsible for writing all the manuscripts. In addition, the author performed the experimental procedure and analysis of the thermally sprayed coatings and measurements of their mechanical and tribological characteristics at different temperatures presented in this dissertation.

The papers that form chapters in this dissertation are as follows:

Chapter 2:

A. Roy, P. Patel, N. Sharifi, R. R. Chromik, P. Stoyanov, C. Moreau. "Binary and Ternary Lubricious Oxides for High Temperature Tribological Applications: A Review." *Results in Surfaces and Interfaces* (2023): 100117.

Chapter 3:

A. Roy, N. Sharifi, V.N.V. Munagala, SA. Alidokht, P. Patel, M. Makowiec, R. R. Chromik, C. Moreau, P. Stoyanov. "Microstructural evolution and tribological behavior of suspension plasma sprayed CuO as high-temperature lubricious coatings." *Wear* (2023): 204874.

Chapter 4:

A. Roy, V.N.V. Munagala, P. Patel, N. Sharifi, SA. Alidokht, M. Makowiec, R. R. Chromik, C. Moreau, P. Stoyanov. "Friction and wear behavior of suspension plasma sprayed tantalum oxide coatings at elevated temperatures." *Surface and Coatings Technology* 452 (2023): 129097.

Chapter 5:

A. Roy, V. Jalilvand, S. Mohammadkhani, P. Patel, A. Dolatabadi, L. Roue, D. Guay, R. R. Chromik, C. Moreau, P. Stoyanov. "Enhanced wear resistance of cobalt oxide over nickel oxide." *Tribology Letters* 71.3 (2023): 99.

Chapter 6:

A. Roy, V. Jalilvand, S. Mohammadkhani, P. Patel, A. Dolatabadi, L. Roue, D. Guay, R. R. Chromik, P. Stoyanov, C. Moreau. "Microstructural and tribological characteristics of thermally sprayed Co-Ni-O ternary oxide coatings." *Manuscript is ready to submit "Tribology International"*.

Chapter 7:

A. Roy, R. R. Chromik, C. Moreau, P. Stoyanov "Influencing factors on the lubricity of the oxide coatings." *Manuscript is ready to submit "MRS Communication"*.

Table of Contents

List of Figures xiv
List of Tables xx
List of Abbreviations xxi
Chapter 1 1
1.1 Introduction 1
1.2 Thermal Spray Process 2
1.2.1 Suspension Plasma Spray (SPS) 3
1.2.2 High-Velocity Oxygen Fuel (HVOF) 5
1.3 Objectives 7
1.4 Organization of dissertation 8
1.5 References 11
Chapter 2 13
Binary and Ternary Lubricious Oxides for High Temperature Tribological Applications: A Review 13
2.1 Introduction 14
2.2 High temperature tribology and its application 16
2.2.1 What is high temperature tribology? 16
2.2.2 High temperature tribology applications 16
2.2.3 Materials in high temperature tribological applications 18
2.2.4 Mechanisms and interfacial processes at elevated temperature 19
2.2.5 Limitations at elevated temperature and motivation to binary and ternary oxides 23
2.3 Binary Oxides 24
2.4 Ternary Oxides 32
2.5 Interfacial Processes and Wear Mechanism of Oxides 46
2.6 Summary 48
2.7 Future Perspective 49
2.8 References 51
Chapter 3 61
Microstructural Evolution and Tribological Behavior of Suspension Plasma Sprayed CuO as High-Temperature Lubricious Coatings 61
3.1 Introduction 62
3.2 Experimental Details 64

3.3 Results 68
3.4 Discussion 76
3.5 Conclusions 83
3.6 References 84
Chapter 4 87
Friction and Wear Behavior of Suspension Plasma Sprayed Tantalum Oxide Coatings at Elevated Temperatures 87
4.1 Introduction 88
4.2 Experimental details 90
4.3 Results 94
4.4 Discussions 106
4.5 Conclusions 109
4.6 References 110
Chapter 5 113
Enhanced Wear Resistance of Cobalt Oxide Over Nickel Oxide 113
5.1 Introduction 114
5.2 Experimental 116
5.3 Results 118
5.4 Discussion 128
5.5 Conclusions 132
5.6 References 133
Chapter 6 136
Microstructural and Tribological Characteristics of Thermally Sprayed Co-Ni-O Ternary Oxide Coatings 136
6.1 Introduction 137
6.2 Experimental 138
6.3 Results 141
6.4 Discussion 160
6.5 Conclusions 164
6.6 References 166
Chapter 7 170
Influencing Factors on the Lubricity of Oxide Coatings 170
7.1 Introduction 171
7.2 Materials and methods 172

7.3 Results and discussion 173
7.4 Conclusions 181
7.5 References 182
Chapter 8 184
Conclusions and Recommendation 184
8.1 Summary and Conclusions 184
8.2 Contributions to Original Knowledge 186
8.3 Suggestion for Future Work 186
Appendix A 189
Supplementary section 1 189
Appendix B 202
Supplementary section 2 202

List of Figures

Figure 1. 1: The schematic of a suspension plasma spray (SPS) process, (a) radial injection [25,26], (b) axial injection [27] 3
Figure 1. 2: Schematic of various stages leading to coating formation in SPS [31] 4
Figure 1. 3: The schematic of a typical impinging gas-jet system [32] 5
Figure 1. 4: Schematic diagram of the high-velocity oxygen fuel (HVOF) spraying process [37] 6
Figure 1. 5: The flow diagram of the organization of dissertation 8

Figure 2. 1: Friction coefficient of high ionic potential binary oxides. The values are obtained from [14,15]. 15
Figure 2. 2: Air foil bearing systems in turbomachine [22] 16
Figure 2. 3: Example of contact locations and materials used in jet engine [25,26]. 17
Figure 2. 4: Oxidative wear mechanisms at low sliding speeds [53] 19
Figure 2. 5: Relation of friction force ($F = Ar\tau$) to substrate material hardness. **Top**: Hard counterface metal in contact with soft substrate metal (large Ar and small τ), **Middle**: Similar hardness of counterface metal and substrate metal in contact with each other (small Ar and large τ), **Bottom**: Similar hardness of counterface metal and substrate metal separated by a thin film of soft metal deposited on the substrate surface (both Ar and τ are small) [73] 20
Figure 2. 6: Relationship between ionic potentials and averaged friction coefficients of various oxides [15] 22
Figure 2. 7: Ionic potential of two oxides having same cationic charge but different radius (Reprinted from [15]). 22
Figure 2. 8: Variation of the coefficient of friction of simple oxides and binary/mixed oxides with the interaction parameter at T/T_m in the range of (a) 0.3-1, (b) 0.7-0.8 respectively [16] 23
Figure 2. 9: Comparison of the shear strength and Vickers hardness of Magnéli type titania versus their oxygen/titanium ratio [99] 25
Figure 2. 10: The layered structure of V_2O_5 [109] (a) and tribological behavior of vanadium-based oxides (b) 26
Figure 2. 11: Tribological behavior of molybdenum-based oxides 28
Figure 2. 12: Tribological behavior of tungsten-based oxides 29

Figure 2. 13: Schematic representation of the wear mechanism in different sliding cycles (a) start contacting, (b) formation of wear debris, (c) plastic deformation of debris and deformation of patchy layer, and (d) formation of transfer layer on ball [147]. 30
Figure 2. 14: Tribological behavior of copper oxide in various composites 31
Figure 2. 15: Maximum tested temperature of binary oxides in tribological testing.....32
Figure 2. 16: Temperature dependence of COF for VCN-(Ag) coatings [159]. 34
Figure 2. 17: SEM micrographs of VCN-Ag coating taken from areas outside (a) and inside (b,c) wear track after dynamic temperature ramp tribological tests terminated at 700 °C. Silver EDS map obtained from the wear track (d). SEM (e) and TEM (f) images of wear products on the surface of counterpart material with EDS mapping of Ag vanadate particle (insets in (e)) and SAED pattern and high-resolution TEM image (insets in (f)) [159]. 34
Figure 2. 18: Tribological behavior of vanadate-based oxides including [171,172]. 35
Figure 2. 19: Raman spectra of worn surfaces of NiCrAlY-Ag-Mo composite coating: (a) As-sprayed coating, (b) 20°C, (c) 200°C, (d) 400°C, (e) 600°C, and (f) 800°C [180]. 36
Figure 2. 20: Tribological behavior of molybdate-based oxides [173,191,200,201,192–199] 37
Figure 2. 21: Characterization of a selected area of the wear track and elemental mapping after tribotesting at 750°C (Left). Number of Ag/Cu clusters in at the sliding interface from MD simulations of $AgTaO_3$ and $CuTaO_3$ at 750°C as a function time (Right) [211]. 39
Figure 2. 22: Tribological behavior of tantalate-based oxides.....39
Figure 2. 23: *In-situ* Raman spectrum of NbN/Ag at different temperatures while heating ((a) 25°C, (b) 500°C, (c) 600°C, (d) 750°C) and during wear testing ((e) after 500 cycles, and (f) after 10,000 cycles) [212].....40
Figure 2. 24: Tribological behavior of niobate-based oxides 41
Figure 2. 25: Tribological behavior of tungstate-based oxides.....42
Figure 2. 26: Schematic diagram showing the high-temperature self-lubricating mechanism of NiCr–$BaCr_2O_4$ composite [248].....43
Figure 2. 27: Maximum tested temperature of Ternary oxides in tribological testing.....45
Figure 2. 28: Schematic diagram of generalized tentative wear mechanisms of binary and ternary oxides at different temperatures.....46

Figure 2. 29: An approximate range of COF for binary and ternary oxides over the effective temperature range.....48
Figure 2. 30: A possible research trend for different types of oxides in the near future.....50

Figure 3. 1: A schematic of the radial injection suspension plasma spray (SPS) process 65
Figure 3. 2: (a) SEM image of CuO powder morphology and (b) particle size distribution (PSD) of CuO powder.....68
Figure 3. 3: XRD pattern of the CuO feedstock powder and as-sprayed coatings 69
Figure 3. 4: XPS analysis of 3rd spray condition (a) Survey spectra; core spectra for (b) Cu 2p and (c) O 1s subshells. 70
Figure 3. 5: Friction coefficient of CuO coating at 25°C and 300°C 71
Figure 3. 6: Specific wear rate of CuO coatings at 25°C and 300°C.....72
Figure 3. 7: SEM images of the worn surfaces of CuO coatings at 25°C (a–c) and 300°C (d-f). 73
Figure 3. 8: XPS depth analysis of CuO coatings at (a) 25°C and (b) 300°C. 74
Figure 3. 9: Raman spectrum of unworn and worn coatings at (a) 25°C and (b) 300°C.....75
Figure 3. 10: SEM images of the counterball and corresponding EDS element analysis of the counterpart Al_2O_3 ball after sliding at 25°C and 300°C. (+ indicates the EDS point) 76
Figure 3. 11: Cross-sectional SEM micrographs of coatings prepared at different conditions: (a-b) 1st spray [10 wt% solid with spray distance (SD) 40 mm]; (c-d) 2nd spray [20 wt% solid with SD 40 mm]; (e-f) 3rd spray [20 wt% solid with SD 30 mm] 78
Figure 3. 12: Schematic friction and wear mechanisms of suspension plasma sprayed CuO coatings during dry sliding at (a) 25°C and (b) 300°C. ⊗ indicates sliding direction. 81

Figure 4. 1: A schematic of the radial injection suspension plasma spray (SPS) process.....91
Figure 4. 2: a) SEM morphology of tantalum oxide powder [inset: cross-section of powder], b) Ethanol-based particle size distribution of tantalum oxide powder.....95
Figure 4. 3: XRD data of tantalum oxide powders and as-deposited coating 96
Figure 4. 4: (a) Ta4f and (b) O1s spectra of tantalum oxide coating 97
Figure 4. 5: (a) low magnification SEM cross-section of tantalum oxide coating; and (b) high magnification cross-section of tantalum oxide coating (c) SEM top surface of tantalum oxide coating and corresponding (d) surface roughness.....98

Figure 4. 6: (a) Secondary SEM image of the cross-section of tantalum oxide coating and (b) corresponding ECCI showing the grains 98
Figure 4. 7: Coefficient of friction of tantalum oxide coating at 25°C and 300°C 100
Figure 4. 8: (a) Depth vs. lateral distance and (b) corresponding wear rate of tantalum oxide coatings at 25°C and 300°C 101
Figure 4. 9: The SEM wear tracks of tantalum oxide coatings and the corresponding EDS analysis at **(a-c)** 25°C and **(d-e)** 300°C. (+ indicates the EDS point).....102
Figure 4. 10: XPS depth profiles of unworn and worn surfaces of tantalum oxide coatings at 25°C and 300°C 103
Figure 4. 11: The SEM wear tracks cross-section of tantalum oxide coatings after sliding tests at **(a-b)** 25°C and **(c-d)** 300°C. ⊗-indicates sliding direction.....104
Figure 4. 12: The SEM images of counterball Al_2O_3 and corresponding EDS results at **(a, c)** 25°C and **(b, d)** 300°C. The star points indicate the EDS analysis. 105
Figure 4. 13: Schematic of wear mechanisms of tantalum oxide coatings at (a) 25°C and (b) 300°C 108

Figure 5. 1: XRD pattern of coatings prepared from (a) CoO and (b) NiO powder.....118
Figure 5. 2: SEM cross-section of (a) CoO and (b) NiO coating.....119
Figure 5. 3: Cross-sectional SEM line scan of NiO coating, showing the distribution of NiO and metallic Ni 119
Figure 5. 4: Friction coefficient vs no. of cycle of CoO and NiO coatings at room (RT) and high temperature (HT) 120
Figure 5. 5: SEM-EDS mapping of wear track after sliding 500 cycles at high temperature (HT) on the NiO coating 121
Figure 5. 6: Specific wear rate of CoO and NiO coatings at room (RT) and high temperature (HT).....121
Figure 5. 7: SEM micrograph of the wear tracks after dry sliding test of (a) CoO at RT, (b) CoO at HT; (c) NiO at RT and (d) NiO at HT. ↕ indicate sliding directions 122
Figure 5. 8: Raman spectrum of unworn and worn coatings at (a) room temperature (RT) and (b) high temperature (HT).....123
Figure 5. 9: SEM microstructures of Al_2O_3 counterfaces sliding against CoO coatings at (a-b) room temperature (RT), and (c-d) high temperature (HT).....124
Figure 5. 10: SEM microstructures of Al_2O_3 counterfaces sliding against NiO coatings at (a-b) room temperature (RT), and (c-d) high temperature (HT).....125

Figure 5. 11: SEM/FIB image of CoO coatings at (a) room temperature (RT) and (d) high temperature (HT). ECCI micrograph of this FIB cut of CoO wear track at (b-c) RT and (e-f) HT; **Zone I**: nanocrystalline/amorphous layer, **Zone II**: nanocrystalline zone, and **Zone III**: sub-micrometric zone. 126
Figure 5. 12: EDS mapping and line analysis (i.e., top to bottom) of CoO at room temperature (RT) and high temperature (HT) 127
Figure 5. 13: XPS depth profiles of CoO (a) coating, (b) wear track at room temperature (RT), and (c) wear track at high temperature (HT)..... 127
Figure 5. 14: SEM-cross-section of wear tracks of NiO coatings after tribotesting at room temperature (RT). Blue arrows and yellow circles showed spallation and cracks in the tribolayer. ⊗ indicate sliding direction. 128
Figure 5. 15: Friction and wear mechanisms of CoO coatings after dry sliding at (a) room temperature (RT) and (b) high temperature (HT). ⊗ indicate sliding direction. 129
Figure 5. 16: Friction and wear mechanisms of NiO coatings after dry sliding at (a) room temperature (RT) and (b) high temperature (HT). ⊗ indicate sliding direction. 131

Figure 6. 1 : XRD pattern of (a) $Co_{0.75}Ni_{0.25}O$, and (b) $Co_{0.5}Ni_{0.5}O$ coatings prepared from the respective powders. 141
Figure 6. 2: SEM cross-section of (a) $Co_{0.75}Ni_{0.25}O$ and (b) $Co_{0.5}Ni_{0.5}O$..... 142
Figure 6. 3: SEM EDS color map of $Co_{0.75s}Ni_{0.25}O$ coating (a) top surface, (b) cross-section 142
Figure 6. 4: SEM EDS color map of $Co_{0.5}Ni_{0.5}O$ coating (a) top surface, (b) cross-section 143
Figure 6. 5: Electron Channeling Contrast Imaging (ECCI) of the cross-section of $Co_{0.75}Ni_{0.25}O$ at RT (a-b) and after heating at 450°C (c-d) 144
Figure 6. 6: Electron Channeling Contrast Imaging (ECCI) of the cross-section of $Co_{0.5}Ni_{0.5}O$ at RT (a-b) and after heating at 450°C (c-d) 145
Figure 6. 7: Microhardness of $Co_{0.75}Ni_{0.25}O$ and $Co_{0.5}Ni_{0.5}O$ coatings at different temperatures 145
Figure 6. 8: Friction coefficient vs no. of cycles of Co-Ni-O coatings at different temperatures 146
Figure 6. 9: Specific wear rate of Co-Ni-O coatings at RT and HT..... 147
Figure 6. 10: (a-c) Secondary SEM, (b-d) BSE images and their corresponding EDS mapping of $Co_{0.75}Ni_{0.25}O$ at RT and HT. ↕ indicate sliding directions..... 149

Figure 6. 11: (a-c) Secondary SEM, (b-d) BSE images and their corresponding EDS mapping of $Co_{0.5}Ni_{0.5}O$ at RT and HT. ↕ indicate sliding directions. 150
Figure 6. 12: ECCI image of $Co_{0.75}Ni_{0.25}O$ (a-d) worn subsurfaces and corresponding (e) SEM/EDS mapping of (a) at RT. ⊗ indicate sliding directions. 152
Figure 6. 13: ECCI image of $Co_{0.75}Ni_{0.25}O$ (a-d) worn subsurface and corresponding (e) SEM/EDS mapping of (a) at HT. ⊗ indicate sliding directions. 153
Figure 6. 14: ECCI image of $Co_{0.5}Ni_{0.5}O$ (a-d) worn subsurface and corresponding (e) SEM/EDS mapping of (a) at RT. ⊗ indicate sliding directions. 154
Figure 6. 15: ECCI image of $Co_{0.5}Ni_{0.5}O$ (a-d) worn subsurface and corresponding (e) SEM/EDS mapping of (a) at HT. ⊗ indicate sliding directions. 155
Figure 6. 16: Raman spectrum of unworn and worn coatings at (a) 25°C and (b) 300°C 156
Figure 6. 17: (a-c) SEM image, and high magnification (b-d) EDS layered structures and corresponding elemental map distribution of alumina countersurfaces against $Co_{0.75}Ni_{0.25}O$ coating at RT and HT, respectively. ↕ indicate sliding directions. 158
Figure 6. 18: (a-c) SEM image, and high magnification (b-d) EDS layered structures and corresponding elemental map distribution of alumina countersurfaces against $Co_{0.5}Ni_{0.5}O$ coating at RT and HT, respectively. ↕ indicate sliding directions. 159
Figure 6. 19: Schematic of wear mechanisms of (a-b) $Co_{0.75}Ni_{0.25}O$ and (c-d) $Co_{0.5}Ni_{0.5}O$ at different temperatures. 163

Figure 7. 1: High temperature friction coefficient and wear rate of different oxide coatings as a function of (a-c) ionic potential, and (b-d) interaction parameter. * NiO coating worn out after 500 cycles. 174
Figure 7. 2. The specific wear rate of oxide coatings as a function of microhardness at (a) Room and (b) high temperature 177
Figure 7. 3 a) Powder morphology of CoO, CuO, Ta_2O_5, and NiO; (b) The sintering behavior of CoO, CuO, Ta_2O_5, and NiO powders at different temperatures. 178
Figure 7. 4. Room and elevated temperatures (a) friction coefficient, and (b) specific wear rate of different oxide coatings as a function of lattice parameter. 180

List of Tables

Table 2. 1: Chemical compositions of Tribaloy T400 and T800 [46] 19

Table 3. 1: SPS spray parameters used for depositing CuO coatings 66
Table 3. 2: The friction test parameters of the pin on disc tribometer 67
Table 3. 3: EDS analysis of the unworn and worn coatings at 25°C and 300°C 73

Table 4. 1: SPS parameters used for depositing tantalum oxide coating 91
Table 4. 2: The friction test parameters of the pin on disc tribometer 94
Table 4. 3: Characteristics of the tantalum oxide coatings..... 99
Table 4. 4: Wear rate of counterface Al_2O_3 against tantalum oxide coatings at 25°C and 300°C after dry sliding wear testing..... 106

Table 5. 1: Thermal spraying parameters used for depositing CoO and NiO coating 116
Table 5. 2: Wear rate of Al_2O_3 counterface against CoO and NiO coatings at RT and HT after dry sliding wear testing. 124

Table 6. 1: HVOF spraying parameters used for depositing $Co_{0.75}Ni_{0.25}O$ and $Co_{0.5}Ni_{0.5}O$ coatings 139
Table 6. 2: Characteristics of HVOF sprayed Co-Ni-O coatings..... 143
Table 6. 3: Average coefficient of friction and specific wear rate 147
Table 6. 4: Wear rate of counterface Al_2O_3 against $Co_{0.75}Ni_{0.25}O$ and $Co_{0.5}Ni_{0.5}O$ coatings at RT and HT after dry sliding wear testing. 157

List of Abbreviations

SPS	Suspension Plasma Spray
APS	Atmospheric Plasma Spray
HVOF	High Velocity Oxy Fuel
HVAF	High Velocity Air Fuel
COF	Coefficient of Friction or Friction Coefficient
RT	Room or Atmospheric Temperature
HT	High Temperature
XRD	X-ray Diffraction
XPS	X-ray Photoelectron Spectroscopy
SEM	Scanning Electron Microscopy
FESEM	Field Emission Scanning Electron Microscopy
EDS/EDX	Energy Dispersive X-ray Spectroscopy
FIB	Focused Ion Beam
ECCI	Electron Channeling Contrast Imaging
PVP	Polyvinylpyrrolidone
HV	Vickers Microhardness

Chapter 1

1.1 Introduction

Surface engineering has been an essential technology in enhancing the life cycle and efficiency of various contact interfaces such as power generation, transportation, materials processing, and aircraft engines. This can be achieved by minimizing the friction and improvement of wear resistance behavior of the components [1]. The science and technology of friction and wear behavior of the interacting surfaces is known as tribology. The word tribology derived from the Greek word, "*tribo*" meaning rubbing and "*logos*" meaning study [2]. In 1966, Peter Jost in the UK first coined the word tribology [3]. Friction is the force resisting the relative motion of two solid surfaces in contact. When any of these surfaces slide or move as compared to other the surfaces convert the kinetic energy into thermal or heat energy [4]. Generally, the friction coefficient (μ) is used to describe the friction. Mathematically, the coefficient of friction is the ratio of the frictional force arriving from the surfaces to the applied normal load.

$$\text{Friction coefficient } (\mu) = \frac{\text{Friction force } (F_F)}{\text{Applied force } (F_N)} \qquad (1.1)$$

On the other hand, wear is the removal of the material or progressive damage of the surfaces in contact due to rolling, sliding or impact [5]. Surfaces are generally not perfectly smooth and microscopically all the smooth surfaces have some roughness (i.e., asperities). Whenever the two surfaces are in relative motion, the asperities can be displaced from the interacting surfaces. The displacement of the materials can transfer to the counter surfaces or may break as wear debris. The generation of the wear debris could be the reason for mechanical or chemical means and normally induced through frictional heating. However, based on different conditions the wear can be classified in different ways such as abrasive, adhesive, fatigue, erosion, corrosion and many more [6]. Therefore, proper knowledge of tribology in various fields can save an estimated 1.3% to 1.6% of a developed nation's gross domestic product (GDP) [7].

The wear resistance of the contacting interfaces can be improved by applying coatings. For instance, conventional alloys and composites are widely used as coating materials in various contact interfaces in the gas turbine engine and aerospace industries [8–10]. These alloys form *in-situ* lubricious oxides during sliding at high temperatures, which help to reduce friction and wear [11–13]. However, the formation of an oxide-based film on the contact zones

takes a long time and can vary depending on the chemical behavior of the materials as well as the contact conditions and environment. In most cases, the traditional alloys or composites lead to a long running-in period, which ultimately causes a gradual increase in friction and wear. Since the lubricious oxide is responsible for low wear and steady state friction coefficient at high temperatures, one idea is to replace the conventional alloys/composites and use such oxides instead. Based on the prior work, Peterson's data [14,15], ionic potential [16,17], and interaction parameters [18,19], which emphasis the lubricity at high temperatures (more details can be found in **Chapter 2**), examples of such oxides include CuO, Ta_2O_5, CoO, NiO, Co-Ni-O.

In order to produce or mimic the *in-situ* oxides or lubricious oxides as a coating material on the components or substrates, thermal spray technique offers promising advantages such as lower cost, lower complexity, atmospheric deposition condition, ease of application to large surfaces, and high deposition efficiency in comparison to conventional thin film coating deposition processes. These advantages make it easier to deposit the coating on a large and wide surface of any machinery components [1,20].

1.2 Thermal Spray Process

In general, in thermal spray process, a heat source, which can be a combustion or a non-combustion source such as an electric arc or a plasma, is used to fully or partially melt the feedstock materials that are pushed at high velocities toward a substrate by a stream of gas or an atomization liquid jet. A variety of materials, (i.e., metals, ceramics, ceramics, cermet, polymers, and a mixture of them), can be deposited by propelling the molten materials on the substrate. The feedstock can be in the form of powders, wires, cored wires, ceramic cords or rods, suspensions, or solution precursors. Upon impact, the molten or semi-molten droplets form splats that rapidly cool down and solidify. Thus, a layer of coating is formed by the collection of these splats on the surface of the substrate [21]. Various processes can be used in thermal spraying that can differ significantly, most notably in how thermal and kinetic energy are produced [20].

By 2025, the global thermal spray market is expected to grow to 14.99 B$ at a rate of 6.7 %. The main focused areas are aerospace (32.3 % in 2017), industrial gas turbines, and wear and corrosion-resistant coatings for the oil and gas industry [22]. Thermal spraying in North America is mainly concentrated on pulp and paper, aero-engine repair, process industry (valves), power generation, and mechanical engineering. Of these, the aerospace industry, especially engine components, is one of the most critical areas, where hard metal and ceramic

coatings are used along with metallic bond coats mainly for wear, corrosion, and thermal protection. The surface morphology, microstructure, and characteristics of the coatings can be governed by controlling the spray parameters. Various thermal spray techniques were used, such as high-velocity oxygen fuel (HVOF), high-velocity air fuel (HVAF), atmospheric plasma spray (APS), and suspension plasma spray (SPS).

In this dissertation, two approaches are used to prepare CuO, Ta_2O_5, CoO, NiO, Co-Ni-O coatings. CuO, Ta_2O_5, and NiO coatings were deposited by SPS, on the other hand, CoO, and Co-Ni-O coatings were developed by using HVOF.

1.2.1 Suspension Plasma Spray (SPS)

The SPS process was invented in the mid-1990s and has shown its ability to deposit submicron size materials especially ceramics or oxides [23]. These submicron size powders are usually challenging to deposit with other conventional processes such as HVOF, HVAF, APS due to the difficulties associated with injection and low flowability. This situation raises the need for a relatively new technique such as suspension plasma spray (SPS) to overcome these problems [24]. In plasma spraying, the plasma plume is generated by an electric arc between an anode and a cathode. The plasma gas injected in the torch is heated by the arc and exits the nozzle as a plasma jet with high temperature and high velocity.

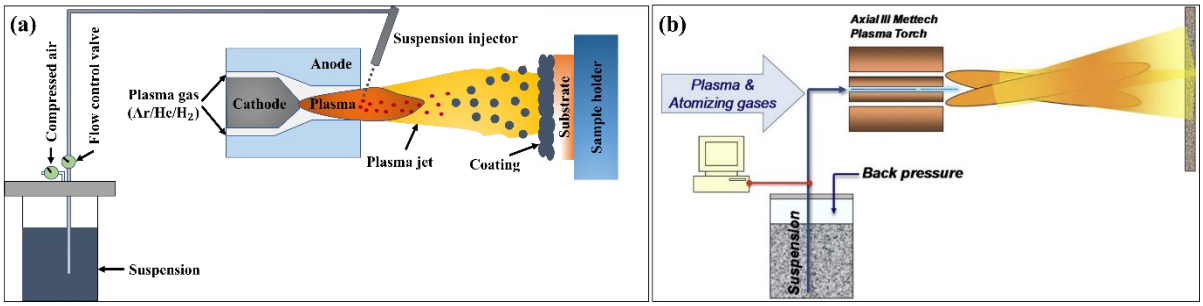

Figure 1. 1: The schematic of a suspension plasma spray (SPS) process, (a) radial injection [25,26], (b) axial injection [27]

In the SPS process, the feedstock powders are dispersed in a liquid (typically ethanol or water) with a dispersing agent (i.e., help to stabilize the suspension) to form a suspension slurry and are injected into the plasma jet to be deposited [25,26]. The injection of liquid suspension in the plasma jet can be either radial or axial. The schematic of SPS process with radial and axial injection is shown in **Figure 1. 1**. Upon exposure to the high temperature and speed of the plasma jet, the suspension breaks up into micro-droplets, the liquid evaporates in flight while the solid particles agglomerate, melt, and impact on the substrate to build up a coating [28,29]. The coating formation stages in the SPS process are schematically presented

in **Figure 1. 2**. In the SPS process, the spray parameters such as, nozzle size, gas composition, plasma powder, spray distance, preheating substrate temperatures, and solid loading in the suspension play an important role for varying the coating microstructures. The unique microstructures resulting from SPS deposition from the accumulation of thin splats on the substrate can be beneficial to the wear resistance of the coating [30].

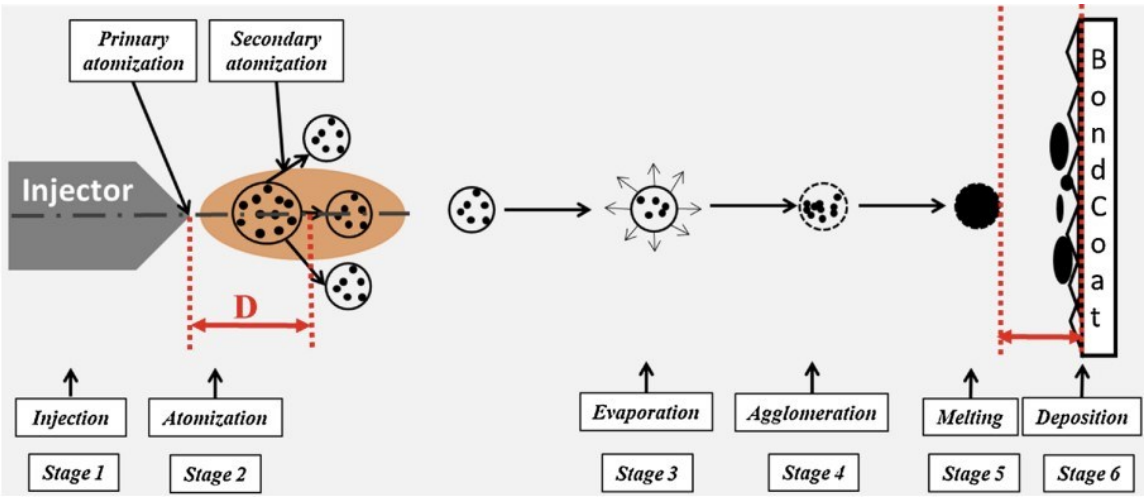

Figure 1. 2: Schematic of various stages leading to coating formation in SPS [31]

An important feature of SPS is its unique columnar microstructure. The formation of columnar structures in SPS coatings can be explained by the shadowing effect that affects the deposition of individual particles or droplets on the surface. When the plasma jet hits the substrate surface, the molten particles or droplets follow different trajectories depending on their size, and momentum, as shown in the **Figure 1. 3** [32]. The smaller and lighter particles with low momentum are entrained by the plasma stream, follow trajectories almost parallel to the substrate surface, and attach to the surface asperities at a shallow angle rather than impacting them normally. In contrast to these small particles, the larger particles with higher momentum continue along their initial trajectory and impinge on the substrate.

Furthermore, the columnar type of microstructure can be understood by considering the Stokes number (St) [33] as per equation (1.2).

$$St = \frac{\rho d^2 V}{\mu \, l_{BL}} \qquad (1.2)$$

where ρ is the density of the particle, d is its diameter, v is its velocity, μ is plasma viscosity, and l_{BL} is the boundary layer thickness. Alternatively, the Stokes number is the ratio of the time taken for momentum transfer from fluid to particles to the time of the direction change of the flow [34]. The micron-size particle momentum is relatively low; hence, they are heavily influenced by the drag force of the plasma stream in the boundary layer close to the

substrate. Thus, when St < 1, the porosity and cauliflower shape microstructure is more prominent as most of the particles impact the substrate at a shallow angle.

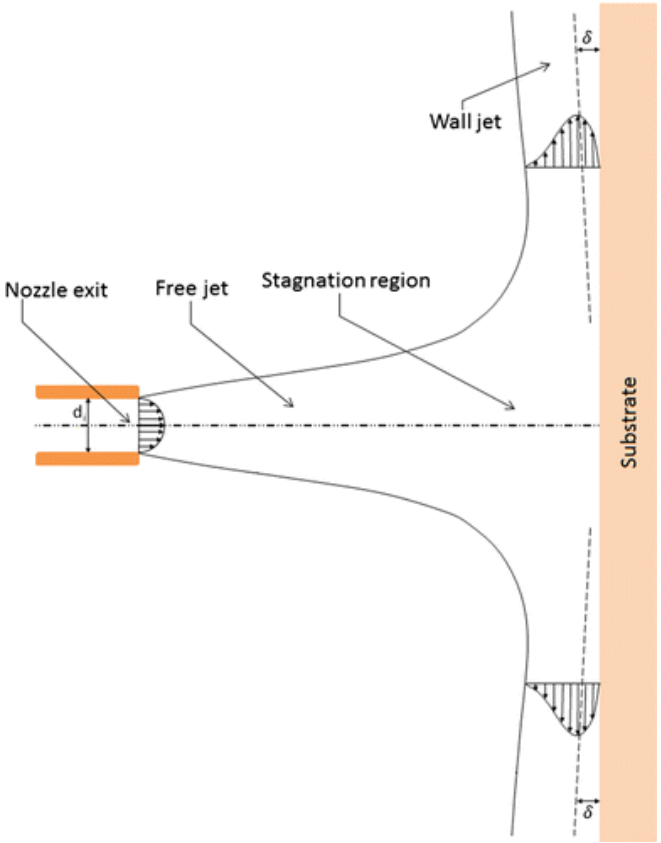

Figure 1. 3: The schematic of a typical impinging gas-jet system [32]

1.2.2 High-Velocity Oxygen Fuel (HVOF)

In the early 1980s, high velocity oxy-fuel technology was commercially introduced. In this process, the fuel gas or liquid (i.e., hydrogen, kerosene, propylene, ethylene, acetylene, etc.), and pure oxygen are introduced into the combustion chamber and then ignited and combusted [35,36]. The exhaust gas is accelerated in a converging-diverging nozzle connected to the chamber, where supersonic gas velocity can be achieved. As the high velocity flow (500-1200 m/s) exits the nozzle, shock diamonds are formed due to the pressure difference between the high velocity flow and the ambient atmosphere. The coating material in the form of powder (nominal size range 10-45 μm) can be injected radially or axially into the gas with nitrogen or argon as the carrier gas. The powder feedstock melts or partially melts in the flame and is deposited on the substrate. This process is typically used to produce not only metal and cermet coatings, which have relatively low melting points, but also ceramic coatings such as alumina [37]. A schematic diagram of a typical HVOF system is shown in **Figure 1. 4**.

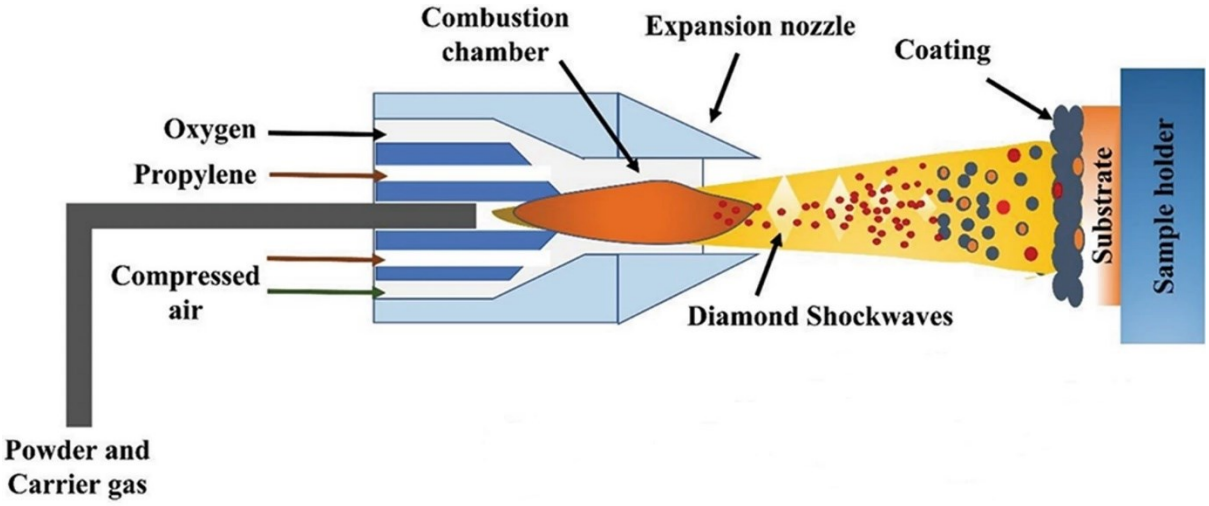

Figure 1. 4: Schematic diagram of the high-velocity oxygen fuel (HVOF) spraying process [37]

Because the process temperature in HVOF is much lower than in plasma spraying, the particles may not be completely melted during HVOF deposition. Nevertheless, the high particle velocity results in the formation of a dense stack of flattened particles on the substrate, resulting in smooth and uniform coatings with good adhesion to the substrate. In the HVOF process, the shorter residence time of the powder in the flame and the lower flame temperature compared to plasma spraying methods result in a reduced possibility of reduction, oxidation or decomposition of the powder particles during spraying [1].

1.3 Objectives

The main objective of this work is to develop thermally sprayed coatings that will mimic lubricous glaze layers (i.e., CuO, Ta_2O_5, and CoO-based) and consequently will improve the tribological performance in demanding conditions. The following sub-objectives have been identified.

- Identify the effect of spray parameters on the coating microstructure of different oxides.
- Critically evaluate the friction and wear resistance behavior of oxides at different temperatures.
- Identify the interfacial processes leading to low friction and wear of oxide-based coatings in various environments.
- Provide recommendations to the research community regarding coating deposition processes, innovative lubrication strategies, and critical parameters affecting the endurance life of oxide-based coatings.

1.4 Organization of dissertation

This dissertation comprises eight chapters and an appendix. **Figure 1. 5** shows the overall organization of the thesis and the motivation between each chapter. Each chapter is also described in detail below.

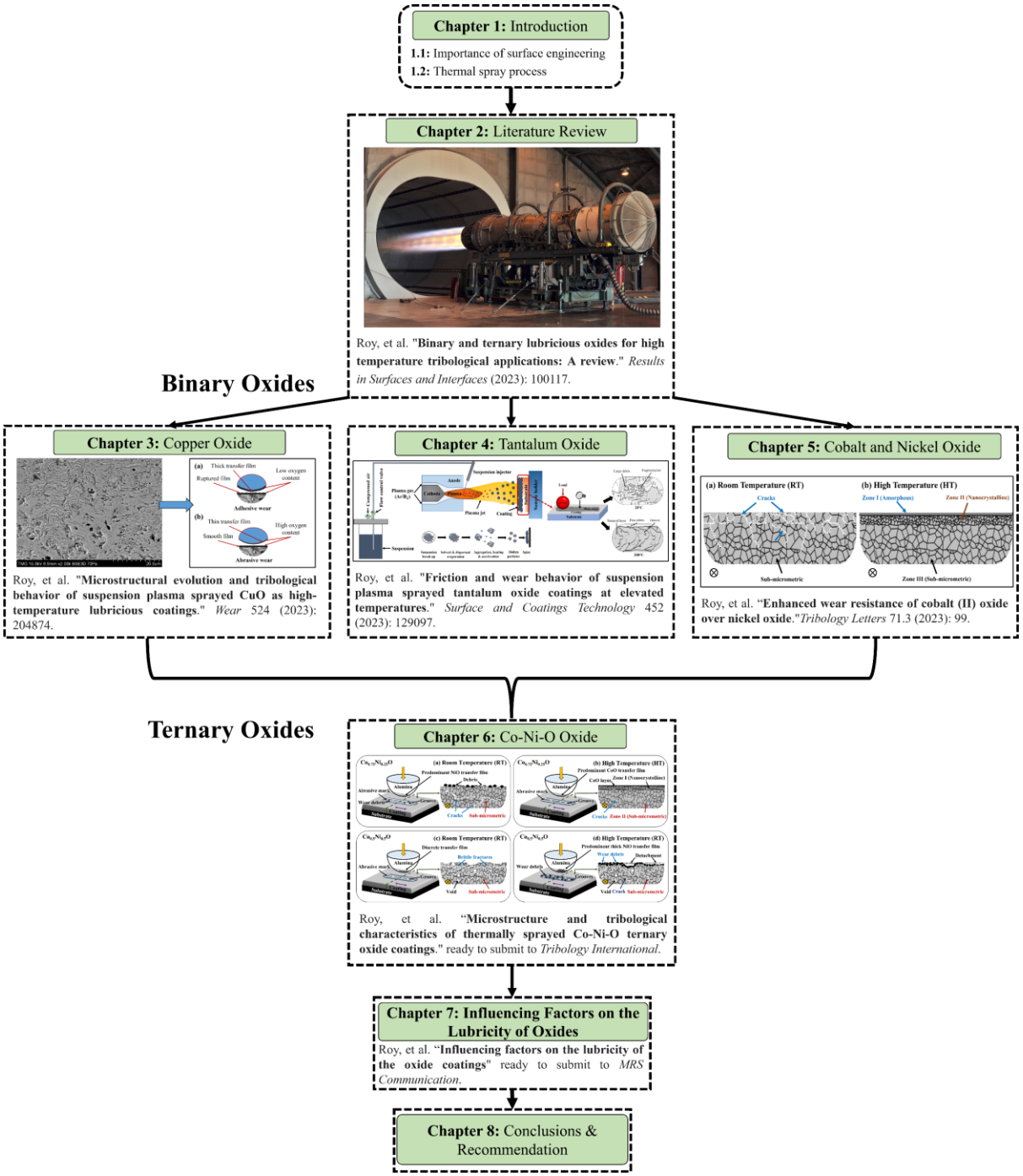

Figure 1. 5: The flow diagram of the organization of dissertation

Chapter 1 contains the description of surface engineering, its importance, and the brief introduction of tribology. In addition, **Chapter 1** includes a brief explanation of the thermal spray techniques used in this dissertation (i.e., SPS and HVOF). Finally, the objectives and organization of the dissertation are presented.

Chapter 2 is basically a review article that comprehensively focuses on the tribology of binary and ternary oxides at different temperatures. This chapter also prioritizes the importance of high temperature tribology, materials, and advantages of oxides or oxide coatings compared to the traditionally used various alloys. Furthermore, a generalized and tentative wear reduction mechanism of oxides at different temperatures has been highlighted. In addition, the future perspective of various oxides in the field of tribology has been incorporated.

Chapter 3 includes the investigation of suspension plasma sprayed copper oxide coatings and their chemical reduction mechanisms to Cu_2O and pure metallic Cu. The effect of solid loading in suspension and spraying parameters i.e., nozzle size, spraying distance were also included in this study. Furthermore, the friction and wear resistance mechanisms of the copper oxide at atmospheric and elevated temperature were discussed using SEM worn surface morphology, counterface analysis, and XPS technique.

Chapter 4 discusses the tribology of the tantalum oxide coating developed by the SPS process. A dense microstructure of the coating was developed by trial or varying the spraying parameters. A tiny amount of sub-oxide (i.e., tantalum oxide) was found on the powder and coating. It was confirmed by XRD and ECCI techniques. The grain size and crystallite size of the coatings were also determined using ECCI and Scherrer equation, respectively. The friction and wear of this coating was critically evaluated. It was concluded that brittle and ductile wear behaviors are the dominant wear mechanisms at room and elevated temperatures, respectively.

Chapter 5 covers the coating of cobalt and nickel oxides using SPS and HVOF, respectively. The reduction of pure metallic Ni during NiO spraying is briefly discussed. In addition, the formation of amorphous phase of CoO near the wear track during high temperature sliding is discussed. The reasons for the wear of the nickel oxide coating after 500 cycles at elevated temperatures were also discussed. The superior wear resistance mechanism of CoO over NiO was highlighted using Focused Ion Beam (FIB) and Electron Channeling Contrast Imaging (ECCI). Based on the *ex-situ* or experimental, the proposed wear resistance mechanisms of CoO and NiO were discussed.

Chapter 6 incorporates the Co-Ni-O coatings produced by the HVOF process. The varying amount of CoO and NiO content in Co-Ni-O ternary solid solution was discussed in terms of coating microstructure and tribology. It was shown that the Co-Ni-O solid solution becomes brittle with increasing NiO content. In addition, the tribological behavior of the Co-Ni-O coatings decreases with increasing NiO content at high temperatures. However, the opposite trend was observed in room or atmospheric conditions.

Chapter 7 compares the friction and specific wear rate of the oxides (i.e., CuO, Ta_2O_5, CoO, NiO, Co-Ni-O). Furthermore, the friction and wear values or more specifically the lubricity of the oxides were discussed with the sintering ability, ionic potential, interaction parameter, hardness, thermal conductivity, and lattice parameter.

Chapter 8 summarizes the main messages, conclusions and contributions of this research work and provides the recommendation for the future work.

Appendix A includes the supplementary data for review article (i.e., Chapter 2).

Appendix B includes the supplementary data for chapter 7.

1.5 References

[1] Fauchais PL, Heberlein JVR, Boulos MI. Thermal spray fundamentals: from powder to part. Springer Science & Business Media; 2014.

[2] Czichos H, Woydt M. Introduction to tribology and tribological parameters. ASM handbook. Vol. 18, Frict. Lubr. wear Technol., ASM International; 2017, p. 3–15.

[3] Jost HP. Lubrication: Tribology; Education and Research; Report on the Present Position and Industry's Needs (submitted to the Department of Education and Science by the Lubrication Engineering and Research) Working Group. HM Stationery Office; 1966.

[4] Popov VL. Contact mechanics and friction. Springer; 2010.

[5] Chattopadhyay R. Surface wear: analysis, treatment, and prevention. ASM international; 2001.

[6] Varenberg M. Towards a unified classification of wear. Friction 2013;1:333–40.

[7] STLE. What is Tribology? 2023. WWW.stle.org.

[8] Aouadi SM, Gao H, Martini A, Scharf TW, Muratore C. Lubricious oxide coatings for extreme temperature applications: A review. Surf Coatings Technol 2014;257:266–77. https://doi.org/10.1016/j.surfcoat.2014.05.064.

[9] Stone DS, Harbin S, Mohseni H, Mogonye JE, Scharf TW, Muratore C, et al. Lubricious silver tantalate films for extreme temperature applications. Surf Coatings Technol 2013;217:140–6. https://doi.org/10.1016/j.surfcoat.2012.12.004.

[10] Gassner G, Mayrhofer PH, Kutschej K, Mitterer C, Kathrein M. A new low friction concept for high temperatures: Lubricious oxide formation on sputtered VN coatings. Tribol Lett 2004;17:751–6. https://doi.org/10.1007/s11249-004-8083-z.

[11] Viat A, Dreano A, Fouvry S, De Barros Bouchet MI, Henne JF. Fretting wear of pure cobalt chromium and nickel to identify the distinct roles of HS25 alloying elements in high temperature glaze layer formation. Wear 2017;376–377:1043–54. https://doi.org/10.1016/j.wear.2017.01.049.

[12] Viat A, De Barros Bouchet MI, Vacher B, Le Mogne T, Fouvry S, Henne JF. Nanocrystalline glaze layer in ceramic-metallic interface under fretting wear. Surf Coatings Technol 2016;308:307–15. https://doi.org/10.1016/j.surfcoat.2016.07.100.

[13] Viat A, Guillonneau G, Fouvry S, Kermouche G, Sao Joao S, Wehrs J, et al. Brittle to ductile transition of tribomaterial in relation to wear response at high temperatures 2017;392:60–8.

[14] Peterson MB, Murray SF, Florek JJ. Consideration of lubricants for temperatures above 1000 f. ASLE Trans 1959;2:225–34. https://doi.org/10.1080/05698195908972374.

[15] Peterson MB, Florek JJ, Lee RE. Sliding characteristics of metals at high temperatures. ASLE Trans 1960;3:101–9.

[16] Erdemir A. A crystal-chemical approach to lubrication by solid oxides. Tribol Lett 2000;8:97–102. https://doi.org/10.1023/a:1019183101329.

[17] Erdemir A. A crystal chemical approach to the formulation of self-lubricating nanocomposite coatings. Surf Coatings Technol 2005;200:1792–6.

[18] Dimitrov V, Komatsu T. Classification of simple oxides: A polarizability approach. J Solid State Chem 2002;163:100–12. https://doi.org/10.1006/jssc.2001.9378.

[19] Prakash B, Celis J-P. The lubricity of oxides revised based on a polarisability approach. Tribol Lett 2007;27:105–12.

[20] Fauchais PL, Heberlein JVR, Boulos MI. Overview of thermal spray. Therm. spray Fundam., Springer; 2014, p. 17–72.

[21] Davis JR. Handbook of thermal spray technology. ASM international; 2004.

[22] Size DIM, Growth DIMS. Share & Trends Analysis Report By Product (Titanium Implants, Zirconium Implants), By Region (North America, Europe, Asia Pacific, Latin America, MEA), And Segment Forecasts, 2018-2024. Pers Med Mark Anal By Prod Segm Forecast To 2022 2018.

[23] Gitzhofer F, Bouyer E, Boulos MI. Suspension plasma spray 1997:U.S. Patent No. 5,609,921.

[24] Vardelle PF and A. Solution and Suspension Plasma Spraying of Nanostructure Coatings. Adv Plasma Spray Appl 2012:149–88.

[25] Roy A, Sharifi N, Munagala VN V, Alidokht SA, Patel P, Makowiec M, et al. Microstructural evolution and tribological behavior of suspension plasma sprayed CuO as high-temperature lubricious coatings. Wear 2023:204874.

[26] Roy A, Munagala VNV, Patel P, Sharifi N, Alidokht SA, Makowiec M, et al. Friction and wear behavior of suspension plasma sprayed tantalum oxide coatings at elevated temperatures. Surf Coatings Technol 2023;452:129097.

[27] Tarasi F, Medraj M, Dolatabadi A, Oberste-Berghaus J, Moreau C. Amorphous and crystalline phase formation during suspension plasma spraying of the alumina–zirconia composite. J Eur Ceram Soc

2011;31:2903–13.
[28] Kozerski S, Łatka L, Pawlowski L, Cernuschi F, Petit F, Pierlot C, et al. Preliminary study on suspension plasma sprayed ZrO2+8wt.% Y2O3 coatings. J Eur Ceram Soc 2011;31:2089–98. https://doi.org/10.1016/j.jeurceramsoc.2011.05.014.
[29] Pawlowski L. Suspension and solution thermal spray coatings. Surf Coatings Technol 2009;203:2807–29. https://doi.org/10.1016/j.surfcoat.2009.03.005.
[30] Darut G, Ben-Ettouil F, Denoirjean A, Montavon G, Ageorges H, Fauchais P. Dry sliding behavior of sub-micrometer-sized suspension plasma sprayed ceramic oxide coatings. J Therm Spray Technol 2010;19:275–85. https://doi.org/10.1007/s11666-009-9415-1.
[31] Ganvir A, Calinas RF, Markocsan N, Curry N, Joshi S. Experimental visualization of microstructure evolution during suspension plasma spraying of thermal barrier coatings. J Eur Ceram Soc 2019;39:470–81.
[32] Jadidi M, Mousavi M, Moghtadernejad S, Dolatabadi A. A three-dimensional analysis of the suspension plasma spray impinging on a flat substrate. J Therm Spray Technol 2015;24:11–23.
[33] Fauchais P, Vardelle M, Vardelle A, Goutier S. What Do We Know, What are the Current Limitations of Suspension Plasma Spraying? J Therm Spray Technol 2015;24:1120–9. https://doi.org/10.1007/s11666-015-0286-3.
[34] Mauer G, Vaßen R. Coatings with Columnar Microstructures for Thermal Barrier Applications. Adv Eng Mater 2020;22:1–9. https://doi.org/10.1002/adem.201900988.
[35] Pawlowski L. The science and engineering of thermal spray coatings. John Wiley & Sons; 2008.
[36] Oksa M, Turunen E, Suhonen T, Varis T, Hannula S-P. Optimization and characterization of high velocity oxy-fuel sprayed coatings: techniques, materials, and applications. Coatings 2011;1:17–52.
[37] Patel P, Alidokht SA, Sharifi N, Roy A, Harrington K, Stoyanov P, et al. Microstructural and Tribological Behavior of Thermal Spray CrMnFeCoNi High Entropy Alloy Coatings. J Therm Spray Technol 2022:1–17.

Chapter 2

Binary and Ternary Lubricious Oxides for High Temperature Tribological Applications: A Review[1]

Abstract

Oxides and oxide-based coatings have been widely used as solid lubricants in demanding operating conditions to achieve low friction and wear due to their higher thermal and chemical stability. However, their tribological performance is highly dependent on the test temperatures and the surrounding environment. This article provides a comprehensive review of low-friction oxides and oxide-based coatings in relation to the influence of operating temperature on their tribological performance and their potential use as solid lubricants. Special emphasis is placed on the tribological behavior of binary and ternary oxides developed over the last few decades. Furthermore, this review summarizes the high temperature tribology, mechanisms and interfacial processes of the oxides leading to low friction coefficient and wear in high temperature applications.

Keywords: Binary oxides, ternary oxides, solid lubricants, high-temperature, tribology

[1] This chapter has been published as a review article in the *Results in Surfaces and Interfaces.* **A. Roy**, P. Patel, N. Sharifi, R. R. Chromik, P. Stoyanov, C. Moreau. "Binary and Ternary Lubricious Oxides for High-Temperature Tribological applications: A Review." *Results in Surfaces and Interfaces* (2023): 100117.

2.1 Introduction

Liquid and solid lubricants have traditionally been used to reduce friction as well as wear on mating or sliding surfaces. However, many of these lubricants are not suitable for applications in extreme environments (e.g., high-temperature, vacuum or high pressure as they evaporate quickly under these conditions) [1]. Failure to lubricate the sliding components results in poor tribological performance, high maintenance, and material replacement cost, and interruption of the operating cycle. The challenges of handling bulk liquid lubricants and their environmental concerns are other reasons that limit their use. However, the complexity of the sliding interface and the high temperature requirements inhibit the use of liquid lubricants, making a protective coating highly desirable. Coatings have to withstand very high temperatures due to the higher frictional stress in the sliding contacts. The reduction of this temperature (i.e., frictional heating) and the improvement of the wear resistance of the sliding parts in dry conditions could be achieved by using coatings based on solid lubricants. Some solid lubricants, such as graphite and MoS_2, provide excellent lubricity at low to moderate temperatures of 300°C due to their so-called layer structure and transfer film formation. However, the tribological performance of graphite is limited by the working environment because moisture or condensable vapor is needed to activate its lubricity [2]. On the other hand, MoS_2 exhibit a low coefficient of friction in dry atmosphere and vacuum conditions, whereas, MoS_2 oxidizes rapidly under normal atmospheric/humidity conditions and increases the coefficient of friction (COF) by more than two orders of magnitude [2,3]. Soft materials such as Ag, Au, etc. are reliable metal lubricants in air and vacuum but at high temperatures they undergo excessive plastic deformation and are extruded from the contact zone, thus limiting their improved tribological performance [4,5].

Oxidation is the inevitable phenomenon of metal or alloy when subjected to extreme working conditions in the presence of air. Oxidation continually thins the material object and leads to the possibility of failure [6]. Oxides or oxide-based coatings (i.e., made, or deposited in the form of oxides) could be the possible solution to prevent oxidation of the components in high-temperature applications due to their chemical and structural stability. However, such oxides have strong covalent bonds in the plane, which favors the difficulty of shearing the surfaces [7]. As a result, many oxide ceramics can exhibit high coefficients of friction (greater than 0.8), high contact stresses, and produce surface cracks and wear debris. However, these disadvantages of the materials can be turned into advantages if it is possible to produce *in-situ* lubricious oxide by tribo-oxidation [8]. For instance, two types of low friction oxides can be

formed either directly or during sliding at high temperatures; (i) Magnéli phases or substoichiometric oxides (Me_nO_{2n-1}, Me_nO_{3n-1}, Me_nO_{3n-2}) [9–12], and (ii) inherently lubricious oxides. The purpose of this article is to provide an overview of up-to-date research on low friction oxides and oxide-based binary and ternary coatings, and their operating principles under harsh working conditions. It should be noted that the comparison of the tribological performance that has been reported here has been taken as a generalized value since the friction and wear are not the intrinsic properties of the materials, but the system response [13]. The author believes that this review of the oxides will help to identify the research gap as well as the selection of suitable oxides according to their applications.

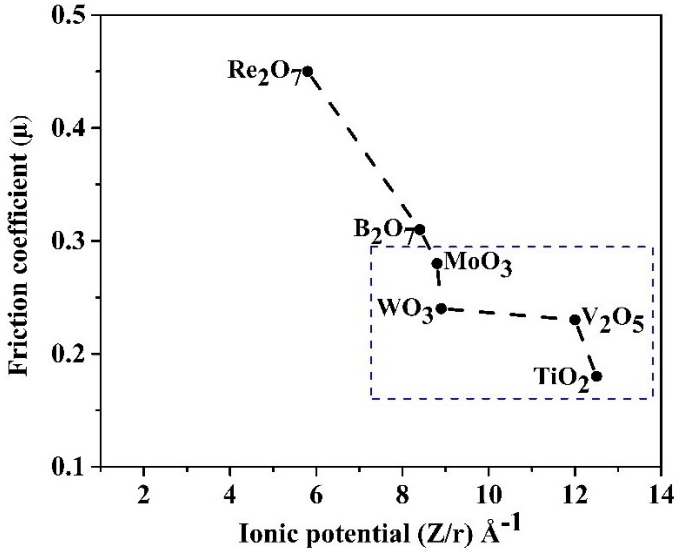

Figure 2. 1: Friction coefficient of high ionic potential binary oxides. The values are obtained from [14,15].

This review article is divided into four main categories: (i) high temperature tribology, its applications, materials, and interfacial processes (**section 2.2**), (ii) friction coefficient and interfacial mechanisms of binary oxides with high ionic potential as shown in **Figure 2. 1** with the dotted rectangle (**section 2.3**). It should be noted that lubricious binary oxides with low ionic potential ($\varphi = 2.4$) such as CuO are also discussed in this section. However, despite their high ionic potential, Re_2O_7 and B_2O_7 based oxides are not discussed in this paper due to the limited research and quite different frictional behavior as compared to other oxides at different temperatures [16]. **Section 2.4** focuses on (iii) the friction and wear mechanisms of the ternary oxides. These oxides can be further classified into Ag/non-Ag based and other ternary oxides such as sulfates, carbonates, and chromates based on the wear mechanisms at elevated temperatures. Finally, in **section 2.5** it has been proposed a (iv) interfacial and wear mechanisms of oxides over a wide temperature range.

2.2 High temperature tribology and its application

2.2.1 What is high temperature tribology?

Tribology is the science and technology of interacting surfaces in relative motion. It comprises of the principles and applications of friction, wear, and lubrication [17]. The term "high temperature tribology" is sometimes ambiguous, and the definition can change depending on the materials in the tribosystem. The temperature that is considered high for the polymer will not be high for metals or ceramics. When working with traditional lubricants such as oils and greases, "high temperature" indicates the temperatures at which these systems start to break down and exhibit high friction and wear [18]. The focus of this article is on oxides and oxide-based coatings, so tribological testing at anywhere between 500°C and 1000°C falls into the category of high temperature tribology. This temperature range is closely associated with the use of oxide-based lubricants, which can maintain desired lubricating properties up to their melting temperatures. In particular, high temperature tribology has recently gained significant interest in severe operating environments, sometimes exceeding 900°C. The increased demand for the development of durable and efficient technologies in various applications also emphasizes the interest in high temperature tribology [19].

2.2.2 High temperature tribology applications

With the advancement of science and technology, extreme tribology or high temperature tribology has gained significant interest in the last few decades in various fields, such as aerospace (airfoil bearings, rolling element bearings, hot and cold sections of the engine, satellite components), automotive (engine bearings, pistons, traction drive), metal forming, power generation industries [19–21].

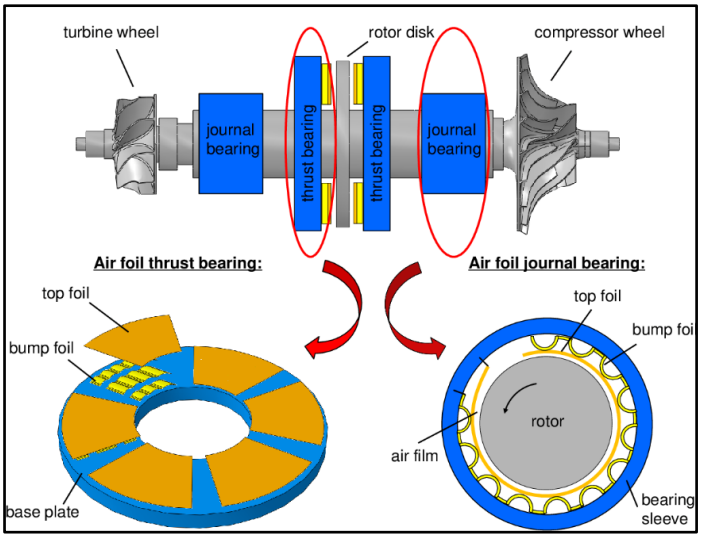

Figure 2. 2: Air foil bearing systems in turbomachine [22]

Air foil bearings are an example of components used at elevated temperatures without the need for liquid lubrication (**Figure 2. 2**). The system consists of a top and a bump foil that support the rotating shaft as shown in **Figure 2. 2**. The foil is in contact with the shaft at rest and at higher speeds, a thin film/gap is created between the top foil and the journal due to hydrodynamic pressure [23]. Thus, at low speeds i.e., during acceleration at startup (room temperature) and deceleration at shutdown (high temperature), the bearing makes contact with the raceway. The variation in these operating conditions presents a challenge because the materials must provide lubricity over a wide range of temperatures for an extended period of time. Similar to the air foil bearing, the rolling element bearing of the gas turbine engine, the bearing of an automotive diesel engine and it's piston also operate under high temperature conditions [24]. Therefore, maintaining solid lubrication to minimize the friction and wear during startup and shutdown periods is a challenging demand.

The next-generation gas turbine engines are required to reduce fuel consumption by a significant amount, which requires a step-change in the design and operating environment of the mechanical systems (e.g., higher temperature, higher speeds and contact pressures) [25,26]. **Figure 2. 3** shows the complete cross-section of a jet engine and the contacting interfaces which are further divided into two categories: (i) clearance control and (ii) tribological interfaces. Engine performance is dependent on the tied clearances. Just a 1% reduction in engine bleed results in a 0.4% reduction in specific fuel consumption [27]. Furthermore, the tribological materials used in jet engines are classified into three groups: (i) hard coatings, (ii) soft coatings, and (iii) solid lubricants. It can be seen that under high temperature conditions oxide-based materials are recommended to reduce friction and wear.

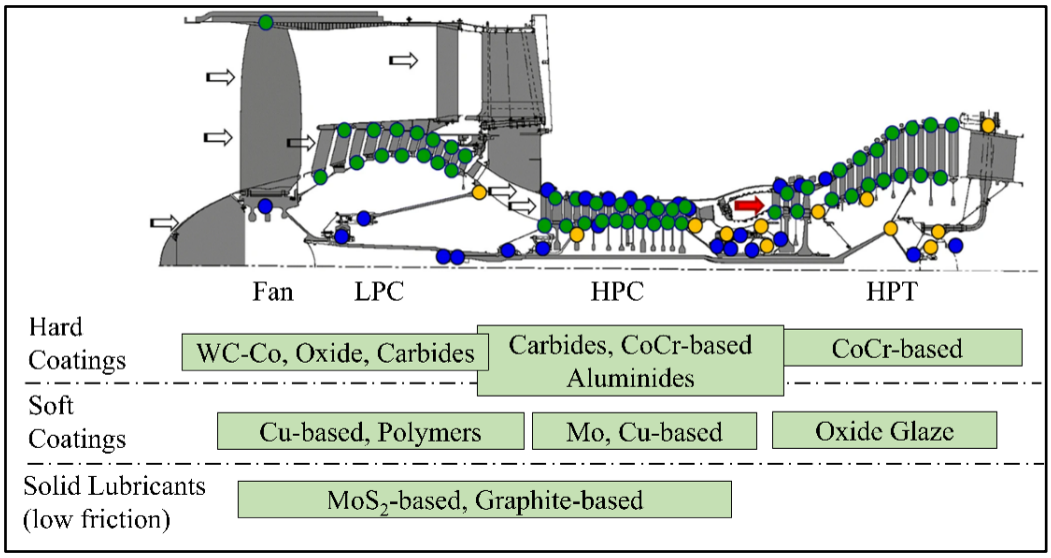

Figure 2. 3: Example of contact locations and materials used in jet engine [25,26].

Metal forming or metal working processes can involve temperatures of greater than 800°C [28]. Such a high temperature can cause degradation of the workpiece, resulting in premature failure. Therefore, friction (i.e., frictional heating) between metal and forming tools has a great influence on process performance and finished products [29]. The use of solid lubricants as a coating on the tool surface could provide low friction and wear, as well as help minimize frictional heat. However, the high temperature working conditions and lubricant residues could be problematic in the production line [30]. On the other hand, high temperature is also an important factor for the high-speed machine tool. The tool speed, the feed rate and the interface temperature between the cutting tool and the workpiece determine the production of the final products. The solid lubricating materials or oxide-forming metals at high temperature are preferred as cutting tools to create wear-resistant and minimize the excessive frictional heat [31,32].

2.2.3 Materials in high temperature tribological applications

A series of plasma sprayed (PS) solid lubricant coatings, PS100, PS200, PS300, and PS400, have been developed by NASA over the past 40 years to provide lubricity in various aerospace systems from low temperature to high temperature [33–36]. All PS series contain Ag and fluoride solid lubricants along with various binders and hardeners. The soft Ag provides low temperature lubrication while the fluoride provides medium to high temperature lubrication. In addition, at high temperatures different binders and hardeners of PS100 (NiCr+Glass), PS200 (NiCo+Cr_3C_2), PS300 (NiCr+Cr_3O_2) and PS400 (NiMoAl+Cr_3O_2) form the respective oxide phase and provide strong lubrication. However, PS400 overcomes the problems of PS300 that lead to dimensional swelling at high temperature and poor initial surface finish [37–43]. Although this PS series coating is applied to high temperature lubrication such as air foil bearing, there is no doubt that further research is still necessary to explore the high temperature oxidation resistance, mechanical properties along with tribological behavior.

Tribaloy T400 and T800 are well known high temperature wear-resistant alloys. Their wear-resistant behavior can be attributed to the formation of Co-based oxide layers as well as Laves intermetallic phases [35,44,45]. These Tribaloy are widely used for gas exchange valves and seat rings in gas turbine engines where they are subjected to severe operating conditions [46,47]. Tribaloy T800 offers superior performance in terms of wear and oxidation resistance [48], while Tribaloy T400 is more susceptible to oxidation due to its relatively low Cr content (8.5wt%) [**Table 2. 1**] and high amount of Mo and Co [49]. Further investigation is desirable to correlate their specific friction and wear behavior under defined loads and temperatures [47].

Table 2. 1: Chemical compositions of Tribaloy T400 and T800 [46]

Tribaloy	Co (wt.%)	Cr (wt.%)	Mo (wt.%)	Si (wt.%)	C (wt.%)	Others
T400	Bal.	8.5	28.5	2.6	< 0.1	Ni, Fe
T800	Bal.	17.5	28.5	3.5	< 0.1	Ni, Fe

2.2.4 Mechanisms and interfacial processes at elevated temperature

Materials or coatings operating in sliding contacts at elevated temperatures generally form oxide films at the interface due to tribochemical reactions. However, it is important to note that that not all *in-situ* formed layers beneficial [50,51]. As shown in **Figure 2. 4**, the formed oxide layers in the beginning (i.e., stage 1 & 2) can be hard and brittle, which could detach from the surface during further sliding and lead to increased friction and wear. On the other hand, the layers can be soft-ductile and lubricious, thus avoiding direct contact with the substrate and ultimately reducing friction (i.e., stage 3 & 4). However, the oxide formation in the contact pairs depends on various parameters such as chemical composition of the testing materials, applied load, counterpart materials, sliding velocity, surrounding environment [52]. Apart from the lubricious oxide formation in the contact interfaces, there are several principles and mechanisms responsible for low friction and enhanced wear resistance at elevated temperatures.

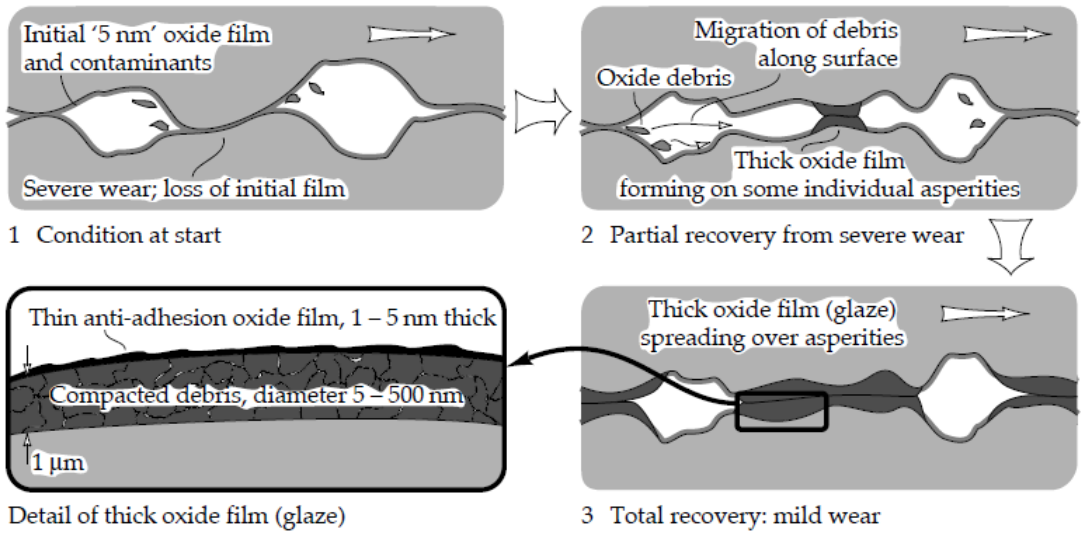

Figure 2. 4: Oxidative wear mechanisms at low sliding speeds [53]

At elevated temperatures, a glaze layer that promotes low friction and wear [54–56] is formed in the contact zone from mixed, ground, and sintered debris that reacts with the surrounding oxygen and air. Viat et al [57] observed a 20 µm thick glaze layer in the contact between HS25 and silicate ceramics at 700°C under fretting test conditions. In HS25, Co is the

main driving element for the formation of the glaze layer and also the oxidation rate is higher than that of Cr or Ni due to the diffusion of cobalt in Co_3O_4 [58]. A considerable amount of research has been conducted by various researchers and found the evidence of the formation of lubricious oxide glaze layer of cobalt, chromium, nickel at elevated temperatures [59–61]. Other than the glaze layer, there is a term widely used in tribology called "tribofilm" and it indirectly indicates the formation of oxide or glaze layer or lubricious film in the contact interfaces at elevated temperatures [**Figure 2. 4**]. This film avoids direct contact between asperity to asperity, ultimately contributing to reduced friction and improved wear resistance properties of the tribo-pairs [62,63]. However, three different tribofilm such as mechanically mixed, chemically generated and thermally activated have different roles in friction and wear properties depending on the tribological system [64–66].

When materials are heated to a temperature of about 40% to 70% of their absolute melting point (in degrees kelvin, °K), they undergo plastic deformation as well as softening, accommodating interacting surfaces and, hence reducing the friction and wear [67,68]. Viat et al. showed the brittle and ductile behavior of oxide or glaze layer formed between ceramic vs cobalt-based alloy at below 200°C and above 450°C respectively [69]. This mechanism corresponds to the brittle to ductile transition of the oxides and contributes to the reduction of friction and wear. Viat et al. [69] also suggested that the presence of ductile behavior is not important for the stability of the glaze layer at elevated temperature, but rather the absence of brittleness. Moreover, the soft metals i.e. Au, Ag enhanced lubricity at high temperature was due to the increased ductility and low shear strength [70–72]. However, excessive softening at elevated temperature may cause the soft metal present in the oxides to be extruded from the contact zone [5].

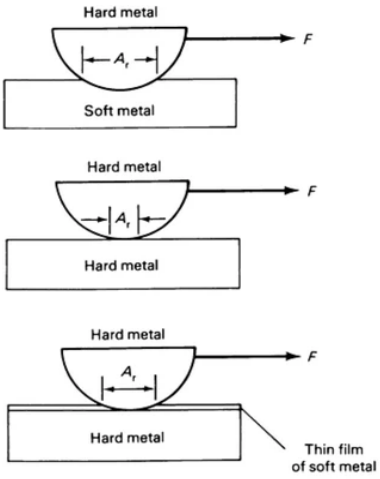

Figure 2. 5: Relation of friction force ($F = A_r\tau$) to substrate material hardness. **Top**: Hard counterface metal in contact with soft substrate metal (large A_r and small τ), **Middle**: Similar hardness of counterface metal and substrate metal in contact with each other (small A_r and large τ), **Bottom**: Similar hardness of counterface metal and substrate metal separated by a thin film of soft metal deposited on the substrate surface (both A_r and τ are small) [73]

As described by Bowden and Tabor [73], the friction can be correlated to the hardness of the materials. For example, as shown in **Figure 2. 5**, hard materials sliding on hard surfaces have high shear strength and thus, high friction values. Similarly, a hard material sliding against a soft one. Since most of the oxide glaze layers formed at high temperature exhibit softening and low shear strength at high temperatures, a hard on soft combination follows to improve the friction and wear performance of the tribological materials [73]. In addition, the combination pattern of the mating surface and the nature of the coating determine the wear mechanisms at elevated temperatures [74].

Aside from the hardness of the tribo-couples, the thermal conductivity also plays an important role in the tribological performance. Higher thermal conductivity means the greater dissipation of frictional heat to the surrounding regions, maintaining a constant temperature at the contact surface [75,76]. This phenomenon minimizes the chances of overheating the contact zone and consequently protects the coating from excessive wear. Most ceramics or oxides have low thermal conductivity compared to metals, and therefore create large thermal stresses in the real contact area. The incorporation of high thermal conductivity materials such as Ag, Cu into the ceramics can overcome this problem and help to improve the tribological performance [76]. Furthermore, these highly conductive pure nanometallic solid lubricants can be generated by the decomposition of the oxides during sliding wear [77].

Ali Erdemir [14,15] postulated a crystal-chemical approach to understand the frictional behavior of the oxides and it is based on the ionic potential of the binary oxides, $\varphi = Z/r$, where Z is the cationic charge and r is the radius of the cation. According to this model, the higher ionic potential of the oxides correlates with a reduction in the friction coefficient at high temperature, as shown in **Figure 2. 6**. More specifically, at the high ionic potential, the cation is effectively surrounded by the anion, and thus, the chemical interactions of the cation with other cations are greatly hindered, as shown in **Figure 2. 7**. Their bonding is mainly with the surrounding oxygen anions, resulting in low interfacial shear strength at elevated temperatures and subsequent in low friction. On the other hand, the low ionic potential difference compound has an opposite mechanism (i.e., it forms a strong ionic or covalent bond with a nearby cation, which is difficult to shear at high temperature). However, the degree of screening by oxygen anions may vary depending on the cationic radius as well as the coordination number of the oxides in their crystal structure.

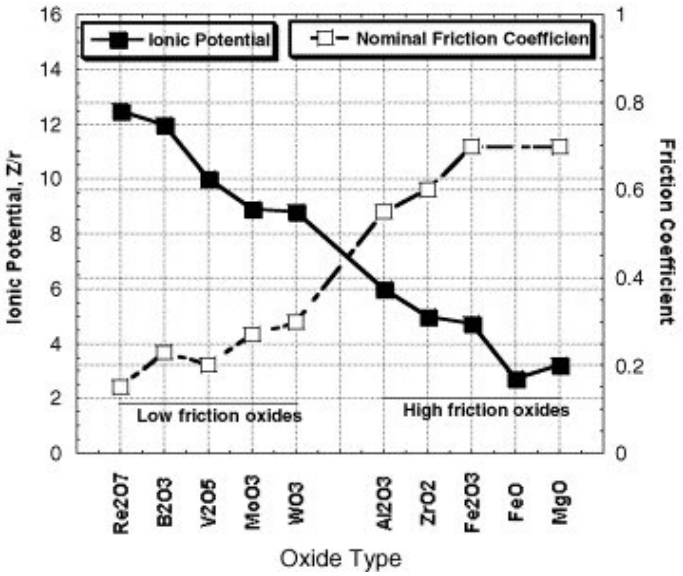

Figure 2. 6: Relationship between ionic potentials and averaged friction coefficients of various oxides [15].

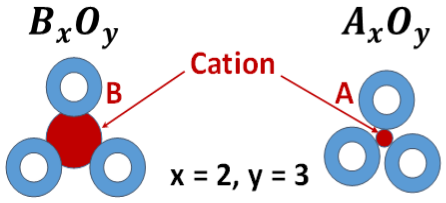

Oxide Case	Cationic Charge	Cation Radius (Å)	Ionic Potential
B_xO_y	3	0.5	6
A_xO_y	3	0.2	15

Figure 2. 7: Ionic potential of two oxides having same cationic charge but different radius (Reprinted from [15]).

According to Erdemir [15], this crystal-chemical model can also be applied to the ternary compound to predict the lubricity. The absolute differences in ionic potential of the system must be taken into account. As the difference in ionic potential increases, the ability of these oxides to form a low-melting or low-shear compound improves; therefore, they exhibit less hardness than their components and can be easily sheared at high temperatures. However, Dimitrov et al. [78] and Prakash et al. [16] identified some limitations with the ionic potential as it measures the friction value by considering the oxides above the melting point to below the melting point. In addition, the ionic potential does not provide a clear interaction between cation and anion in oxides. Thus, they recommended the interaction parameter, which ultimately depends on the polarizing power, as the appropriate term to explain the friction characteristics of the oxides, as shown in **Figure 2. 8**. The interaction parameter decreases as the polarizing power of anions increases (i.e., the electron density in the oxide orbital increases and ultimately the bond strength between the cation and anion decreases, which helps to reduce

the friction coefficient). Varying the wt% of the oxides in the mixture also affects the interaction parameter, A, which is given by Dimitrov et al. [78].

$$A = X_1 A_1 + X_2 A_2 \qquad (2.1)$$

Where, X_i and A_i are the wt% or mol% of the individual oxides and the interaction parameters of the respective oxides, respectively. This interaction parameter also depends on the polarizing power of the cation and anion in the oxides. This crystal-chemical approach is widely used despite its limitations for oxide selection and friction coefficient prediction. Recently, Wang et al. [79] and Yao et al. [80] selected the double oxides TiO_2/Bi_2O_3 and MoO_3/CuO respectively, for high-temperature application based on the crystal-chemical approach and interaction parameters. They found that the combination of TiO_2/Bi_2O_3 and MoO_3/CuO has the lowest friction coefficient values (i.e., 0.07 and 0.16 respectively) at 800°C, which correlates with the cation polarizability.

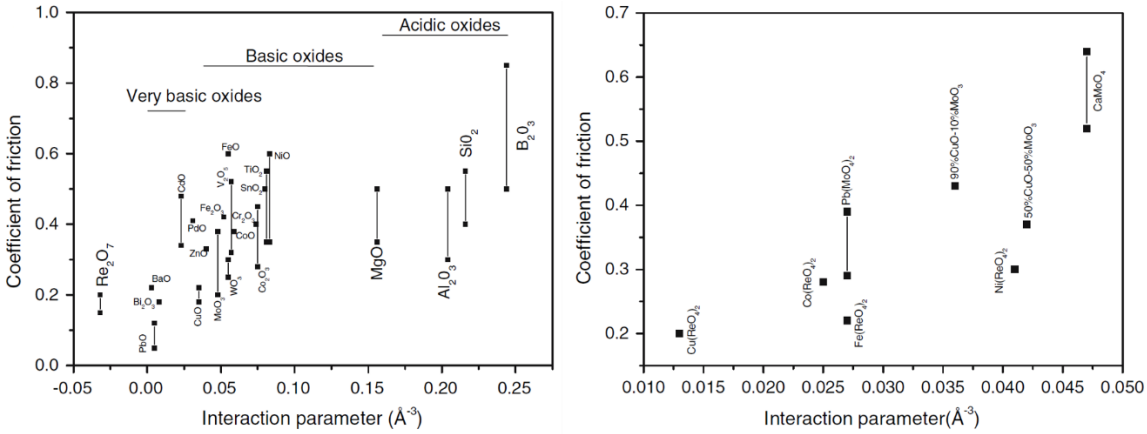

Figure 2. 8: Variation of the coefficient of friction of simple oxides and binary/mixed oxides with the interaction parameter at T/T_m in the range of (a) 0.3-1, (b) 0.7-0.8 respectively [16].

2.2.5 Limitations at elevated temperature and motivation to binary and ternary oxides

As discussed in the **Introduction** section, traditional solid lubricants such as MoS_2, hexagonal BN, and graphite are widely used in different industrial applications to achieve low friction and wear and to increase machine performance [81,82]. Although these solid lubricants can improve tribological performance due to their so-called lamellar structure, their performance is limited by test environments and conditions. In addition, most of these lubricants can thermally degrade at elevated temperatures and show an increase in friction and wear. In particular, oxidation of these lubricants at high temperature conditions reduces the wear performance abruptly [83,84].

In modern industrial applications such as advanced metal cutting machines, gas turbine engines, hot forming, the contact interface is commonly exposed to atmospheric air and

experiences a temperature of more than 500°C [85]. The degradation of metallic coatings in those applications due to oxidation and thermal softening at high temperatures is an issue of increasing concern. In such a case, there is a necessary for novel lubrication systems, since most materials will oxidize at such high temperatures which can increase friction and wear suddenly causing premature failure of the system [86].

Therefore, oxide materials with low shear strength at high temperature could be an alternative and new concept of solid lubrication to improve the tribological performance in modern machinery. In fact, higher oxidation stability and low adhesion tendency make it possible to use oxides under high temperature conditions [87].

Based on the mechanism and principle described in **section 2.2**, the authors will review low friction and wear oxides formed *in-situ* or as added binary and ternary oxides (i.e., **section 2.3** and **2.4**, respectively). In addition, the authors also will critically review their role in improving tribological performance under extreme contact conditions.

2.3 Binary Oxides

Binary oxides are two element's compounds with one or more oxygen atoms combined with other elements. In this paper, the emphasis is placed on the oxides with high ionic potential as shown in **Figure 2. 1**. The binary oxides are classified into two categories: - (i) Magnéli phases or sub-stoichiometric oxides whose tribological performance is predominantly characterized by their reduced binding strength (i.e., crystallographic shear planes); and (ii) Solid oxide lubricants (i.e., CuO), which usually do not form Magnéli phases but exhibit increased wear resistance due to their lubricious behavior at elevated temperature.

2.3.1 Titanium-based oxide phase

2.3.1.1 Industrial relevance

Titanium dioxide is an important oxide material for applications in various advanced fields such as solar cells [88], photocatalysts [89], sensors [90], and protective coatings [91]. Apart from these applications, the non-toxicity and biocompatibility behavior make TiO_2 attractive for tribological applications. Also, the stoichiometric and substoichiometric behavior of titania at elevated temperatures provides promising tribological performance that can be exploited for numerous practical applications [92,93].

2.3.1.2 Friction and wear behavior

Titanium undergoes thermal oxidation above 600°C, forming a thick protective oxide layer on the surface during sliding and improving the poor tribological properties [94,95]. These oxides basically appeared as Magnéli phases in the form of Ti_nO_{2n-1} (γ-Ti_3O_5, Ti_5O_9, and Ti_9O_{17}) at elevated temperatures, which is beneficial for reducing friction and wear [8]. Also, Gardos et al. [96,97] reported the low friction coefficient of oxygen-deficient titania, which is around 0.08 for x = 1.98 due to the low shear strength. The friction coefficients of rutile polymorph of titania were in the range of 0.15 to 1.5 with wear rates between 10^{-6} to 10^{-4} mm^3/Nm depending on the ambient conditions (air or nitrogen). This result was attributed to its anion vacancy concentration at low to high temperature and decreased shear strength from 21 MPa to 8 MPa [12]. On the contrary, this Magnéli phase is unstable at high temperature due to its increased vacancy formation, as well as structural and stoichiometric changes. Moreover, TiO_2 formed *in-situ* during the oxidation of TiN coatings produced by unbalanced magnetron sputtering has no effect on solid lubrication at high temperatures [87]. However, Wong et al. [98] optimized the deposition temperature of reactive magnetron sputtering (i.e. 500°C) to obtain TiO_x films with high mechanical properties. They found that the hardness of the ceramic TiO_x is ordered according to the different oxide phases (i.e., TiO > Ti_2O_3 > Magnéli phase). This low hardness of the Magnéli phase can be correlated with the low shear strength at high temperatures, which helps to reduce friction, as shown in **Figure 2. 9** [99]. A thorough review of titanium nitride-based coatings by various techniques (i.e. PVD, CVD, thermal spraying) can be found elsewhere [100].

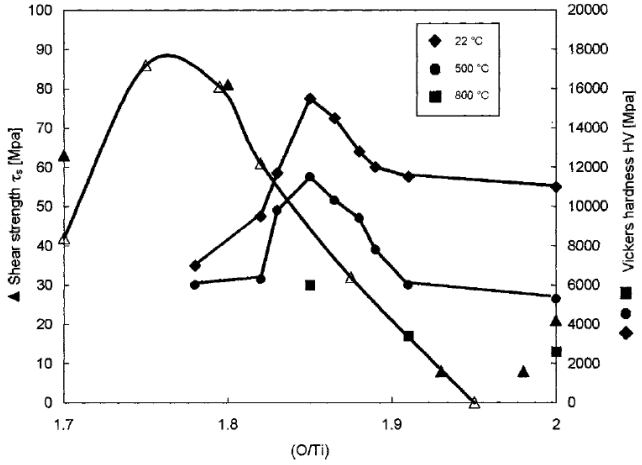

Figure 2. 9: Comparison of the shear strength and Vickers hardness of Magnéli type titania versus their oxygen/titanium ratio [99]

2.3.2 Vanadium-based oxide phase

2.3.2.1 Industrial relevance

Machine tool material failure due to thermal degradation is the most common problem in dry cutting operations [1]. Therefore, such cutting operations require a protective coating that can withstand high temperatures with low material degradation. Vanadium-based self-lubricating coating materials provide lubricating oxide for such application and can help improve the wear resistance of the tool [1,101].

2.3.2.1 Friction and wear behavior

Friction reduction for the vanadium-based oxides has been previously observed and correlated with the formation of V_nO_{2n-1} and V_nO_{3n-1} Magnéli series. At temperatures above the melting point (i.e., 685°C) of V_2O_5, the low friction is attributed to liquid lubrication at the interface. During prolonged exposure at elevated temperatures, V_2O_5 transforms to VO_2, which does not increase friction because both the V_2O_5 and VO_2 phases exhibit the Magnéli properties [102]. Ouyang et al. [103] used a cathodic arc ion-plating process to deposit (V,Ti)N coatings. The authors observed two types of protective oxides (i.e., V_2O_5 and TiO_2 phases) in the contact interface at 500°C. The oxides can plastically deform and consequently, reduce the friction and wear at these temperatures. Similarly, Fateh et al. [104] observed the reduction in friction of V and VN-based coatings at high temperatures due to the formation of similar oxides. A possible decrease in the friction coefficient at high temperatures was observed by the formation of a low shear strength V_2O_5 tribolayer as shown in **Figure 2. 10**. However, a further increase in the temperature to 700°C resulted in partial coating damage due to surface melting and eventually increased the wear rate [103]. More information on the vanadium-based oxide coatings can be found in the review article published by Franz et al. [1]. However, the behavior of the tribological results of the vanadium-based coating is shown in **Figure 2. 10** and the summarized friction and wear values are included in **Table S1** [87,102–108].

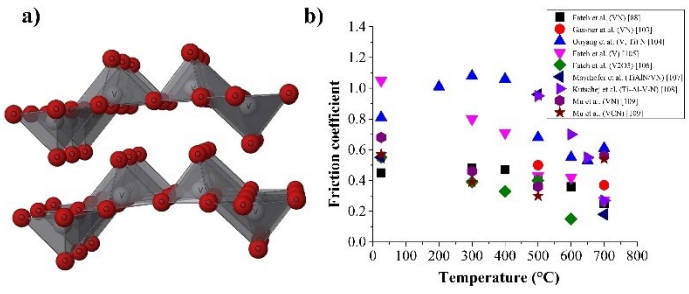

Figure 2. 10: The layered structure of V_2O_5 [109] (a) and tribological behavior of vanadium-based oxides (b)

2.3.3 Molybdenum-based oxides phase

2.3.3.1 Industrial relevance

Molybdenum based oxides are commonly used to improve wear resistance, mainly due to their high wear resistance [110]. The low wear is generally attributed to the formation of lubricious MoO_x oxide and thus, it is employed in different areas such as automotive, aerospace, pulp and paper industries [111]. Apart from this, Mo thin films have been traditionally used in nuclear energy, missile and aircraft parts application [112]. In addition, MoO_3 can also be added to diamond-like carbon (DLC) coatings, which further improves the tribological performance, mechanical properties and thermal stability for automotive industries (i.e., tappet valve) [113].

2.3.3.2 Friction and wear behavior

MoO_x Magnéli phase formation on MoN_2 and MoN coatings at high temperature has been investigated by Suszko et al. [114], and Gassner et al. [31]. At 250°C, it was shown that molybdenum trioxide was formed due to the tribo-oxidation, resulting in oxide softening. This oxide formation continued up to 500°C, thereby reducing friction [31,114]. However, the application of Mo-N and MoN_2 coatings at high temperatures is limited to 500°C because the formation of the Magnéli phase MoO_3 is volatile, and its evaporation starts above 550°C. The volatility behavior of MoO_3 damages the coating and results in an increased wear rate [31,115]. Therefore, low friction coefficients of these MoN_2 and MoN coatings were observed when they were tested near their threshold temperature. Wang et al. [116] varied the molybdenum and vanadium atomic ratios in Mo-V-N films and optimized that the $Mo_{52}V_{22}N_{26}$ film has a low friction coefficient around 0.27 due to lubricious glaze layers mainly composed of V_2O_5 and MoO_3 on the wear track at 700°C. Mo has also been previously been added to Al_2O_3 in order to reduce the friction at high temperatures due to its Magnéli phase formation [117–119]. The addition of Mo to other materials such as Mo-V-Cu-N [120], Mo-SN [121,122], Mo-CrMoN/MoS_2 [123], Ni-B-Mo [124], and Ni-based self-lubricating composites has been extensively studied in terms of the MoO_x formation and contribution to friction reduction at high temperature [125]. A summary of the tribological results of the *in-situ* produced MoO_x phase conducted by various researchers including [126,127], is shown in **Figure 2. 11** and **Table S2**.

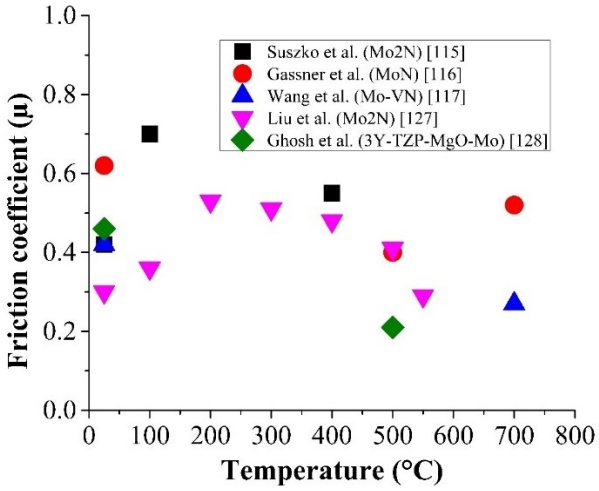

Figure 2. 11: Tribological behavior of molybdenum-based oxides

2.3.4 Tungsten-based oxides phase

2.3.4.1 Industrial relevance

The abrasion, tribo-oxidation and surface fatigue limit the tool life of the machining processes such as high-speed or dry cutting. Therefore, reducing the contact temperatures and providing low friction and wear can optimize the production process, which is in-line with the industrial needs [128]. Tungsten-based coatings have the property of forming an oxide film in tribological contacts at elevated temperatures, ultimately increasing tool life by reducing friction and wear of the materials. In addition, this oxide film acts as a solid lubricant, avoiding the challenges of handling liquid oils in advanced machining processes [129].

2.3.4.2 Friction and wear behavior

Similar to other oxides, Magnéli phase formation for W-based oxides is also the main reason for lubricity at elevated temperatures [31,130,131]. Gassner et al. [31] prepared W-N coatings on AISI 611 steel by unbalanced DC magnetron sputtering method and tested their tribological performance from RT to 700°C in combination with steel and alumina ball. With increasing temperature (i.e., from RT to 500°C), the friction initially increased (i.e., $\mu = 0.3$ to 0.5), but with further increase in temperature (i.e., to 700°C), the friction decreased ($\mu = 0.45$) due to the formation of low shear strength Magnéli phase. The authors showed that the friction coefficient of W-N at elevated temperatures is slightly higher than that of Mo-N, since the WO_3 could function up to 700°C. Unlike with MoO_x, the WO_x did not show any signs of volatility at high temperatures, which helps to enhance the endurance life of WO_x in more extreme environments.

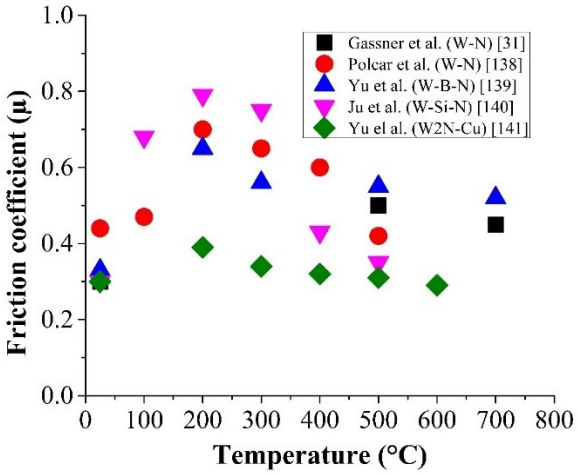

Figure 2. 12: Tribological behavior of tungsten-based oxides

However, the addition of W to various conventional hard coatings (i.e. nitride and carbide) produces lubricious oxides and improves load carrying capacity at high operating temperatures [132–135]. More details on the effect of tungsten oxides on friction coefficient and wear at high temperature can be found in the research article published by Javdošňák et al. [136]. **Figure 2. 12** and **Table S3** show the trend of friction and tribological results of W and W-N coatings, respectively, including the references [31,137–140].

2.3.5 Copper-based oxides phase

2.3.5.1 Industrial relevance

CuO is a lubricious oxide that has been shown to reduce friction and wear as a thin coating and in different oxide ceramic composites [141–143]. These high temperature stable oxides can be used in advanced power generation systems, (i.e. turbomachinery, gas turbines, and hot adiabatic diesel engines) as alternatives to existing solid lubricants [144]. However, pure oxides may not meet all requirements in certain high temperature sliding applications. Therefore, soft CuO is usually combined with hard phases, referred to as self-lubricating composites [145]. The hard phase supports the applied normal load and the soft lubricating interfacial film provides easy shear and thus, reduced friction and wear in high temperature applications [146].

2.3.5.2 Friction and wear behavior

CuO is a widely used lubricious oxide solid lubricant [36], and many researchers have incorporated this oxide with other elements into 3Y-TZP to study its high-temperature lubricating behavior [145–149]. This addition of CuO to TZP leads to a 35%–50% reduction in COF at high-temperature tribo-testing. This addition of CuO to TZP results in a 35-50% reduction in COF in high temperature tribological tests. In addition, CuO reduces the fracture

toughness of 3Y-TZP-CuO composites compared to pure 3Y-TZP due to the formation of a Cu-rich grain boundary phase at elevated temperatures. This also contributes to the increased wear resistance of the composites [147].

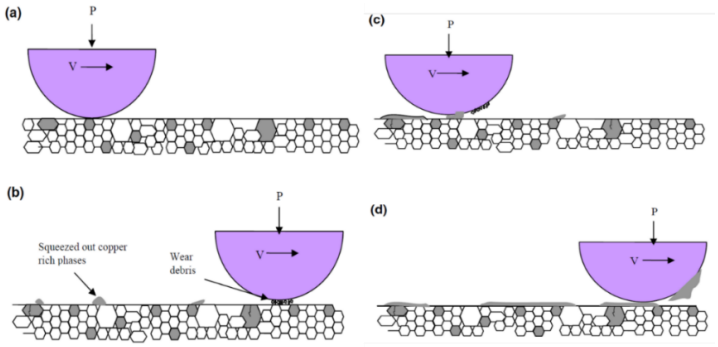

Figure 2. 13: Schematic representation of the wear mechanism in different sliding cycles (a) start contacting, (b) formation of wear debris, (c) plastic deformation of debris and deformation of patchy layer, and (d) formation of transfer layer on ball [147].

Additional mechanisms for increasing the wear resistance of the 3Y-TZP-CuO composite coating included the presence of a CuO (T_m = 1300°C) and $Y_2Cu_2O_5$ (T_m = 1110°C). The CuO (T_m = 1300°C) and $Y_2Cu_2O_5$ soften at 450°C-800°C and 520°C-920°C, respectively. During sliding, the copper-rich phase is squeezed into the surface due to the plastic deformation at elevated temperatures. Consequently, a smooth patchy layer is accumulated on the counter body, sheared, and restored in the interfaces during further sliding, which decreases the COF as shown in **Figure 2. 13**. Furthermore, the combined effect of the lubricous patchy layer of CuO and MoO_3 drastically reduced the friction in 3Y-TZP-Mo-CuO composites at high temperatures [148]. The same patchy layer formation has been observed in other CuO integrated materials such as NiAl [149–151], 3Y-TZP [152], FeCr [153]. A summary of the friction and wear value of CuO in different materials is depicted in **Figure 2. 14** and a **Table S4** is included for the friction wear value.

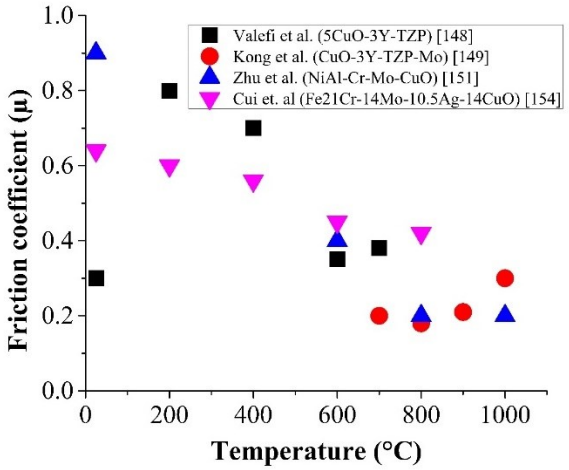

Figure 2. 14: Tribological behavior of copper oxide in various composites

2.3.6 Summary and Challenges of Binary Oxides

The formation of binary oxides at elevated temperatures generally correlates well with the reduction of friction and wear. Due to the tribochemical reaction under harsh contact conditions, the *in-situ* formation of the Magnéli series (TiO_x, V_xO_y, MoO_x, WO_x) works as a solid lubricant to improve tribological performance. Also, CuO in different materials worked as a lubricating oxide. However, limited research has been conducted in a vacuum and varying (N_2) media. Some of the challenges with binary oxides are described are detailed below:

- Titania-based oxides showed improved tribological properties at high temperature, but the re-oxidization at 380°C resulted in an unstable friction coefficient [154].
- Vanadium Magnéli phases have been reported to have great potential for reducing friction at high temperature by shearing the crystallographic planes as well as melting the V_2O_5 phase at 685°C providing liquid-like lubrication. However, the transformation of V_2O_5 to VO_2 occurs during prolonged exposure under severe conditions, which is detrimental to the coating.
- Volatilization of the MoO_3 phase limits use in high-temperature environments. WO_3 has better thermal stability than MoO_3 and is therefore more appropriate for harsh tribological applications. These W and Mo based oxides produce various sub-stoichiometric oxygen-deficient oxides at high temperature, which dominate the lubrication mechanisms and improve the tribological performance during sliding.
- Oxides other than Magnéli phases (e.g., CuO) form a smooth, patchy lubricating film at elevated temperatures in the contact interfaces, which enhances the wear resistance of the composites.

- **Figure 2. 15** shows the maximum tested temperatures of the binary oxides based on the literature review and the results presented in this article. While the friction and wear mechanisms vary depending on the deposition methods and test conditions, **Figure 2. 15** provides an overview of the temperature limits of the various binary oxides. Moreover, the oxides shown in **Figure 2. 15** are either generated in situ in the wear track during testing or are added to various compounds as oxides or metallic elements.

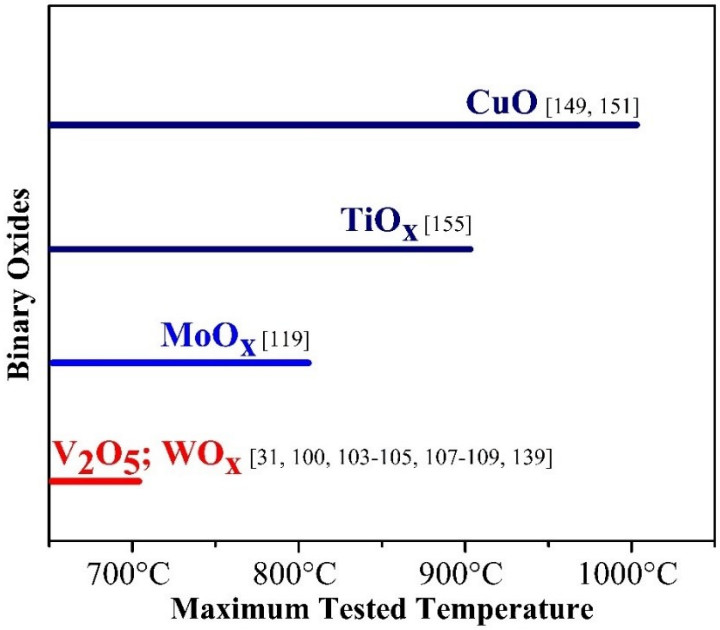

Figure 2. 15: Maximum tested temperature of binary oxides in tribological testing

- Binary oxides have mostly been produced by powder metallurgy and PVD techniques while very few have been produced by thermal spraying and laser cladding. Therefore, there is a strong desire to explore thermal spraying and laser cladding process to directly produce binary oxides and explore their tribological behavior at different temperatures.

2.4 Ternary Oxides

Similar to binary oxides the ternary oxide phase (i.e., three-element compound) can be formed either *in-situ* by tribo-oxidation or directly produced. Such oxide phase can certainly play an effective role in improving wear resistance at elevated temperatures. The ternary oxides can be classified into Ag-based, non-Ag based and other ternary oxides such as sulfates, carbonates, and chromates. The silver (or other soft metals) in the composite coatings provides the lubricity from low to medium temperature ranges and helps to form ternary phases of layered crystal structure and improve the tribological properties at high temperatures.

2.4.1 Vanadate Ternary Oxide Phase

2.4.1.1 Industrial relevance

Novel wear-resistant materials that provide effective lubrication under harsh operating conditions are in constant demand in the aerospace industry [155]. For example, such high-temperature (T>500°C) lubricants are commonly used in propulsion bearings, fasteners, and moving parts within hypersonic aircraft and missiles [156]. Ternary oxides such as vanadate can be used to replace conventional solid lubricants and binary oxide in such applications due to their high temperature lubricity.

2.4.1.2 Friction and wear behavior

Vanadate phase formation by tribo-oxidation at high temperature in the air plays a vital role in reducing friction and wear of the oxide coatings, as observed by Gulbiński et al. [157]. The authors doped Ag with V_2O_5 by reaction magnetron sputtering and formed the β-$Ag_{0.33}V_2O_5$ oxide phase. Tribological testing of this system showed increased friction at a lower temperature compared to pure V_2O_5 coatings. However, when tested at 600°C, the friction was lower (< 0.25) with the Ag doped coatings. Similarly, Singh et al. [158] observed that the ternary oxide phase $AgVO_3$ provided good lubricity at 700°C. This oxide changed to $Ag_2V_4O_{11}$ and Ag with an increase in temperature from RT to 700°C, resulting in a friction coefficient of 0.2-0.3. In addition, Bondarev et al. [159] deposited Ag-VCN coating by PVD technique and studied the *in-situ* formation and presence of Magnéli and ternary vanadate phases during sliding at elevated temperatures. **Figure 2. 16** shows the decrease in friction to values as low as 0.18 at 700°C. At low temperatures up to 200°C, the COF is nearly equivalent for VCN and VCN-Ag coatings, indicating that the addition of Ag to the VCN did not have a significant effect on the tribofilm formation. Above 200°C, the COF decreases due to the self-oxidation initiated by Ag in the VCN-Ag coating and the formation of the lubricious Magnéli $V_nO_{2n\pm1}$ phase. A further increase in temperature causes a tribochemical reaction that forms $AgVO_3$ in the presence of Ag, leading to low COF of the VCN-Ag coating. The formation of the Ag-based ternary oxide phase is shown in **Figure 2. 17**.

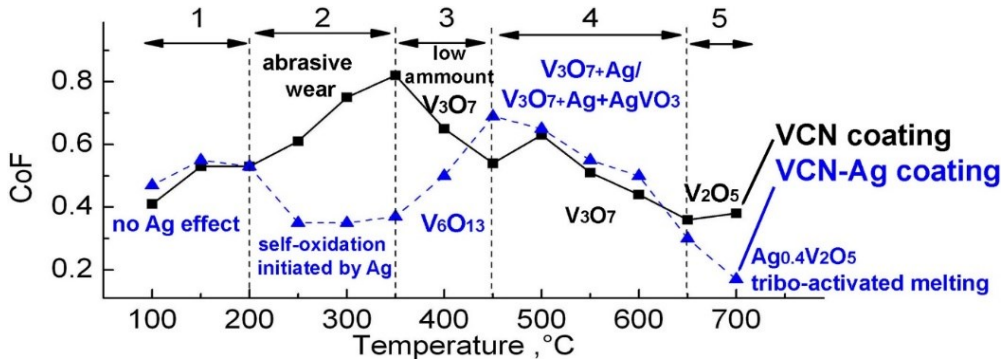

Figure 2. 16: Temperature dependence of COF for VCN-(Ag) coatings [159].

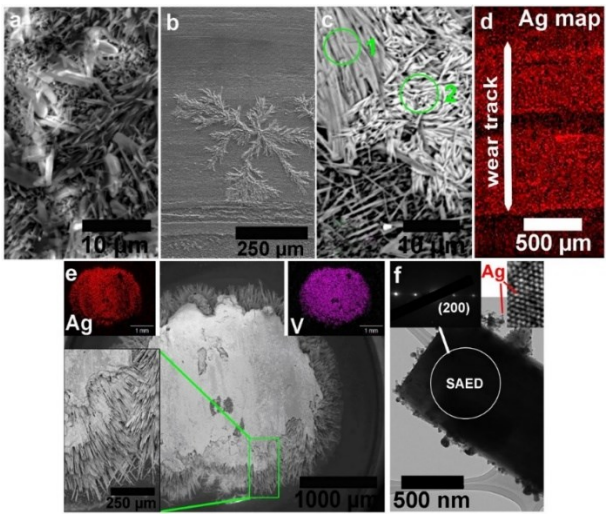

Figure 2. 17: SEM micrographs of VCN-Ag coating taken from areas outside (a) and inside (b,c) wear track after dynamic temperature ramp tribological tests terminated at 700 °C. Silver EDS map obtained from the wear track (d). SEM (e) and TEM (f) images of wear products on the surface of counterpart material with EDS mapping of Ag vanadate particle (insets in (e)) and SAED pattern and high-resolution TEM image (insets in (f)) [159].

Figure 2. 17 shows the presence of needle-like $Ag_{0.4}V_2O_5$ crystal on the surface as well as dendritic crystal on the wear track **(b)** [159]. This dendritic crystal has different concentrations of elongated Ag (point 1-11 at. % and point 2-17 at. %) vanadates as shown in (**c**). In addition, Ag enrichment in the wear track of the VCN-Ag coating was confirmed by EDS mapping of the wear track after tribotesting at 700°C, which ensured the presence of Ag vanadate crystals of different stoichiometries (**Figure 2. 17 (d)**). A relatively thick layer of VCN-Ag was transferred to the Al_2O_3 counter ball (**Figure 2. 17 (e)**), suggesting the formation of a tribo-film in the sliding contact. These components of the tribo-film were also confirmed by TEM analysis (**Figure 2. 17 (f)**) (i.e., silver vanadate rods and nano-sized metallic Ag). Thus, the results showed that the formation of Ag vanadate by tribochemical reaction provides low coefficient of friction and good lubrication between the sliding surfaces at high temperature.

In different studies, a wide range of Ag, and AgV_3O_4 were added in VN or VN-VN y PVD techniques [160–165]. Xin et al. [166] observed the friction reduction of NiCrAlY/Cr_3C_2 (NiCr)/V_2O_5/Ag_2O composite by laser cladding process at high temperature due to ternary vanadate phase. Moreover, the lubricating effect of silver vanadate has also been investigated in the nickel-based intermetallic matrix or hard matrix such as NiCrAlY [166], NiAl [167,168], NiCr [169], NiCoCrAlY [170] under severe working conditions. In almost all the cases, the tribological performance was improved by the presence of self-lubricating ternaries, i.e., $AgVO_3$ and Ag_3VO_4 as well as binary vanadium oxides and pure metallic elements on the worn surface. The friction and wear values of these ternary vanadates are incorporated in **Table S5** and shown in **Figure 2. 18**. To the best of the author's knowledge, there is currently insufficient information in the literature regarding the formation of copper vanadate ternary oxide at elevated temperatures. Therefore, there is a strong desire to study its *in-situ* formation by tribo-oxidation, mechanisms and tribological behavior at high temperatures.

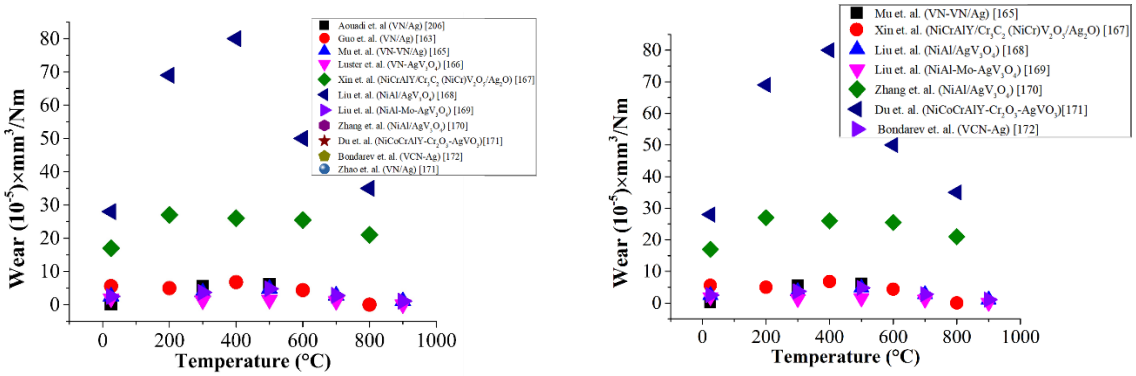

Figure 2. 18: Tribological behavior of vanadate-based oxides including [171,172].

2.4.2 Molybdate Ternary Oxide Phase

2.4.2.1 Industrial relevance

The *in-situ* formation of molybdate ternary oxides in chameleon coatings (YSZ-Ag-Mo-MoS2) provided lubrication from medium to high temperatures. This adaptive nanocomposite coating automatically adapts the surface structure and composition to reduce friction in different environments (i.e., low, medium and high temperatures, vacuum and atmospheric) [173]. This type of coating is highly demanded in hypersonic flight and advanced aerospace applications, especially during takeoff and landing [173,174].

2.4.2.2 Friction and wear behavior

The ternary Ag molybdate was produced by heating (0°C to 650°C) of MoO_3-Ag_2O and by varying the amount of silver oxide (20 mol% to 50 mol%), which also changed the

stoichiometry of the Ag molybdates [175]. Turutoğlu et al. [176] deposited Mo_2N-Ag coating on HSS by PVD techniques and predicted the lubricity at elevated temperatures. In a more recent study, Gulbiński et al [177,178] observed the formation of lubricious ternary silver molybdates $Ag_2Mo_4O_{13}$, $Ag_2Mo_2O_7$ and Ag_2MoO_4 by Ag and MoO_3 at high temperatures. These ternary molybdates significantly reduced friction and wear in high temperature sliding conditions.

The friction and wear of *in-situ* produced ternary molybdates during friction tests of NiCrAlY-Ag-Mo by powder metallurgy has been shown to be comparatively lower than the coating produced by atmospheric plasma spraying [179,180]. This may be due to the relatively dense and homogeneous distribution of the materials in the microstructure of the composites obtained by powder metallurgy. Mo oxidizes to form MoO_3 and subsequently reacts with Ag & O_2 to form $Ag_2Mo_4O_{13}$ during sliding at 600°C. This is shown in **Figure 2. 19** where the peak corresponds to $Ag_2Mo_4O_{13}$ in the Raman spectrum. While AgO and MoO_3 spectra were observed at a comparatively lower temperature, these oxides transformed to $Ag_2Mo_4O_{13}$ during sliding at higher temperatures (600°C-800°C). A further increase in temperature showed multiple molybdate peaks. The effective formation of the glaze layer (i.e. composed of silver molybdates and molybdenum oxide) at the sliding interface reduced friction and wear at high temperatures [180].

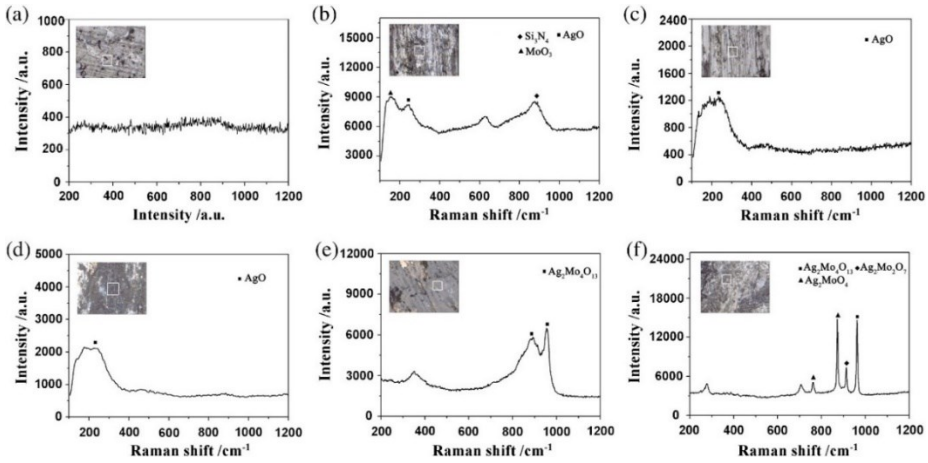

Figure 2. 19: Raman spectra of worn surfaces of NiCrAlY-Ag-Mo composite coating: (a) As-sprayed coating, (b) 20°C, (c) 200°C, (d) 400°C, (e) 600°C, and (f) 800°C [180].

The direct incorporation of the ternary molybdates into Ni-based materials provides lubricity over a wide temperature range as shown by Liu et al. [181][182]. The combination of Ag, Mo [183], and MoS_2 as a lubricant in the Ag-Mo-YSZ [184][185] produces molybdates at high temperatures and maintains low friction of the composites. The Ag and Mo provided lubricity at low temperatures and the formation of oxides (i.e., the binary and ternary) detected

at elevated temperatures that create the adaptive or chameleon coating surfaces [174][186]. On the other hand, copper and molybdenum as a metallic element have also been previously used for the formation of lubricious oxides. It has been shown that the Cu-Mo coating deposited by ion beam deposition on alumina substrate can be converted to $CuMoO_4$ and MoO_3 by exposure at temperature ± 530°C which reduces the friction from 0.5 to 0.2 [67]. Varying the wt% of Cu in Mo_2N films changes the stoichiometry of the oxides as well as the friction and wear [187]. Similar formation of $CuMoO_4$ in tribotesting at 600°C and 800°C has been observed by Yao et al. [80] in thermally sprayed NiAl/MoO_3/CuO composite coating. Additionally, a group of researchers conducted research on the tribological performance of Ca [188], Ba [189] and Sr [190] based ternary molybdates at elevated temperatures. It was shown that these metal-based molybdates have lubricating properties like Ag/Cu molybdates at high temperatures. More specifically, the high wear resistance of the molybdates (i.e., Ag/Cu based or others) at high temperature is due to the combined effect of ternary, binary compounds as well as their decomposed pure metallic elements. A summary of the tribological performance of the molybdate ternary oxide phase is shown in **Figure 2. 20** and **Table S6**.

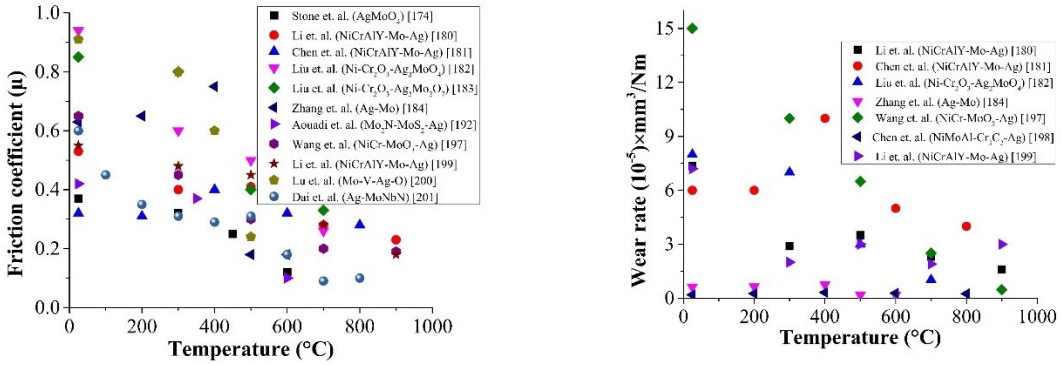

Figure 2. 20: Tribological behavior of molybdate-based oxides [173,191,200,201,192–199]

2.4.3 Tantalate Ternary Oxide Phase

2.4.3.1 Industrial relevance

Tantalate ternary oxide can provide high temperature lubricity and wear-resistance. These oxides have been found to be a very promising alternative to the Magnéli phase [156]. Therefore, tantalate based ternary oxides have shown promise for components in modern aviation, aerospace, nuclear power and other high-tech industries that operate in extreme environments (i.e., high temperature, high speed and high load) with the purpose of minimizing the friction and wear in the contacting interfaces [202].

2.4.3.2 Friction and wear behavior

Tantalate ternary oxide is a perovskite-type crystal with a layered structure, which has shown promising lubricating behavior at high temperatures as observed by Stone et al. [203,204]. It can be mentioned that the lubricity of individual silver and tantalum oxide at elevated temperatures has been found by the researchers [205,206]. Therefore, Stone et al. [203,204], prepared silver tantalate oxides powder from Ag_2O and Ta_2O_5 by solid-state synthesis and deposited it on a substrate by burnishing, and produced tantalates ($AgTaO_3$, $Ag_2Ta_4O_{11}$) by magnetron sputtering. In this study, the authors suggested that the reconstruction of $AgTaO_3$ into a mechanically mixed layer (MML) of $AgTaO_3$, Ta_2O_5, and Ag at elevated temperature 750°C during tribotesting resulted in low friction (i.e. in the range of 0.04-0.06) [203,204,207,208]. Moreover, at low-temperature, the friction is influenced by the chemical nature (i.e., adhesion and relaxation energy of the oxides) of the surface, whereas at high temperature, the aggregation of metallic silver on the contact surface plays a significant role in improving the tribological performance of the coatings [209,210]. Similar to silver-based tantalate, copper-based tantalate could be a promising solid lubricant for applications in harsh working conditions due to its low cost, which has been investigated by Gao et al. [211]. While the $CuTa_2O_6$ based thin films exhibited high friction at low temperature, they showed remarkably higher wear resistance than $AgTaO_3$ at 750°C. *Ex-situ* analysis by means of SEM and elemental mapping of the wear track is shown in **Figure 2. 21**. The Cu content decreased dramatically on the worn surface, while the Ta content increased at the edge of the wear track. This was attributed to the formation of Cu or copper oxide clusters as a result of the dissociation of $CuTa_2O_6$. This is less pronounced than $AgTaO_3$ due to the higher energy required to dissociate $CuTa_2O_6$ as the Cu-O bonds are stronger than the Ag-O bonds [209]. **Figure 2. 21** also shows that after a certain period of time, Ag cluster formation is twice that of Cu. Cu is less likely to segregate and form clusters than Ag under the same sliding conditions. Therefore, the low mobility of Cu resulted in high friction but low wear volume in $CuTa_2O_6$ compared to $AgTaO_3$ [203,211]. The *in-situ* formation of lubricious ternary oxides $AgTaO_3$ and $Ag_2Ta_4O_{11}$ at 750°C was observed in NiCrAlY/Ag_2O/Ta_2O_5 laser cladded coatings by by Zhu et al. [202].

A limited amount of research work has been carried out on the tribological behavior of tantalate based ternary oxide as a solid lubricant for high-temperature applications. Other than burnishing, PVD, and laser cladding process, there is limited work performed on other deposition methods i.e., thermal spraying. Therefore, there is room for further exploration of the working mechanism as well as their deposition techniques. A summary of the tribological performance of tantalate based ternary oxides is shown in **Table S7** and in **Figure 2. 22**.

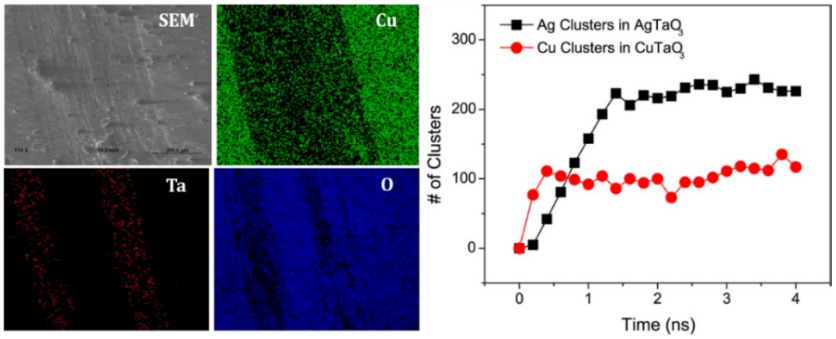

Figure 2. 21: Characterization of a selected area of the wear track and elemental mapping after tribotesting at 750°C (Left). Number of Ag/Cu clusters in at the sliding interface from MD simulations of $AgTaO_3$ and $CuTaO_3$ at 750°C as a function time (Right) [211].

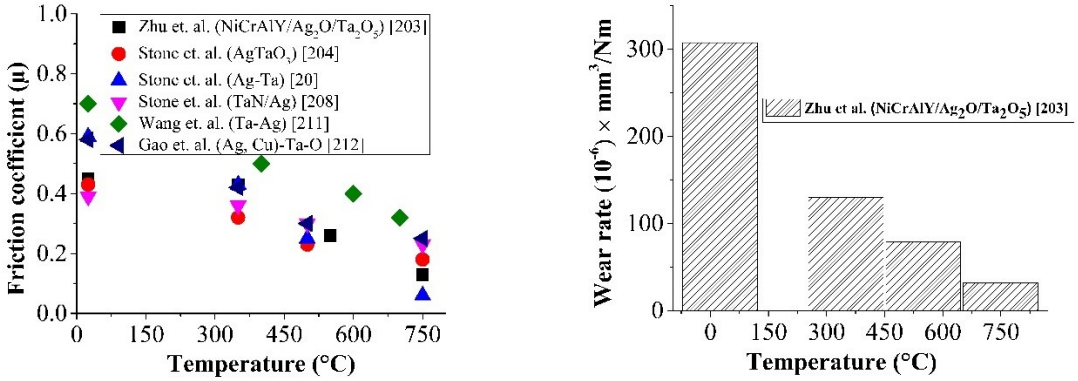

Figure 2. 22: Tribological behavior of tantalate-based oxides

2.4.4 Niobate Ternary Oxide Phase

2.4.4.1 Industrial relevance

Similar to other ternary oxides, the niobate ternary oxides have also been investigated in high temperature applications where it shows promising tribological performance. The niobate ternary phase has been observed in chameleon/adaptive coatings that can be used over a wide temperature range [212][213]. In addition, the ionic potential of the Nb_2O_5 is similar to that of Ta_2O_5 (φ = 6.41) and thus, in terms of industrial relevance, the tantalate ternary phase could be replaced by niobate.

2.4.4.2 Friction and wear behavior

The combination of binary metal oxides along with noble or transition metals may be an effective strategy to reduce friction at moderate and high temperatures. Such an experimental work has been carried out by Stone et al. [212]. The authors observed the *in-situ* formation of silver niobates ($AgNbO_3$) on the worn surface at elevated temperatures. While this ternary

oxide provided a low friction coefficient at high temperature, it became abrasive at RT because of its high COF of around 0.40-0.55 depending on the Ag content [213]. *In-situ* Raman measurements at high temperatures provided valuable information on the formation of binary and ternary oxide phases during wear testing (**Figure 2. 23**). At RT, the as-deposited coating elements were NbN, while the formation of $AgNbO_3$ was detected mainly at 500°C and 600°C. The presence of Nb_2O_5 together with $AgNbO_3$ at 700°C ensured the decomposition of the ternary phase to the binary phase, thus increasing the wear. However, the Nb_2O_5 oxides disappeared after 2000 cycles. The results of this article provide a clear distinction between the formation of chemical phases during rubbing at elevated temperatures, which are responsible for improving the tribological performance of coatings.

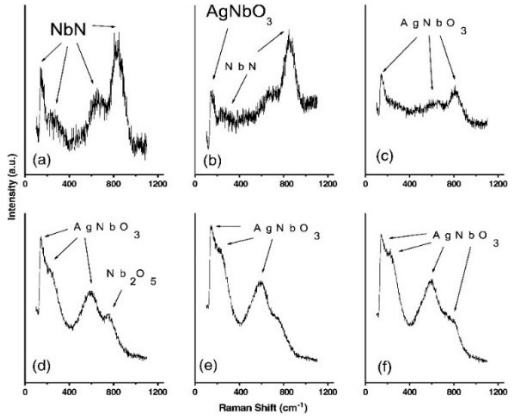

Figure 2. 23: *In-situ* Raman spectrum of NbN/Ag at different temperatures while heating ((a) 25°C, (b) 500°C, (c) 600°C, (d) 750°C) and during wear testing ((e) after 500 cycles, and (f) after 10,000 cycles) [212].

Shirani et al. [214] investigated the surface reconstruction mechanisms of Nb_2O_5 and Ag_2O systems ($Nb_2O_5 + Ag_2O \rightarrow 2AgNbO_3$) during sliding at elevated temperatures. The results showed the formation of lubricious ternary niobates [215] and acted as self-healing [216] providing high wear resistance. In a different context, Feng et al. [217,218] incorporated $AgNbO_3$ into NiAl intermetallic matrix by means of powder metallurgy. The authors concluded that the following chemical reactions occurred in the friction process at 600°C and 800°C.

$$4Ag + O_2 \rightarrow 2Ag_2O$$

$$4NbC + 5O_2 \rightarrow 2Nb_2O_5 + 4C$$

$$Ag_2O + 2Nb_2O_5 \rightarrow Ag_2Nb_4O_{11}$$

$$Ag_2O + Nb_2O_5 \rightarrow 2AgNbO_3$$

$$Ag_2Nb_4O_{11} \rightarrow AgNbO_3 + AgNb_3O_8$$

The formation of ternary phase along with binary compounds has also been observed in NbN-Cu [219], NbCN-Ag [220] coatings at high temperatures. **Figure 2. 24** shows the friction and wear results of *in-situ* niobate ternary oxide solid lubricants and powder forms that were added to intermetallic compounds.

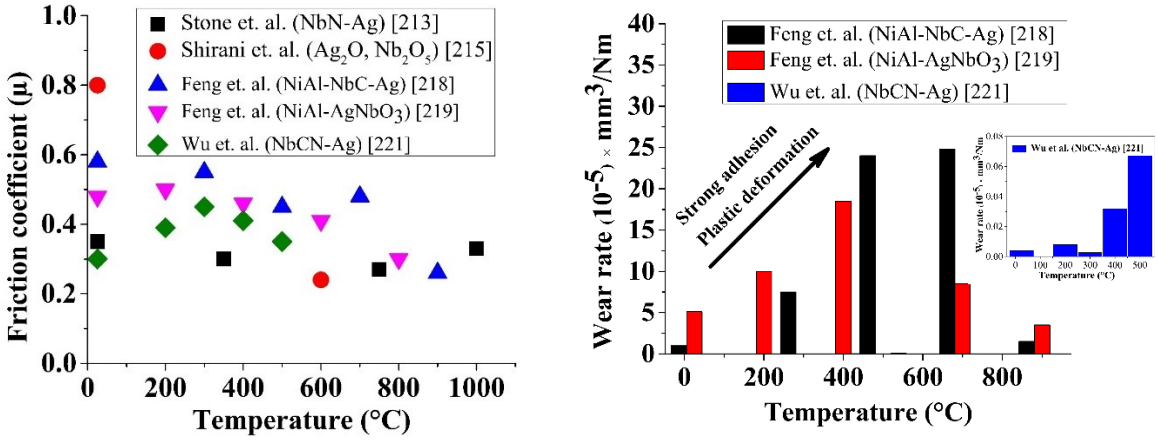

Figure 2. 24: Tribological behavior of niobate-based oxides

2.4.5 Tungstates Ternary Oxide Phase

2.4.5.1 Industrial relevance

Tungstates are considered high temperature lubricious ternary oxides due to their low shear strength at elevated temperatures. Examples of such tungstates including $ZnWO_4$ [221,222], $CaWO_4$ [223], $BaWO_4$ [223] and $PbWO_4$ [224,225], have shown their contribution in improving the wear resistance property of the materials mentioned in **section 2.4.5.2**. This property makes the tungstates suitable for use in extreme environments application.

2.4.5.2 Friction and wear behavior

Tungsten disulfide (WS_2) is thermally more stable than MoS_2 and served to increase the operating temperature by about 100°C [226]. Thus, the addition of nanocrystalline ZnO to this WS_2 can provide adaptive lubrication in various applications as shown by Walck et al. [221] and Prasad et al. [222]. They observed that ZnO enhanced the tribochemical reaction rate and provided a denser coating by filling the voids of tungsten disulfide, leading to the formation of durable transfer films on the counterface [221,222]. Likewise, the *in-situ* formation of $ZnWO_4$ during tribo-oxidation at elevated temperatures ensured the adaptive lubricant phenomena in the WS_2-ZnO nanocomposite coating. The low shear strength $BaWO_4$, $CaWO_4$ formed on the worn surface by a tribochemical reaction at 800°C and reduced the friction and wear in Ni_3Al-Ag- BaF_2/CaF_2-W composites. However, the formation of the protective film was disrupted by the formation of $BaCO_4$ at 600°C, thereby increasing the wear rate [223]. Furthermore, the

direct addition of ternary $Ag_2W_2O_7$ in $M_{n+1}AX_n$ (i.e. Ti_3SiC_2) by spark plasma sintering, showed improved wear resistance in high temperature sliding [173,227]. The result revealed that the decomposition of $Ag_2W_2O_7$ into metallic Ag and $CrWO_4$ and the formation of oxide layer during elevated temperature tribotesting enhanced the tribological performance of the composites. In addition, the synergistic effect of NiO, MoO_3, Cr_2O_3, WO_3, along with $NiWO_4$ oxides was observed in Ni-Cr-W-Al-Ti-MoS_2 sintered disk, which avoided direct contact between contact pairs and hence reduced friction at high temperature [228]. Similar to other ternary tungstates, the $CuWO_4$ also showed lubricating phenomena in high temperature (900°C) sliding in W-Cu alloy [229]. **Figure 2. 25** and **Table S9** show the summary of the tribological behavior of the tungstate oxides. It should be noted that the use of tungstates as solid lubricants for high temperature tribological applications is limited. Therefore, further study needs to be carried out to explore its wear mechanism.

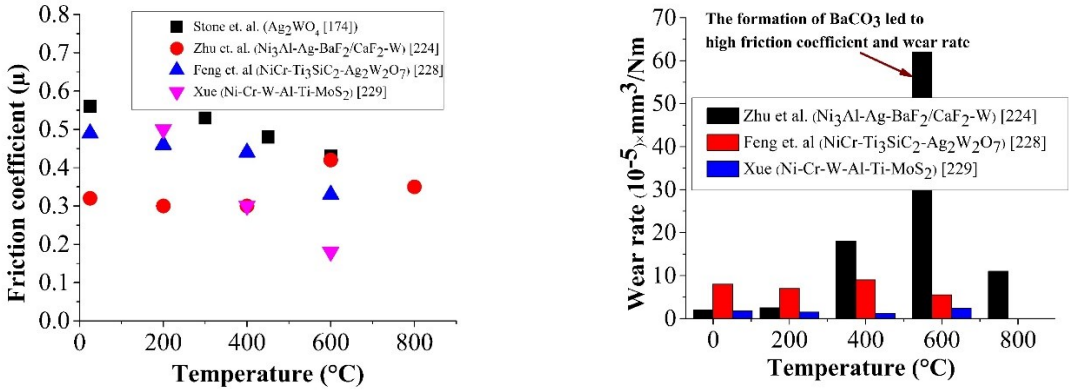

Figure 2. 25: Tribological behavior of tungstate-based oxides

2.4.6 Other Ternary Oxide Phase

2.4.6.1 Industrial relevance

Ceramic materials are extensively used in hot section components in gas turbine engines and advanced engines due to their high temperature resistance. However, their high friction and high wear at elevated temperatures make the system undesirable and unstable [230,231]. Thus, various sulfates such as $CaSO_4$, $SrSO_4$, $BaSO_4$ have been added to the metal or ceramic matrix to improve their high temperature lubricity. These ternary sulfates form a lubricating film in the contact interfaces and reduce the friction and wear over a wide temperature range, which could be beneficial in extreme environment applications.

2.4.6.2 Friction and wear behavior

A series of ternary sulfates $CaSO_4$, $SrSO_4$, $BaSO_4$, which have the orthorhombic crystal structure of barite and melting point of all three around 1500°C, have been studied as solid lubricants for high-temperature tribological applications [232,233]. While the mechanism for the improved tribological performance of sulfates at elevated temperatures is not well understood yet, however it has been suggested that the formation of a layered structure of carbonates ($CaCO_3$, $SrCO_3$, and $BaCO_3$) at high temperatures improves the lubricity. Also, the addition of these carbonates such as $SrCO_3$ to NiCr-30 wt% Al_2O_3 resulted in the formation of $SrAl_{12}O_{19}$ and other oxide tribofilm at 800°C, which enhanced the tribological performance of the composites [234]. However, these ternary sulfates do not possess easy to shear plane phenomena and their high-temperature lubricity mechanism is still unclear, but Al_2O_3–$50BaSO_4$–20Ag, Al_2O_3–$50BaSO_4$–$10SiO_2$, Al_2O_3–$50SrSO_4$, Al_2O_3–$50PbSO_4$–$5SiO_2$, Al_2O_3–$50BaSO_4$ and Al_2O_3–$50BaCrO_4$ composites still showed decreased friction with increasing temperature [235–238]. Another ternary sulfate known as barite structure $Ba_xSr_{1-x}SO_4$ (x = 0.25, 0.5, 0.75) which is hard and brittle at atmosphere, but its lubricity becomes active at above 500°C, maintaining a COF of 0.19-0.29, wear rate of 10^{-5} mm^3/Nm at 600-800°C in Fe_3Al based composite [239]. The composites become soft and ductile at high temperatures, and form a barite lubricating film at the contact interfaces, contributing to improved tribological performance [240]. A wide range of research has been conducted to find the lubricity of $CaSO_4$, $SrSO_4$, $BaSO_4$ in composites at high temperature [241–247].

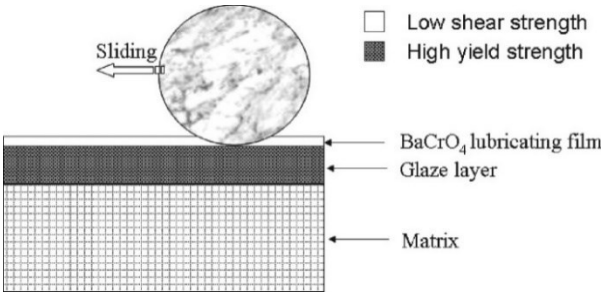

Figure 2. 26: Schematic diagram showing the high-temperature self-lubricating mechanism of NiCr–$BaCr_2O_4$ composite [248].

Unlike sulfates, $BaCr_2O_4$ has high friction and wear at low temperatures due to the brittle fracture wear mechanism. However, at elevated temperatures, it undergoes oxidation and produces a soft lubricating film of $BaCrO_4$, which improves the wear resistance properties of the coatings [249]. Ouyang et al. [248] tested the wear resistance characteristics of NiCr-$BaCr_2O_4$ composites at 600°C and recommended that the addition of $BaCr_2O_4$ promoted the densification of the oxide layer in the tribo-pair. Subsequently to the wear test at 600°C, the

worn surface of the NiCr-$BaCr_2O_4$ composites consisted of three layers (**Figure 2. 26**)-(i) undeformed NiCr matrix, (ii) a hard (5.1 ± 0.6GPa) oxide glaze layer on top of the NiCr matrix, which reduced the contact-stress, and finally, (iii) a soft $BaCrO_4$-based lubricating film with low shear strength, which reduced the friction and wear of the composites. However, severe oxidation of the composites at 800°C reduced the relative density and increased the wear. The same $BaCrO_4$ lubricating film has been produced in Ni_3Al composites at high temperatures [250,251]. The low shear strength or lamellar crystal structure is necessary to achieve a low friction coefficient in ternary compounds at elevated temperatures. However, it has been observed that the while sulfates/chromates do not possess an intrinsic weakness in the crystal lattice for achieving low friction, their barite structure sulfates become softer or more ductile at a high temperature, which reduces the adhesion at the interface. As a result, the coefficient of friction and wear of the coating at elevated temperatures is reduced. Further work can be done to explore the lubrication mechanism of sulfates, carbonates and chromates under severe sliding conditions.

2.4.7 Summary and Challenges of Ternary Oxides

Ternary oxides such as vanadates, molybdates, tantalates, niobates, and tungstates are excellent solid lubricants for enhancing the tribological performance of the composites at high temperature contact interfaces. On the other hand, the wear reduction mechanism of the directly deposited ternary sulfates in the composite coatings is still not clear and needs further investigation. Based on the above discussion, the summary and major challenges of ternary oxides are mentioned in below:

- Silver vanadates have consistently improved tribological performance, varying the coefficient of friction from 0.35 at 25°C to 0.15-0.2 in the temperature range of 700°C to 1000°C in VN/Ag nanocomposite coatings [160]. However, there is not enough information on the formation of copper vanadate ternary oxide at elevated temperatures. Therefore, there might be an opportunity to explore the in-situ formation of Cu vanadate due to tribo-oxidation mechanisms and investigate its tribological behavior at high temperatures.
- It has been shown that the molybdates have lubricity like Ag vanadates at elevated temperatures. The high wear resistance of the molybdate at high temperatures was due to the collective effect of ternary and binary compounds as well as their decomposed pure metallic elements formation, whether it is Ag/Cu based.
- Tantalate oxides have shown promising wear resistance behavior at severe tribo-contacts and its structure and tribological performance was similar to niobates. However, only a

limited amount of research has been carried out on Ag/Cu tantalate in harsh tribological applications and has been limited to a maximum test temperature of 750°C [203]. Therefore, more work needs to be done to better understand their high temperature stability. In addition, other deposition methods, such as thermal spraying, could be explored to understand the high temperature wear mechanisms of the tantalates.

- Tungstates as solid lubricants improved the frictional resistance due to the higher thermal stability compared to molybdenum oxide [226]. In addition, other than Ba/Ca/Pb tungstate's pure Ag, Cu, Au can be included in the tungstate and could be observed their lubricating performance at elevated temperatures.
- In NiCr-$BaCr_2O_4$ composite, a thin soft $BaCrO_4$ lubricating film with low shear strength was observed just above a hard glaze layer (**Figure 2. 26**), which improved the wear resistance of the composite [248]. This type of investigation could be performed on other types of oxide composites to explore their friction and wear reduction mechanisms at elevated temperatures.

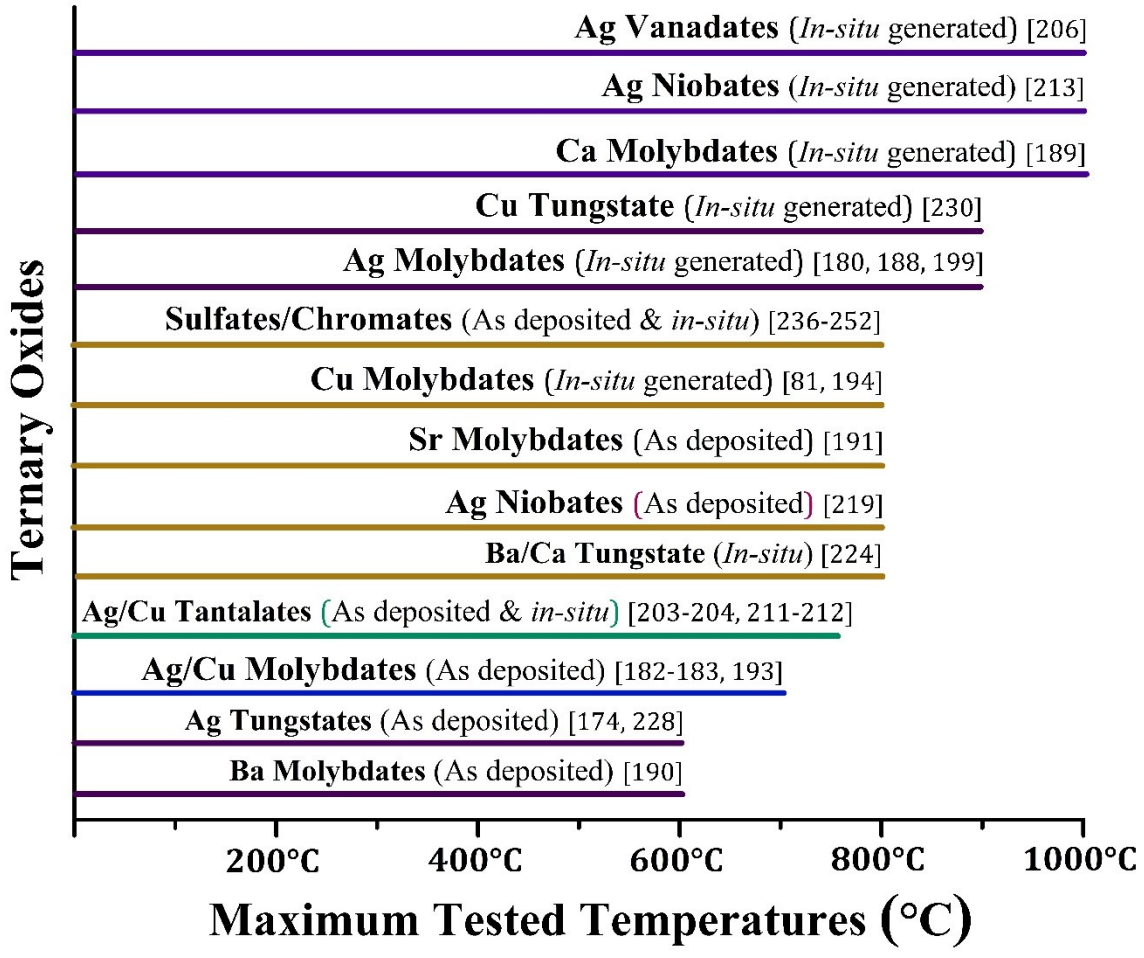

Figure 2. 27: Maximum tested temperature of Ternary oxides in tribological testing

- A summary of the ternary oxides with maximum testing temperature is plotted in **Figure 2. 27** based on the literature mentioned here. However, these ternary oxides are mostly *in-situ* generated that has been produced at high temperature tribotesting and could be different if deposited directly as ternary compounds by plasma spraying or laser cladding processes.
- Like binary oxides, powder metallurgy and PVD are preferred techniques for the formation of ternary oxides composites. Few ternary oxides are also deposited by thermal spray and laser cladding processes, which require additional studies to understand their tribological behavior at high temperatures.

2.5 Interfacial Processes and Wear Mechanism of Oxides

The friction and wear characteristics of any interacting surfaces in dry conditions at high temperatures are highly dependent on the properties of the tribo pairs (discussed in **section 2.2**) as the mating parts undergo chemical, mechanical, and microstructural changes at elevated temperatures. More specifically, the oxidation of the interrelating surfaces is predominant in high atmospheric temperatures. In this review, the *in-situ* formation of binary and ternary oxide lubricants on the worn surfaces due to tribochemical reaction at elevated temperatures has been demonstrated, resulting in reduced friction and increased wear resistance. A generalized wear mechanism of various binary and ternary oxides at low, medium, and high temperatures is shown in **Figure 2. 28** based on a literature survey.

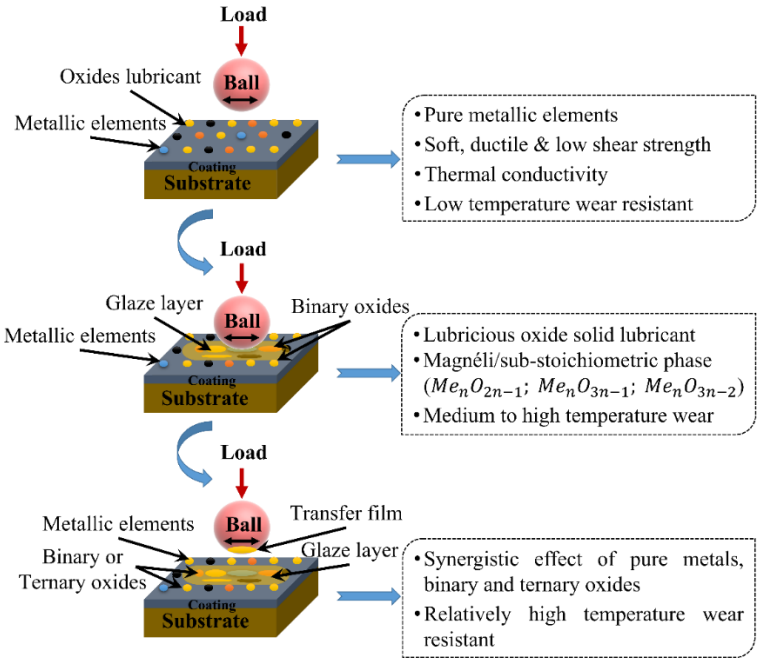

Figure 2. 28: Schematic diagram of generalized tentative wear mechanisms of binary and ternary oxides at different temperatures.

- At low temperatures, the pure metallic elements (i.e., Ag, Cu) dominate the wear behavior in the lubricious coating due to their soft, ductile, and high thermal conductivity properties. The source of the pure elements could be either the addition of metallic components to the composite coating, the decomposition of the compounds into pure elements during thermal spraying, or during frictional heating.
- At medium to high temperatures, the metallic elements produce lubricious oxides through tribochemical reaction. In addition, the binary oxides added to the matrix remain unchanged or sometimes decompose into pure metallic elements along with the formation of the glaze layer. In general, the binary oxides transformed to Magnéli or sub-stoichiometric oxide phase at elevated temperatures and contributed to the reduction of friction and wear due to their layered crystal structure. However, the conversion of the oxides to the magnesia phase depends on their chemical nature and melting point.
- At relatively high temperatures, a lubricious layer of ternary oxides adheres to the mating surface, known as the transfer film, and the glaze layer of ternary oxides is formed on the wear track. The lubricious ternary oxides with their low shear strength structure mainly reduce friction and improve the wear resistance of materials at high temperatures. Nevertheless, the high temperature tribo-oxidation produces metallic elements, binary and ternary compounds. Ultimately, the synergistic effects of pure elements, substoichiometric oxides and ternary oxides improve tribological performance at relatively high temperatures.
- **Figure 2. 29** shows a graphical approximation of the coefficient of friction (COF) for various binary and ternary oxides over an effective temperature range. It should be noted that the comparison of the coefficient of friction reported here has been taken as a generalized value, since friction and wear are not intrinsic properties of the materials, but the response of the system [13]. In general, binary oxides contributed more to friction reduction at elevated temperatures, while ternary oxides and synergistic effect contributed greatly at high temperatures. There is a need for more detailed study of various binary and ternary oxides over a wide temperature range.

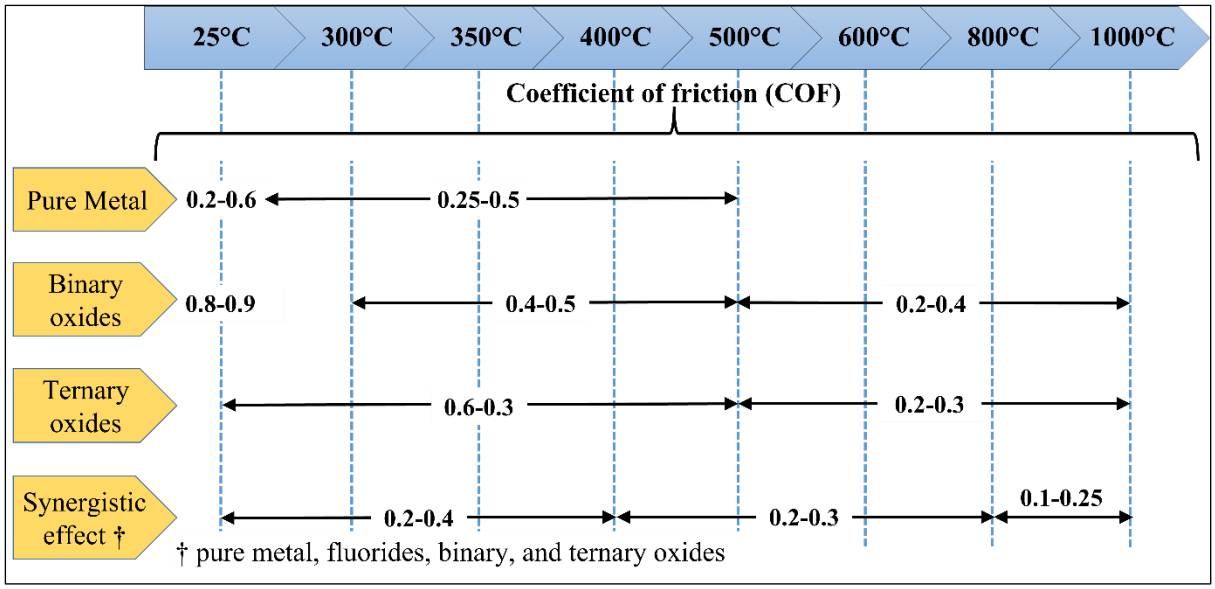

Figure 2. 29: An approximate range of COF for binary and ternary oxides over the effective temperature range.

2.6 Summary

This paper reviews the most common high ionic potential (TiO_2, V_2O_5, WO_3, MoO_3) and low ionic potential (CuO) binary oxides as well as ternary based oxides in high temperature environments. The importance of oxides in extreme conditions is highly appreciated by researchers due to their greater thermal stability and inertness. This property of oxide ceramics is applicable in areas where the performance of conventional solid lubricants and materials is limited by the working conditions. In general, oxides are abrasive at low temperatures but become lubricious at high temperatures due to their softness and lamellar structure. However, further research on binary and ternary oxides is needed to better understand the actual mechanisms for the variation of friction and wear at elevated temperatures. The following is a summary of the main findings in the literature on binary and ternary oxides:

- High temperature tribology has become a significant research area over the last couple of years in advanced machine tools, gas turbine engines, metal forming and automobile industries. In particular, oxide/glaze layer and tribofilm formation, materials softening, ductile to brittle transition as well as thermal conductivity are the main interfacial mechanisms for the improved tribological performance in high temperature tribology system. However, enhanced wear resistance of the materials will also depend on the tribosystem, as friction and wear are system dependent.
- The binary oxides enhanced the wear performance at high temperatures in two ways: (i) formation of Magnéli phases or sub-stoichiometric oxides (Me_nO_{2n-1}, Me_nO_{3n-1}, Me_nO_{3n-2}),

which have crystallographic shear planes with reduced bond strength due to the planar lattice defects resulting in crystallographic shear planes with reduced bond strength. Oxides with high ionic potential (i.e., TiO_2, V_2O_5, WO_3, MoO_3) followed this mechanism to reduce friction and wear at high temperatures, and (ii) on the other hand, oxides with low ionic potential, i.e., CuO, form a soft uniform patchy layer in the contact interfaces. Also, with the incorporation of hard phase, this soft CuO provides easy shear and thus, enhanced friction reduction in high temperature applications.

- In ternary oxides, a lamellar crystal structure at high temperature helps minimize friction and wear. However, the synergistic effect of the pure metallic elements, both binary and ternary oxides, enhances the wear resistance of the tribosystem. All the in-situ or directly added ternary phases i.e., vanadates, molybdates, tantalates, niobates, tungstates in the composites exhibit lubricity and show similar types of friction reduction mechanisms at elevated temperatures. In addition, the barite structure such as $CaSO_4$, $SrSO_4$, $BaSO_4$ do not process layered structure but still reduce friction and therefore further investigation is needed.
- CuO is the material with the highest tested temperature among the binary oxides studied here, showing predominant lubricity up to 1000°C. On the other hand, a group of *in-situ* formed ternary oxide phases such as molybdates, vanadates and niobates in the contact interfaces withstood extreme temperature lubrication.
- An interfacial wear mechanism of the oxides over a wide temperature range (i.e., RT to high temperatures) has been proposed. Pure metallic elements, binary oxides, and ternary oxides were considered to play a predominant role in reducing friction in the composites at low temperature, low to medium high temperature, and relatively high temperature, respectively.

2.7 Future Perspective

A great deal of research has been done on the *in-situ* oxides formed during sliding of conventional metals, alloys, and composites. These oxides have helped to reduce friction and wear, but tribological research on directly formed oxides is quite limited.

- Powder metallurgy and PVD techniques have been widely used to prepare samples or coatings; however, plasma spraying, and laser cladding have been greatly underestimated despite their advantages such as lower cost, lower complexity, atmospheric deposition

conditions, ease of application to large surfaces, and high deposition efficiency compared to conventional thin film deposition processes.

- The mechanisms for improving the tribology of different oxides at high temperatures are different. The most common are high ionic potential, low shear strength and ductile behavior, etc. In addition, low interaction parameters, sintering effect, and activation energy or diffusion coefficient played a significant role in reducing oxide friction under extreme conditions. The authors believe that much research is needed to find out the main driving mechanisms for improving the friction and wear resistance of oxides.
- Currently, more efforts are directed towards in-situ generated oxides for their improved friction and wear resistance. However, very little information is available on the research of various binary and ternary oxides. **Figure 2. 30** shows the possible future trend of tribological research on different oxides. In the era of high entropy, the authors believe that the high entropy oxides (HEOs) could be an important topic for the investigation of wear resistance behavior due to their unique mechanical and thermal properties.

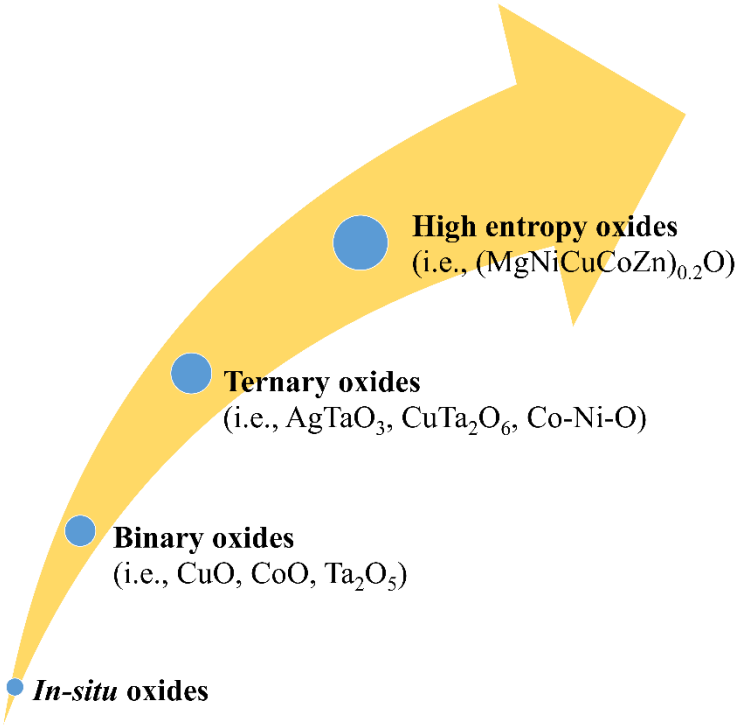

Figure 2. 30: A possible research trend for different types of oxides in the near future

2.8 References

[1] Franz R, Mitterer C. Vanadium containing self-adaptive low-friction hard coatings for high-temperature applications: a review. Surf Coatings Technol 2013;228:1–13.

[2] Allam IM. Solid lubricants for applications at elevated temperatures. J Mater Sci 1991;26:3977–84.

[3] Sliney HE. Solid lubricant materials for high temperatures—a review. Tribol Int 1982;15:303–15.

[4] Hilton MR, Fleischauer PD. Applications of solid lubricant films in spacecraft. Surf Coatings Technol 1992;54:435–41.

[5] Voevodin AA, Muratore C, Aouadi SM. Hard coatings with high temperature adaptive lubrication and contact thermal management. Surf Coatings Technol 2014;257:247–65.

[6] Merz R, Brodyanski A, Kopnarski M. On the role of oxidation in tribological contacts under environmental conditions. Conf. Pap. Sci., vol. 2015, Hindawi; 2015.

[7] Muratore C, Voevodin AA. Chameleon Coatings: Adaptive Surfaces to Reduce Friction and Wear in Extreme Environments. Annu Rev Mater Res 2009;39:297–324. https://doi.org/10.1146/annurev-matsci-082908-145259.

[8] Woydt M, Skopp A, Dörfel I, Witke K. Wear engineering oxides/anti-wear oxides. Wear 1998;218:84–95.

[9] Magnéli A. Structures of the ReO3-type with recurrent dislocations of atoms:homologous series' of molybdenum and tungsten oxides. Acta Crystallogr 1953;6:495–500.

[10] Peterson MB, Li SZ, Murray SF. Wear-resisting oxide films for 900 {degree} C. Final report. Argonne National Lab., IL (United States); 1994.

[11] Peterson MB, Murray SF, Florek JJ. Consideration of lubricants for temperatures above 1000 F. ASLE Trans 1959;2:225–34.

[12] Gardos MN, Hong H-S, Winer WO %J TT. The effect of anion vacancies on the tribological properties of rutile (TiO2-x), Part II: experimental evidence 1990;33:209–20.

[13] Kato K. Wear in relation to friction—a review. Wear 2000;241:151–7.

[14] Erdemir A. A crystal-chemical approach to lubrication by solid oxides. Tribol Lett 2000;8:97–102. https://doi.org/10.1023/a:1019183101329.

[15] Erdemir A. A crystal chemical approach to the formulation of self-lubricating nanocomposite coatings. Surf Coatings Technol 2005;200:1792–6.

[16] Prakash B, Celis J-P. The lubricity of oxides revised based on a polarisability approach. Tribol Lett 2007;27:105–12.

[17] Czichos H, Woydt M. Introduction to tribology and tribological parameters. ASM handbook. Vol. 18, Frict. Lubr. wear Technol., ASM International; 2017, p. 3–15.

[18] Yonggang M, Xu J, Jin Z, Braham P, Yuanzhong H %J F. A review of recent advances in tribology 2020;8:221–300.

[19] Blau PJ. Elevated-temperature tribology of metallic materials. Tribol Int 2010;43:1203–8. https://doi.org/10.1016/j.triboint.2010.01.003.

[20] Botto D, Lavella M. High temperature tribological study of cobalt-based coatings reinforced with different percentages of alumina. Wear 2014;318:89–97.

[21] Becker EP. Trends in tribological materials and engine technology. Tribol Int 2004;37:569–75. https://doi.org/10.1016/j.triboint.2003.12.006.

[22] Lehn A. Air foil thrust bearings: A thermo-elasto-hydrodynamic analysis 2017.

[23] Agrawal GL. Foil air/gas bearing technology—an overview. Turbo Expo Power Land, Sea, Air, vol. 78682, American Society of Mechanical Engineers; 1997, p. V001T04A006.

[24] Harris TA, Barnsby RM. Tribological performance prediction of aircraft gas turbine mainshaft ball bearings. Tribol Trans 1998;41:60–8. https://doi.org/10.1080/10402009808983722.

[25] Stoyanov P, Harrington KM, Frye A. Insights into the tribological characteristic of Cu-based coatings under extreme contact conditions. JOM 2020;72:2191–7.

[26] Ross E, Ignatov A, Stoyanov P. Tribological Characteristics of Manufactured Carbon Under Extreme Contact Conditions. Tribol Ind 2021;43.

[27] Chupp RE, Hendricks RC, Steinetz BM. Gas Turbine Engines: Seals. Encycl Aerosp Eng 2010.

[28] Wen S, Huang P. Principles of tribology. Wiley Online Library; 2012.

[29] Nilsson M. Tribology in Metal Working 2012.

[30] Schey JA %J L, Wear AS for M. Tribology in metalworking: Friction 1983:573–616.

[31] Gassner G, Mayrhofer PH, Kutschej K, Mitterer C, Kathrein M. Magnéli phase formation of PVD Mo–N and W–N coatings. Surf Coatings Technol 2006;201:3335–41.

[32] Gajrani KK, Suresh S, Sankar MR. Environmental friendly hard machining performance of uncoated and MoS2 coated mechanical micro-textured tungsten carbide cutting tools. Tribol Int 2018;125:141–55. https://doi.org/10.1016/j.triboint.2018.04.031.

[33] Sliney HE. Wide temperature spectrum self-lubricating coatings prepared by plasma spraying. Thin Solid

Films 1979;64:211–7. https://doi.org/10.1016/0040-6090(79)90511-X.
[34] DellaCorte C, Thomas F, Edmonds BJ. The effect of composition on the surface finish of PS400: a new high temperature solid lubricant coating 2010.
[35] A. Alidokht S, Gao Y, De Castilho B, Sharifi N, Harfouche M, Stoyanov P, et al. Microstructure and mechanical properties of Tribaloy coatings deposited by high-velocity oxygen fuel. J Mater Sci 2022:1–13.
[36] Roy A, Sharifi N, Munagala VN V, Alidokht SA, Patel P, Makowiec M, et al. Microstructural evolution and tribological behavior of suspension plasma sprayed CuO as high-temperature lubricious coatings. Wear 2023:204874.
[37] Dellacorte C. Tribological composition optimization of chromium-carbide-based solid lubricant coatings for foil gas bearings at temperatures to 650° C. Surf Coatings Technol 1988;36:87–97.
[38] Dellacorte C. Experimental evaluation of chromium-carbide-based solid lubricant coatings for use to 760 C 1987.
[39] Dellacorte C, Fellenstein JA. The Effect of Compositional Tailoring on the Thermal Expansion and Tribological Properties of PS300: A Solid Lubricant Composite Coating The Effect of Compositional Tailoring on the Thermal Expansion and Tribological Properties of PS300: A Solid Lubricant composite Coating@. Taylor Fr 2008;40:639–42. https://doi.org/10.1080/10402009708983703.
[40] Dellacorte C, Laskowski JA %J T transactions. Tribological Evaluation of PS300: A New Chrome Oxide-Based Solid Lubricant Coating Sliding Against Al2O3 from 25° to 650° C© 1997;40:163–7.
[41] DellaCorte C, Edmonds BJ. NASA PS400: a new high temperature solid lubricant coating for high temperature wear applications. National Aeronautics and Space Administration, Glenn Research Center Cleveland; 2009.
[42] Radil K, DellaCorte C %J TT. The performance of PS400 subjected to sliding contact at temperatures from 260 to 927 C 2017;60:957–64.
[43] Dellacorte C, Sliney HE. Tribological Properties of PM212: A High-Temperature, Self-Lubricating, Powder Metallurgy Composite. 1989.
[44] Munagala VNV, Alidokht SA, Sharifi N, Makowiec ME, Stoyanov P, Moreau C, et al. Room and elevated temperature sliding wear of high velocity oxy-fuel sprayed Diamalloy3001 coatings. Tribol Int 2022:108069.
[45] Patel P, Alidokht SA, Sharifi N, Roy A, Harrington K, Stoyanov P, et al. Microstructural and Tribological Behavior of Thermal Spray CrMnFeCoNi High Entropy Alloy Coatings. J Therm Spray Technol 2022:1–17.
[46] Peng J, Fang X, Marx V, Jasnau U, Degradation MPM, 2018 U. Isothermal oxidation behavior of Tribaloy TM T400 and T800. NatureCom n.d.
[47] Renz A, Prakash B, Hardell J, Wear OL-, 2018 U. High-temperature sliding wear behaviour of Stellite® 12 and Tribaloy® T400. Elsevier n.d.
[48] Durejko T, Łazińska M, Dworecka-Wójcik J, Lipiński S, Varin RA, Czujko T %J M. The Tribaloy T-800 Coatings Deposited by Laser Engineered Net Shaping (LENSTM) 2019;12:1366.
[49] Schmidt R, Wear DF-, 1975 undefined. New materials resistant to wear and corrosion to 1000 C. Elsevier n.d.
[50] Hardell J. High Temperature Tribology of High Strength Boron Steel and Tool Steels. 2007.
[51] Patel P, Roy A, Sharifi N, Stoyanov P, Chromik RR, Moreau C. Tribological Performance of High-Entropy Coatings (HECs): A Review. Materials (Basel) 2022;15:3699.
[52] Luo DB, Fridrici V, Kapsa P. A systematic approach for the selection of tribological coatings. Wear 2011;271:2132–43.
[53] Stachowiak GW, Batchelor AW. Engineering tribology. Butterworth-heinemann; 2013.
[54] Korashy A, Attia H, Thomson V, Oskooei S. Characterization of fretting wear of cobalt-based superalloys at high temperature for aero-engine combustor components. Wear 2015;330:327–37.
[55] Peterson MB, Florek JJ, Lee RE. Sliding characteristics of metals at high temperatures. ASLE Trans 1960;3:101–9. https://doi.org/10.1080/05698196008972392.
[56] Stott F, Lin D, Wood G, Wear CS-, 1976 U. The tribological behaviour of nickel and nickel-chromium alloys at temperatures from 20 to 800 C. Elsevier n.d.
[57] Viat A, Bouchet M-IDB, Vacher B, Le Mogne T, Fouvry S, Henne J-F. Nanocrystalline glaze layer in ceramic-metallic interface under fretting wear. Surf Coatings Technol 2016;308:307–15.
[58] Viat A, Dreano A, Fouvry S, Bouchet M-IDB, Henne J-F. Fretting wear of pure cobalt chromium and nickel to identify the distinct roles of HS25 alloying elements in high temperature glaze layer formation. Wear 2017;376:1043–54.
[59] Scharf TW, Prasad S V, Kotula PG, Michael JR, Robino C V. Elevated temperature tribology of cobalt and tantalum-based alloys. Wear 2015;330:199–208.
[60] Stott FH, Stevenson CW, Wood GC. Friction and wear properties of Stellite 31 at temperatures from 293

to 1073K. Met Technol 1977;4:66–74.
[61] Stoyanov P, Dawag L, Goberman DG, Shah D. Friction and wear characteristics of single crystal Ni-based superalloys at elevated temperatures. Tribol Lett 2018;66:1–9.
[62] Yang Q, Senda T, Kotani N, Hirose A %J S, Technology C. Sliding wear behavior and tribofilm formation of ceramics at high temperatures 2004;184:270–7.
[63] Kato H, Komai K. Tribofilm formation and mild wear by tribo-sintering of nanometer-sized oxide particles on rubbing steel surfaces. Wear 2007;262:36–41.
[64] Biswas SK %J W. Some mechanisms of tribofilm formation in metal/metal and ceramic/metal sliding interactions 2000;245:178–89.
[65] Stoyanov P, Boyne A, Ignatov A. Tribological characteristics of Co-based plasma sprayed coating in extreme conditions. Results in Surfaces and Interfaces 2021;3:100007.
[66] Harrington KM, Miller EC, Frye A, Stoyanov P. Tribological insights of Co-and Ni-based alloys in extreme conditions. Wear 2021;477:203827.
[67] Wahl KJ, Seitzman LE, Bolster RN, Singer IL, Peterson MB. Ion-beam deposited Cu-Mo coatings as high temperature solid lubricants. Surf Coatings Technol 1997;89:245–51.
[68] Stoyanov P, Merz R, Romero PA, Wählisch FC, Abad OT, Gralla R, et al. Surface softening in metal–ceramic sliding contacts: An experimental and numerical investigation. ACS Nano 2015;9:1478–91.
[69] Viat A, Guillonneau G, Fouvry S, Kermouche G, Sao Joao S, Wehrs J, et al. Brittle to ductile transition of tribomaterial in relation to wear response at high temperatures 2017;392:60–8.
[70] Wan S. Solid lubricant: soft metal. Encycl Tribol New York Springer US 2013:3152–9.
[71] Stoyanov P, Chromik RR, Goldbaum D, Lince JR, Zhang X. Microtribological performance of Au–MoS 2 and Ti–MoS 2 coatings with varying contact pressure. Tribol Lett 2010;40:199–211.
[72] Stoyanov P, Gupta S, Chromik RR, Lince JR. Microtribological performance of Au–MoS2 nanocomposite and Au/MoS2 bilayer coatings. Tribol Int 2012;52:144–52.
[73] Bowden FP, Bowden FP, Tabor D. The friction and lubrication of solids. vol. 1. Oxford university press; 2001.
[74] Lugscheider E, Knotek O, Bärwulf S, Bobzin K %J S, Technology C. Characteristic curves of voltage and current, phase generation and properties of tungsten-and vanadium-oxides deposited by reactive dc-MSIP-PVD-process for self-lubricating applications 2001;142:137–42.
[75] Bhushan B. Solid lubricants and self-lubricating films. Mod. Tribol. Handbook, Two Vol. Set, CRC Press; 2000, p. 817–56.
[76] Erdemir A, Nichols FA, Fenske GR, Hsieh J-H. Sliding friction and wear of ceramics with and without soft metallic films. MRS Bull 1991;16:49–53.
[77] Aouadi SM, Gao H, Martini A, Scharf TW, Muratore C. Lubricious oxide coatings for extreme temperature applications: A review. Surf Coatings Technol 2014;257:266–77.
[78] Dimitrov V, Komatsu T. Classification of simple oxides: a polarizability approach. J Solid State Chem 2002;163:100–12.
[79] Wang X, Feng X, Lu C, Yi G, Jia J, Li H. Mechanical and tribological properties of plasma sprayed NiAl composite coatings with addition of nanostructured TiO2/Bi2O3. Surf Coatings Technol 2018;349:157–65.
[80] Yao Q, Jia J, Chen T, Xin H, Shi Y, He N, et al. High temperature tribological behaviors and wear mechanisms of NiAl-MoO3/CuO composite coatings. Surf Coatings Technol 2020;395:125910.
[81] Navinšek B, Panjan P, Čekada M, Quinto DT %J S, Technology C. Interface characterization of combination hard/solid lubricant coatings by specific methods 2002;154:194–203.
[82] PalDey S, Deevi SC %J MS, Engineering: A. Single layer and multilayer wear resistant coatings of (Ti, Al) N: a review 2003;342:58–79.
[83] Meng F, Yang C, Han Part J: Journal of Engineering Tribology H %J P of the I of ME. Study on tribological performances of MoS2 coating at high temperature 2018;232:964–73.
[84] Lofaj F, Mikula M, Grancic B, Cempura G, Hornak P, Kus P, et al. Tribological properties of TiBx and WC/C coatings 2011;55:305–11.
[85] Bhushan B. Modern tribology handbook, two volume set. CRC press; 2000.
[86] Erdemir A, Donnet C %J M, series materials science. Modern tribology handbook 2001:787–825.
[87] Fateh N, Fontalvo GA, Gassner G, Mitterer C. Influence of high-temperature oxide formation on the tribological behaviour of TiN and VN coatings. Wear 2007;262:1152–8.
[88] O'regan B, Grätzel M %J nature. A low-cost, high-efficiency solar cell based on dye-sensitized colloidal TiO 2 films 1991;353:737–40.
[89] Khatibnezhad H, Ambriz-Vargas F, Ettouil F Ben, Moreau C. An investigation on the photocatalytic activity of sub-stoichiometric TiO2-x coatings produced by suspension plasma spray. J Eur Ceram Soc 2020:0–1. https://doi.org/10.1016/j.jeurceramsoc.2020.08.017.
[90] Traversa E, Gnappi G, Montenero A, Gusmano G %J S, Chemical AB. Ceramic thin films by sol-gel

processing as novel materials for integrated humidity sensors 1996;31:59–70.
[91] Gardon M, Guilemany JM %J J of thermal spray technology. Milestones in functional titanium dioxide thermal spray coatings: A review 2014;23:577–95.
[92] Piwoński I %J TSF. Preparation method and some tribological properties of porous titanium dioxide layers 2007;515:3499–506.
[93] Krishna DSR, Sun Y %J S, Technology C. Effect of thermal oxidation conditions on tribological behaviour of titanium films on 316L stainless steel 2005;198:447–53.
[94] Aniołek K, Kupka M, Barylski A. Characteristics of the tribological properties of oxide layers obtained via thermal oxidation on titanium Grade 2. Proc Inst Mech Eng Part J J Eng Tribol 2019;233:125–38.
[95] Stoyanov P, Strauss HW, Chromik RR. Scaling effects between micro-and macro-tribology for a Ti–MoS2 coating. Wear 2012;274:149–61.
[96] Gardos MN. Magnéli phases of anion-deficient rutile as lubricious oxides. Part I. Tribological behavior of single-crystal and polycrystalline rutile (Ti n O 2n− 1). Tribol Lett 2000;8:65–78.
[97] Gardos MN. The Effect of Anion Vacancies on the Tribological Properties of Rutile (TiO2–x). Tribol Trans 1988;31:427–36.
[98] Wong M-S, Lin Y-J, Pylnev M, Kang W-Z. Processing, structure and properties of reactively sputtered films of titanium dioxide and suboxides. Thin Solid Films 2019.
[99] Woydt M %J TL. Tribological characteristics of polycrystalline Magnéli-type titanium dioxides 2000;8:117–30.
[100] Santecchia E, Hamouda AMS, Musharavati F, Zalnezhad E, Cabibbo M, Spigarelli S. Wear resistance investigation of titanium nitride-based coatings. Ceram Int 2015;41:10349–79. https://doi.org/10.1016/j.ceramint.2015.04.152.
[101] Stoyanov P, Schneider J, Rinke M, Ulrich S, Nold E, Dienwiebel M, et al. Microstructure, mechanical properties and friction behavior of magnetron-sputtered VC coatings. Surf Coatings Technol 2017;321:366–77.
[102] Gassner G, Mayrhofer PH, Kutschej K, Mitterer C, Kathrein M. A new low friction concept for high temperatures: lubricious oxide formation on sputtered VN coatings. Tribol Lett 2004;17:751–6.
[103] Ouyang JH, Murakami T, Sasaki S. High-temperature tribological properties of a cathodic arc ion-plated (V, Ti) N coating. Wear 2007;263:1347–53.
[104] Fateh N, Fontalvo GA, Gassner G, Mitterer C %J T letters. The beneficial effect of high-temperature oxidation on the tribological behaviour of V and VN coatings 2007;28:1–7.
[105] Fateh N, Fontalvo GA, Mitterer C. Tribological Properties of reactive magnetron sputtered V 2 O 5 and VN–V 2 O 5 coatings. Tribol Lett 2008;30:21–6.
[106] Mayrhofer PH, Hovsepian PE, Mitterer C, Münz W-D. Calorimetric evidence for frictional self-adaptation of TiAlN/VN superlattice coatings. Surf Coatings Technol 2004;177:341–7.
[107] Kutschej K, Mayrhofer PH, Kathrein M, Polcik P, Mitterer C. Influence of oxide phase formation on the tribological behaviour of Ti–Al–V–N coatings. Surf Coatings Technol 2005;200:1731–7.
[108] Mu Y, Liu M, Zhao Y. Carbon doping to improve the high temperature tribological properties of VN coating. Tribol Int 2016;97:327–36.
[109] Beke S %J TSF. A review of the growth of V2O5 films from 1885 to 2010 2011;519:1761–71.
[110] Lyo I-W, Ahn H-S, Lim D-S %J S, Technology C. Microstructure and tribological properties of plasma-sprayed chromium oxide–molybdenum oxide composite coatings 2003;163:413–21.
[111] Jin G, Xu B, Wang H, Li Q, Wei S %J S, Technology C. Tribological properties of molybdenum coatings sprayed by electro-thermal explosion directional spraying 2007;201:6678–80.
[112] Deambrosis SM, Miorin E, Montagner F, Zin V, Fabrizio M, Sebastiani M, et al. Structural, morphological and mechanical characterization of Mo sputtered coatings 2015;266:14–21.
[113] Kolawole FO, Ramirez MA, Kolawole SK, Varela LB, Tschiptschin AP %J ML. Deposition and characterization of molybdenum oxide (MoO3) nanoparticles incorporated diamond-like carbon coatings using pulsed-DC PECVD 2020;278:128420.
[114] Suszko T, Gulbiński W, Jagielski J. The role of surface oxidation in friction processes on molybdenum nitride thin films. Surf Coatings Technol 2005;194:319–24.
[115] Solak N, Ustel F, Urgen M, Aydin S, Cakir AF. Oxidation behavior of molybdenum nitride coatings. Surf Coatings Technol 2003;174:713–9.
[116] Wang W, Zheng S, Pu J, Cai Z, Wang H, Wang L, et al. Microstructure, mechanical and tribological properties of Mo-VN films by reactive magnetron sputtering. Surf Coatings Technol 2020:125532.
[117] Broniszewski K, Wozniak J, Czechowski K, Jaworska L, Olszyna A. Al2O3–Mo cutting tools for machining hardened stainless steel. Wear 2013;303:87–91.
[118] Qi Y, Zhang Y-S, Hu L-T. High-temperature self-lubricated properties of Al2O3/Mo laminated composites. Wear 2012;280:1–4.
[119] Cura ME, Liu XW, Kanerva U, Varjus S, Kivioja A, Söderberg O, et al. Friction behavior of

alumina/molybdenum composites and formation of MoO3− x phase at 400 C. Tribol Int 2015;87:23–31.
[120] Mei H, Luo Q, Huang X, Ding JC, Zhang TF, Wang Q. Influence of lubricious oxides formation on the tribological behavior of Mo-V-Cu-N coatings deposited by HIPIMS. Surf Coatings Technol 2019;358:947–57.
[121] Hudec T, Mikula M, Satrapinskyy L, Roch T, Truchlý M, Švec Jr P, et al. Structure, mechanical and tribological properties of Mo-SN solid lubricant coatings. Appl Surf Sci 2019;486:1–14.
[122] Fu Y, He T, Yang W, Xu J, Mu B, Pang X, et al. Structure, mechanical and tribological properties of MoSN/MoS2 multilayer films. Coatings 2019;9:108.
[123] Lu C, Jia J, Fu Y, Yi G, Feng X, Yang J, et al. Influence of Mo contents on the tribological properties of CrMoN/MoS2 coatings at 25–700° C. Surf Coatings Technol 2019;378:125072.
[124] Mukhopadhyay A, Barman TK, Sahoo P. Tribological characteristics of electroless Ni–B–Mo coatings at different operating temperatures. Surf Rev Lett 2019;26:1850175.
[125] Zhao Y, Feng K, Yao C, Li Z. Effect of MoO3 on the microstructure and tribological properties of laser-clad Ni60/nanoCu/h-BN/MoO3 composite coatings over wide temperature range. Surf Coatings Technol 2020;387:125477.
[126] Liu C, Ju H, Yu L, Xu J, Geng Y, He W, et al. Tribological properties of Mo2N films at elevated temperature. Coatings 2019;9:734.
[127] Ghosh K, Mazumder S, Kumar Singh B, Hirani H, Roy P, Mandal N. Tribological Property Investigation of Self-Lubricating Molybdenum-Based Zirconia Ceramic Composite Operational at Elevated Temperature. J Tribol 2020;142.
[128] Mitterer C, Holler F, Üstel F, Heim D %J S, Technology coatings. Application of hard coatings in aluminium die casting—soldering, erosion and thermal fatigue behaviour 2000;125:233–9.
[129] Stoyanov P, Stemmer P, Jarvi TT, Merz R, Romero PA, Scherge M, et al. Friction and wear mechanisms of tungsten–carbon systems: A comparison of dry and lubricated conditions. ACS Appl Mater Interfaces 2013;5:6123–35.
[130] Lugscheider E, Knotek O, Bärwulf S, Bobzin K. Characteristic curves of voltage and current, phase generation and properties of tungsten-and vanadium-oxides deposited by reactive dc-MSIP-PVD-process for self-lubricating applications. Surf Coatings Technol 2001;142:137–42.
[131] Polcar T, Parreira NMG, Cavaleiro A. Tribological characterization of tungsten nitride coatings deposited by reactive magnetron sputtering. Wear 2007;262:655–65.
[132] Pimentel J V, Polcar T, Evaristo M, Cavaleiro A. Examination of the tribolayer formation of a self-lubricant W–S–C sputtered coating. Tribol Int 2012;47:188–93.
[133] Polcar T, Evaristo M, Cavaleiro A. Comparative study of the tribological behavior of self-lubricating W–S–C and Mo–Se–C sputtered coatings. Wear 2009;266:388–92.
[134] Gustavsson F, Jacobson S, Cavaleiro A, Polcar T. Ultra-low friction W–S–N solid lubricant coating. Surf Coatings Technol 2013;232:541–8.
[135] Huang X, Xie Z, Li K, Chen Q, Gong F, Chen Y, et al. Microstructure, wear and oxidation resistance of CrWN glass molding coatings synthesized by plasma enhanced magnetron sputtering. Vacuum 2020;174:109206.
[136] Javdošňák D, Musil J, Soukup Z, Haviar S, Čerstvý R, Houska J. Tribological properties and oxidation resistance of tungsten and tungsten nitride films at temperatures up to 500° C. Tribol Int 2019;132:211–20.
[137] Polcar T, Parreira NMG, Cavaleiro A %J W. Structural and tribological characterization of tungsten nitride coatings at elevated temperature 2008;265:319–26.
[138] Yu L, Zhao H, Xu J %J A surface science. Mechanical, tribological and corrosion performance of WBN composite films deposited by reactive magnetron sputtering 2014;315:380–6.
[139] Ju H, He X, Yu L, Xu J %J S, Technology C. The microstructure and tribological properties at elevated temperatures of tungsten silicon nitride films 2017;326:255–63.
[140] Yu L, Zhao H, Ju H, Xu J %J TSF. Influence of Cu content on the structure, mechanical and tribological properties of W2N-Cu films 2017;624:144–51.
[141] Österle W, Prietzel C, Kloß H, Dmitriev AI. On the role of copper in brake friction materials. Tribol Int 2010;43:2317–26.
[142] Goto M, Kasahara A, Oishi T, Konishi Y, Tosa M. Lubricative coatings of copper oxide for aerospace applications. J Appl Phys 2003. https://doi.org/10.1063/1.1588355.
[143] Pasaribu HR, Sloetjes JW, Schipper DJ. Friction reduction by adding copper oxide into alumina and zirconia ceramics. Wear 2003;255:699–707.
[144] Allam IM. Solid lubricants for applications at elevated temperatures - A review. J Mater Sci 1991;26:3977–84. https://doi.org/10.1007/BF00553478.
[145] CuO_2007_Pasaribu_Effect of Microstructure on the Tribological and Mechanical Properties of CuO-Doped 3Y-TZP Ceramics.pdf n.d.

[146] Ran S, Winnubst L, Blank DHA, Pasaribu HR, Sloetjes J-W, Schipper DJ. Dry-sliding self-lubricating ceramics: CuO doped 3Y-TZP. Wear 2009;267:1696–701.
[147] Valefi M, de Rooij M, Schipper DJ, Winnubst L. High-Temperature Tribological and Self-Lubricating Behavior of Copper Oxide-Doped Y-TZP Composite Sliding Against Alumina. J Am Ceram Soc 2011;94:4426–34.
[148] Kong L, Bi Q, Zhu S, Qiao Z, Yang J, Liu W. Effect of CuO on self-lubricating properties of ZrO2 (Y2O3)–Mo composites at high temperatures. J Eur Ceram Soc 2014;34:1289–96.
[149] Mazumder S, Kumar OP, Kotnees DK, Mandal N. Tribological Influences of CuO Into 3Y-TZP Ceramic Composite in Conformal Contact. J Tribol 2019;141. https://doi.org/10.1115/1.4041894.
[150] Zhu S, Cheng J, Qiao Z, Tian Y, Yang J. High Temperature Lubricating Behavior of NiAl Matrix Composites with Addition of CuO. J Tribol 2016;138:1–9. https://doi.org/10.1115/1.4033133.
[151] Zhu S, Bi Q, Niu M, Yang J, Liu W. Tribological behavior of NiAl matrix composites with addition of oxides at high temperatures. Wear 2012;274–275:423–34. https://doi.org/10.1016/j.wear.2011.11.006.
[152] Pasaribu HR, Reuver KM, Schipper DJ, Ran S, Wiratha KW, Winnubst AJA, et al. Environmental effects on friction and wear of dry sliding zirconia and alumina ceramics doped with copper oxide. Int J Refract Met Hard Mater 2005;23:386–90. https://doi.org/10.1016/j.ijrmhm.2005.05.001.
[153] Cui G, Liu Y, Gao G, Liu H, Kou Z. Microstructure and high-temperature wear performance of FeCr matrix self-lubricating composites from room temperature to 800 °C. Materials (Basel) 2020;13. https://doi.org/10.3390/ma13010051.
[154] Berger L-M, Stahr CC, Saaro S, Thiele S, Woydt M, Kelling N %J W. Dry sliding up to 7.5 m/s and 800 C of thermally sprayed coatings of the TiO2–Cr2O3 system and (Ti, Mo)(C, N)–Ni (Co) 2009;267:954–64.
[155] Voevodin AA, Zabinski JS %J CS, Technology. Nanocomposite and nanostructured tribological materials for space applications 2005;65:741–8.
[156] Aouadi SM, Luster B, Kohli P, Muratore C, Voevodin AA. Progress in the development of adaptive nitride-based coatings for high temperature tribological applications. Surf Coatings Technol 2009;204:962–8.
[157] Gulbinski W, Suszko T, Sienicki W, Warcholiński B. Tribological properties of silver-and copper-doped transition metal oxide coatings. Wear 2003;254:129–35. https://doi.org/10.1016/S0043-1648(02)00292-2.
[158] Singh DP, Polychronopoulou K, Rebholz C, Aouadi SM. Room temperature synthesis and high temperature frictional study of silver vanadate nanorods. Nanotechnology 2010;21:325601.
[159] Bondarev A V, Kvashnin DG, Shchetinin I V, Shtansky D V. Temperature-dependent structural transformation and friction behavior of nanocomposite VCN-(Ag) coatings. Mater Des 2018;160:964–73.
[160] Aouadi SM, Singh DP, Stone DS, Polychronopoulou K, Nahif F, Rebholz C, et al. Adaptive VN/Ag nanocomposite coatings with lubricious behavior from 25 to 1000 °c. Acta Mater 2010;58:5326–31. https://doi.org/10.1016/j.actamat.2010.06.006.
[161] Muratore C, Bultman JE, Aouadi SM, Voevodin AA. In situ Raman spectroscopy for examination of high temperature tribological processes. Wear 2011;270:140–5.
[162] Guo H, Han M, Chen W, Lu C, Li B, Wang W, et al. Microstructure and properties of VN/Ag composite films with various silver content. Vacuum 2017;137:97–103.
[163] Guo H, Lu C, Zhang Z, Liang B, Jia J. Comparison of microstructures and properties of VN and VN/Ag nanocomposite films fabricated by pulsed laser deposition. Appl Phys A 2018;124:694.
[164] Mu Y, Liu M, Wang Y, Liu E. PVD multilayer VN–VN/Ag composite coating with adaptive lubricious behavior from 25 to 700 C. RSC Adv 2016;6:53043–53.
[165] Luster B, Stone D, Singh DP, to Baben M, Schneider JM, Polychronopoulou K, et al. Textured VN coatings with Ag3VO4 solid lubricant reservoirs. Surf Coatings Technol 2011;206:1932–5.
[166] Xin B, Yu Y, Zhou J, Wang L, Ren S, Li Z. Effect of silver vanadate on the lubricating properties of NiCrAlY laser cladding coating at elevated temperatures. Surf Coatings Technol 2016;307:136–45.
[167] Liu E, Bai Y, Gao Y, Yi G, Jia J. Tribological properties of NiAl-based composites containing Ag3VO4 nanoparticles at elevated temperatures. Tribol Int 2014;80:25–33.
[168] Liu E, Gao Y, Bai Y, Yi G, Wang W, Zeng Z, et al. Tribological properties of self-lubricating NiAl/Mo-based composites containing AgVO3 nanowires. Mater Charact 2014;97:116–24.
[169] Zhang W, Du L, Lan H, Huang C, Zhang W. Wear behavior of a NiCr/AgVO 3 self-lubricating composite. Acta Metall Sin (English Lett 2013;26:435–40.
[170] Du L, Zhang W, Zhang W, Zhang T, Lan H, Huang C. Tribological and oxidation behaviors of the plasma sprayed NiCoCrAlY-Cr2O3-AgVO3 coating. Surf Coatings Technol 2016;298:7–14. https://doi.org/10.1016/j.surfcoat.2016.04.042.
[171] Bondarev A V, Golizadeh M, Shvyndina N V, Shchetinin I V, Shtansky D V. Microstructure, mechanical, and tribological properties of Ag-free and Ag-doped VCN coatings. Surf Coatings Technol 2017;331:77–

84.
[172] Zhao Y, Mu Y, Ming LIU. Mechanical properties and friction− wear characteristics of VN/Ag multilayer coatings with heterogeneous and transition interfaces. Trans Nonferrous Met Soc China 2020;30:472–83.
[173] Stone D, Liu J, Singh DP, Muratore C, Voevodin AA, Mishra S, et al. Layered atomic structures of double oxides for low shear strength at high temperatures. Scr Mater 2010;62:735–8.
[174] Muratore C, Voevodin AA, Hu JJ, Zabinski JS. Tribology of adaptive nanocomposite yttria-stabilized zirconia coatings containing silver and molybdenum from 25 to 700 C. Wear 2006;261:797–805.
[175] Wenda E. High temperature reactions in the MoO3-Ag2O system. J Therm Anal Calorim 1998;53:861–70.
[176] Turutoğlu T, Ürgen M, Çakir AF, Öztürk A. Characterization of Mo2N/Ag nanocomposite coatings produced by magnetron sputtering. Key Eng Mater 2004;264–268:489–92. https://doi.org/10.4028/www.scientific.net/KEM.264-268.489.
[177] Gulbiński W, Suszko T. Thin films of MoO3–Ag2 O binary oxides–the high temperature lubricants. Wear 2006;261:867–73.
[178] Gulbiński W, Suszko T. Thin films of Mo2N/Ag nanocomposite—the structure, mechanical and tribological properties. Surf Coatings Technol 2006;201:1469–76.
[179] Li B, Gao Y, Han M, Guo H, Wang W, Jia J. Microstructure and tribological properties of NiCrAlY-Mo-Ag composite by vacuum hot-press sintering. Vacuum 2017;143:1–6.
[180] Chen J, An Y, Yang J, Zhao X, Yan F, Zhou H, et al. Tribological properties of adaptive NiCrAlY-Ag-Mo coatings prepared by atmospheric plasma spraying. Surf Coatings Technol 2013;235:521–8. https://doi.org/10.1016/j.surfcoat.2013.08.012.
[181] Liu E, Wang W-Z, Gao Y, Jia J-H. Tribological properties of adaptive Ni-based composites with addition of lubricious Ag 2 MoO 4 at elevated temperatures. Tribol Lett 2012;47:21–30.
[182] Liu E-Y, Gao Y-M, Wang W-Z, Zhang X-L, Wang X, Yi G-W, et al. Effect of Ag2Mo2O7 incorporation on the tribological characteristics of adaptive Ni-based composite at elevated temperatures. Tribol Trans 2013;56:469–79.
[183] Zhang T, Huang C, Lan H, Du L, Zhang W. Tribological properties and lubrication mechanisms of a Ag–Mo composite. Lubr Sci 2016;28:141–56.
[184] Muratore C, Voevodin AA. Molybdenum disulfide as a lubricant and catalyst in adaptive nanocomposite coatings. Surf Coatings Technol 2006;201:4125–30.
[185] Hu JJ, Muratore C, Voevodin AA. Silver diffusion and high-temperature lubrication mechanisms of YSZ-Ag-Mo based nanocomposite coatings. Compos Sci Technol 2007;67:336–47. https://doi.org/10.1016/j.compscitech.2006.09.008.
[186] Muratore C, Voevodin AA, Hu JJ, Zabinski JS. Multilayered YSZ–Ag–Mo/TiN adaptive tribological nanocomposite coatings. Tribol Lett 2006;24:201–6.
[187] Suszko T, Gulbiński W, Jagielski J. Mo2N/Cu thin films—the structure, mechanical and tribological properties. Surf Coatings Technol 2006;200:6288–92.
[188] Kong L, Zhu S, Qiao Z, Yang J, Bi Q, Liu W. Effect of Mo and Ag on the friction and wear behavior of ZrO2 (Y2O3)–Ag–CaF2–Mo composites from 20° C to 1000° C. Tribol Int 2014;78:7–13.
[189] Ouyang JH, Shi CC, Liu ZG, Wang YM, Wang YJ. Fabrication and high-temperature tribological properties of self-lubricating NiCr-BaMoO4 composites. Wear 2015;330–331:272–9. https://doi.org/10.1016/j.wear.2015.01.063.
[190] Li X bing, Li YF. Tribological Properties of Spark Plasma Sintering TZ3Y20A–SrMoO4 Composites at Elevated Temperature. Tribol Lett 2017;65:1–10. https://doi.org/10.1007/s11249-017-0905-x.
[191] Aouadi SM, Paudel Y, Luster B, Stadler S, Kohli P, Muratore C, et al. Adaptive Mo 2 N/MoS 2/Ag tribological nanocomposite coatings for aerospace applications. Tribol Lett 2008;29:95–103.
[192] Aouadi SM, Paudel Y, Simonson WJ, Ge Q, Kohli P, Muratore C, et al. Tribological investigation of adaptive Mo2N/MoS2/Ag coatings with high sulfur content. Surf Coatings Technol 2009;203:1304–9.
[193] Shtansky D V, Bondarev A V, Kiryukhantsev-Korneev P V, Rojas TC, Godinho V, Fernández A. Structure and tribological properties of MoCN-Ag coatings in the temperature range of 25–700° C. Appl Surf Sci 2013;273:408–14.
[194] Wang J-Y, Shan Y, Guo H, Li B, Wang W, Jia J. Friction and Wear Characteristics of Hot-Pressed NiCr–Mo/MoO 3/Ag Self-Lubrication Composites at Elevated Temperatures up to 900 C. Tribol Lett 2015;59:48.
[195] Chen J, Zhao X, Zhou H, Chen J, An Y, Yan F. Microstructure and tribological property of HVOF-sprayed adaptive NiMoAl–Cr3C2–Ag composite coating from 20° C to 800° C. Surf Coatings Technol 2014;258:1183–90.
[196] Li B, Gao Y, Jia J, Han M, Guo H, Wang W. Influence of heat treatments on the microstructure as well as mechanical and tribological properties of NiCrAlY-Mo-Ag coatings. J Alloys Compd 2016;686:503–10.
[197] Lu C, Fu Y, Jia J, Yi G, Xie E, Guo H. Effect of substrate temperatures on the properties of PLD Mo–V–

Ag–O nanocomposite thin films. Vacuum 2019;167:357–63.
[198] Dai X, Wen M, Wang J, Cui X, Wang X, Zhang K. The tribological performance at elevated temperatures of MoNbN-Ag coatings. Appl Surf Sci 2020:145372.
[199] Wang W, Pu J, Cai Z, Zheng S, Wei Y. Insights into friction properties and mechanism of self-lubricating MoVN-Ag films at high temperature. Vacuum 2020:109332.
[200] Takeichi Y, Inada M, Minami K, Kawamura M, Dzimko M. Tribological properties of copper molybdate powder solid lubricants under high temperature conditions. Tribol Online 2015;10:127–37.
[201] Xin B, Yu Y, Zhou J, Wang L, Ren S. Effect of copper molybdate on the lubricating properties of NiCrAlY laser clad coating at elevated temperatures. Surf Coatings Technol 2017;313:328–36. https://doi.org/10.1016/j.surfcoat.2017.01.098.
[202] Zhu R, Zhang P, Yu Z, Yan H, Li S, Wu D, et al. Microstructure and wide temperature range self-lubricating properties of laser cladding NiCrAlY/Ag2O/Ta2O5 composite coating. Surf Coatings Technol 2020;383:125248.
[203] Stone DS, Harbin S, Mohseni H, Mogonye J-E, Scharf TW, Muratore C, et al. Lubricious silver tantalate films for extreme temperature applications. Surf Coatings Technol 2013;217:140–6.
[204] Stone DS, Gao H, Chantharangsi C, Paksunchai C, Bischof M, Jaeger D, et al. Load-dependent high temperature tribological properties of silver tantalate coatings. Surf Coatings Technol 2014;244:37–44.
[205] Aouadi SM, Singh DP, Stone DS, Polychronopoulou K, Nahif F, Rebholz C, et al. Adaptive VN/Ag nanocomposite coatings with lubricious behavior from 25 to 1000° C. Acta Mater 2010;58:5326–31.
[206] Roy A, Munagala VN V, Patel P, Sharifi N, Alidokht SA, Makowiec M, et al. Friction and wear behavior of suspension plasma sprayed tantalum oxide coatings at elevated temperatures. Surf Coatings Technol 2022:129097.
[207] Stone DS, Gao H, Chantharangsi C, Paksunchai C, Bischof M, Martini A, et al. Reconstruction mechanisms of tantalum oxide coatings with low concentrations of silver for high temperature tribological applications. Appl Phys Lett 2014;105:191607.
[208] Gao H, Stone DS, Mohseni H, Aouadi SM, Scharf TW, Martini A. Mechanistic studies of high temperature friction reduction in silver tantalate. Appl Phys Lett 2013;102:121603.
[209] Gao H, Otero-de-la-Roza A, Aouadi SM, Martini A, Johnson ER. Chemical basis of the tribological properties of AgTaO3 crystal surfaces. J Phys Chem C 2014;118:17577–84.
[210] Wang J, Li J, Li H, Zhang X, Huang J, Xiong D. Friction and wear properties of amorphous and nanocrystalline Ta-Ag films at elevated temperatures as function of working pressure. Surf Coatings Technol 2018;353:135–47.
[211] Gao H, Otero-de-la-Roza A, Gu J, Stone D, Aouadi SM, Johnson ER, et al. (Ag, Cu)–Ta–O ternaries as high-temperature solid-lubricant coatings. ACS Appl Mater Interfaces 2015;7:15422–9.
[212] Stone DS, Migas J, Martini A, Smith T, Muratore C, Voevodin AA, et al. Adaptive NbN/Ag coatings for high temperature tribological applications. Surf Coatings Technol 2012;206:4316–21.
[213] Ju H, Xu J. Microstructure and tribological properties of NbN-Ag composite films by reactive magnetron sputtering. Appl Surf Sci 2015;355:878–83.
[214] Shirani A, Gu J, Wei B, Lee J, Aouadi SM, Berman D. Tribologically enhanced self-healing of niobium oxide surfaces. Surf Coatings Technol 2019;364:273–8.
[215] Ren P, Zhang K, He X, Du S, Yang X, An T, et al. Toughness enhancement and tribochemistry of the Nb-Ag-N films actuated by solute Ag. Acta Mater 2017;137:1–11.
[216] Gu JJ, Steiner D, Mogonye JE, Aouadi SM. Precipitation-induced healing of Nb2O5. J Eur Ceram Soc 2017;37:4141–6.
[217] Feng X, Jia J, Wang W, Shan Y. Mechanical and tribological properties of NiAl–NbC–Ag composites prepared by hot-pressing sintering. J Mater Res 2017;32:2361–72.
[218] Feng X, Lu C, Jia J, Xue J, Wang Q, Sun Y, et al. High temperature tribological behaviors and wear mechanisms of NiAl–NbC–Ag composites formed by in-situ decomposition of AgNbO3. Tribol Int 2020;141:105898.
[219] Ezirmik KV, Rouhi S. Influence of Cu additions on the mechanical and wear properties of NbN coatings. Surf Coatings Technol 2014;260:179–85.
[220] Wu F, Yu L, Ju H, Asempah I, Xu J. Structural, mechanical and tribological properties of NbCN-Ag nanocomposite films deposited by reactive magnetron sputtering. Coatings 2018;8:50.
[221] Walck SD, Zabinski JS, McDevitt NT, Bultman JE. Characterization of air-annealed, pulsed laser deposited ZnO-WS2 solid film lubricants by transmission electron microscopy. Thin Solid Films 1997;305:130–43.
[222] Prasad S V, McDevitt NT, Zabinski JS. Tribology of tungsten disulfide–nanocrystalline zinc oxide adaptive lubricant films from ambient to 500 C. Wear 2000;237:186–96.
[223] Zhu S, Bi Q, Yang J, Liu W. Ni 3 Al matrix composite with lubricious tungstate at high temperatures. Tribol Lett 2012;45:251–5.

[224] Yezhong WJMXH, Jinlin ZGO %J T. Study on the High Temperature Lubricating Properties of the Lead Tungstate [J] 1992:9.
[225] Yiezhong H, Jingbo W, Jinlin O %J 摩擦学学报. Study on the WC-Ni-Mo-PbO High Temperature Self-Lubricating Metal-Cermet-Material and Its Properties [J] 1994;1.
[226] Sliney HE. Decomposition Kinetics of Some Solid Lubricants Determined by Elevated-Temperature X-Ray Diffraction Techniques. Proceedings, AF Materials Laboratory, Research and Technology Division, Air Force Systems …; 1964, p. 350.
[227] Feng S, Zhou X, Zhang Q. Tribological Behavior of Ni-based Self-lubricating Composites with the Addition of Ti 3 SiC 2 and Ag 2 W 2 O 7. J Wuhan Univ Technol Sci Ed 2019;34:698–706.
[228] Xue M. High temperature oxidation and wear behaviour of powder metallurgically developed Ni-Cr-W-Al-Ti-MoS2 composite. Indian J Eng Mater Sci 2009;16:111–5.
[229] Huang Y, Zhou X, Hua N, Que W, Chen W. High temperature friction and wear behavior of tungsten – copper alloys. Int J Refract Met Hard Mater 2018;77:105–12. https://doi.org/10.1016/j.ijrmhm.2018.08.001.
[230] Ouyang JH, Sasaki S, Murakami T, Umeda K %J W. Tribological properties of spark-plasma-sintered ZrO2 (Y2O3)–CaF2–Ag composites at elevated temperatures 2005;258:1444–54.
[231] Ouyang JH, Sasaki S, Umeda K %J W. Microstructure and tribological properties of low-pressure plasma-sprayed ZrO2–CaF2–Ag2O composite coating at elevated temperature 2001;249:440–51.
[232] John PJ, Zabinski JS. Sulfate based coatings for use as high temperature lubricants. Tribol Lett 1999;7:31–7.
[233] John PJ, Prasad S V, Voevodin AA, Zabinski JS. Calcium sulfate as a high temperature solid lubricant. Wear 1998;219:155–61.
[234] Liu F, Feng L, Liu H, Zhao W. High-Temperature Tribological Performance of Vacuum Hot-Pressed NiCr Matrix Composite Containing SrAl12O19. J Mater Eng Perform 2020;29:470–9. https://doi.org/10.1007/s11665-020-04562-x.
[235] Murakami T, Ouyang JH, Sasaki S, Umeda K, Yoneyama Y. High-temperature tribological properties of spark-plasma-sintered Al2O3 composites containing barite-type structure sulfates. Tribol Int 2007;40:246–53.
[236] Murakami T, Ouyang JH, Umeda K, Sasaki S. High-temperature friction properties of BaSO4 and SrSO4 powder films formed on Al2O3 and stainless steel substrates. Mater Sci Eng A 2006;432:52–8.
[237] Murakami T, Umeda K, Sasaki S, Ouyang J. High-temperature tribological properties of strontium sulfate films formed on zirconia-alumina, alumina and silicon nitride substrates. Tribol Int 2006;39:1576–83.
[238] Murakami T, Ouyang J, Korenaga A, Umeda K, Sasaki S, Yoneyama Y. High-temperature tribological properties of Al2O3-X (X: BaCrO4, BaSO4 and CaSO4) spark-plasma-sintered composites containing sintering additives. Mater Trans 2004;45:2614–7.
[239] Li Y-F, Ouyang J-H, Sasaki S. Tribological properties of spark-plasma-sintered ZrO 2 (Y 2 O 3)–Al 2 O 3–Ba x Sr 1− x SO 4 (x= 0.25, 0.5, 0.75) composites at elevated temperature. Tribol Lett 2012;45:291–300.
[240] Zhang X, Cheng J, Niu M, Tan H, Liu W, Yang J. Microstructure and high temperature tribological behavior of Fe3Al–Ba0. 25Sr0. 75SO4 self-lubricating composites. Tribol Int 2016;101:81–7.
[241] Ouyang JH, Li YF, Wang YM, Zhou Y, Murakami T, Sasaki S. Microstructure and tribological properties of ZrO2 (Y2O3) matrix composites doped with different solid lubricants from room temperature to 800° C. Wear 2009;267:1353–60.
[242] Ouyang JH, Sasaki S, Murakami T, Umeda K. Spark-plasma-sintered ZrO2 (Y2O3)-BaCrO4 self-lubricating composites for high temperature tribological applications. Ceram Int 2005;31:543–53.
[243] Ouyang JH, Murakami T, Sasaki S, Li YF, Wang YM, Umeda K, et al. High temperature tribology and solid lubrication of advanced ceramics. Key Eng. Mater., vol. 368, Trans Tech Publ; 2008, p. 1088–91.
[244] Ouyang JH, Sasaki S, Umeda K. The friction and wear characteristics of low-pressure plasma-sprayed ZrO2-BaCrO4 composite coating at elevated temperatures. Surf Coatings Technol 2002;154:131–9.
[245] Li YF, Ouyang JH, Wang YM, Zhou Y, Murakami T, Sasaki S. Influences of SrSO4 and Ag on high temperature tribological properties of spark-plasma-sintered ZrO2 (Y2O3)-Al2O3 composites. Key Eng. Mater., vol. 434, Trans Tech Publ; 2010, p. 138–43.
[246] Liu F, Yi G, Wang W, Shan Y, Jia J. Tribological properties of NiCr–Al2O3 cermet-based composites with addition of multiple-lubricants at elevated temperatures. Tribol Int 2013;67:164–73.
[247] Liu F, Jia J. Tribological properties and wear mechanisms of NiCr–Al 2 O 3–SrSO 4–Ag self-lubricating composites at elevated temperatures. Tribol Lett 2013;49:281–90.
[248] Ouyang J-H, Liang X-S, Liu Z-G, Yang Z-L, Wang Y-J. Friction and wear properties of hot-pressed NiCr–BaCr2O4 high temperature self-lubricating composites. Wear 2013;301:820–7.
[249] Liang XS, Ouyang JH, Liu ZG, Yang ZL. Friction and wear characteristics of BaCr 2O 4 ceramics at elevated temperatures in sliding against sintered alumina ball. Tribol Lett 2012;47:203–9.

https://doi.org/10.1007/s11249-012-9984-x.
[250] Zhu S, Bi Q, Kong L, Yang JU, Liu W. Barium chromate as a solid lubricant for nickel aluminum. Tribol Trans 2012;55:218–23.
[251] Zhu S, Li F, Ma J, Cheng J, Yin B, Yang J, et al. Tribological properties of Ni3Al matrix composites with addition of silver and barium salt. Tribol Int 2015;84:118–23.

Chapter 3

Microstructural Evolution and Tribological Behavior of Suspension Plasma Sprayed CuO as High-Temperature Lubricious Coatings[2]

Abstract

Suspension plasma spraying (SPS) was used to produce three different CuO coatings by varying spray distance and solid loading within the suspension. The low spray distance (30 mm) and high solid loading (20 wt%) in the suspension resulted in the deposition of dense coatings as compared to other spray conditions (i.e., a distance of 40 mm and solid loading of 10 wt%). The tribological performance of the dense coating was investigated at 25°C and 300°C under dry sliding conditions. Scanning electron microscopy (SEM), X-ray diffraction (XRD), and Raman analysis were used to characterize the coating, and corresponding wear tracks to determine the wear mechanisms. The results showed that the friction coefficient of the CuO coating decreased from 0.7 at 25°C to 0.46 at 300°C. Similarly, the wear rate at 300°C decreased by 50% compared to the wear rate at 25°C. *Ex-situ* analysis showed an increased oxygen content on the worn surfaces at 300°C and the formation of a smooth uniform tribofilm. At 25°C, a thicker transfer film was observed on the counterface, which leads to a different velocity accommodation mode and, thus, relatively high friction.

Keywords: *Suspension plasma spraying, CuO coatings, microstructures, solid lubricant, tribology*

[2] This chapter has been published as a research article in the *Wear*. **A. Roy**, N. Sharifi, V.N.V. Munagala, SA. Alidokht, P. Patel, M. Makowiec, R. R. Chromik, C. Moreau, P. Stoyanov. "Microstructural evolution and tribological behavior of suspension plasma sprayed CuO as high-temperature lubricious coatings." *Wear* (2023): 204874.

3.1 Introduction

With the recent advancements in mechanical systems within the aerospace and energy generation sectors, the conditions in which materials are expected to operate in their tribological interfaces is becoming more demanding [1–6]. For instance, in high-temperature conditions, the tribological contacts usually suffer severe wear, which affects the service life and stability of the system [7–9]. Thus, there is a strong desire to find suitable materials or coatings which can operate effectively in such harsh conditions. It has been previously proposed that materials with favorable mechanical properties, such as high hardness and fracture toughness, results in improved tribological performance in these applications [10–12]. Among various materials, oxide ceramics are potential candidates for solid lubricants to reduce friction and wear in such severe sliding interfaces due to their outstanding chemical and thermal stability above 1000°C [13]. Out of numerous oxides, copper oxides, in particular, have recently become potential candidates due to their excellent lubricity behavior at elevated temperatures [14–16]. More specifically, copper oxide is a comparatively softer oxide with reduced shear strength at elevated temperatures [17,18]. Peterson et al. [19] investigated the tribological behavior of CuO at high temperatures and showed favorable lubricating characteristics with relatively low friction values (< 0.5). In addition, Masahiro Goto et al. [20,21] deposited CuO coatings by magnetron sputtering on a stainless steel substrate. They studied the tribological behavior in atmospheric pressure and ultrahigh vacuum for different crystallographic orientations. The authors found that the friction coefficient increases with an increase in surface energy which was controlled by the CuO crystal orientation. J S Lehmann et al. [14] investigated the tribological behavior of pure copper and its oxides. The authors reported that high-purity copper exhibits high friction, even with the formation of an oxide layer during sliding, compared to copper oxides. The reasons for having low friction of copper oxides were attributed to an increase in hardness and a change in the interfacial shear strength. Furthermore, CuO incorporated in numerous intermetallic and ceramic composites, such as NiAl [22,23], 3Y-TZP [24–26], and Al_2O_3 [27], showed lower friction and wear compared to unreinforced coatings. This improvement in friction and wear was due to the formation of a soft patchy lubricating film in the contacting interfaces, mainly in the form of CuO. While this research has shown that CuO could be a potential candidate as a solid lubricant in high temperature applications, the tribological behavior of such coatings alone under extreme conditions has received little attention. In addition, to the best of authors knowledge, there have

been no studies reported on the tribological behavior of CuO coatings deposited by thermal spray processes.

With the recent advancements in thermal spray, these technologies have become attractive for high-temperature wear-resistant materials. In particular, suspension plasma spraying (SPS) is a novel process compared to other thermal spray techniques, capable of spraying ultrafine or nanosized particles from 100 nm to several microns in diameter. Such sub-micron particles typically can not be sprayed with other thermal spraying techniques such as Atmospheric Plasma Spray (APS), High Velocity Oxygen Fuel (HVOF), and High Velocity Air Fuel (HVAF), etc. In SPS, these sub-micron size powder particles are usually dispersed in a solvent (typically water/alcohol or sometimes both) to produce suspension [28]. The suspension is injected in plasma through the suspension feed or injector. Subsequently, the suspension is fragmented into a droplet before the vaporization of the solvent. However, the solvent and dispersant consequently undergo evaporation in contact with the plasma jet while the solid particles aggregate, accelerate, melt and subsequently form coating upon impacting the substrate [29]. In this process, a thin splat is formed on the substrate, which benefits the wear resistance properties [30]. However, the microstructures and properties of these coatings mainly depend on the spray parameters in correlation with the materials used and suspension characteristics. The SPS process used to produce TiC and Cr_3C_2 coatings by S. Mahade et al. [31], showed the splat was an order of magnitude lower than that of typical APS, demonstrating improved wear resistance properties. Also, it was revealed that the shorter spray distance of suspension plasma sprayed ZrO_2 + 8wt% Y_2O_3 (YSZ) coatings has greater cohesion, higher adhesion to the substrate, and high hardness and wear resistance [32]. Moreover, the near-nanometric structures of Al_2O_3-TiO_2 coatings were obtained by SPS, directly associated with the reduction of grain size and microstructure defects [33]. While the SPS process seems promising for the deposition of ceramic coatings, to the best of the author's knowledge, no studies have been carried out on the deposition, and tribological behavior of the suspension plasma sprayed CuO coatings from room to high temperatures.

In the present study, CuO coatings were developed by the SPS process as potential solid lubricants for elevated temperatures applications. CuO coating's microstructural morphology and tribological characteristics from room to high temperatures were investigated. In addition, the underlying wear and lubrication mechanisms at atmospheric and elevated temperatures were analyzed based on worn surface morphologies.

3.2 Experimental Details

3.2.1 Materials and Methodology

Commercially available CuO powder (PI-KEM, UK) with a nominal average particle size of about 0.7 μm was used as a feedstock for the coating deposition. A Spraytec (Malvern Instruments, UK) unit equipped with a wet dispersion accessory was used for the measurement of the particle size distribution (PSD) of the CuO powder.

The CuO powder was dispersed in ethanol in order to prepare the suspension for spraying. Ethanol was used as a solvent due to its low toxicity, availability as well as low energy required for vaporization (1.01 MJ/kg) as compared to water (2.63 MJ/kg) [34]. As a dispersing agent, Polyvinylpyrrolidone (PVP) (Sigma-Aldrich, Canada) was used in the ethanol to minimize the aggregation of the submicron-sized particles. The dispersant molecules were adsorbed on the surface of the powder particles and provided efficient particle dispersion by producing long polymeric chains [35]. The solid content of the suspensions was 10 wt.% and 20 wt.%, while the dispersing agent was 5 wt.% of the solid content. Initially, the PVP was dissolved in ethanol. Then, the CuO was added gradually to the solution while mechanically stirring and sonicating at 50 W power. The suspension was stirred for an additional 15 minutes to ensure the proper dispersion of the particles. Furthermore, the suspension was kept in soft ball milling overnight to break the nanoparticle agglomeration before feeding into the SPS system.

The prepared suspension was sprayed onto 304L stainless steel substrates (25mm× 25mm× 5 mm) using SPS process. Before spraying, the substrates were grit blasted with 80 grit alumina particles and cleaned by blowing compressed air to remove any grit residue on the substrate surface. Subsequently, the substrates were ultrasonically cleaned with ethanol and acetone to remove dust, dirt, or oil. The plasma torch preheated the substrate to approximately 300°C before spraying. Also, the maximum substrate temperature was maintained at around 450°C-500°C during coating deposition by pausing with the gun off the substrate in between passes. The temperature of the substrate and the deposited coating was monitored continuously by an A320 ThermoVision infrared camera (FLIR Systems, MA). Additionally, the inflight particle's velocity and temperatures were measured by accuraspray (tecnar, Canada). The detailed working principle of the radial injection SPS process was discussed in the previously published article [36].

A 3 MB plasma gun (Oerlikon Metco, Switzerland) was used for the SPS process. The in-house built pressure-based feeding system was used to inject the suspension feedstock radially into the plasma, as shown in **Figure 3. 1**. The internal diameter of the suspension injector was

150 µm and was made out of stainless steel. This injector was positioned at an approximately 15° angle with respect to the perpendicular axis. The injector axis was focused in such a way that the suspension jet entered the plasma only at the exit of the nozzle. Also, the injector tip was precisely aligned with the plasma torch orifice approximately 25 mm from the torch axis by a micro-positioning system installed next to the injector container [**Figure 3. 1**].

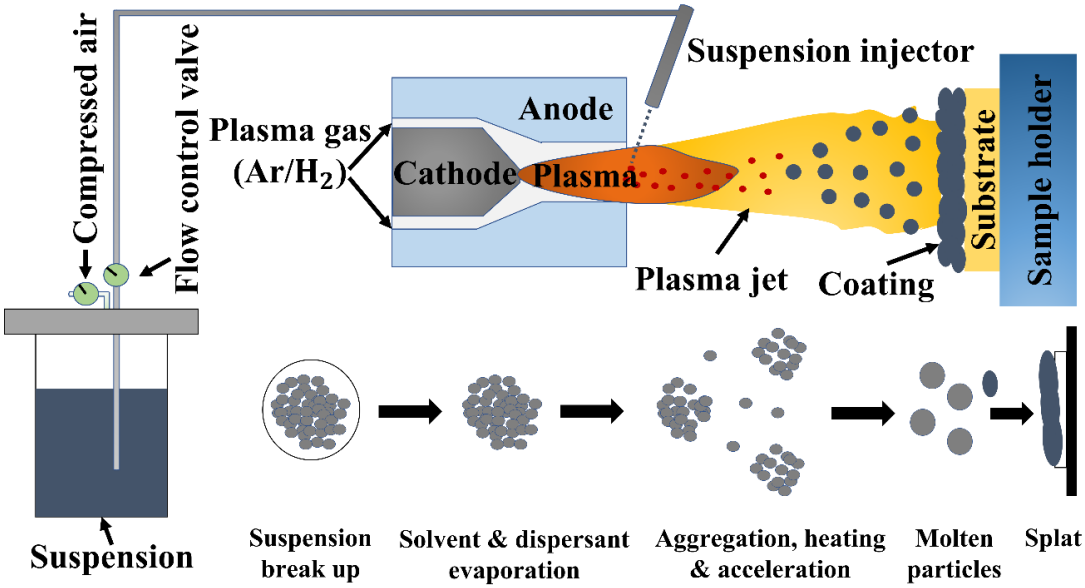

Figure 3. 1: *A schematic of the radial injection suspension plasma spray (SPS) process*

Moreover, a magnetic stirrer was continuously running in the suspension container to avoid the sedimentation of the solid particles during spraying. Three different spray conditions were used to deposit the coatings, e.g.,1st spray [10 wt% solid with spray distance (SD) 40 mm], 2nd spray [20 wt% solid with SD 40 mm], and 3rd spray [20 wt% solid with SD 30 mm] by keeping plasma power 20 kW constant. The spraying parameters used for depositing CuO coating by SPS process are shown in **Table 3. 1**. The selected parameters [**Table 3. 1**] were chosen based on some initial sets of trial depositions and by considering the following hypotheses to obtain the dense microstructures: (i) the smaller nozzle size (i.e., 5 mm instead of 8 mm) increases the particle velocity and decreases the particle's in-flight residence time, which can densify the coatings [37], (ii) the shorter standoff distance utilizes the high speed or the momentum of the in-flight particles onto the substrate and can contribute to improving coating structures [38], (iii) the solid loading in the suspensions, feed rate, and optimal plasma power also affect the microstructures of the coatings [36].

Table 3. 1: *SPS spray parameters used for depositing CuO coatings*

Deposition Parameters	Values		
	1st Spray (10 wt% solid; SD 40 mm)	2nd Spray (20 wt% solid; SD 40 mm)	3rd Spray (20 wt% solid; SD 30 mm)
Plasma nozzle diameter (mm)	5	5	5
Solid content (wt%)	10	20	20
Current (A)	500	500	500
Voltage (V)	40	40	40
Power (kW)	20	20	20
Gun transverse speed (m/s)	1	1	1
Ar gas flow rate (l/min)	50	50	50
H_2 gas flow rate (l/min)	1	1	1
Spray distance (SD) (mm)	40	40	30
Suspension feed rate (ml/min)	35	35	35
Number of Passes	30	40	40

3.2.2 Characterization

The morphology and composition of the CuO powder were determined using Scanning Electron Microscopy (SEM) (S-3400N, Hitachi High Technologies America, Inc., Japan). The phase analysis of powder and coatings was characterized by using X-ray diffraction (XRD) (Bruker, Germany) with Co-Kα radiation (λ = 1.78 Å, 2θ range of 10°–115°) and operated at a power of 40 kV and 40 mA. The obtained data were analyzed with the International Centre for Diffraction Data (ICDD) database using diffrac.eva software provided with the XRD system.

The as-sprayed samples were cross-sectioned using a high-speed abrasive cutting machine (Struers, Canada) and then cold-mounted using epoxy resin and hardener (ANAMET, Canada). The samples were polished using SiC abrasive paper of 240 to 800 grit, subsequently by 9 µm, 5 µm, and 1 µm water-based diamond suspensions in an automatic grinding-polishing machine (Struers, Canada). Colloidal silica of 0.4 µm suspension was used as a final step in the polishing machine. Finally, the samples were rinsed in soapy water and sonicated in acetone to remove any residual colloidal silica and dried in hot air.

Scanning electron microscopy (SEM) coupled with energy-dispersive X-ray spectroscopy (EDS) was used for metallographic observations of the deposited coatings. In addition, X-ray photoelectron spectroscopy (XPS) was performed with a VG ESCALAB 250 Xi (Thermo VG

Scientific, Canada) Mg K_α X-ray source set to 15 kV and 300 W on the unworn and worn surfaces of the coatings deposited using the 3rd spraying conditions.

3.2.3 Sliding testing and post-test characterization

A ball-on-disc tribometer (Anton Paar TriTec SA, Switzerland) was used to measure tribological behavior in a reciprocating motion against an alumina counterball. Alumina was chosen as counterbody for wear testing to minimize chemical reactions (i.e., it is considered chemically inert) at atmospheric and elevated temperature conditions. It was also used because of its comparatively high hardness [39]. The testing parameters are listed in **Table 3. 2**. The parameters were chosen based on the complicated contacting and moving assemblies in aerospace engines in high-temperature conditions [36,40].

Table 3. 2: The friction test parameters of the pin on disc tribometer

Friction Testing Parameters	Values
Applied load (N)	5
Sliding velocity (cm/s)	3.14
Test frequency (Hz)	1
Track length (mm)	10
Total sliding cycles	2500
Counter body	Al_2O_3
Counter body diameter (mm)	6.35
Test temperatures (°C)	25°C and 300°C

For the elevated temperature wear tests, the furnace was initially heated to 450°C at a heating rate of 10-12°C/min. The samples were placed in the furnace, and the surface of the coating was measured to be at around 300°C (i.e., using a thermocouple). This temperature of 300°C was reported as the testing temperature. The computer connected to the tribometer arm and pin through a strain gauge and recorded the friction coefficient by considering the applied load & friction force during sliding. A total of three repeats were performed for each condition. A 3D non-contact optical surface profiler (Zygo corporation, USA) was used to measure the surface roughness of the coatings. Similarly, the same profiler measured the depths of the wear tracks and wear of the counterballs. A total of 30 cross-sectional profiles were taken and averaged to calculate the wear volume. The wear volume is used to calculate the specific wear rate (k) (mm^3/N.m.) as per the equation below [41].

$$k = \frac{V}{S.W} = \frac{V}{2.f.L.N.W} \qquad (3.1)$$

where, V = volume loss (mm^3), S is the total sliding distance (m), obtained by multiplying the frequency f (s^{-1}), stroke length L (mm); and number of cycles (N); and W is the applied load (N).

Additionally, the worn surfaces after wear testing and counterball were investigated by using this SEM. Raman measurements were performed using an InVia spectrometer (Renishaw, UK). An optical microscope with a 50X objective was used to focus the excitation radiation λ = 514.5 nm from an Ar^+ ion laser source. The scattering was performed at different locations of unworn and worn coatings subjected to wear tests. The spectra were matched with the corresponding wave numbers from the literature to identify the present phases.

3.3 Results

3.3.1 Feedstock powder and coating

SEM image of the CuO powder (shown in **Figure 3. 2 (a)**) revealed an irregular aggregated morphology. **Figure 3. 2 (b)** shows CuO powder's particle size distribution (PSD). The Dv (10), Dv (50), and Dv (90) values are 0.90 µm, 1.73 µm, and 3.50 µm, respectively.

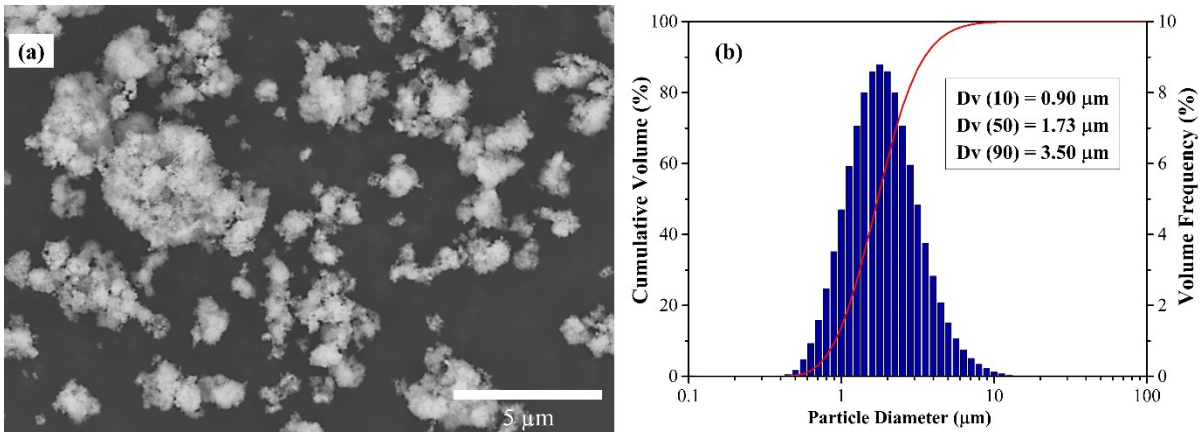

Figure 3. 2: *(a) SEM image of CuO powder morphology and (b) particle size distribution (PSD) of CuO powder*

The XRD pattern of the CuO powder is shown in **Figure 3. 3**. The major diffraction peaks identified at 37.96°, 41.5°, 45.29°, 57.26°, 62.98°, 68.9°, 72.9°, 78.81°, 81.17°, 86.65°, and 90.31° were associated with the (110), (-111), (111), (-202), (020), (202), (-113), (-311), (220), (311), and (-222) planes respectively of the monoclinic CuO crystal structure. This phase matched with the ICDD card: 00-041-0254.

The coatings were deposited using three different conditions, as shown in **Table 3. 2**, and XRD analysis of these as-sprayed coatings is shown in **Figure 3. 3**. A reduction of the CuO phase to cubic Cu_2O and into pure metallic cubic Cu phases has been observed in all three spray conditions. The main diffraction peaks of Cu_2O appear at 34.49°, 42.56°, 49.56°, 61.77°,

72.70°, 88.06°, and 93.09°, which corresponds to (110), (111), (200), (211), (220), (311), and (222) respectively (i.e., aligned to ICDD 04-007-9767). The diffraction peaks at 50.73°, 59.31°, 88.84°, and 110.30° are assigned to cubic Cu and matched with ICDD 00-004-0836.

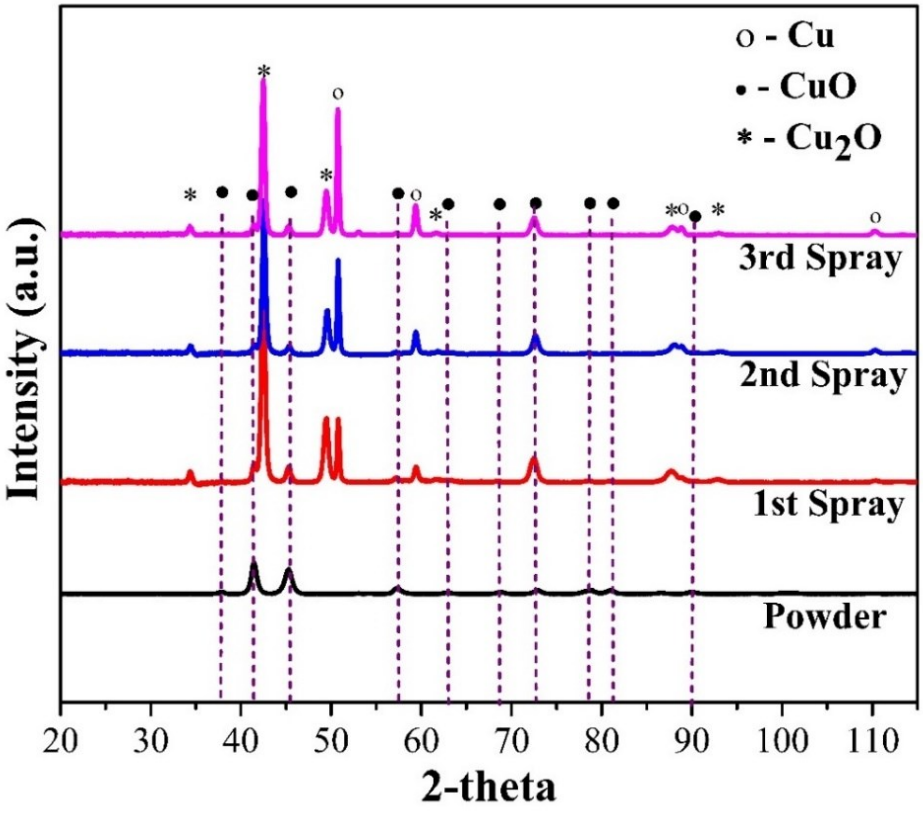

Figure 3. 3: XRD pattern of the CuO feedstock powder and as-sprayed coatings

In addition to the XRD characterization, XPS analysis was performed on the 3rd spray conditions, as shown in **Figure 3. 4**. **Figure 3. 4 (a)** shows the survey spectrum of the deposited coatings, where Cu 3p, 2p, 3s, 2s, and O 1s peaks were found. The high-resolution core spectra of Cu 2p and O 1s are represented in **Figure 3. 4 (b)** and **Figure 3. 4 (c)**. The core spectra of Cu 2p, shown in **Figure 3. 4 (b)**, contain peaks attributed to Cu 2p3/2 and Cu 2p1/2 caused by the spin-orbit coupling of the 2p level. The deconvolution of these peaks revealed the presence of two peaks within it; however, the Cu_2O peak was expected at the same Cu2p photoelectron binding energy (B.E.) as the Cu metal (Cu metal and Cu (I) oxide expected B.E. ~ 932.6 eV, CuO ~ BE 933.1-934.0 eV). The findings suggested that the coating contained a mix of pure metallic Cu, Cu_2O, and CuO, which correlated well with the XRD findings [**Figure 3. 3**]. In addition to the primary peaks, two satellite peaks were found in higher binding energy regions at 941.11 and 943.6 eV. The shakeup satellite peaks are a characteristic of Cu ion species due to the presence of d^9 configuration [42]. The interaction between the emitted photoelectron and

the valence electron caused these electrons to get excited to higher energy levels, which resulted in the reduction of the kinetic energy (i.e., an increase in binding energy), giving a shakeup peak towards the higher binding energy region of the core peak [43]. **Figure 3. 4 (c)** shows the deconvoluted core spectrum of O 1s. Two peaks relating to different chemical states were observed. The major peak at 529.51 eV was allocated to the normal O^{2-}, which cooperates with Cu^{2+} to form a Cu-O bond. In addition, the minor peak at 531.18 eV was ascribed to Cu^2O. The observed XPS results correlated well with the previously published findings on copper oxide-based systems [42].

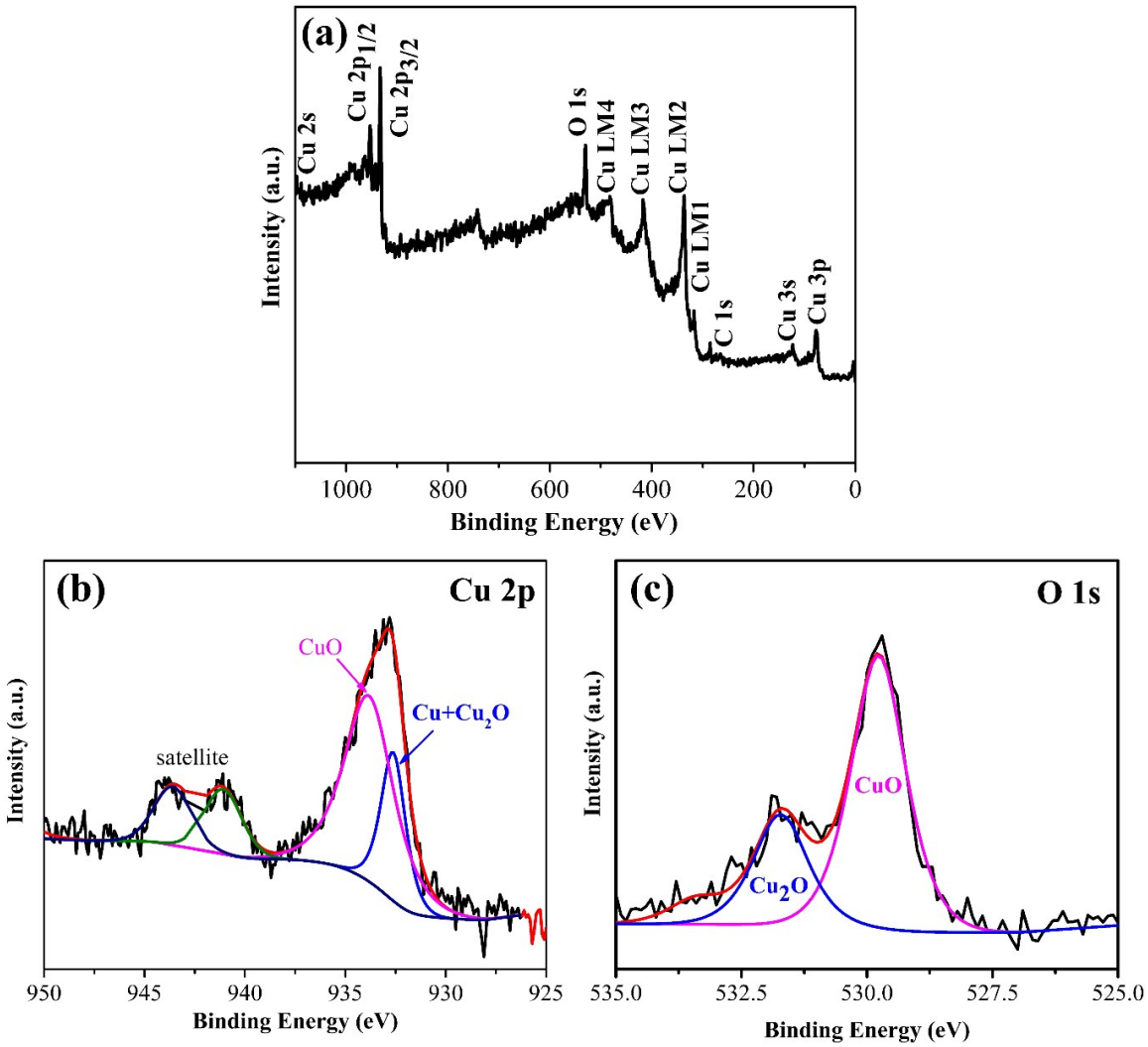

Figure 3. 4: XPS analysis of 3rd spray condition (a) Survey spectra; core spectra for (b) Cu 2p and (c) O 1s subshells.

3.3.2 Sliding wear behavior

3.3.2.1 Friction coefficient and specific wear rate

The friction coefficient versus number of cycles for the CuO coatings tested at 25°C and 300°C is shown in **Figure 3. 5**. Upon initial sliding, the friction coefficient for the tests performed at 25°C increased rapidly up to 120 cycles and subsequently increased at a slower rate throughout the remainder of the test and reached a maximum of 0.73. For the test performed at 300°C, on the other hand, a steady-state friction behavior was obtained just after 100 cycles and maintained at 0.46 over the sliding distance of 2500 cycles (50 m).

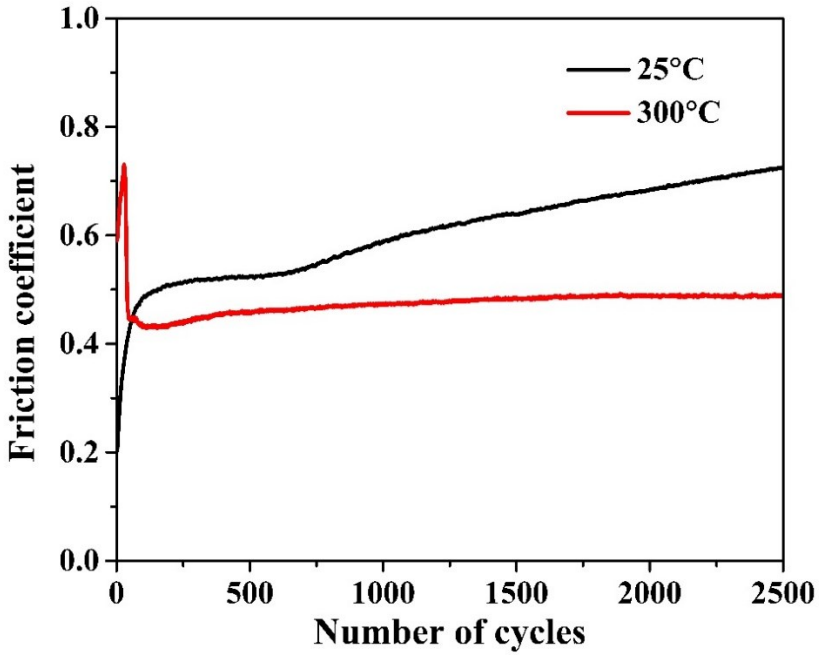

Figure 3. 5: Friction coefficient of CuO coating at 25°C and 300°C

The specific wear rate of CuO coatings at 25°C and 300°C is shown in **Figure 3. 6**. The analysis revealed that the wear rate at 300°C after 2500 cycles was 32 $\times 10^{-5}$ mm^3/N.m., which was more than 50% lower than the wear rate at 25°C (i.e., 68 $\times 10^{-5}$ mm^3/N.m.). It should also be noted that the standard deviation was lower with the tests performed at elevated temperatures due to a smoother wear track.

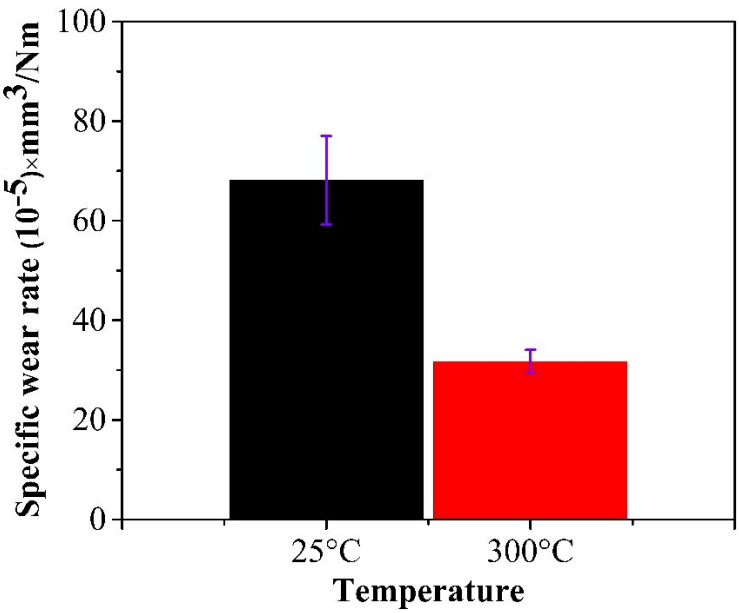

Figure 3. 6: Specific wear rate of CuO coatings at 25°C and 300°C

3.3.2.2 Worn surface morphologies

SEM images of the worn surfaces produced at 25°C and 300°C are shown in **Figure 3. 7**. The width of the wear track at 25°C was significantly higher than the width of the wear track at 300°C. The worn surface of the CuO coatings at 25°C showed the presence of grooves parallel to the sliding direction [**Figure 3. 7 (a-c)**]. These grooves were generated due to the entrapment of the wear debris produced by breaking/ploughing the asperities during sliding [44]. The high-magnification SEM images showed indications of splat delamination, formation of pits, and ruptured film throughout the worn surface. Moreover, at 25°C, the asperity plowing, asperity polishing, and adhesive wear were apparent on the worn surface. In contrast, when testing at 300°C, the wear track area was mainly covered with uniform smooth regions [**Figure 3. 7 (e-f)**]. This smooth film or lubricating layer on the worn surface at 300°C could be created by the deformation of the wear debris in the contact interfaces [45]. However, a microcrack was visible in the smooth layer along with the wear debris on the wear track. At 15 kV and 60 Pa variable pressure, the SEM/EDS point and area analysis performed on randomly different locations of the unworn and worn coatings tested at 25°C and 300°C is shown in **Table 3. 3**. In these conditions, the EDS spot usually covers 1 µm or less in the surrounding area and can go up to ~ 4 µm in depth.

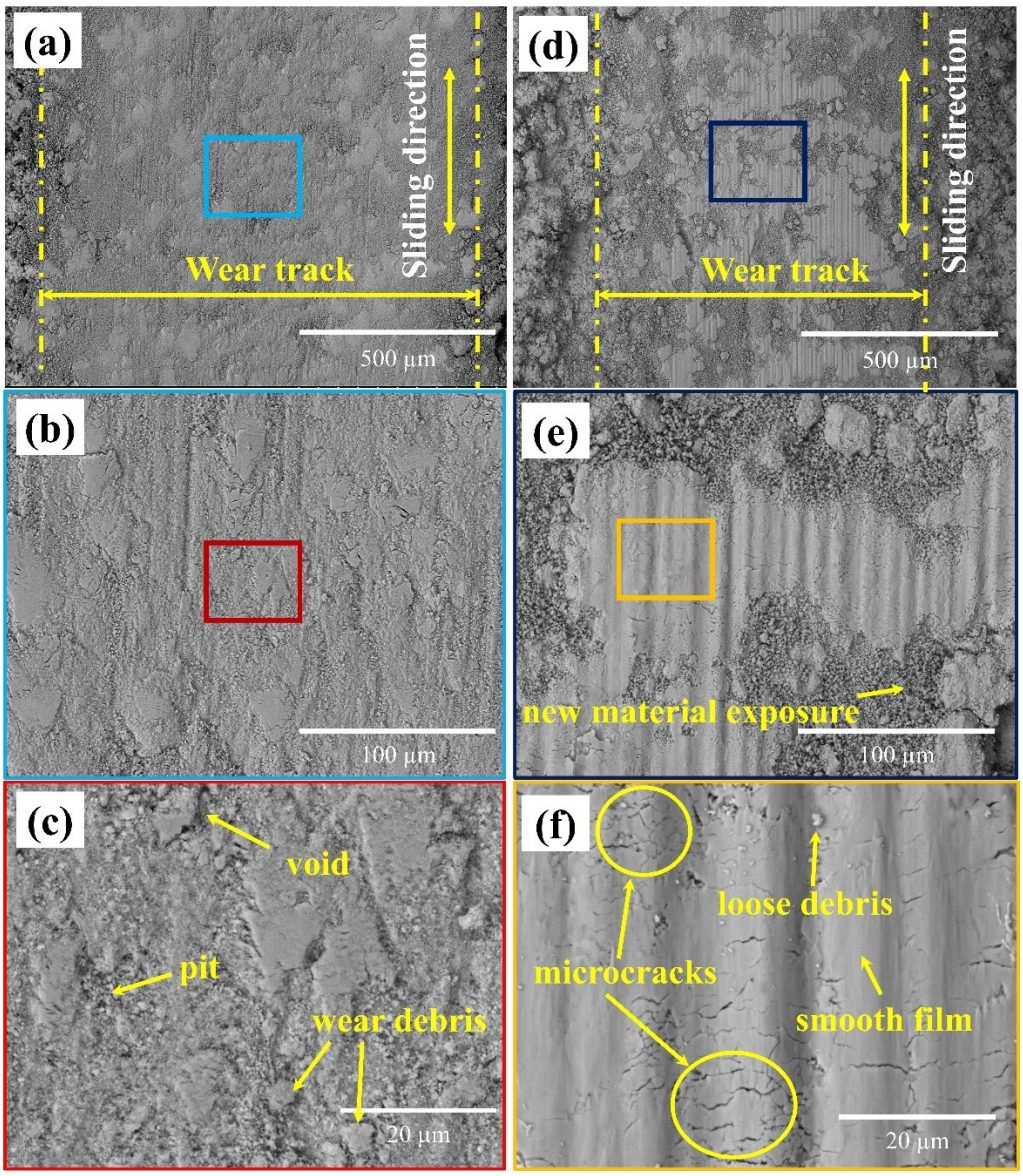

Figure 3. 7: SEM images of the worn surfaces of CuO coatings at 25°C (a–c) and 300°C (d-f).

Table 3. 3: EDS analysis of the unworn and worn coatings at 25°C and 300°C

Elements	25°C		300°C	
	unworn	worn	unworn	worn
Cu (at%)	50.05 ± 0.23	53.56 ± 1.35	50.64 ± 0.32	45.02 ± 0.80
O (at%)	49.95 ± 0.23	46.44 ± 1.35	49.36 ± 0.32	54.30 ± 0.66
Al (at%)	---	---	---	0.67 ± 0.15

Additionally, both samples (25°C and 300°C) were inserted into the SEM chamber simultaneously to avoid discrepancies in the results. The copper percentage increased, and the oxygen content decreased (Cu ~ 54 at% and O ~ 46 at%) in the worn coatings after the dry

sliding wear test at 25°C as compared to unworn coatings (Cu ~ 50 at% and O ~ 50 at%). At 300°C, the Cu and O were no significant changes in the unworn region. However, the worn coatings observed substantial copper and oxygen changes after the sliding test at 300°C. The oxygen concentration increased to ~ 54 at%, and the copper amount reduced to ~ 45 at% compared to unworn coatings. In addition, a small fraction of aluminum < 1 at% was found on worn coatings after sliding at 300°C [**Table 3. 3**], possibly coming from alumina counterball during sliding. In addition, XPS analysis was performed on the worn surfaces and sub-surfaces (i.e., 25°C and 300°C after wear testing) up to approximately 100 nm in order to elucidate the elemental changes leading to the difference in the friction and wear behavior (see **Figure 3. 8**). The oxide content on worn surfaces for the samples tested at 300°C was higher than the ones tested at 25°C, which correlates well with the EDS analysis [**Table 3. 3**].

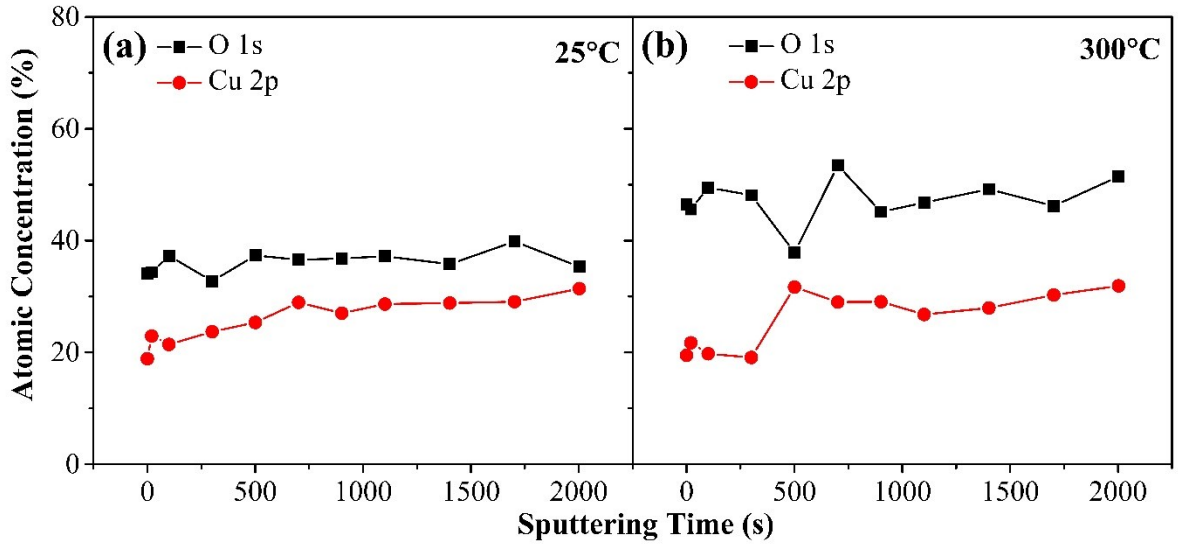

Figure 3. 8: XPS depth analysis of CuO coatings at (a) 25°C and (b) 300°C.

3.3.2.3 Raman analysis

A Raman analysis was performed on the deposited coatings and worn surfaces after sliding at 25°C and 300°C. Raman analysis [**Figure 3. 9**] on the unworn coatings confirmed the presence of cupric and cuprous oxide, as observed with the XRD analysis [**Figure 3. 3**]. However, pure metallic copper was not detected in the Raman spectrum as it is not Raman active.

The characteristic peaks at Raman shift 143 cm^{-1} and 213 cm^{-1} in the unworn coatings [**Figure 3. 9 (a), Figure 3. 9 (b)**] correspond to the Cu_2O phase [46,47]. The peaks at Raman shift 293 cm^{-1}, 340 cm^{-1}, 626 cm^{-1}, and 1118 cm^{-1} correspond to the CuO phase [48–50]. Both at 25°C and 300°C, the unworn coatings showed CuO and Cu_2O, while the worn coatings demonstrated the CuO phase, as shown in **Figure 3. 9 (a)** and **Figure 3. 9 (b)**.

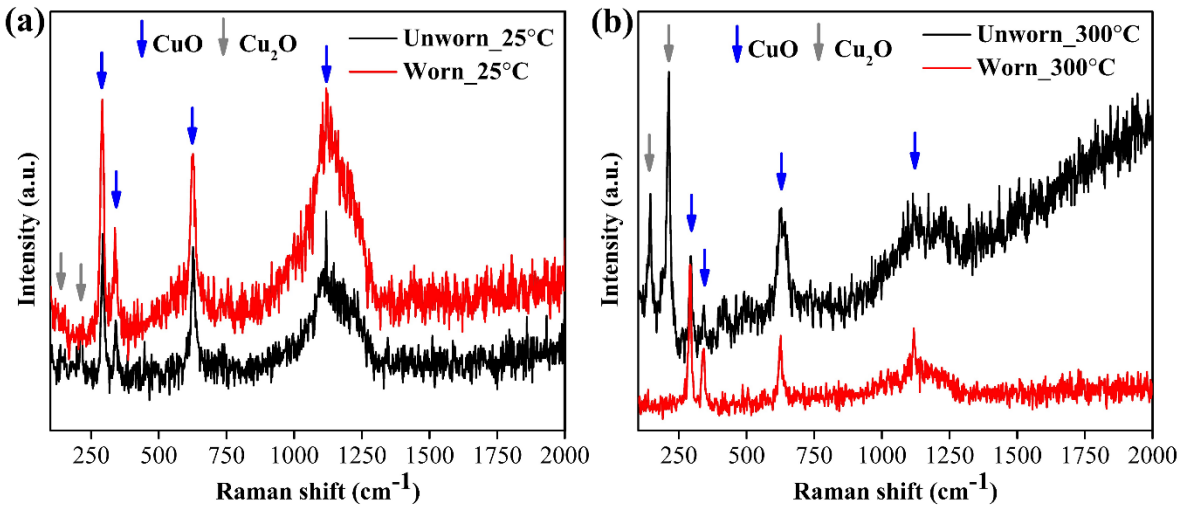

Figure 3. 9: Raman spectrum of unworn and worn coatings at (a) 25°C and (b) 300°C

3.3.2.4 Counterface analysis

SEM micrographs of the Al_2O_3 counterballs after the wear testing against the CuO coatings at 25°C and 300°C are shown in **Figure 3. 10**. At 25°C [**Figure 3. 10 (a)**], the counterface showed no visible wear but transferred material of ~ 3 µm thick on its surface. SEM/EDS analysis of these adhered layers confirmed the presence of Cu and O. Similar transfer of the Cu and O materials were also observed on the aluminum oxide counterface after sliding at 300°C [**Figure 3. 10 (b)**]; however, the layer of material was relatively thin (~ 0.5 µm) on the contact periphery of the ball. Furthermore, the EDS analysis [**Figure 3. 10 (b)**] confirmed the lower copper concentration (at%) in the counterball tested at 300°C compared to the counterball from the 25°C test. In addition, minor ball wear of ~ 1.5 µm depth was observed in the center of the alumina countersurface after wear testing against CuO coating at 300°C. This could be attributed to the ploughing of the asperities of the coatings during the break-in period as well as to the increased oxygen content on the worn surface [41,51].

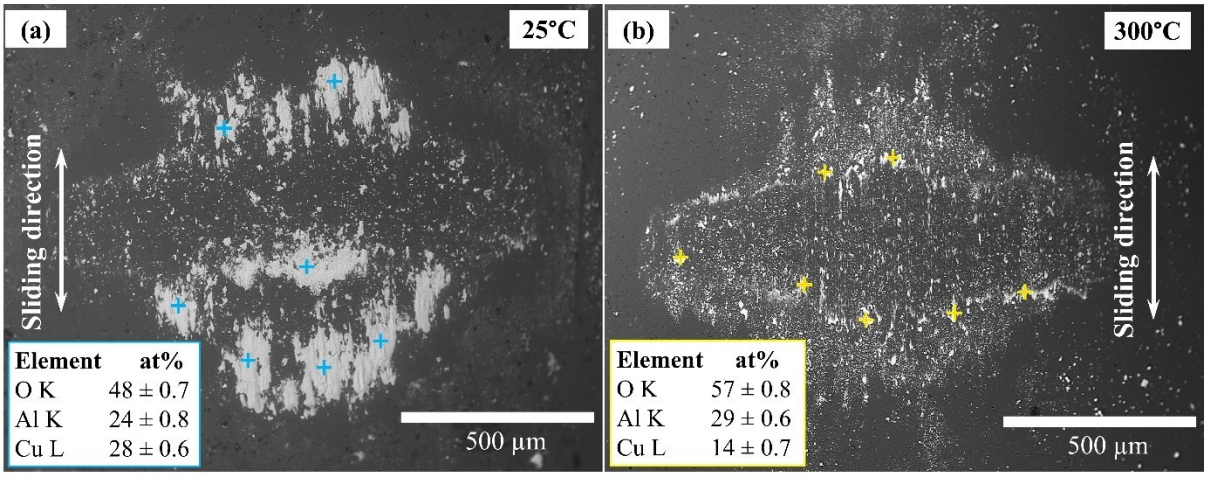

Figure 3. 10: SEM images of the counterball and corresponding EDS element analysis of the counterpart Al_2O_3 ball after sliding at 25°C and 300°C. (+ indicates the EDS point)

3.4 Discussion

3.4.1 Coating characteristics

It is worth mentioning that the decomposition and boiling temperatures of CuO and Cu_2O are 1100-1200°C, 2000°C [52] and 1232°C, 1800°C [53], respectively. On the other hand, the in-flight particle temperatures in the suspension plasma spraying (SPS) system reached more than 2500°C; therefore, the particles were fully melted during spraying. The oxide vaporization occurred with a significant chemical reduction in-flight into Cu_2O and Cu (melting point 1083°C, boiling point 2562°C). Similar behavior has been observed by B. Subhasree et al. [54], where authors deposited CuO by atmospheric plasma spraying (APS). It was assumed that the substantial chemical reduction of the CuO particles occurred in-flight during spraying. The CuO was reduced to metallic Cu in the plasma, which was further oxidized in comparatively colder downstream zones and formed cuprous and cupric oxides. Furthermore, some of the metallic copper could be deposited on the substrate surface before oxidation in the solid state. In addition, according to the CuO Ellingham diagram [55], the hydrogen molecule and hydrogen atom act as a reducing agents for CuO. Therefore, during spraying, CuO with hydrogen undergoes chemical reduction. The reduction mechanisms proposed by B. Subhasree et al. [54] for the plasma spraying process are shown below-

$CuO \rightarrow L(Cu, O)$ Melting

$L(Cu, O) + H_2 \rightarrow L(Cu, O_{1-x}) + H_2O$ In-flight reduction

$L(Cu, O_{1-x}) \rightarrow Cu_2O + Cu$ Rapid solidification: $Ar - H_2$ plasma with significant reduction

Similarly, the presence of mixed phases of CuO and Cu_2O was observed by Toshiro Maruyama [56] when copper oxide films were deposited on a preheated substrate (300°C) by a chemical vapor deposition process. Moreover, Akgul et al. [57] and Raship et al. [58] observed the Cu_2O phase with increased crystallinity of the coatings when the annealing temperatures of the CuO deposited coatings were above 300°C. However, the CuO phases were dominant as compared to the Cu_2O phase. In this study, the CuO was deposited on preheated (300°C) substrate, and the maximum temperatures of the substrate and coatings were> 450°C during spraying. Therefore, as per the literature, the substrate temperature (300°C to > 450°C) could also play a significant role in having the cupric and cuprous oxides while depositing CuO suspension by suspension plasma spraying process.

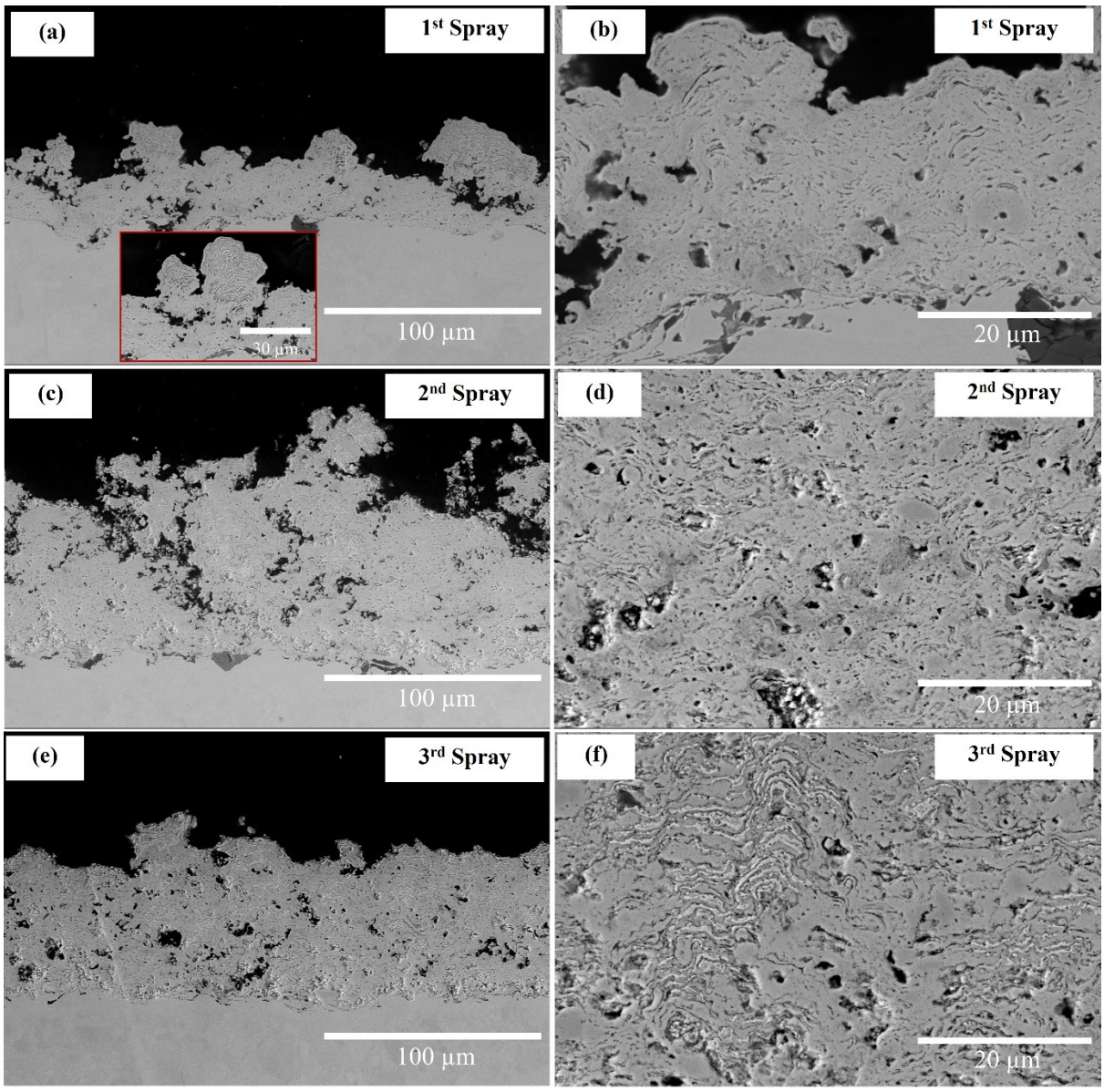

Figure 3. 11: Cross-sectional SEM micrographs of coatings prepared at different conditions: (a-b) 1st spray [10 wt% solid with spray distance (SD) 40 mm]; (c-d) 2nd spray [20 wt% solid with SD 40 mm]; (e-f) 3rd spray [20 wt% solid with SD 30 mm]

Figure 3. 11 shows the cross-sectional SEM images of the coatings at different conditions: (a-b) 10 wt%, SD 40 mm; (c-d) 20 wt%, SD 40 mm; (e-f) 20 wt%, SD 30 mm. All the coatings showed a similar pattern consisting of dark, grey, and bright regimes throughout the coating. As per a previously published article [54], these regions could be associated with CuO, Cu_2O, and pure metallic Cu, respectively. However, other than three spray conditions [**Figure 3. 11**], a 10 wt% solid with SD 50 mm at 20 kW and 25 kW power with nozzle diameter 8 mm were sprayed (not shown here) to understand the effect of spray parameters of CuO coatings. These coatings showed heavily porous microstructures with cauliflower shapes. It was assumed that the 8 mm nozzle diameter provided a comparatively low impact velocity of the particles on the substrate while spraying. In addition, high spray distance (SD 50 mm) with 20 kW and 25 kW power prolonged the residence time of the particles in flight [37,59]. These characteristics fully melted the particles with increasing plasma power. They evaporated most of the CuO particles before impacting and solidifying onto the substrate due to their low melting and low evaporation point [as explained above]. While the evaporation of particles with a power of 20 kW was low compared to 25 kW, the large spray distance of 50 mm provided almost the same effect (i.e., increasing evaporation during spraying). By considering these factors, the nozzle diameter was changed to 5 mm from 8 mm, and the spray distances were reduced to 40 mm & 30 mm while keeping the power constant at 20 kW for three conditions [**Table 3. 1**]. The thickness of the as-sprayed coatings of 1st spray, 2nd spray, and 3rd spray was 31 ± 6 µm, 81 ± 12 µm, and 73 ± 10 µm respectively, and produced around 1 µm to 2 µm coating per pass as shown in **Figure 3. 11**. The reasons of having low coating build up rate per pass could possibly be explained by the vaporization of the oxides particles during spraying [52]. It should be noted that the deposition efficiency of these three conditions were approximately 41%, 72%, and 68% respectively. There was no peeling of the coatings from the substrate in all three conditions could indicate sufficient adhesion of the coatings with the substrate.

Figure 3. 11 (a-b) coating microstructure corresponds to the 10 wt% solid in the suspension with a spray distance of 40 mm. It produced 1 µm coating per pass and a significant number of cauliflowers throughout the whole coating. The typical cauliflower shape microstructure which appeared throughout the coating is shown in **Figure 3. 11 (a)** inset. This type of microstructure can be explained by Stokes number (St) [60] as per equation (3.2).

$$St = \frac{\rho d^2 V}{\mu\, l_{BL}} \qquad (3.2)$$

where ρ is the density of the particle, d is the diameter of the particle, v is the velocity of the particle, μ plasma viscosity, and l_{BL} is the boundary layer thickness. Alternatively, the stokes number is the ratio of the time taken for momentum transfer from liquid to particles to the time of the direction change of the flow [61]. The micron-size particle momentum is relatively low; hence, they are heavily influenced by the drag force of the plasma stream in the boundary layer close to the substrate. Thus, when St < 1, the porosity and cauliflower shape microstructure is more prominent. Therefore, a 40 mm spray distance could be high enough to lose the sufficient velocity of these 10 wt% solid particles as the increased spray distance further reduced the Stokes number [61]. Also, the secondary gas H_2 is responsible for the arc voltage fluctuations, leading to the gas velocity variation [62]. The variation of the voltage fluctuation could easily affect the 10 wt% solids flowability, which considerably affects the coating microstructures.

When the solid loading was changed to 20 wt% from 10 wt% by keeping all the parameters the same [**Table 3. 1**], the cauliflower shape microstructure was significantly reduced and increased the coating thickness [**Figure 3. 11 (c-d)**]. However, coating porosity increased considerably. Again, this could be due to the spray distance of 40 mm, which reduced the particle's momentum in-flight (i.e., the particle's velocity was 384 m/s) and increased the residence time. This ultimately caused the deviation of the particles from the plasma plume. Some of the particles may have vaporized and potentially increased the porosity of the coating microstructures.

For the 3rd spray condition, the inflight particle velocity increased from 384 m/s to 427 m/s; the spray distance changed from 40 to 30 mm while maintaining the solid content at 20wt% and the power at 20 kW [**Table 3. 1**]. The high velocity of the particles reduced the inflight residence time, prevented excessive evaporation, and produced comparatively dense coatings [**Figure 3. 11 (e-f)**]. While the coating thickness was decreased slightly from the 2nd spray condition, it eliminated the cauliflower shape microstructure and reduced the porosity of the coatings. Furthermore, the lamellar-type microstructures appeared in all three conditions; however, the uniform distribution of these lamellae was more visible in the 3rd spray conditions.

The surface roughness (Sa) (not shown) of the as-sprayed coatings of 1st spray, 2nd spray, and 3rd spray conditions were 8 ± 0.45 µm, 20 ± 3.0 µm, and 11 ± 1.5 µm, respectively. The reduction of surface roughness from the 2nd condition to the 3rd condition was due to the increased coating density. Also, low surface roughness in the first spray condition may be

attributed mainly to the cauliflower morphology [**Figure 3. 11 (a) inset**]. Generally, the coating microstructures of suspension plasma sprayed coatings largely depend on the suspension characteristics, variation of plasma gas compositions, torch speed, and power [63]. Based on the findings in this study, it is evident that the microstructure of the copper oxide coatings was influenced by the solid (wt%) in the suspensions and the spray distance (SD) at 20 kW power.

The challenges highlighted in this study can be minimized or improve the coating quality by varying plasma power, changing the secondary gas (H_2), and using He instead. Also, HVOF could be a viable option to avoid reducing CuO particles in-flight or on the substrate, as it uses bigger particles and low flame temperatures than the SPS process. Also, the further characterization needs to be studied to investigate the mechanical performance (i.e., hardness, elastic modulus, fracture toughness) of these coatings.

3.4.2 Friction and wear mechanisms

The tribology (friction, wear & lubrication) is a complex process that affects many factors during sliding, such as materials, environment, contact type, etc. [64]. Therefore, friction and wear are not the material's intrinsic properties but a system response. However, the variation of friction and wear of thermally sprayed ceramic oxides coatings is considerably associated with the chemical composition of the ceramic and their physical and microstructural characteristics (i.e., porosity, lamellar microstructure, bonding between splats, or numerous discontinuities) [65]. The most common wear mechanisms in ceramic vs. ceramic contact are abrasion, adhesion, delamination, and micro-fractures [33]. In this study, since the 3rd spray condition (i.e., 20 wt% solid with SD 30 mm) gave comparatively dense microstructure with low porosity and cauliflowers, this coating was further utilized for the wear testing at 25°C and 300°C under dry sliding without further polishing the surface of the coatings.

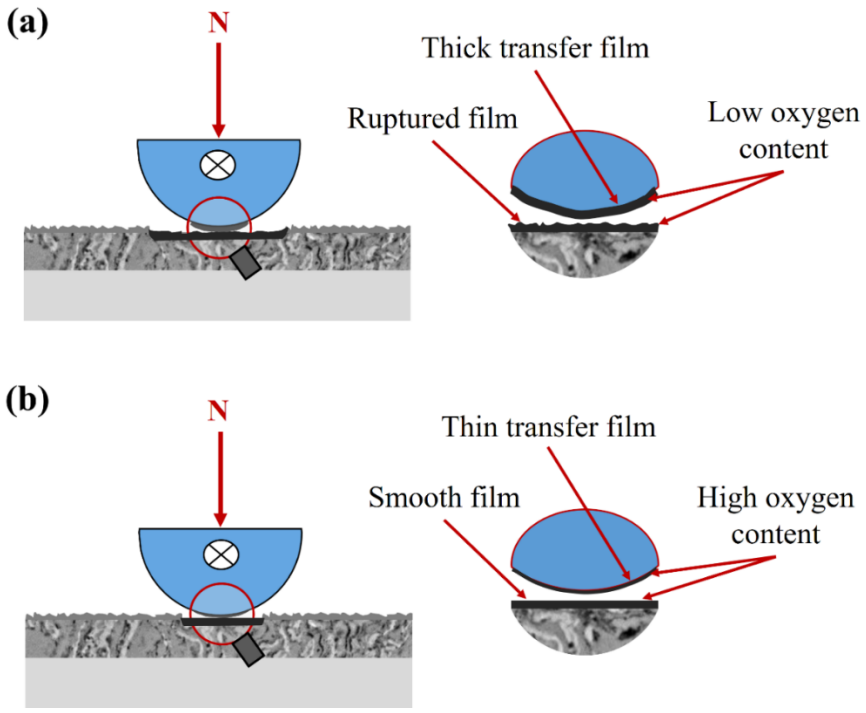

Figure 3. 12: Schematic friction and wear mechanisms of suspension plasma sprayed CuO coatings during dry sliding at (a) 25°C and (b) 300°C. ⊗ indicates sliding direction.

Based on the *ex-situ* analysis **(3.3.2)**, the friction and wear mechanisms phenomenon for the different testing conditions of the CuO coatings is shown in **Figure 3. 12**. Upon initial sliding at room temperature; there could be some adhesion between counterball alumina and the CuO coating. However, upon further sliding and at the end of the test, various pits, voids, cavities, and broken films appeared on the wear tracks [**Figure 3. 7 (a-c)**], which could be linked to the adhesive wear mechanisms [66]. These observations correlated well with the high friction and wear values of the CuO coatings at 25°C [**Figure 3. 5** & **Figure 3. 6**]. The high friction for the test at room temperature can be explained with the following equations (3.3) and (3.4) [67].

$$F = F_a + F_d \qquad (3.3)$$

$$\mu = \mu_a + \mu_d \qquad (3.4)$$

where in equation (3.3), F is the friction force, F_a is the adhesion force between two surfaces, and F_d is the deformation force due to the deformation of the surfaces. Moreover, equation (3.4) is linked to the friction coefficient of equation (3.3). When sliding at room temperature, the adhesive component could dominate the friction coefficient, which resulted in higher values. In addition, the thicker transfer film formation due to the greater adhesion led to an additional velocity accommodation mode (i.e., shearing off the transfer film) [68] [**Figure 3. 10 (a);**

Figure 3. 12 (a)]. This eventually increased friction at the atmospheric condition, as shown in **Figure 3. 5**.

In terms of wear, the high wear rate for the testing performed at room temperature correlated well with the reduction in the oxygen content [**Table 3. 3**] on the worn surfaces when compared to the unworn coating as well as with the transferred materials on the counterface [**Figure 3. 10 (a)**]. The low oxygen content could reduce hardness [56] and, consequently, a higher amount of adhesion to the counterball caused by high wear during sliding. The relationship between hardness and adhesion has been previously reported by Sikorski et al. [69].

At 300°C, the friction and wear were overall lower compared to the one at room temperature. This can be connected with the observations from the *ex-situ* analysis, which indicated the formation of a smooth uniform tribofilm [**Figure 3. 12 (b) and Figure 3. 7 (d-f)**]. In addition, evident abrasive marks parallel to the sliding direction were visible on the wear track, which indicated that the wear was dominated by abrasion during steady state [**Figure 3. 7 (d-f)**]. More specifically, upon initial sliding at elevated temperature (i.e., during the running-in phase), it was likely that the main wear mechanism was adhesion, which led to the removal of materials from the coatings and, subsequently, the formation of the tribofilm [**Figure 3. 7 (f)**]. As shown in **Table 3. 3**, the tribofilm generated at the elevated temperature showed an increased oxygen content, which increased the hardness [70] and consequently reduced the amount of adhesion [69]. Compared to the test performed at room temperature, the abrasion component at elevated temperature dominated the overall friction and wear, resulting in a lower friction coefficient [**Figure 3. 5** & **Figure 3. 6**]. More specifically, considering equation (4), the deformation component dominated the coefficient of friction, and due to the minimal adhesive contribution, the friction was relatively low. It can be noted that the adhesion force played a role in the running-in state due to the asperity-to-asperity contact and their detachment during sliding, which correlated well with the high friction during the initial sliding cycles. During a steady state at 300°C, a thin tribofilm and a transfer film were formed [**Figure 3. 10 (b)** & **Figure 3. 12 (b)**], which reduced the adhesion and, thus, decreased the shear strength. The reduced shear strength and contact area led to a decrease in the overall friction coefficient. The reduction in adhesion during a steady state could be explained by the higher oxygen content observed within the tribo- and transfer film [**Figure 3. 10 (b)** & **Figure 3. 12 (b)**], which increased the hardness and decreased the adhesion.

To elaborate on the oxidation phenomena, based on Raman analysis [**Figure 3. 9**], the unworn coatings at 25°C and 300°C have both CuO and Cu_2O phases. Similarly, the EDS

analysis confirmed that there was no change in the compositions of copper and oxygen before and after heating the unworn surfaces [**Table 3. 3**]. However, prior work on similar copper oxide systems showed that Cu underwent oxidation during sliding [14]. Compared to native oxidation, the tribological loading accelerated greater oxidation [15]. Likewise, it can be noted that CuO is thermally more stable than Cu_2O because of the high oxidation number [58]. Therefore, the applied load and frictional heating in the contact point between tribopairs could be the reason for having CuO phase only after wear testing both at 25°C and 300°C [**Figure 3. 9 (a)** and **Figure 3. 9 (b)**]. However, at elevated temperatures (i.e., 300°C), sliding could cause more oxides formation in the contact interfaces by transferring Cu into Cu_2O and eventually transforming to CuO [71]. This was observed in this study through the *ex-situ* analysis, which showed high oxides content compared to the tests at atmospheric conditions [**Table 3. 3**].

3.5 Conclusions

CuO coatings were produced by SPS process with varying solid loading (10 wt% and 20 wt%) in the suspension and spray distance (40 mm and 30 mm) at constant power (i.e., 20 kW). During spraying, the CuO was chemically reduced to Cu_2O and pure metallic Cu in all spray conditions. The 20 wt% solid in the suspension with a spray distance of 30 mm showed a comparatively dense microstructure due to the high particle speed and low residence time in flight. Subsequently, the relatively dense microstructures of CuO coatings obtained by SPS (20wt% solid, SD 30 mm) were used for sliding wear testing at 25°C and 300°C. The friction and wear of the coatings at 25°C were higher than the tests performed at 300°C. The high friction and wear were attributed to the adhesion and shearing of thick transfer film. The reduced content of oxides on the wear track explained the adhesive wear causing large materials to transfer to the counterface. At 300°C, on the other hand, a smooth film on the wear surface and a thin transfer film on the counterface were observed, which resulted in lower friction and wear than at 25°C.

3.6 References

[1] Stoyanov P, Harrington KM, Frye A. Insights into the tribological characteristic of Cu-based coatings under extreme contact conditions. JOM 2020;72:2191–7.

[2] Stoyanov P, Dawag L, Goberman DG, Shah D. Friction and wear characteristics of single crystal Ni-based superalloys at elevated temperatures. Tribol Lett 2018;66:1–9.

[3] Aouadi SM, Singh DP, Stone DS, Polychronopoulou K, Nahif F, Rebholz C, et al. Adaptive VN/Ag nanocomposite coatings with lubricious behavior from 25 to 1000 °c. Acta Mater 2010;58:5326–31. https://doi.org/10.1016/j.actamat.2010.06.006.

[4] Bagde P, Sapate SG, Khatirkar RK, Vashishtha N. Friction and abrasive wear behaviour of Al2O3-13TiO2 and Al2O3-13TiO2+Ni Graphite coatings. Tribol Int 2018;121:353–72. https://doi.org/10.1016/j.triboint.2018.01.067.

[5] Stoyanov P, Dawag L, Joost WJ, Goberman DG, Ivory S. Insights into the static friction behavior of Ni-based superalloys. Surf Coatings Technol 2018;352:634–41.

[6] Wang Z, Ye R, Xiang J. The performance of textured surface in friction reducing: A review. Tribol Int 2022:108010.

[7] Harrington KM, Miller EC, Frye A, Stoyanov P. Tribological insights of Co-and Ni-based alloys in extreme conditions. Wear 2021;477:203827.

[8] Du L, Zhang W, Zhang W, Zhang T, Lan H, Huang C. Tribological and oxidation behaviors of the plasma sprayed NiCoCrAlY-Cr2O3-AgVO3 coating. Surf Coatings Technol 2016;298:7–14. https://doi.org/10.1016/j.surfcoat.2016.04.042.

[9] Stoyanov P, Boyne A, Ignatov A. Tribological characteristics of Co-based plasma sprayed coating in extreme conditions. Results in Surfaces and Interfaces 2021;3:100007. https://doi.org/10.1016/j.rsurfi.2021.100007.

[10] Ross E, Ignatov A, Stoyanov P. Tribological Characteristics of Manufactured Carbon Under Extreme Contact Conditions. Tribol Ind 2021;43.

[11] Cheng JB, Liang XB, Xu BS. Devitrification of arc-sprayed FeBSiNb amorphous coatings: Effects on wear resistance and mechanical behavior. Surf Coatings Technol 2013;235:720–6.

[12] Hong S, Mei D, Wu J, Lin J, Wu Y, Li J, et al. Hydro-abrasive erosion and cavitation-silt erosion characteristics of HVOF sprayed WC-Ni cermet coatings under different flow velocities and sand concentrations. Ceram Int 2023;49:74–83.

[13] Aouadi SM, Gao H, Martini A, Scharf TW, Muratore C. Lubricious oxide coatings for extreme temperature applications: A review. Surf Coatings Technol 2014;257:266–77. https://doi.org/10.1016/j.surfcoat.2014.05.064.

[14] Lehmann JS, Schwaiger R, Rinke M, Greiner C. How Tribo-Oxidation Alters the Tribological Properties of Copper and Its Oxides. Adv Mater Interfaces 2021;8. https://doi.org/10.1002/admi.202001673.

[15] Rau JS, Balachandran S, Schneider R, Gumbsch P, Gault B, Greiner C. High diffusivity pathways govern massively enhanced oxidation during tribological sliding. Acta Mater 2021;221:117353. https://doi.org/10.1016/j.actamat.2021.117353.

[16] Rau JS, Schmidt O, Schneider R, Greiner C. Three regimes in the tribo-oxidation of high purity copper at temperatures of up to 150 ° C n.d.

[17] Erdemir A. A crystal-chemical approach to lubrication by solid oxides. Tribol Lett 2000;8:97–102. https://doi.org/10.1023/a:1019183101329.

[18] Sterle W, Prietzel C, Kloß H, Dmitriev AI. On the role of copper in brake friction materials. Tribol Int 2010;43:2317–26. https://doi.org/10.1016/j.triboint.2010.08.005.

[19] Peterson MB, Calabrese SB, Stupp B, Circle M, Quincy N. Lubrication with naturally ocurring double oxide films. Wear Sci Inc Arnold MD 1982.

[20] Goto M, Kasahara A, Oishi T, Konishi Y, Tosa M. Lubricative coatings of copper oxide for aerospace applications. J Appl Phys 2003;94:2110–4. https://doi.org/10.1063/1.1588355.

[21] Goto M, Kasahara A, Tosa M. Low frictional property of copper oxide thin films optimised using a combinatorial sputter coating system. Appl Surf Sci 2006;252:2482–7. https://doi.org/10.1016/j.apsusc.2005.03.236.

[22] Zhu S, Cheng J, Qiao Z, Tian Y, Yang J. High Temperature Lubricating Behavior of NiAl Matrix Composites with Addition of CuO. J Tribol 2016;138:1–9. https://doi.org/10.1115/1.4033133.

[23] Zhu S, Bi Q, Niu M, Yang J, Liu W. Tribological behavior of NiAl matrix composites with addition of oxides at high temperatures. Wear 2012;274–275:423–34. https://doi.org/10.1016/j.wear.2011.11.006.

[24] Ran S, Winnubst L, Blank DHA, Pasaribu HR, Sloetjes J, Schipper DJ. Effect of Microstructure on the Tribological and Mechanical Properties of CuO-Doped 3Y-TZP Ceramics. J Am Ceram Soc 2007;90:2747–52.

[25] Pasaribu HR, Reuver KM, Schipper DJ, Ran S, Wiratha KW, Winnubst AJA, et al. Environmental effects on friction and wear of dry sliding zirconia and alumina ceramics doped with copper oxide. Int J Refract Met Hard Mater 2005;23:386–90.
[26] Kong L, Bi Q, Zhu S, Qiao Z, Yang J, Liu W. Effect of CuO on self-lubricating properties of ZrO2(Y2O3)-Mo composites at high temperatures. J Eur Ceram Soc 2014;34:1289–96. https://doi.org/10.1016/j.jeurceramsoc.2013.11.027.
[27] Valefi M, de Rooij M, Schipper DJ, Winnubst L. High-Temperature Tribological and Self-Lubricating Behavior of Copper Oxide-Doped Y-TZP Composite Sliding Against Alumina. J Am Ceram Soc 2011;94:4426–34.
[28] Waldbillig D, Kesler O. The effect of solids and dispersant loadings on the suspension viscosities and deposition rates of suspension plasma sprayed YSZ coatings. Surf Coatings Technol 2009;203:2098–101. https://doi.org/10.1016/j.surfcoat.2008.11.027.
[29] Chen D, Jordan EH, Gell M. Microstructure of suspension plasma spray and air plasma spray Al 2O 3-ZrO 2 composite coatings. J Therm Spray Technol 2009;18:421–6. https://doi.org/10.1007/s11666-009-9306-5.
[30] Darut G, Ben-Ettouil F, Denoirjean A, Montavon G, Ageorges H, Fauchais P. Dry sliding behavior of sub-micrometer-sized suspension plasma sprayed ceramic oxide coatings. J Therm Spray Technol 2010;19:275–85. https://doi.org/10.1007/s11666-009-9415-1.
[31] Mahade S, Narayan K, Govindarajan S, Björklund S, Curry N, Joshi S. Exploiting suspension plasma spraying to deposit wear-resistant carbide coatings. Materials (Basel) 2019;12:1–9. https://doi.org/10.3390/ma12152344.
[32] Łatka L, Szala M, Macek W, Branco R. Mechanical Properties and Sliding Wear Resistance of Suspension Plasma Sprayed YSZ Coatings 2020. https://doi.org/10.12913/22998624/128574.
[33] Klyatskina E, Espinosa-Fernández L, Darut G, Segovia F, Salvador MD, Montavon G, et al. Sliding wear behavior of Al2O3-TiO2 coatings fabricated by the suspension plasma spraying technique. Tribol Lett 2015;59. https://doi.org/10.1007/s11249-015-0530-5.
[34] Fauchais P, Etchart-Salas R, Rat V, Coudert JF, Caron N, Wittmann-Ténèze K. Parameters controlling liquid plasma spraying: Solutions, sols, or suspensions. J Therm Spray Technol 2008;17:31–59. https://doi.org/10.1007/s11666-007-9152-2.
[35] Chin CH, Muchtar A, Azhari CH, Razali M, Aboras M. Optimization of pH and dispersant amount of Y-TZP suspension for colloidal stability. Ceram Int 2015;41:9939–46. https://doi.org/10.1016/j.ceramint.2015.04.073.
[36] Roy A, Munagala VNV, Patel P, Sharifi N, Alidokht SA, Makowiec M, et al. Friction and wear behavior of suspension plasma sprayed tantalum oxide coatings at elevated temperatures. Surf Coatings Technol 2023;452:129097.
[37] Rezania O. Anelastic Behavior of Suspension Plasma Sprayed Ceramic Coatings. MASc Thesis 2016.
[38] Aghasibeig M, Tarasi F, Lima RS, Dolatabadi A, Moreau C. A Review on suspension thermal spray patented technology evolution. J Therm Spray Technol 2019;28:1579–605.
[39] de Castilho BCNM, Munagala VNV, Alidokht SA, Sharifi N, Bessette S, Makowiec ME, et al. Insights on Silver Migration Mechanisms and their Influence on the Wear Behavior of Thermally Sprayed Self-lubricating Coatings Up to 350° C. Tribol Lett 2022;70:120.
[40] Patel P, Alidokht SA, Sharifi N, Roy A, Harrington K, Stoyanov P, et al. Microstructural and Tribological Behavior of Thermal Spray CrMnFeCoNi High Entropy Alloy Coatings. J Therm Spray Technol 2022:1–17.
[41] Küçük Y. Effect of counterbody on the dry sliding wear performance of plasma sprayed calcia-stabilized zirconia coating. Int J Refract Met Hard Mater 2020;92. https://doi.org/10.1016/j.ijrmhm.2020.105284.
[42] Prakash A, VS GK, Moger SN, Mahesha MG. Spectroscopic and electrical analysis of spray deposited copper oxide thin films. Mater Today Commun 2022;32:103926.
[43] Biesinger MC, Payne BP, Grosvenor AP, Lau LWM, Gerson AR, Smart RSC. Resolving surface chemical states in XPS analysis of first row transition metals, oxides and hydroxides: Cr, Mn, Fe, Co and Ni. Appl Surf Sci 2011;257:2717–30.
[44] Grairia A, Beliardouh NE, Zahzouh M, Nouveau C, Besnard A. Dry sliding wear investigation on tungsten carbide particles reinforced iron matrix composites. Mater Res Express 2018;5:116528.
[45] Yang M-S, Liu X-B, Fan J-W, He X-M, Shi S-H, Fu G-Y, et al. Microstructure and wear behaviors of laser clad NiCr/Cr3C2–WS2 high temperature self-lubricating wear-resistant composite coating. Appl Surf Sci 2012;258:3757–62.
[46] Debbichi L, Marco De Lucas MC, Pierson JF, Krüger P. Vibrational properties of CuO and Cu 4O 3 from first-principles calculations, and raman and infrared spectroscopy. J Phys Chem C 2012;116:10232–7. https://doi.org/10.1021/jp303096m.
[47] Prabu RD, Valanarasu S, Kulandaisamy I, Ganesh V, Shkir M, Kathalingam A. Studies on copper oxide

thin films prepared by simple nebulizer spray technique. J Mater Sci Mater Electron 2017;28:6754–62. https://doi.org/10.1007/s10854-017-6371-2.
[48] Chen XK, Irwin JC, Franck JP. Evidence for a strong spin-phonon interaction in cupric oxide. Phys Rev B 1995;52:130–3. https://doi.org/10.1103/PhysRevB.52.R13130.
[49] Murthy PS, Venugopalan VP. Antibiofilm Activity ofNano sized CuO 2011:580–3.
[50] Joya MR, Barba-Ortega J, Raba AM. Vibrational Raman modes and particle size analysis of cupric oxide with calcination temperature. Indian J Pure Appl Phys 2019;57:268–71.
[51] Küçük Y. Effect of counter body on wear behavior of plasma-sprayed TiO2-45Cr2O3 coating. J Asian Ceram Soc 2021;9:214–29. https://doi.org/10.1080/21870764.2020.1863574.
[52] Schramm L, Behr G, Löser W, Wetzig K. Thermodynamic reassessment of the Cu-O phase diagram. J Phase Equilibria Diffus 2005;26:605–12. https://doi.org/10.1361/154770305X74421.
[53] Hallstedt B, Risold D, Gauckler LJ. Thermodynamic assessment of the copper-oxygen system. J Phase Equilibria 1994;15:483–99. https://doi.org/10.1007/BF02649399.
[54] Bhaskar S, Baroutian S, Jones MI, Matthews SJ. Plasma spraying of transition metal oxide coatings. Surf Eng 2021;0:1–15. https://doi.org/10.1080/02670844.2021.1886655.
[55] Sabat KC, Paramguru RK, Mishra BK. Reduction of Copper Oxide by Low-Temperature Hydrogen Plasma. Plasma Chem Plasma Process 2016;36:1111–24. https://doi.org/10.1007/s11090-016-9710-9.
[56] Toshiro Maruyama. Copper oxide thin films prepared by chemical vapor deposition from copper dipivaloylmethanate. Sol Energy Mater Sol Cells 1998;56:85–92.
[57] Akgul FA, Akgul G, Yildirim N, Unalan HE, Turan R. Influence of thermal annealing on microstructural, morphological, optical properties and surface electronic structure of copper oxide thin films. Mater Chem Phys 2014;147:987–95. https://doi.org/10.1016/j.matchemphys.2014.06.047.
[58] Raship NA, Sahdan MZ, Adriyanto F, Nurfazliana MF, Bakri AS. Effect of annealing temperature on the properties of copper oxide films prepared by dip coating technique. AIP Conf Proc 2017;1788. https://doi.org/10.1063/1.4968374.
[59] Fauchais P, Montavon G, Lima RS, Marple BR. Engineering a new class of thermal spray nano-based microstructures from agglomerated nanostructured particles, suspensions and solutions: An invited review. J Phys D Appl Phys 2011;44. https://doi.org/10.1088/0022-3727/44/9/093001.
[60] Fauchais P, Vardelle M, Vardelle A, Goutier S. What Do We Know, What are the Current Limitations of Suspension Plasma Spraying? J Therm Spray Technol 2015;24:1120–9. https://doi.org/10.1007/s11666-015-0286-3.
[61] Mauer G, Vaßen R. Coatings with Columnar Microstructures for Thermal Barrier Applications. Adv Eng Mater 2020;22:1–9. https://doi.org/10.1002/adem.201900988.
[62] Etchart-Salas R, Rat V, Coudert JF, Fauchais P, Caron N, Wittman K, et al. Influence of plasma instabilities in ceramic suspension plasma spraying. J Therm Spray Technol 2007;16:857–65. https://doi.org/10.1007/s11666-007-9084-x.
[63] Waldbillig D, Kesler O. Effect of suspension plasma spraying process parameters on YSZ coating microstructure and permeability. Surf Coatings Technol 2011;205:5483–92. https://doi.org/10.1016/j.surfcoat.2011.06.019.
[64] Kato K. Wear in relation to friction - A review. Wear 2000;241:151–7. https://doi.org/10.1016/S0043-1648(00)00382-3.
[65] Michalak M, Sokołowski P, Szala M, Walczak M, Łatka L, Toma F-L, et al. Wear Behavior Analysis of Al2O3 Coatings Manufactured by APS and HVOF Spraying Processes Using Powder and Suspension Feedstocks. Coatings 2021;11:879. https://doi.org/10.3390/coatings11080879.
[66] M.H.J. Surface effects in adhesion, friction, wear and lubrication. vol. 85. 1983. https://doi.org/10.1016/0043-1648(83)90069-8.
[67] K. Holmberg AM. Coatings tribology: properties, mechanisms, techniques and applications in surface engineering. vol. 56. 2nd ed. Elsevier; 2009.
[68] Berthier Y, Godet M, Brendle M. Velocity accommodation in friction. Tribol Trans 1989;32:490–6.
[69] Sikorski ME. Correlation of the coefficient of adhesion with various physical and mechanical properties of metals. J Fluids Eng Trans ASME 1963;85:279–85. https://doi.org/10.1115/1.3656577.
[70] Suzuki T, Inoue J, Saito H, Hirai M, Suematsu H, Jiang W, et al. Influence of oxygen content on structure and hardness of Cr–N–O thin films prepared by pulsed laser deposition. Thin Solid Films 2006;515:2161–6.
[71] Choudhary S, Sarma JVN, Pande S, Ababou-Girard S, Turban P, Lepine B, et al. Oxidation mechanism of thin Cu films: A gateway towards the formation of single oxide phase. AIP Adv 2018;8. https://doi.org/10.1063/1.5028407.

Chapter 4

Friction and Wear Behavior of Suspension Plasma Sprayed Tantalum Oxide Coatings at Elevated Temperatures[3]

Abstract

Tantalum oxide-based coatings have recently become potential candidates for high-temperature tribological applications due to their high thermal stability and ionic potential. This study focuses on developing suspension plasma sprayed (SPS) tantalum oxide coatings and evaluating their tribological behavior at elevated temperatures. The coating morphology, oxide phases, and mechanical properties were characterized using Scanning electron microscopy (SEM), X-ray diffraction (XRD), X-ray photoelectron spectroscopy (XPS), and microhardness. Microstructural observations showed uniform and dense nanostructure coatings with no phase transformation after deposition. The tribological results illustrated that the friction coefficient of the tantalum oxide coating slightly decreased from 0.9 at 25°C to 0.8 at 300°C. On the other hand, the wear rate at 300°C decreased by more than 50% compared to 25°C. *Ex-situ* analysis indicated the brittle-fracture behavior of the coating during sliding at 25°C, which resulted in higher friction and wear. However, the friction and wear decreased at 300°C, which was attributed to the formation of a smeared or continuous smooth layer on the wear tracks with a stable transfer film on the counterface.

Keywords: *Suspension plasma spray, Tantalum oxide, tribology, elevated temperature, Transfer film*

[3] This chapter has been published as a research article in the *Surface and Coating Technology*. **A. Roy**, V.N.V. Munagala, P. Patel, N. Sharifi, SA. Alidokht, M. Makowiec, R. R. Chromik, C. Moreau, P. Stoyanov. "Friction and wear behavior of suspension plasma sprayed tantalum oxide coatings at elevated temperatures." *Surface and Coatings Technology* 452 (2023): 129097.

4.1 Introduction

With the recent advancement in mechanical systems for aerospace applications, the operating conditions in which materials are required to operate under severe conditions have become more demanding. The lubricity of the traditional solid lubricants such as graphite and MoS_2 is limited by the working environments [1]. Thus, there is a strong desire to develop next-generation materials capable of operating effectively in such harsh conditions [1–5]. Consequently, oxide-based systems are being extensively investigated as potential solutions for high-temperature solid lubrication owing to their high thermal and chemical stability [6,7]. The lubricating behavior of various oxide film for high temperature conditions were initially studied by Peterson and co-researchers [8–11]. The authors showed that while some oxides are abrasive at lower temperatures due to their strong ionic bond [12,13], at elevated temperatures, they exhibit low interfacial shear strength and ultimately can reduce friction coefficient. With the purpose of explaining the low friction behavior of oxides at high temperatures, Erdemir [14,15] proposed a crystal-chemical approach that relates the ionic potential of solid oxides with tribological characteristics, where the ionic potential (φ) is the ratio between the cationic charge and the radius of the cation of the oxides. It was suggested that [14,15] oxides with higher ionic potential exhibit low friction coefficient at high temperatures, which is mainly attributed to the greater screening of cations by surrounding anions. The surrounding anions make it difficult to interact with other cations and consequently, this result in low shear strength at high temperatures. Similarly, Dimitrov et al. [16] co-related the lubricating behavior of the solid oxides with polarizability or interaction parameters at elevated temperatures. With a low interaction parameter of the oxides, the bond energy between cation and anion weaken, which eventually decreases the friction and effectively improves the lubricity [16,17]. This low interaction parameter indicates excellent lubricity compared to the ionic potential/crystal chemical model proposed by Erdemir [14]. Hence, the ionic potential and interaction parameter provide a tentative guideline for the selection of lubricious oxides. A summary of this frictional behavior in regards to the ionic potential and interaction parameter is explained elsewhere [14,18,19]. In relation to this, the ionic potential and interaction parameter of tantalum oxide are 6.4 and 0.08 [16], respectively. Therefore, according to the ionic potential and interaction parameter value, tantalum oxide could provide good lubrication at elevated temperatures. Additionally, the melting temperature of tantalum oxide is 1800°C, and thus, it has good thermal and chemical stability in high-temperature environments against water vapor [20,21].

Aside from the low friction behavior at elevated temperatures, tantalum pentoxide has low toxicity, biocompatibility, high corrosion resistance [22,23], and high wear-resistant due to its relatively high hardness [24]. It has been previously reported that the reinforcement of hard Ta_2O_5 in Ta enhanced the corrosion and wear resistance [25]. Similarly, Wen Qin et al. [26] described that Ta-Cu films deposited on steel substrate by magnetron sputtering provided excellent wear resistance due to the formation of tantalum oxide (Ta_2O_5) on the worn surface by the tribochemical reaction. The tantalum oxide as reinforcement in NiCrAlY/Ag_2O/Ta_2O_5 composite coatings on Inconel 625 deposited by laser cladding process, helped to form ternary phase $AgTaO_3$, $Ag_2Ta_4O_{11}$ and reduced the friction and wear [27]. This ternary phase has also been observed by D. S. Stone et al. [28] due to the mechanical mixing of Ta_2O_5 and Ag on the wear track during sliding. Furthermore, the tantalum oxide increased the load carrying capacity in the composite coatings and contributed to improve the tribological properties. A thick Ta_2O_5 coating deposited by air plasma spraying on stainless steel with MCoAlY bond coat provided good ablation resistance which was observed by Jiayi Zheng et al. [29]. Additionally, the potentiality of the tantalum oxide in friction tailored and oxidation resistant applications has been previously predicted by Peterson et al. [9]. Nevertheless, the wear-resistant characteristics of the suspension plasma sprayed tantalum oxide coating alone in dry sliding conditions at elevated temperatures have not been previously reported.

Suspension plasma spraying (SPS) offers promising advantages such as lower cost, lower complexity, atmospheric deposition condition, ease of application to large surfaces and high deposition efficiency in comparison to conventional thin film coating deposition processes. These advantages make it easier to deposit the coating on a large and wide surface of any machinery components. Additionally, SPS allows using fine-grained, nano and submicron-sized feedstock powders, which is impossible in other plasma spraying techniques such as APS, HVOF and HVAF, resulting in a variety of coating microstructures. The feedstock powders are dispersed in a liquid (typically ethanol or water) to form a suspension slurry and are injected into the plasma jet to be deposited. Upon exposure to the high temperature in the plasma jet, the suspension breaks-up into microdroplets, the liquid evaporates in flight while the solid particles agglomerate, melt, and impact on the substrate to build up a coating [30,31]. The unique microstructures resulting from SPS deposition from the accumulation of thin splats on the substrate can be beneficial to the wear resistance of the coating [32].

The main purpose of this study was to critically evaluate the tribological behavior of tantalum oxide coatings as a potential high temperature lubricating oxide. The tantalum oxide coatings were prepared by radial injection SPS process and their tribological performance was

investigated up to 300°C. The phases and microstructures of the coatings, as well as worn surfaces after dry sliding at elevated temperatures, were characterized using high resolution electron microscopy, X-ray diffraction, X-ray photoelectron spectroscopy.

4.2 Experimental details

4.2.1 Feedstock material

As feedstock for the suspension plasma spraying (SPS) process, the sub-micrometer size tantalum oxide powder (PI-KEM, UK) with a nominal particle size of about 0.7 μm were acquired. A Spraytec (Malvern, UK) instrument was used to measure the particle size distribution (PSD) via diffraction of a He-Ne laser with a wavelength 632.8 nm. The powder particles were dispersed in the ethanol, and measurements were carried out in a wet dispersion accessory.

4.2.2 Suspension preparation

A suspension of tantalum oxide in ethanol was used as the feedstock. The total solid content of the suspension was selected to be 10 wt.% to avoid increasing the viscosity of the suspension to problematic levels which may reduce the flowability or cause clogging during spraying [33]. The Polyvinylpyrrolidone (PVP) (Mm: 360,000 g/mol) (Sigma-Aldrich, Canada) was used as a dispersing agent in the preparation of the feedstock suspension. The stability of the suspensions in ethanol with various amounts of PVP (ranging from 0 to 10 wt.% of the total solid) was studied and the sedimentation rate was measured after 48 hours. To achieve a particle sedimentation lower than 1 mm per hour, typically considered suitable for spraying [34], the 5 wt% of PVP was selected as the optimal amount for a stable suspension. For preparing suspension, initially, the PVP was dissolved in ethanol and then, the tantalum oxide was gradually dispersed in the solution by simultaneous magnetic stirring (ThermoFisher Scientific, USA) and sonicating (Qsonica, USA) at 50 kW power for 30 minutes. The prepared suspension was kept in soft ball milling overnight to break the agglomeration of the particles before feeding into the SPS system.

4.2.3 Coating deposition

A radial injection 3-MB plasma gun (Oerlikon Metco, USA) with 5 mm nozzle diameter was used for the SPS process. The schematic of the SPS process is shown in **Figure 4. 1**. The suspension from the pressurized container was fed into the plasma jet radially by suspension feed. The 304L stainless-steel substrates with dimensions of 25mm×25mm×5 mm were used,

and grit blasted with 80 grit Al_2O_3 before spraying. The substrates were cleaned with compressed air to remove any embedded grit residue from the surface and de-greased using acetone.

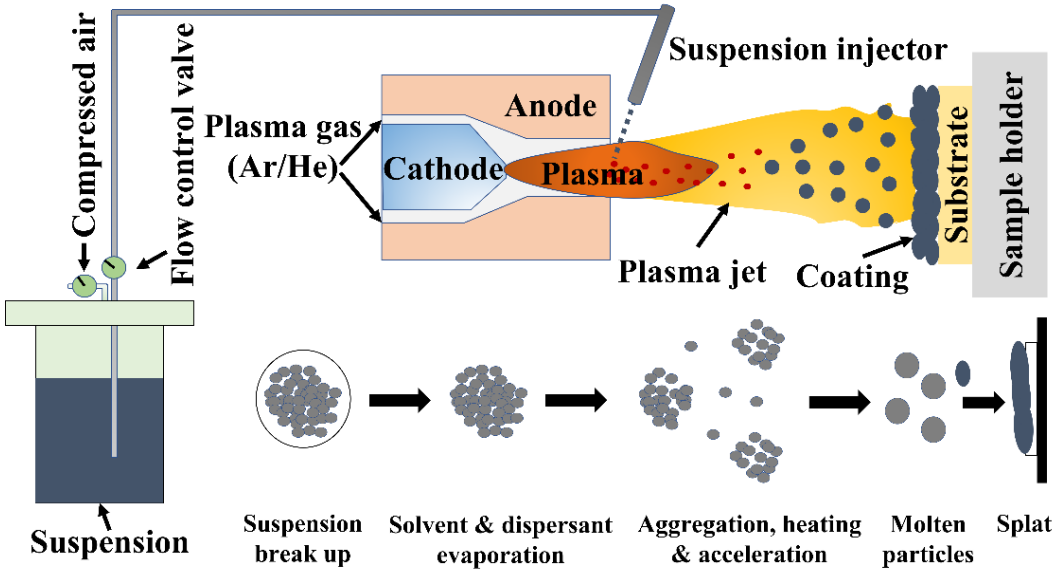

Figure 4. 1: A schematic of the radial injection suspension plasma spray (SPS) process

Prior to coating deposition, the substrate was preheated to 150°C while the maximum temperature of the substrates surface was maintained approximately at 400°C during spraying. An A320 ThermoVision infrared camera (FLIR System, USA) was used to monitor the substrate temperature. The in-flight particle velocity (550 m/s) and temperatures (>4000°C) were measured by Accuraspray (Tecnar, Canada). However, it is important to note that the Accuraspray particle temperature measurements for SPS process are not typically accurate since the point of measurement (spray distance) falls within the plasma jet, which is a significant source of optical noise [35]. The spraying parameters used for SPS process are summarized in **Table 4. 1**.

Table 4. 1: SPS parameters used for depositing tantalum oxide coating

Deposition parameters	Values
Plasma nozzle diameter (mm)	5
Solid loading (wt.%)	10
Current (A)	600
Voltage (V)	40
Power (kW)	24
Ar gas flow rate (l/min)	50
He gas flow rate (l/min)	10

Plasma gun transverse speed (m/s)	1
Suspension feed rate (ml/min)	33
Spray distance (mm)	30
Number of passes	85

The spray parameters in **Table 4. 1** were selected in order to achieve a dense microstructure in the coatings. There are several parameters, other than suspension characteristics, affecting the final microstructure of the coatings, including nozzle size, standoff distance, plasma gas composition, power, etc. [36]. The selected parameters [**Table 4. 1**] were chosen based on some initial sets of trial depositions and by considering the following hypotheses: (i) A relatively smaller nozzle diameter (5 mm rather than the 8 mm alternative) increases the particle jet velocity and decreases the particle's in-flight residence time. This creates a denser deposited layer and reduces the chance of overheating the particles (melting point of tantalum oxide, i.e., about 1800°C) [37]. (ii) During suspension plasma spraying, the heating and cooling rates of the sub-micron size particles are high, and consequently, the thermal and kinetic inertia of the hot particles are low [38]. This phenomenon requires a shorter standoff distance, which utilizes the high speed or the momentum of the in-flight particles onto the substrate. A relatively low spray distance of 30 mm allowed the plasma jet to impose a very strong heat flux on the coating/substrate during deposition, and eventually densified the coating and reduced the porosity [39]. (iii) The high viscosity of the He (up to about 14000 K) as the secondary plasma gas (compared to H_2 as the alternative) contributed to form a stable plasma jet and prevented the mixing of the surrounding air with in-flight particles [40]. (iv) The plasma power of 24 kW provided sufficient heat to melt the oxide particles well to produce a dense coating.

4.2.4 Characterization

The morphology of the tantalum oxide powders was determined using a Scanning Electron Microscopy (SEM) (S-3400N, Hitachi High Technologies America, Inc., Japan). The as-sprayed coatings were mounted and polished according to ASTM E-3 standard practice. The top surface and cross-section of the suspension plasma sprayed coatings were analysed using SEM. A 3D optical surface profiler (Zygo Corporation, USA) was used for the measurement of the as-sprayed coatings surface roughness. Electron channeling contrast imaging (ECCI) was performed on the cross-sections of the coatings to reveal the grain size and grain orientation. ECCI on the cross sections was performed using a cold field emission SEM (SU8230, Hitachi, Japan) fitted with a photodiode BSE detector. An X-ray diffraction (XRD)

system (Bruker, Germany) with Co-Kα radiation (step size = 0.02°, frame rate = 200 per second, λ = 1.78 Å, 2θ range of 10°–120°) was used and operated at a power of 40 kV and 40 mA for the phase analysis of powders and coatings. The obtained diffractograms were analysed with the ICDD database using the software diffrac.eva provided with the XRD system.

An X-ray photoelectron spectroscopy (XPS) was performed on as-sprayed coatings and wear tracks after sliding tests with a VG ESCALAB 250 Xi (Thermo VG Scientific, Canada) Al K_α X-ray source set to 14 kV and 218 W. The atomic concentration and chemical states of the coatings were evaluated with this XPS analysis. In addition, XPS analysis was performed on the worn surface and sub-surface using a sputtering rate of 0.18 nm/s in order to elucidate the elemental changes leading to the difference in the friction and wear behavior. The Vickers microhardness of the coatings was measured on the top polished surface under a load of 2 N ($HV_{0.2}$), using a Micro combi tester-MCT^3 (Anton Paar, Switzerland) according to the EN ISO 4516 standard [41]. For each condition (25°C & 300°C), a total of 9 readings were considered the average value was presented. For measuring the microhardness at 300°C, the sample was placed in the furnace (temperature was set at 450°C) and then heated for around 25 to 30 minutes before performing microhardness testing. The same testing approach was used to perform the high-temperature tribology tests. The value of the maximum indentation depth was 6-10 µm during the microhardness testing, which was within the range of 10-20% of the coating thickness. Thus, there is no influence of the substrate on the hardness values. Indentation was performed such that the distance between any two indents was at least five times greater than the length of the diagonal of the previous indent. The porosity measurement was carried out with ImageJ software, open source, by considering more than ten backscattered SEM images at 2.00 k magnification (20 µm scale bar) in different locations of coating according to standard ASTM E2109-01 [42]. The average values, as well as standard deviations, were considered for presentable data.

4.2.5 Tribology testing and post-test characterization

A reciprocating ball-on-disc tribometer (Anton Paar TriTec SA, Switzerland) was used for wear testing of the tantalum oxide coatings. The testing parameters are given in **Table 4. 2**, which were adopted from previous studies done in the same research group [43]. For the elevated temperature wear tests, the furnace was initially heated to 450°C. The samples were placed in the furnace, and the surface of the coating was measured to be at around 300°C (i.e., using a thermocouple). The test parameters [**Table 4. 2**] were selected based on the practical application of moving mechanical assemblies [43].

Table 4. 2: The friction test parameters of the pin on disc tribometer

Tribology Testing Parameters	
Applied load (N)	5
Sliding velocity (cm/s)	3.14
Track length (mm)	10
Frequency (Hz)	1
Total sliding cycle	2500
Total sliding distance (m)	50
Counter body	Al_2O_3
Counter body dia. (mm)	6.35
Test temperatures (°C)	25 and 300

A total of three repeats were performed, and the average value was presented in the figures. The depth of wear tracks and wear volume of counterball alumina were measured using a 3D optical surface profiler (Zygo Corporation, USA). The wear area (mm^2) was calculated by integrating the wear track profiles, and the wear area was multiplied by track length (mm) to determine the wear volume (mm^3). The material pile-up was subtracted from the total volume during the wear rate calculation. Finally, the wear volume was normalized by dividing with applied load (N) and total sliding distance (m) to obtain the wear rate (mm^3/N.m.).

The wear tracks and counterballs after testing were analyzed using a SEM and the chemical composition was determined by energy-dispersive X-ray spectroscopy (EDS). The samples were mounted and cut in the perpendicular direction to the wear track length. Subsequently, the polished cross-sections were analyzed under the SEM to reveal the changes within the sub-surface.

4.3 Results

4.3.1 Feedstock and coating analysis

SEM morphology and cross-section of the tantalum oxide powder in the as-received condition are shown in **Figure 4. 2 (a)** and **Figure 4. 2 (a) (inset),** respectively. The tantalum oxide powder is mostly spherical and agglomerated [**Figure 4. 2 (a)**]. The spherical agglomerated morphology in the cross-section showed large, irregularly shaped pores [**Figure 4. 2 (a) (inset)**]. **Figure 4. 2 (b)** shows the particle size distribution of tantalum oxide powder with a maximum frequency of 4 µm. The values of Dv (10), Dv (50), and Dv (90) were 1.28 µm, 2.72 µm, and 5.32 µm respectively [Dv: Median for Volume Distribution], which are

typical sizes for the suspension plasma spraying process. The narrow particle size in the SPS process helps to produce a dense microstructure of the coatings due to a homogeneous thermal treatment among the particles [44]. However, the particle size distribution Dv (50) ~ 2.72 µm was not correlating with the average size (0.7 µm) [**Figure 4. 2 (a) (inset)**] due to the agglomeration of the particles [**Figure 4. 2 (a)**].

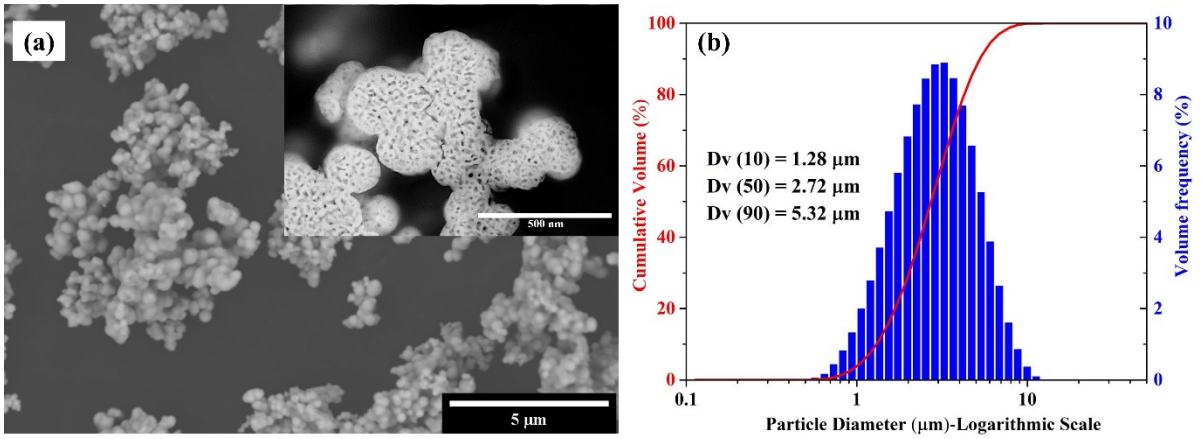

Figure 4. 2: a) SEM morphology of tantalum oxide powder [inset: cross-section of powder], b) Ethanol-based particle size distribution of tantalum oxide powder

Figure 4. 3 shows the XRD results of the feedstock powder and the as-sprayed coating. X-ray diffractograms showed no phase transformation of the powder particles before and after spraying. The diffraction peaks associated with 26.66° (001); 33.20° (141); 36.24° (0 14 0); 38.29° (270); 41.08° (290); 42.85° (1 11 1); 53.07° (350); 54.79° (002); 59.34° (152); 65.43° (1 11 2); 69.16° (2 22 0); 75.50° (2 22 1); 85.32° (4 16 0) can be indexed to β-orthorhombic (β- Ta_2O_5), PDF 00-025-0922 with lattice parameters a = 6.1980 Å, b = 40.2900 Å, c = 3.8880 Å, a/b = 0.15383, c/b = 0.0965, and $\alpha = \beta = \gamma = 90°$ for the space group Pmm2. Similar results have been previously reported by Israel Perez, et al. [45]. A trace amount of tantalum suboxide was found on the powders and the coatings, which is also associated with an orthorhombic structure (PDF 05-001-0683). According to Debye-Scherrer, the peaks at 2θ =26.75°, 33.23°, and 43.01° corresponding to β = 0.31°, 0.61°, and 0.58° indicated that the crystallite size is D = 30 nm, 16 nm, and 17 nm, respectively.

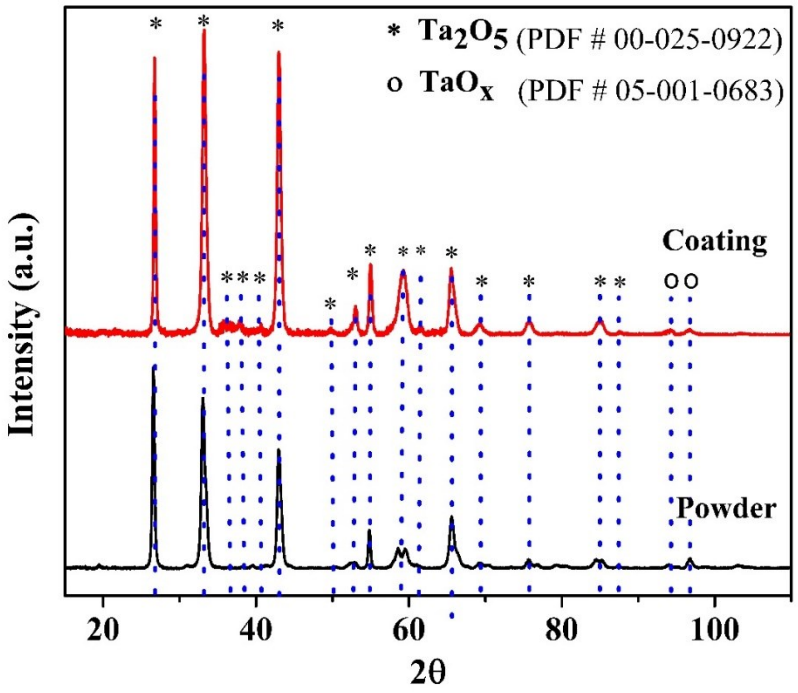

Figure 4. 3: XRD data of tantalum oxide powders and as-deposited coating

Figure 4. 4 (a) shows Ta4f spectra collected from the surface of the tantalum oxide coatings. The Ta 4*f* core level is a spin-orbit doublet corresponding to the levels Ta 4f7/2 and Ta 4f5/2 at the binding energies of 26.3 eV and 28.1 eV, respectively. These binding energy positions correspond to the +5 oxidation state of Ta, which corresponds to Ta_2O_5 [46,47]. Moreover, peaks in the lower binding energies (around 24.8 eV and 26.8 eV) can also be observed, which corresponds to sub-oxides [46]. [**Figure 4. 4 (a)**]. In addition, two main O1s peaks are found at binding energies (BE) of around 530.0 eV and 531.0 eV. The peak observed at BE=530.0 eV is identified as O1, which is present in metal oxides, and the one found at BE=531.0-531.5 eV is identified as O2, which is generally present in deficient metal oxide [48] [**Figure 4. 4 (b)**]. The XPS surface analysis of the coatings corresponds to the XRD results, as shown in **Figure 4. 3**.

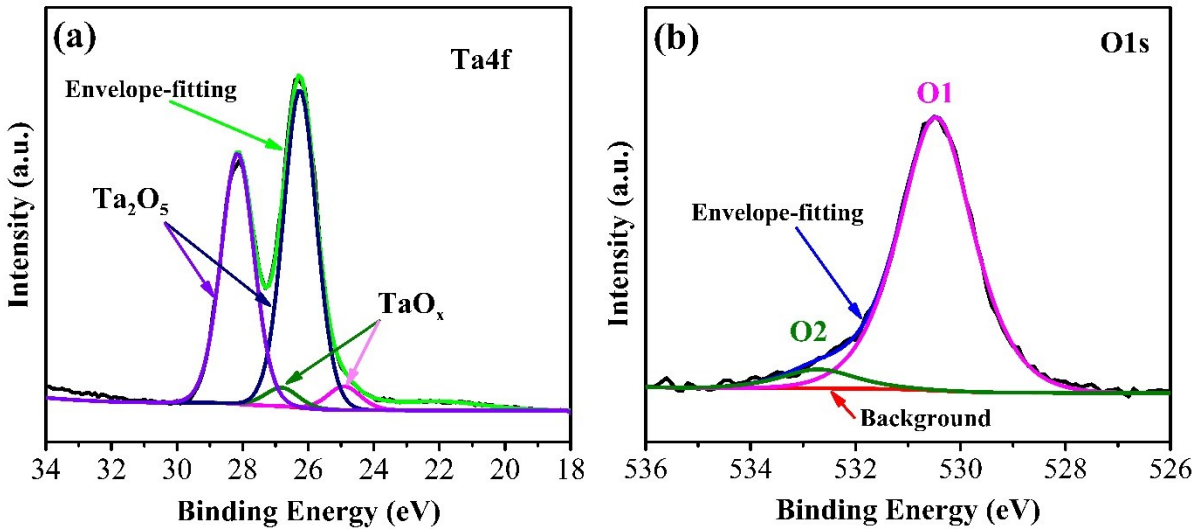

Figure 4. 4: (a) Ta4f and (b) O1s spectra of tantalum oxide coating

The ethanol-based tantalum oxide suspension was deposited on the 304L stainless steel substrates resulting in an 84 ± 4 µm thick dense coating [**Figure 4. 5 (a)]**. **Figure 4. 5 (b)** shows the high magnification SEM image of the cross-section with visible pores (i.e., porosity was 8 ± 0.6%). Additionally, the top surface of the as-sprayed tantalum oxide coating is shown in **Figure 4. 5 (c)**. From this micrograph, the coatings appear to mainly consist of fully spread splats, while some of the splats have broken up and some are present as semi-molted agglomerated particles. Consequently, the surface roughness of the as-deposited coatings was Sa = 5±1 µm [**Figure 4. 5 (d)**]. The porosity (8 ± 0.6%) and surface roughness (Sa = 5±1 µm) of tantalum oxide coatings were comparable to literature on SPS deposited ceramic coatings [49–51]. It should be noted that the roughness and porosity of the coatings can be significantly influenced by the degree of melting of the feedstock particles and spraying parameters [29,52].

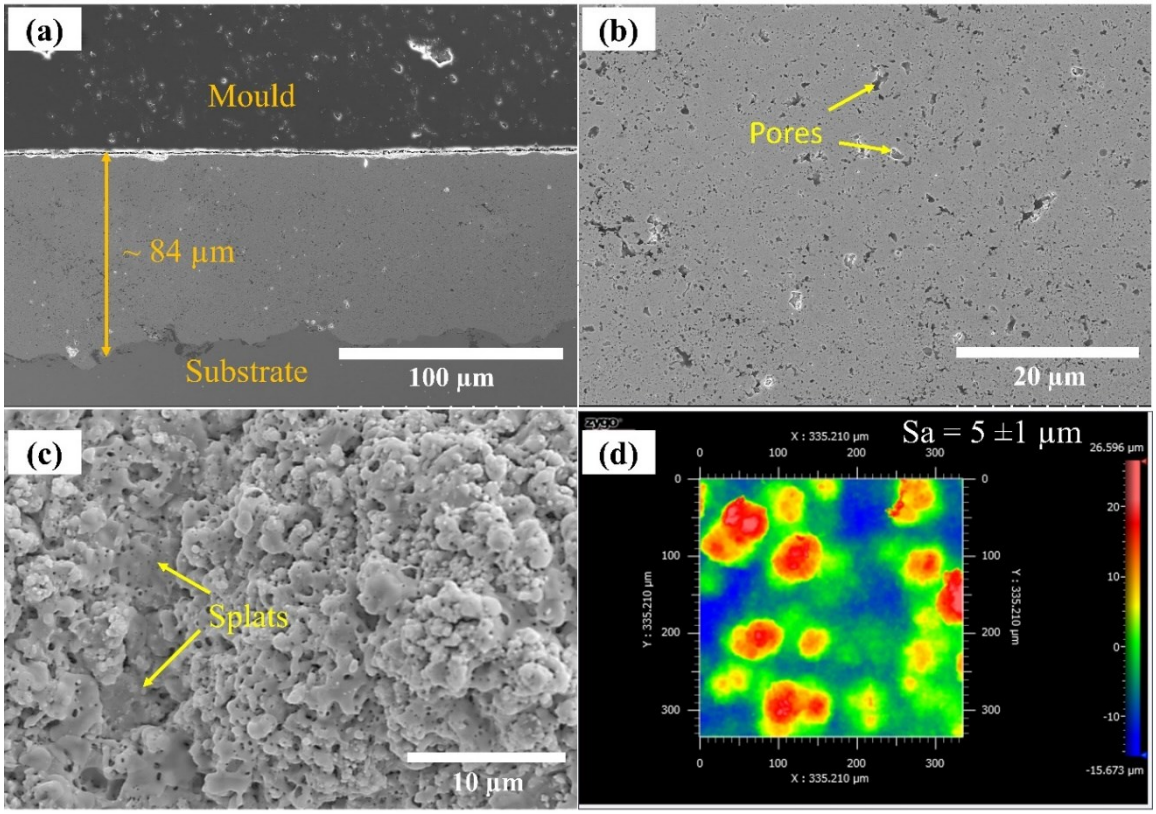

Figure 4. 5: (a) low magnification SEM cross-section of tantalum oxide coating; and (b) high magnification cross-section of tantalum oxide coating (c) SEM top surface of tantalum oxide coating and corresponding (d) surface roughness

High magnification secondary SEM [**Figure 4. 6 (a)**] and corresponding ECCI [**Figure 4. 6 (b)**] imaging has been performed on the cross-section of the tantalum oxide coatings to determine the grain size. The grains are more visible in ECCI imaging [**Figure 4. 6 (b)**]. The grain size of the coating varied from 150 nm to 340 nm (not to be confused with the crystallite size above).

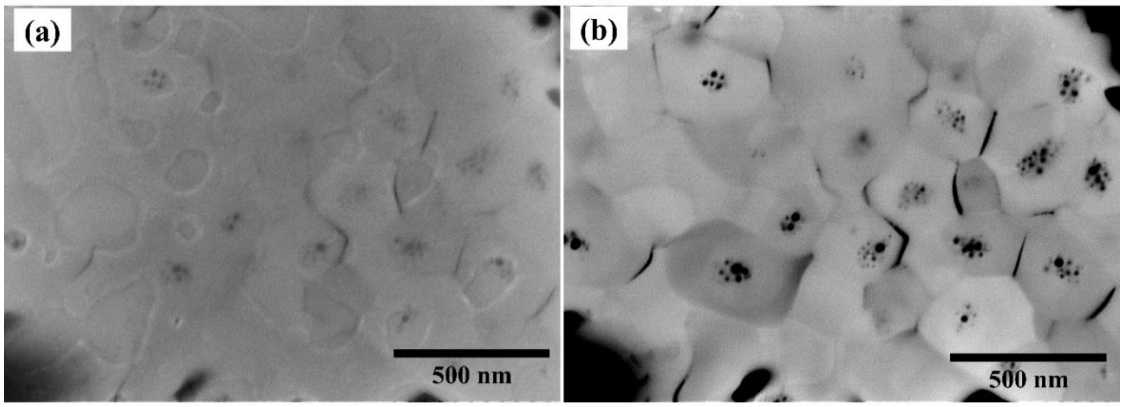

Figure 4. 6: (a) Secondary SEM image of the cross-section of tantalum oxide coating and (b) corresponding ECCI showing the grains

Interestingly, some of black spots have been observed within the grains [**Figure 4. 6 (b)**]. EDS analysis (not shown here) on these black spots did not show significant difference in the atomic (at%) concentration of Ta and O. These black spots could be due to the presence of another oxide phase of Ta, most probably the hexagonal (δ) phase of Ta_2O_5 or a suboxide (TaO_x) as previously reported in [45,53]. This correlates well with the observations of the XRD [**Figure 4. 3**] and XPS [**Figure 4. 4**] results.

The microhardness at 25°C & 300°C as well as the characteristics of the tantalum oxide coatings are shown in **Table 4. 3**. The hardness value of the tantalum oxide coating was 595 ± 41 $HV_{0.2}$ at 25°C and 513 ± 48 $HV_{0.2}$ at 300°C. No cracks were observed on the coatings during the microhardness experiment. The hardness of the coatings at 300°C was decreased by ~15% compared to 25°C.

Table 4. 3: Characteristics of the tantalum oxide coatings

Coating	Thickness	Porosity	Roughness (S_a)	Microhardness
Tantalum oxide	84 ± 4 µm	8 ± 0.5 %	5 ± 1 µm	595 ± 41 $HV_{0.2}$ (25°C)
				513 ± 48 $HV_{0.2}$ (300°C)

4.3.2 Sliding wear behavior

4.3.2.1 Friction and wear

Figure 4. 7 shows the coefficient of friction versus number of cycles for the tantalum oxide coatings at 25°C and 300°C. The **Figure 4. 7 (inset)** shows the friction behavior of the coatings during the break-in phase. The friction coefficient increased rapidly from 0.1 to 0. 9 in the first few cycles (running-in phase) at 25°C and henceforth remained constant throughout the test cycles (steady state) until the end of the test. On the other hand, the friction value was ~0.6 at 300°C in the beginning and then gradually increased up 0.8 at around 100 cycles, where it remained for the rest of the test (steady state). The fluctuations of the friction curve at 300°C was high compared to 25°C. However, at both temperatures, a stable coefficient of friction was reached after 100 cycles.

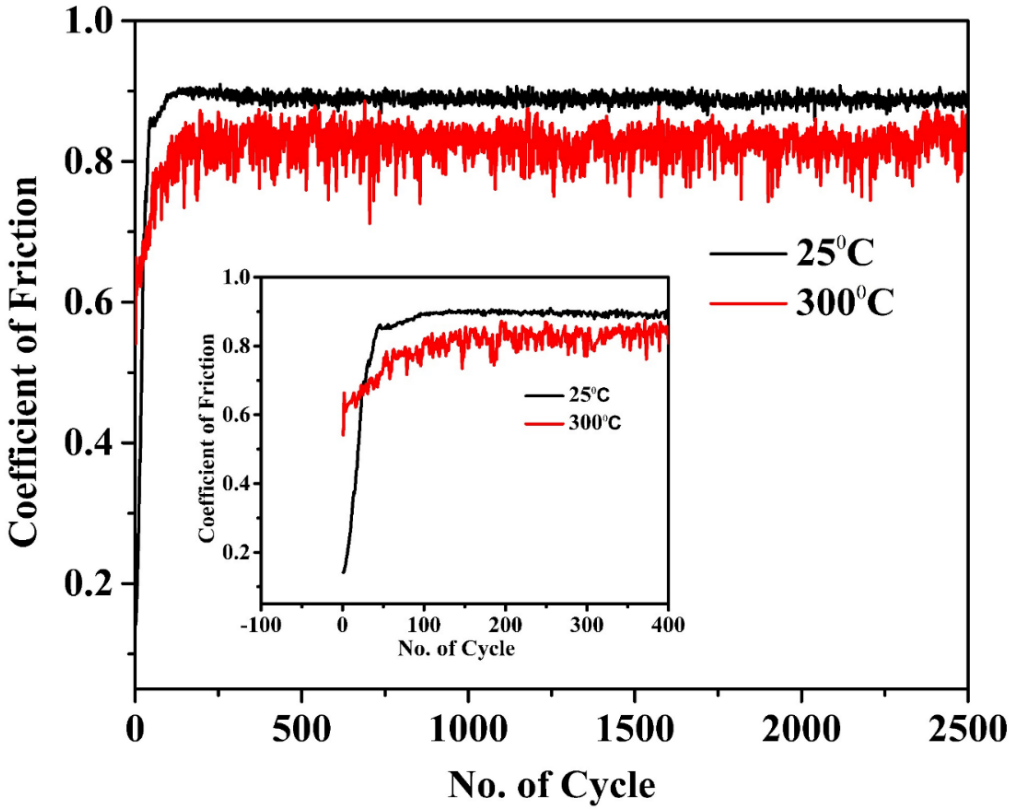

Figure 4. 7: Coefficient of friction of tantalum oxide coating at 25°C and 300°C

The wear depths and wear rates of tantalum oxide coatings (at 25°C and 300°C) are shown in **Figure 4. 8 (a)** and **Figure 4. 8 (b)** respectively. The wear depth of the worn coatings after testing at 25°C was 40 µm and 18 µm at 300°C [**Figure 4. 8 (a)**]. The high wear led to the generation of high amount of wear debris at 25°C, which was accumulated on the edge of wear track, and appeared as high peaks on the sides of the wear track [**Figure 4. 8 (a)**]. Similarly, the low pile up at the edge of the wear track at 300°C corresponded to low generation of wear debris during sliding [**Figure 4. 8 (a)**]. Additionally, the wear track at 300°C (1.4 mm) was comparatively or slightly wider than that at 25°C (1.2 mm). The corresponding wear rates of the tantalum oxide coatings are shown in **Figure 4. 8 (b)**. The specific wear rate of the coating at 300°C (54×10^{-5} mm^3/Nm) was less than 50% compared to that at 25°C (123×10^{-5} mm^3/Nm).

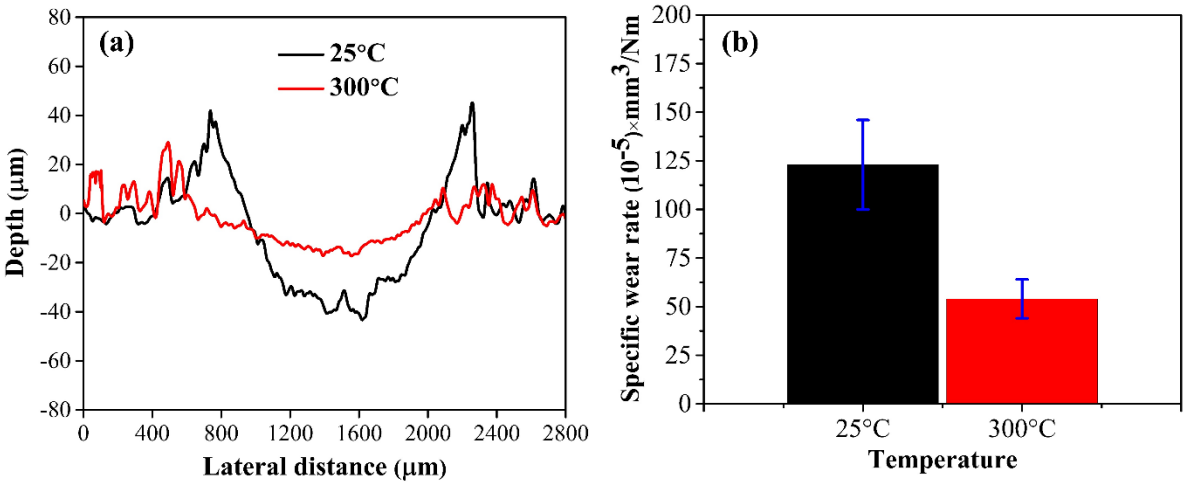

Figure 4. 8: (a) Depth vs. lateral distance and (b) corresponding wear rate of tantalum oxide coatings at 25°C and 300°C

4.3.2.2 Worn surface morphologies

The SEM images of the wear tracks after sliding at 25°C and 300°C are shown in **Figure 4. 9**. Apparently, the figures showed that the width of the wear tracks at 300°C was slightly higher than at room temperatures. Also, the worn surfaces at elevated temperatures were quite smoother than in atmospheric conditions [**Figure 4. 9**]. At 25°C, the presence of fragments, cracks and potentially embedded debris particles appeared throughout the worn surfaces, which is generally an indication of a lack of tribofilm formation [54] [**Figure 4. 9 (b)**]. EDS point (i.e., shown in '+') and area (not shown) analysis were performed on the wear tracks at room temperatures [**Figure 4. 9 (b)**]. The average atomic percentage (Ta = 28±1.49 at% and O = 72±1.49 at%) of tantalum oxide is shown with EDS in **Figure 4. 9 (c)**.

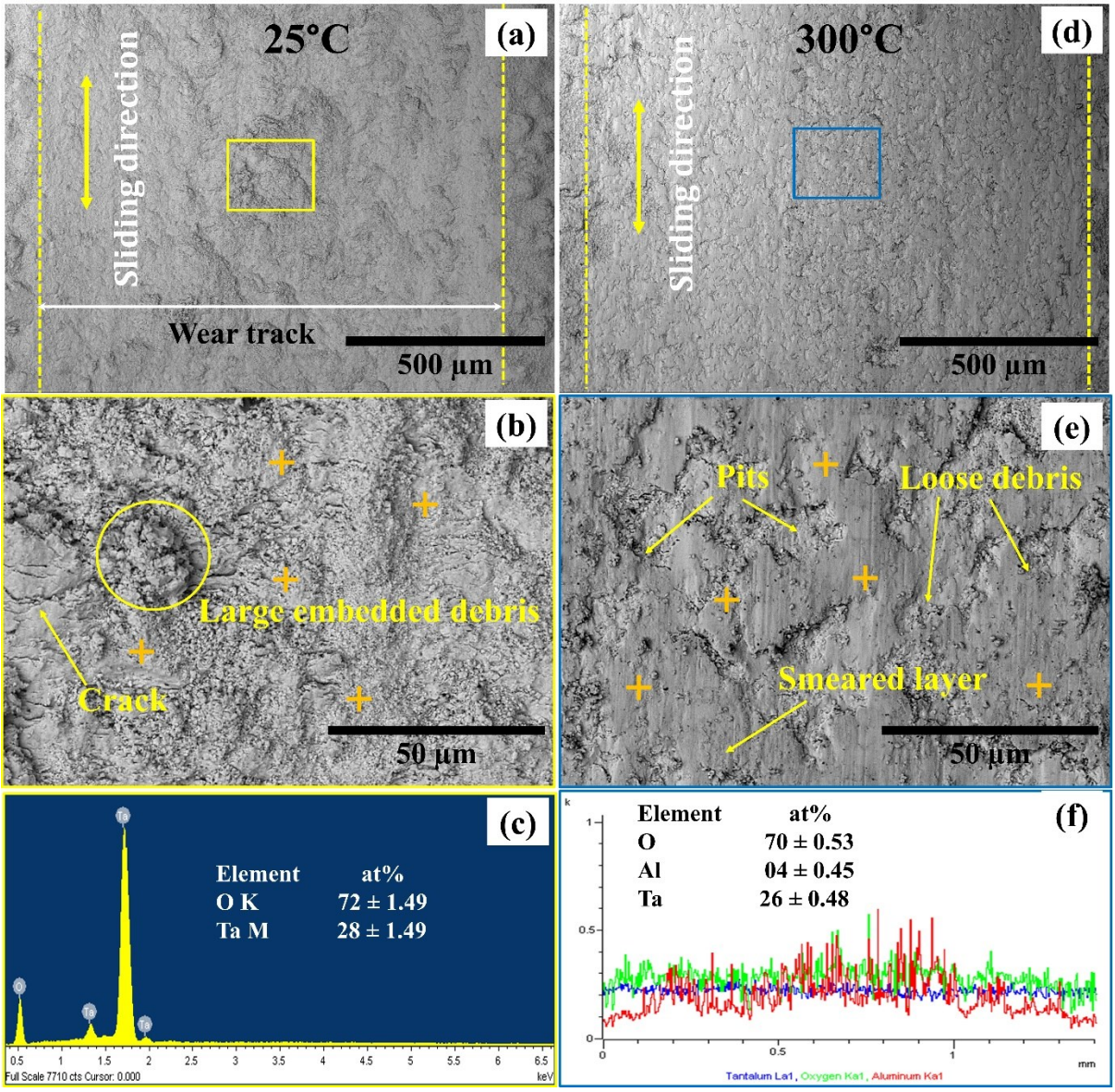

Figure 4. 9: The SEM wear tracks of tantalum oxide coatings and the corresponding EDS analysis at **(a-c)** 25°C and **(d-e)** 300°C. (+ indicates the EDS point)

At 300°C, smearing, pits, and some loose wear debris were observed on the worn surfaces [**Figure 4. 9 (e)**]. Furthermore, a continuous smeared smooth layer with some grooves (i.e., due to plowing) was apparent on the worn surface. Similarly, to the wear track developed at 25°C, the EDS point [shown in '+' orange] and area (not shown) analysis were also performed on the wear tracks at 300°C. This analysis showed a significant amount of aluminium on the worn surfaces. In order to see the distribution of the aluminium, an EDS line scan was performed on the middle of the wear track perpendicular to the sliding direction [**Figure 4. 9 (f)**]. The distribution of Ta (26±0.48 at%) and O (70±0.53 at%) was uniform but the presence of Al was higher in the middle of the wear track and significantly reduces towards the edges of

the wear track [**Figure 4. 9 (f)**]. The aluminium concentration was present due to wear of the Al_2O_3 counterface during sliding.

XPS depth profiles on the unworn and worn surfaces after sliding at 25°C and 300°C were performed to provide more information on the elemental variations, as shown in **Figure 4. 10**. It was shown that the number of different suboxides of tantalum oxides increased with increasing the sputtering time. This could be due to the depletion of O atoms and the temporary generation of O vacancies. It should be pointed out that this may also be due to the Ar^+ bombardment on the surface of tantalum oxide coating [53]. After a sputtering time of 140 seconds, six doublets can be observed corresponding to the Ta^0, Ta^{1+}, Ta^{2+}, Ta^{3+}, Ta^{4+}, and Ta^{5+} states with binding energies 20.6 eV, 21.4 eV, 23.9 eV, 25.5 eV, 25.2 eV and 26.1 eV, respectively. Additionally, the XPS analysis showed the behavior of oxygen (O1) and deficient oxygen (O2) as a function of the sputtering time. The atomic concentration was nearly identical for the unworn and worn surface at elevated temperatures. However, a variation of the oxygen states associated with tantalum oxides or suboxides was observed on the worn surface at 25°C when compared to the unworn surface at 25°C. In addition, the presence of an aluminium peak (associated with alumina) was detected on the surface and near-surface regions due to the counterface's wear (Al_2O_3).

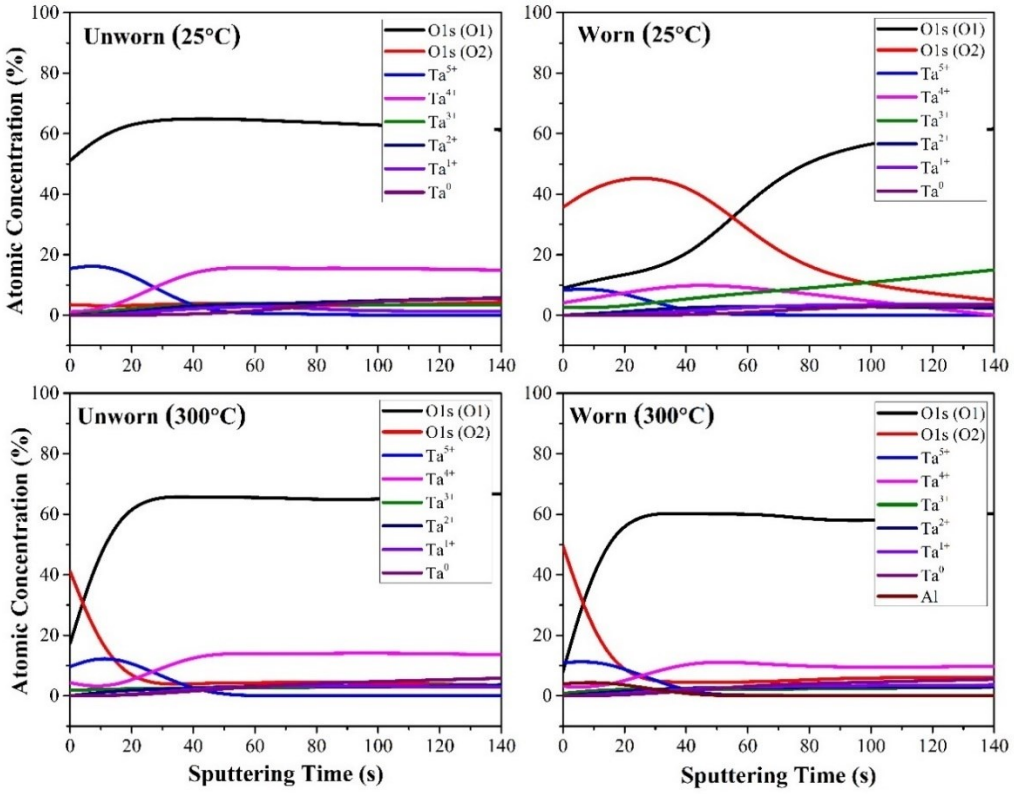

Figure 4. 10: XPS depth profiles of unworn and worn surfaces of tantalum oxide coatings at 25°C and 300°C

4.3.2.3 Subsurface microstructure

SEM imaging of the wear track cross-section after the wear tests at 25°C and 300°C is shown in **Figure 4. 11**. The cross-sections were performed in the middle of the wear tracks perpendicular to the sliding directions. At 25°C, the cross-section of the wear tracks appeared with cracks, brittle fractures, detachments of the top layers of coatings after the sliding tests [**Figure 4. 11 (a, b)**]. The brittle fractures and the detachment of the coatings as a large debris could show as the large, embedded debris particles that appeared throughout the SEM worn surfaces [**Figure 4. 9 (a, b)**]. On the other hand, no evident cracks were observed on the cross-section of the wear tracks after wear tests at 300°C [**Figure 4. 11 (c, d)**], which could be due to the more ductile behavior of the oxide [55]. This smooth wear track cross-sections can be corelated with the smooth and continuous smeared layer of the wear track surfaces [**Figure 4. 9 (a, b)**].

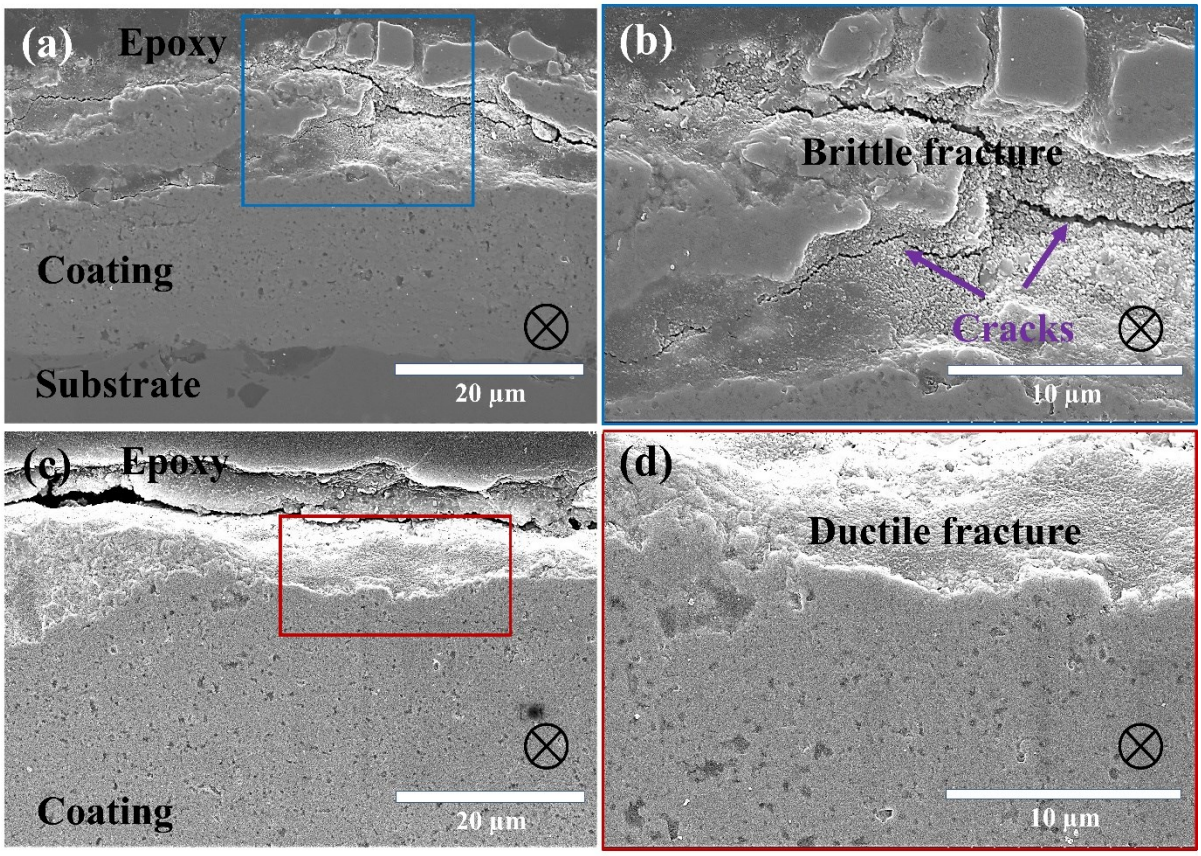

Figure 4. 11: The SEM wear tracks cross-section of tantalum oxide coatings after sliding tests at **(a-b)** 25°C and **(c-d)** 300°C. ⊗-indicates sliding direction.

4.3.2.4 Sliding counterface

SEM images of alumina counterball after sliding at 25°C and 300°C are shown in **Figure 4. 12**. The transfer of the tantalum oxide appeared in a more restricted area at 25°C [**Figure 4. 12 (a)**]. On the other hand, Al_2O_3 counterball for the high-temperature tests appeared to have a higher amount of wear with a large contact area [**Figure 4. 12 (b)**]. The average values of EDS point analysis at different locations on the transfer film indicated the elements Ta (~ 18 at%) and O (~ 72 at%) of the tantalum oxide coatings as well as Al (~ 10 at%), which was from Al_2O_3 ball. Interestingly, there were no differences in the compositional elements observed at 25°C and 300°C [**Figure 4. 12 (c, d)**].

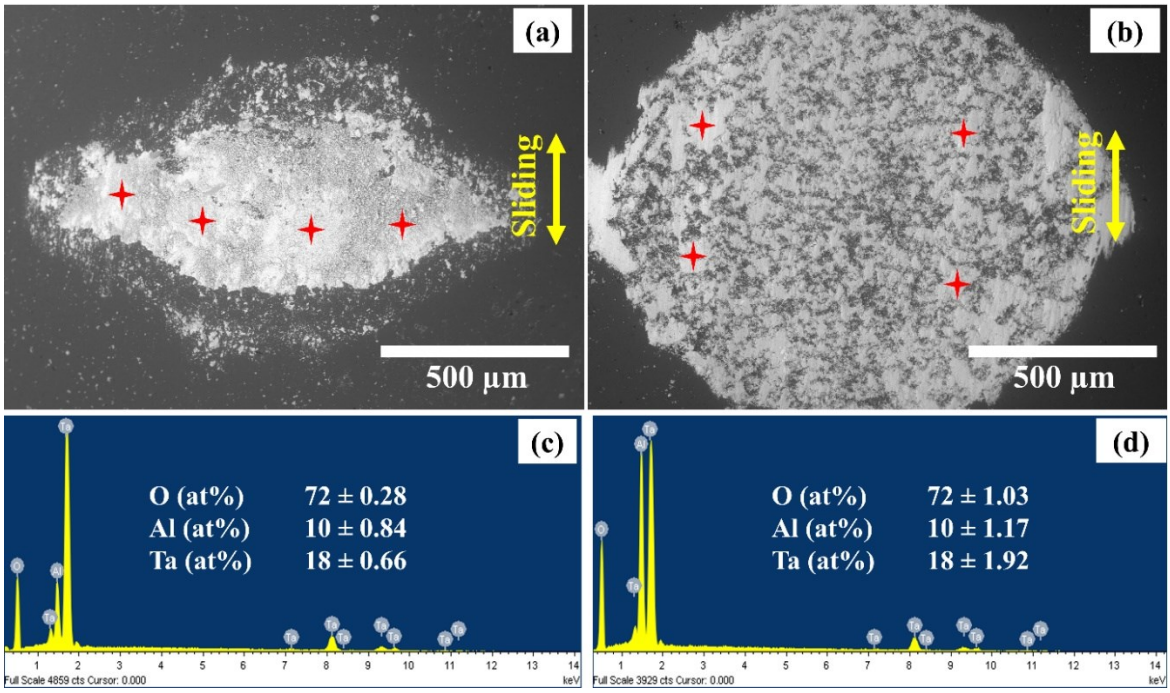

Figure 4. 12: The SEM images of counterball Al_2O_3 and corresponding EDS results at **(a, c)** 25°C and **(b, d)** 300°C. The star points indicate the EDS analysis.

The wear of the alumina counterball is shown in **Table 4. 4**. The calculated wear rate of the worn Al_2O_3 counterball was 10×10^{-6} mm^3/Nm at 25°C and 36×10^{-6} mm^3/Nm at 300°C. The high concentric contact area at 300°C that appeared in **Figure 4. 12 (b)** corresponded to the comparatively wider wear depth in **Figure 4. 8 (a)** and **Figure 4. 9 (d)**. It is possible that the ball wears out at the beginning of the sliding and subsequently builds up the transfer film [**Figure 4. 12 (a, b)**]. Similar behavior of the Al_2O_3 counterface wear has been observed against atmospheric plasma sprayed ZrO_2-5CaO and TiO_2-45Cr_2O_3 coatings [56,57]. The high local contact temperature during sliding could be the reasons of high wear of the alumina counterball at 300°C.

Table 4. 4: Wear rate of counterface Al_2O_3 against tantalum oxide coatings at 25°C and 300°C after dry sliding wear testing.

Testing Temperature	Counterface Wear Rate×10^{-6} (mm^3/Nm)
25°C	10 ± 7.33
300°C	36 ± 4.30

4.4 Discussions

4.4.1 Coating characteristics

A dense microstructure of tantalum oxide coating was produced by means of the radial injection SPS process [**Figure 4. 5 (a, b)**]. The smaller nozzle size (5 mm) and the optimization of the spraying parameters such as the spray distance (30 mm), plasma gas (Ar/He), and power (24 kW), all played a significant role in producing a dense microstructure [36,58]. Consequently, the final coatings comprised of fully dispersed, broken up, and semi-molten agglomerated particles [**Figure 4. 5 (c)**]. Throughout spraying, the particles were in a molten state and impacted onto the substrate at a relatively high velocity (i.e., 550m/sec), resulting in fully dispersed particles (i.e., splat). The broken-up splats may have resulted from evaporation during spraying due to the relatively low evaporation temperature of tantalum oxide. A similar behavior has also been previously reported for the SPS process [59].

The ECCI images of the tantalum oxide coating revealed grain sizes ranging from 150 nm to 340 nm **[Figure 4. 6]**. This indicates the nanocrystalline microstructure of the coatings, which is typical for SPS-deposited coatings. This microstructure can be explained by the formation of thin splats on the substrate or on already deposited material [32].

The microhardness of the tantalum oxide coating was 595 ± 41 $HV_{0.2}$ in atmospheric temperatures, which is comparable to previously published literature on tantalum oxides [60,61]. However, the microhardness of the SPS coatings at 300°C (513 ± 48 $HV_{0.2}$) was approximately 15% lower compared to that at 25°C (595 ± 41 $HV_{0.2}$) [**Table 4. 3**]. The decrement of hardness at high temperatures has also been previously observed with other oxides and can possibly be explained by the softening effect [62].

4.4.2 Friction and wear mechanisms

The friction coefficient of the tantalum oxide coatings developed in this study was 0.9 at 25°C [**Figure 4. 7**]. This was consistent with the study performed by Stone, D. S., et al. [1], who showed that the friction value of tantalum oxide coatings produced by PVD was ~ 0.9 when tested at room temperature. In our study, however, the friction coefficient at room temperature was initially lower (i.e., within the first few cycles) and then increased upon further sliding. The low friction during the early stages of the testing can possibly be attributed to the presence of surface contaminants and, consequently decreased amount of adhesion [63]. Upon further sliding, the contamination layers and elements were removed from the surface, which could increase the amount of adhesion and consequently increase the friction coefficient [43]. In addition, more debris particles were generated and consequently, entrapped particles can further increase the friction. This friction coefficient behavior was consistent with the ones observed with other oxides in literature (i.e., Al_2O_3 [50], TiO_2 [64], Cr_2O_3 [65], and ZrO_2-$3Y_2O_3$ [66]).

At elevated temperatures, the friction coefficient of the tantalum oxide coatings was slightly lower. This is consistent with the behavior observed for tantalum oxide coatings deposited by PVD when tested at elevated temperatures (i.e., 350°C) [1]. The reduction of the friction coefficient can be explained by the softening of the coatings (i.e., low shear strength) [1,14,15], which correlates well with the hardness reduction (i.e., from 595 ± 41 $HV_{0.2}$ to 513 ± 48 $HV_{0.2}$) at 300°C [**Table 4. 3**]. Furthermore, a smeared or continuous smooth layer [**Figure 4. 9 (e)**] was formed on the worn surface at elevated temperatures, which could have experienced ductile deformation and consequently reduced friction [55]. It should be noted that the testing temperature (i.e., 300°C) was relatively low however, taking into consideration the high frictional heating, in part due to the low thermal conductivity of tantalum oxide (i.e., thermal conductivity of tantalum oxide is 5 W/m.K. [67]) at high testing temperatures [46], the local contact temperature during sliding was significantly higher. Thus, the combination of high contact temperature and low shear strength promoted the easier formation of a continuous smooth layer resulting in steady-state conditions (i.e., lower friction compared to room temperature testing). In some cases, the presence of Magnéli's phases or substoichiometric oxides can reduce the friction coefficient [68], which also correlates well with the XPS analysis of the worn surface at elevated temperature, where a thin layer of suboxides was observed [**Figure 4. 10**].

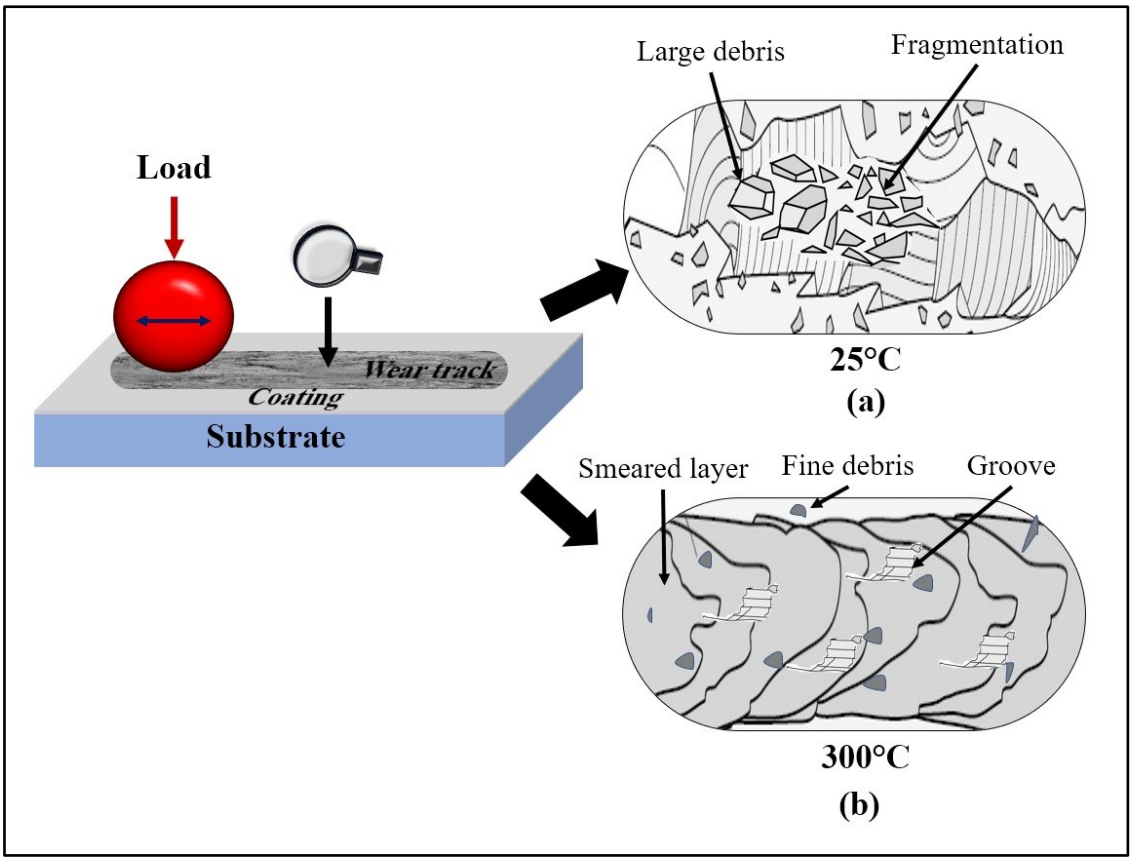

Figure 4. 13: Schematic of wear mechanisms of tantalum oxide coatings at (a) 25°C and (b) 300°C

Based on the ***ex-situ*** analysis, a schematic of wear mechanisms of tantalum oxide coatings at 25°C and 300°C was drawn and shown in **Figure 4. 13**. The higher wear rate at 25°C [**Figure 4. 8**] can be attributed to the lack of a tribofilm formation and the presence of higher amount of debris particles as well as brittle fracture **[see Figure 4. 13 (a)]**, which could have contributed to two or three body abrasion. This is consistent with the XPS analysis on the worn surface at room temperature revealing the presence of a thicker suboxide layer, which could be brittle under these conditions. Crack formation and brittle behavior of ceramics at room temperature have been previously reported to accelerate the detachment of wear fragments during sliding and generate high wear debris [69]. A similar behavior has also been previously observed for plasma-sprayed alumina coatings [50,70,71], where brittle fracture and abrasive grooving were the main wear mechanisms in their findings. In addition, brittle cracks and debris detachment for tribologically induced CoO glaze layer of Haynes 25 at a room to 200°C has been previously observed by Viat et al. [72], which resulted in relatively high wear rates.

At elevated temperatures, due to potentially increased cohesion and more ductile behavior of the ceramic coating, the asperity contacts cause plastic flow and displacement of material rather than fracture, resulting in a smeared layer on the worn surfaces [**Figure 4. 13 (b)**] and

consequently lower wear rates [43]. Low wear rates of other oxides (i.e., CoO and mixed CoO & Cr_2O_3) have also been previously observed and were attributed to their more ductile behavior at elevated temperatures (400°C and above) [72,73]. However, further characterization needs to be performed to fully understand the brittle to ductile behavior of this tantalum oxide coating. Interestingly, the wear on the Al_2O_3 counterface was higher for the tests performed at elevated temperatures [**Figure 4. 12 (b)**]. This can be explained by the relatively high contacting temperatures under these conditions. It should be noted that the presence of alumina on the surface of the wear tracks at elevated temperatures **[Figure 4. 9 (d-f); Figure 4. 10 (Worn (300°C)]** could have also assisted in reducing the wear during sliding [14].

4.5 Conclusions

A radial injection SPS process was utilized to produce dense tantalum oxide coatings by optimizing the spray parameters such as nozzle size, spray distance, plasma gas compositions, and plasma power. It was observed that the friction coefficient of tantalum oxide slightly decreased with increasing temperature (i.e., 0.9 at 25°C and 0.8 at 300°C). Similarly, the tantalum oxide coating showed significantly lower wear rates at 300°C (54×10^{-5} mm^3/Nm) when compared to 25°C (123×10^{-5} mm^3/Nm). This can be attributed to the more ductile behavior of the ceramic coating at elevated temperatures resulting in a displacement of material rather than its removal. The higher frictional heating led to the formation of a smeared or continuous smooth layer on the wear tracks with a stable transfer film on the counterface and consequently decreased wear at 300°C. Thus, based on the results obtained in this study, the nanocrystalline tantalum oxide coatings could be a salient solution in improving wear resistance in demanding conditions. However, the influence of spraying parameters on the coating microstructure and tribological characteristics need to be further investigated under various testing conditions.

4.6 References

[1] Stone DS, Harbin S, Mohseni H, Mogonye JE, Scharf TW, Muratore C, et al. Lubricious silver tantalate films for extreme temperature applications. Surf Coatings Technol 2013;217:140–6. https://doi.org/10.1016/j.surfcoat.2012.12.004.

[2] Pauschitz A, Roy M, Franek F. Mechanisms of sliding wear of metals and alloys at elevated temperatures. Tribol Int 2008;41:584–602. https://doi.org/10.1016/j.triboint.2007.10.003.

[3] Chupp RE, Hendricks RC, Lattime SB, Steinetz BM. Sealing in turbomachinery. J Propuls Power 2006;22:313–49. https://doi.org/10.2514/1.17778.

[4] Stoyanov P, Harrington KM, Frye A. Insights into the Tribological Characteristic of Cu-Based Coatings Under Extreme Contact Conditions. Jom 2020;72:2191–7. https://doi.org/10.1007/s11837-020-04087-7.

[5] Patel P, Roy A, Sharifi N, Stoyanov P, Chromik RR, Moreau C. Tribological Performance of High-Entropy Coatings (HECs): A Review. Materials (Basel) 2022;15:3699.

[6] Aouadi SM, Gao H, Martini A, Scharf TW, Muratore C. Lubricious oxide coatings for extreme temperature applications: A review. Surf Coatings Technol 2014;257:266–77. https://doi.org/10.1016/j.surfcoat.2014.05.064.

[7] Yang JF, Jiang Y, Hardell J, Prakash B, Fang QF. Influence of service temperature on tribological characteristics of self-lubricant coatings: A review. Front Mater Sci 2013;7:28–39. https://doi.org/10.1007/s11706-013-0190-z.

[8] Peterson MB, Calabrese SB, Stupp B, Circle M, Quincy N. Lubrication with naturally ocurring double oxide films. Wear Sci Inc Arnold MD 1982.

[9] Peterson MB, Group T. Wear-resisting oxide films for 900°C. J Mater Sci Technol 1997;13:99–106.

[10] Peterson MB, Florek JJ, Lee RE. Sliding characteristics of metals at high temperatures. ASLE Trans 1960;3:101–9. https://doi.org/10.1080/05698196008972392.

[11] Peterson MB, Murray SF, Florek JJ. Consideration of lubricants for temperatures above 1000 f. ASLE Trans 1959;2:225–34. https://doi.org/10.1080/05698195908972374.

[12] Ouyang JH, Sasaki S. Unlubricated friction and wear behavior of low-pressure plasma-sprayed ZrO2 coating at elevated temperatures. Ceram Int 2001;27:251–60. https://doi.org/10.1016/S0272-8842(00)00072-9.

[13] Shi P, Yi G, Wan S, Sun H, Feng X, Pham ST, et al. High temperature tribological performance of nickel-based composite coatings by incorporating multiple oxides (TiO2–ZnO–MoO3). Tribol Int 2021;155:1–11. https://doi.org/10.1016/j.triboint.2020.106759.

[14] Erdemir A. A crystal-chemical approach to lubrication by solid oxides. Tribol Lett 2000;8:97–102. https://doi.org/10.1023/a:1019183101329.

[15] Erdemir A. A crystal chemical approach to the formulation of self-lubricating nanocomposite coatings. Surf Coatings Technol 2005;200:1792–6.

[16] Dimitrov V, Komatsu T. Classification of simple oxides: a polarizability approach. J Solid State Chem 2002;163:100–12.

[17] Prakash B, Celis J-P. The lubricity of oxides revised based on a polarisability approach. Tribol Lett 2007;27:105–12.

[18] Erdemir A. A crystal chemical approach to the formulation of self-lubricating nanocomposite coatings. Surf Coatings Technol 2005;200:1792–6. https://doi.org/10.1016/j.surfcoat.2005.08.054.

[19] Prakash B, Celis JP. The lubricity of oxides revised based on a polarisability approach. Tribol Lett 2007;27:105–12. https://doi.org/10.1007/s11249-007-9223-z.

[20] Myers DL, Kulis MJ, Horwath JP, Jacobson NS, Fox DS. Interactions of Ta2O5 with water vapor at elevated temperatures. J Am Ceram Soc 2017;100:2353–7.

[21] Moldovan M, Weyant CM, Johnson DL, Faber KT. Tantalum Oxide Coatings as Candidate Environmental Barriers. J Therm Spray Technol 2004;13:51–6. https://doi.org/10.1361/10599630418103.

[22] Rahmati B, Sarhan AAD, Basirun WJ, Abas WABW. Ceramic tantalum oxide thin film coating to enhance the corrosion and wear characteristics of Ti-6Al-4V alloy. J Alloys Compd 2016;676:369–76. https://doi.org/10.1016/j.jallcom.2016.03.188.

[23] Ding Z, Wang Y, Zhou Q, Ding Z, Wu Y, Zhu Y, et al. The preparation and properties of multilayer Cu-MTa2O5 composite coatings on Ti6Al4V for biomedical applications. Nanomaterials 2019;9. https://doi.org/10.3390/nano9101498.

[24] Mulivor AW, Mann AB, Searson PC, Weihs TP. Hardness and wear of electrochemically grown tantalum oxide. Mater Res Soc Symp - Proc 1998;505:211–6. https://doi.org/10.1557/proc-505-211.

[25] Zhang H, Tang H, Yue TM. Fabrication of Ta2O5 reinforced Ta-based coatings on Ta substrates by laser cladding. Int J Met Mater Eng 2018;4.

[26] Qin W, Fu L, Zhu J, Yang W, Li D, Zhou L. Applied Surface Science Tribological properties of self-

lubricating Ta-Cu films. Appl Surf Sci 2018;435:1105–13. https://doi.org/10.1016/j.apsusc.2017.11.220.
[27] Zhu R, Zhang P, Yu Z, Yan H, Li S, Wu D, et al. Microstructure and wide temperature range self-lubricating properties of laser cladding NiCrAlY/Ag2O/Ta2O5 composite coating. Surf Coatings Technol 2020;383. https://doi.org/10.1016/j.surfcoat.2019.125248.
[28] Stone DS, Gao H, Chantharangsi C, Paksunchai C, Bischof M, Martini A, et al. Reconstruction mechanisms of tantalum oxide coatings with low concentrations of silver for high temperature tribological applications. Appl Phys Lett 2014;105:1–6. https://doi.org/10.1063/1.4901817.
[29] Zheng J, Wen K, Liu Y, Gao L, Ma Z, Diao X. Laser irradiation behavior of plasma-sprayed tantalum oxide coatings. Ceram Int 2020;46:3875–81. https://doi.org/10.1016/j.ceramint.2019.10.113.
[30] Kozerski S, Łatka L, Pawlowski L, Cernuschi F, Petit F, Pierlot C, et al. Preliminary study on suspension plasma sprayed ZrO2+8wt.% Y2O3 coatings. J Eur Ceram Soc 2011;31:2089–98. https://doi.org/10.1016/j.jeurceramsoc.2011.05.014.
[31] Pawlowski L. Suspension and solution thermal spray coatings. Surf Coatings Technol 2009;203:2807–29. https://doi.org/10.1016/j.surfcoat.2009.03.005.
[32] Darut G, Ben-Ettouil F, Denoirjean A, Montavon G, Ageorges H, Fauchais P. Dry sliding behavior of sub-micrometer-sized suspension plasma sprayed ceramic oxide coatings. J Therm Spray Technol 2010;19:275–85. https://doi.org/10.1007/s11666-009-9415-1.
[33] Waldbillig D, Kesler O. The effect of solids and dispersant loadings on the suspension viscosities and deposition rates of suspension plasma sprayed YSZ coatings. Surf Coatings Technol 2009;203:2098–101. https://doi.org/10.1016/j.surfcoat.2008.11.027.
[34] Toma F-L, Potthoff A, Barbosa M. Microstructural characteristics and performances of Cr2O3 and Cr2O3-15% TiO2 S-HVOF coatings obtained from water-based suspensions. J Therm Spray Technol 2018;27:344–57.
[35] Aziz B, Gougeon P, Moreau C. Temperature measurement challenges and limitations for in-flight particles in suspension plasma spraying. J Therm Spray Technol 2017;26:695–707.
[36] Waldbillig D, Kesler O. Effect of suspension plasma spraying process parameters on YSZ coating microstructure and permeability. Surf Coatings Technol 2011;205:5483–92. https://doi.org/10.1016/j.surfcoat.2011.06.019.
[37] Rezania O. Anelastic Behavior of Suspension Plasma Sprayed Ceramic Coatings. MASc Thesis 2016.
[38] Aghasibeig M, Tarasi F, Lima RS, Dolatabadi A, Moreau C. A Review on suspension thermal spray patented technology evolution. J Therm Spray Technol 2019;28:1579–605.
[39] Fauchais P, Montavon G, Lima RS, Marple BR. Engineering a new class of thermal spray nano-based microstructures from agglomerated nanostructured particles, suspensions and solutions: An invited review. J Phys D Appl Phys 2011;44. https://doi.org/10.1088/0022-3727/44/9/093001.
[40] Aubreton J, Elchinger MF, Fauchais P, Rat V, André P. Thermodynamic and transport properties of a ternary Ar-H2-He mixture out of equilibrium up to 30 000 K at atmospheric pressure. J Phys D Appl Phys 2004;37:2232–46. https://doi.org/10.1088/0022-3727/37/16/004.
[41] EN ISO 4516: 2002. Metallic and Other Inorganic Coatings - Vickers and Knoop Microhardness Tests. 2004.
[42] ASTM-E2109-01. Standard test methods for determining area percentage porosity in thermal sprayed coatings. 2014.
[43] Patel P, Alidokht SA, Sharifi N, Roy A, Harrington K, Stoyanov P, et al. Microstructural and Tribological Behavior of Thermal Spray CrMnFeCoNi High Entropy Alloy Coatings. J Therm Spray Technol 2022:1–17.
[44] Vardelle PF and A. Solution and Suspension Plasma Spraying of Nanostructure Coatings. Adv Plasma Spray Appl 2012:149–88.
[45] Perez I, Enríquez Carrejo JL, Sosa V, Perera FG, Farias Mancillas JR, Elizalde Galindo JT, et al. Evidence for structural transition in crystalline tantalum pentoxide films grown by RF magnetron sputtering. J Alloys Compd 2017;712:303–10. https://doi.org/10.1016/j.jallcom.2017.04.073.
[46] Song WD, Ying JF, He W, Zhuo VYQ, Ji R, Xie HQ, et al. Nano suboxide layer generated in Ta2O5 by Ar+ ion irradiation. Appl Phys Lett 2015;106:2–6. https://doi.org/10.1063/1.4906395.
[47] Simpson R, White RG, Watts JF, Baker MA. XPS investigation of monatomic and cluster argon ion sputtering of tantalum pentoxide. Appl Surf Sci 2017;405:79–87.
[48] Dupin J-C, Gonbeau D, Vinatier P, Levasseur A. Systematic XPS studies of metal oxides, hydroxides and peroxides. Phys Chem Chem Phys 2000;2:1319–24.
[49] Tejero-Martin D, Bai M, Mata J, Hussain T. Evolution of porosity in suspension thermal sprayed YSZ thermal barrier coatings through neutron scattering and image analysis techniques. J Eur Ceram Soc 2021;41:6035–48.
[50] Goel S, Björklund S, Curry N, Wiklund U, Joshi S V. Axial suspension plasma spraying of Al2O3 coatings for superior tribological properties. Surf Coatings Technol 2017;315:80–7.

https://doi.org/10.1016/j.surfcoat.2017.02.025.
[51] Zhao Y, Yu Z, Planche M-P, Lasalle A, Allimant A, Montavon G, et al. Influence of substrate properties on the formation of suspension plasma sprayed coatings. J Therm Spray Technol 2018;27:73–83.
[52] Richter A, Berger LM, Conze S, Sohn YJ, Vaßen R. Emergence and impact of Al2TiO5 in Al2O3-TiO2 APS coatings. IOP Conf Ser Mater Sci Eng 2019;480. https://doi.org/10.1088/1757-899X/480/1/012007.
[53] Perez I, Sosa V, Perera FG, Elizalde Galindo JT, Enríquez-Carrejo JL, Mani González PG. Effect of ion bombardment on the chemical properties of crystalline tantalum pentoxide films. Vacuum 2019;165:274–82. https://doi.org/10.1016/j.vacuum.2019.04.037.
[54] M.H.J. Surface effects in adhesion, friction, wear and lubrication. vol. 85. 1983. https://doi.org/10.1016/0043-1648(83)90069-8.
[55] Stachowiak GW, Batchelor AW. Engineering tribology. Butterworth-heinemann; 2013.
[56] Küçük Y. Effect of counter body on wear behavior of plasma-sprayed TiO2-45Cr2O3 coating. J Asian Ceram Soc 2021;9:214–29. https://doi.org/10.1080/21870764.2020.1863574.
[57] Küçük Y. Effect of counterbody on the dry sliding wear performance of plasma sprayed calcia-stabilized zirconia coating. Int J Refract Met Hard Mater 2020;92. https://doi.org/10.1016/j.ijrmhm.2020.105284.
[58] Rampon R, Marchand O, Filiatre C, Bertrand G. Influence of suspension characteristics on coatings microstructure obtained by suspension plasma spraying. Surf Coatings Technol 2008;202:4337–42.
[59] Fauchais P, Joulia A, Goutier S, Chazelas C, Vardelle M, Vardelle A, et al. Suspension and solution plasma spraying. J Phys D Appl Phys 2013;46:224015.
[60] Shcherbina OB, Palatnikov MN, Efremov V V. Mechanical properties of Nb2O5 and Ta2O5 prepared by different procedures. Inorg Mater 2012;48:433–8.
[61] Pierson HO. Handbook of chemical vapor deposition: principles, technology and applications. William Andrew; 1999.
[62] Amano T, Okazaki M, Takezawa Y, Shiino A, Takeda M, Onishi T, et al. Hardness of oxide scales on Fe-Si alloys at room-and high-temperatures. Mater. Sci. forum, vol. 522, Trans Tech Publ; 2006, p. 469–76.
[63] Derelizade K, Venturi F, Wellman RG, Kholobysov A, Hussain T. Wear performance of graphene nano platelets incorporated WC-Co coatings deposited by hybrid high velocity oxy fuel thermal spray. Wear 2021;482:203974.
[64] Normand B, Fervel V, Coddet C, Nikitine V. Tribological properties of plasma sprayed alumina–titania coatings: role and control of the microstructure. Surf Coatings Technol 2000;123:278–87.
[65] Su W, Niu S, Huang Y, Wang C, Wen Y, Li X, et al. Friction and wear properties of plasma-sprayed Cr2O3–BaCrO4 coating at elevated temperatures. Ceram Int 2022;48:8696–705.
[66] Liang B, Zhang G, Liao HL, Coddet C, Ding CX. Structure and tribological performance of nanostructured ZrO2-3 mol% Y2O3 coatings deposited by air plasma spraying. J Therm Spray Technol 2010;19:1163–70.
[67] Weyant CM, Faber KT, Almer JD, Guiheen J V. Residual stress and microstructural evolution in tantalum oxide coatings on silicon nitride. J Am Ceram Soc 2005;88:2169–76. https://doi.org/10.1111/j.1551-2916.2005.00396.x.
[68] Magnéli A. Structures of the ReO3-type with recurrent dislocations of atoms:homologous series' of molybdenum and tungsten oxides. Acta Crystallogr 1953;6:495–500.
[69] Alidokht SA, Manimunda P, Vo P, Yue S, Chromik RR. Cold spray deposition of a Ni-WC composite coating and its dry sliding wear behavior. Surf Coatings Technol 2016;308:424–34.
[70] Mahade S, Mulone A, Björklund S, Klement U, Joshi S. Incorporation of graphene nano platelets in suspension plasma sprayed alumina coatings for improved tribological properties. Appl Surf Sci 2021;570:151227.
[71] Erickson LC, Blomberg A, Hogmark S, Bratthäll J. Tribological characterization of alumina and silicon carbide under lubricated sliding. Tribol Int 1993;26:83–92.
[72] Viat A, Guillonneau G, Fouvry S, Kermouche G, Sao Joao S, Wehrs J, et al. Brittle to ductile transition of tribomaterial in relation to wear response at high temperatures. Wear 2017;392:60–8.
[73] Dreano A, Fouvry S, Guillonneau G. Understanding and formalization of the fretting-wear behavior of a cobalt-based alloy at high temperature. Wear 2020;452:203297.

Chapter 5

Enhanced Wear Resistance of Cobalt Oxide Over Nickel Oxide[4]

Abstract

Oxide-based coatings are being extensively investigated as potential solutions for high-temperature solid lubrication owing to their high thermal and chemical stability. Therefore, this study aimed to investigate the tribological behavior of the thermally sprayed CoO and NiO coatings. The dry sliding wear tests were conducted against the alumina counterface at room and high temperatures using a ball-on-disc tribometer. The results revealed that the friction and wear of CoO coatings decreased with increasing temperatures, while the NiO coatings showed opposite behaviors. *Ex-situ* (SEM/FIB, XPS) analysis revealed that the formation of thin amorphous nanocrystalline tribofilm decreased friction and wear at high temperatures. On the other hand, NiO high friction and wear at high temperatures were caused by the worn-out coatings, while at room temperatures, it showed the existence of brittle, cracked, and detached tribofilm on the wear track.

Keywords: *CoO, NiO, thermal spray, glaze layer, tribology*

[4] This chapter has been published as a research article in the *Tribology Letters*. **A. Roy**, V. Jalilvand, S. Mohammadkhani, P. Patel, A. Dolatabadi, L. Roue, D. Guay, R. R. Chromik, C. Moreau, P. Stoyanov. "Enhanced wear resistance of cobalt oxide over nickel oxide." *Tribology Letters* 71.3 (2023): 99.

5.1 Introduction

The performance of mechanical systems or machineries operating in demanding environments (e.g., power generation, transportation, materials processing, and aircraft engines) is often limited by the tribological behavior of employed materials and coatings [1–5]. Co and Ni-based superalloys are widely used in high-temperature tribological applications due to their excellent strength, creep, and fatigue resistance at high temperatures [6–10]. Additionally, these alloys generate wear debris during sliding, which oxidize, and sinter/consolidate within the contacting interfaces forming the so-called "glaze" layer and consequently reducing the wear [3,11,12]. However, this glaze/oxide formation is affected by various factors, including temperatures, sliding speed, applied load, the chemical nature of surfaces, etc. [13–15]. Dellacorte et al. [16] showed that a substantial reduction in friction appeared due to the formation of lubricious oxide layers when Co-based superalloy (i.e., Haynes 188) was sliding against Pt-coated MoRe at ~500°C. A similar observation was observed by Coskun et al. [17], who found that Co-based superalloys (i.e., Haynes 25, Haynes 188, Haynes 214) form Co oxides protective layer along with Ni, Cr, and W oxides against Hastelloy X at 540°C in sliding process. The process of glaze layer formation, spallation, and reformation by the load-bearing oxides during the sliding of Stellite 6 at 600°C was analyzed by Wood et al. [12]. The authors identified six stages of wear: (i) mixed oxide glaze formation, (ii) Co and Cr diffusion to the glaze layer and hence forming Co and Cr dominated oxide layers, (iii) oxygen diffusion to the glaze, (iv) spallation of the glaze, (v) reformation of the glaze, and (vi) elemental diffusion within the glaze. Similarly, Inman et al. [7,8] demonstrated the effect of sliding on glaze layer formation at 750°C for Nimonic 80A against Stellite 6. It was shown that low speed sliding (i.e., 0.314 m/s) resulted in the rapid development of a wear-resistant nano-structured Co/Cr/Ni oxide layer. In contrast, high speed sliding (i.e., 0.905 m/s) caused the formation of abrasive NiO and Cr_2O_3 debris. Furthermore, the authors concluded that lack of retention of a high amount of oxides led to loose abrasive wear debris and an increase in wear rate. In addition, Viat et al. [18] and Korashy et al. [19] showed cracks and a brittle nature of tribologically induced cobalt oxides glaze layer on Haynes 25 up to 200°C, which increased the friction and wear coefficient. A similar behavior has been recently observed by Munagala et al. [20] for their HVOF-sprayed Diamalloy 3001 coatings up to 350°C. They authors noticed the formation of cavity/cracks on the oxides tribolayer, and eventually, detachments of that layer led to an increment of wear rate at high temperatures. While the formation of mixed oxides on the wear tracks during sliding has shown to reduce the friction and wear for Co-

based alloys, researchers claimed that a significant contribution comes from the cobalt oxides glaze layer [21–24]. In addition, more detailed analysis has previously revealed that this cobalt oxide glaze layer is nanocrystalline [11,13,25] and some studies emphasized the presence of amorphous zones near the surface [13,26]. Similar results were also reported by Alixe et al. [27]. The authors showed that a thin 20 nm amorphous layer was present above the cobalt oxide glaze layer closer to the contacting interfaces, which improved the tribology of the Co-based alloy.

Similarly to Co-based alloys, Stott et al. [3] showed that the friction coefficient of nickel-based superalloys (i.e., Nimonic 75, Nimonic C263, Nimonic 108, and Incoloy 601) is reduced at high temperature (i.e., from 200°C to 800°C). This friction reduction could be due to the sintering of debris particles and formation of protective oxide (i.e., NiO, CoO, FeO, Cr_2O_3, $NiCr_2O_4$) layers on the wear track. In a similar study on nickel-based alloys, Laskowski et al. [28] observed the oxidation of the alloys at high temperatures (i.e., 500°C and 800°C). It was shown that the Inconel X-750 vs Rene 41 had the lowest friction coefficient (0.27) at 800°C. In contrast, the Inconel X-750 vs Inconel 909 showed the lowest pin wear (i.e., 2.84×10^{-6} mm^3/N-m) at 500°C due to the formation of tenacious and lubricious oxide (i.e., Ni-Cr oxide) film on the wear tracks.

Thus, the formation of oxides in the contacting interfaces of the cobalt and nickel-based superalloys has been shown to reduce friction and wear, with the main constituent oxides being cobalt oxide and nickel oxide. These oxides play a significant role on the tribological properties at different temperatures, as first predicted by Peterson [29]. The authors studied the frictional behavior of sintered cobalt and nickel oxides at different temperatures and showed that the cobalt oxide has improved lubricity compared to nickel oxide, even though they have similar rock salt crystal structure and ionic potential. However, it still remains unclear on what the driving mechanism is behind the difference in frictional behavior between the cobalt oxide and nickel oxide.

The main purpose of this study is to critically evaluate the friction and wear behavior of thermally sprayed CoO and NiO coatings at room temperature and high temperature. Emphasis is placed on providing a better understanding on the mechanisms behind the lubricating behavior. To the best of the author's knowledge, there is no data available on the tribological behavior of pure CoO and NiO coatings produced by such a thermal spraying process.

5.2 Experimental

CoO and NiO coatings were produced using HVOF and SPS, respectively. The HVOF process permits depositing the particles at a higher velocity and low inflight temperatures, which allows for forming a dense coating with limited porosity [30]. NiO coatings were produced using SPS (Mettech, Canada) due to the lack of availability of larger particle sizes necessary for producing coatings using HVOF. However, the SPS process also allows the formation of coatings with thin splats on the substrate, which can be beneficial for wear-resistance applications [31]. The substrate preparation for spraying, powder morphology and particle size details can be found in previously published articles [32,33]. Moreover, the details of the working principle of the HVOF and SPS process can be found in previously published literature by the authors and co-authors [30,34,35]. The spraying parameters of CoO and NiO coatings are explained in **Table 5. 1**.

Table 5. 1: Thermal spraying parameters used for depositing CoO and NiO coating

Deposition parameters	**(HVOF) Values**	**(SPS) Values**
Oxygen flow	217 lpm	--
Propylene flow	70 lpm	--
Air flow	167 lpm	--
Total gas flow	---	180 lpm
N_2 carrier gas flow	15 lpm	--
Ar gas flow rate	--	45 %
N_2 gas flow rate	--	45 %
H_2 gas flow rate	--	10 %
Current	--	180 amps
Power	--	78 kW
Feed rate	10 gm/min	45 ml/min
Spray distance	180 mm	50 mm
Number of passes	55	80

According to standard metallographic guidelines, the as-sprayed coatings were cold-mounted and polished to a final surface finish of 0.4 μm. The top surface and cross-section of the HVOF and SPS sprayed CoO and NiO coatings were analyzed using scanning electron microscopy (SEM). Likewise, the chemical composition was determined by energy-dispersive X-ray spectroscopy (EDS).

Dry sliding wear tests on the coatings were performed using a reciprocating ball-on-disc tribometer (Anton Paar TriTec SA, Switzerland). The details of the friction testing parameters (i.e., applied load of 5N, sliding speed of 3.14 cm/s, track length of 10 mm, and total sliding cycles of 5000) were adopted from the previously published article [30]. The friction testing parameters were selected based on the conditions of moving mechanical assemblies [30]. An alumina (McMaster-Carr, USA) ball with a diameter of 6.35 mm was used as the counterface. The wear testing was performed on the as-sprayed coatings (i.e., without further polishing the top surfaces of the coatings) at two different temperatures: room or atmospheric temperature (RT), and high temperature (HT). For the high-temperature (HT) testing, the samples (substrate/coating) were placed in the furnace, where they were heated to 450°C. The temperature recorded on the surface of the coating was around 300°C (i.e., using a thermocouple). In this study, the atmospheric and high temperatures friction testing conditions were denoted as RT and HT, respectively. Here, it can be mentioned that friction testing was also performed on the polished coatings (not shown here), but no significant changes in the friction results were noticed. Thus, further characterization was carried out on the as-sprayed coating wear tracks. The main motive behind choosing as-sprayed conditions was to make it applicable in practical applications without performing additional surface finishing processes, which will reduce the lead time and cost of the overall component. The consistency of the wear tests was checked by performing three repeats. The depth of wear tracks and wear volume of counterface alumina was measured using a 3D optical surface profiler (Zygo Corporation, USA). The wear area (mm^2) was calculated by integrating the wear track profiles, and the wear area was multiplied by track length (mm) to determine the wear volume (mm^3). The wear volume was normalized by dividing with applied load (N) and total sliding distance (m) to obtain the specific wear rate, k (mm^3/N.m.), as per the equation above [36].

$$k = \frac{V}{d.w} \qquad (5.1)$$

where, V = volume loss (mm^3), d is the total sliding distance (m), and w is the applied load (N).

To characterize the phases after tribological testing, Raman analysis was performed using an InVia spectrometer (Renishaw, UK) on the unworn and worn coatings with an Ar^+ ion (λ = 514.5 nm) laser source. The obtained Raman shift was matched with published literature data.

In order to reveal wear mechanisms, Focus Ion Beam Scanning (FIB) (FEI Helios 600 NanoLab 660, Thermo Fisher Scientific, USA) was also used to cut the specific position of the worn surface of CoO wear tracks. A Ga/Pt thin layer was deposited on the wear tracks to protect

the surface. An electron channeling contrast imaging (ECCI) was performed on this FIB cut to see the grain refinement and structure. ECCI on the wear tracks cross-sections was performed using a cold field emission SEM (SU8230, Hitachi, Japan) fitted with a photodiode BSE detector. Moreover, worn surfaces and manual cross-sections of wear tracks of NiO coatings were examined using an SEM equipped with energy-dispersive X-ray spectroscopy (EDS).

An X-ray photoelectron spectroscopy (XPS) was performed on as-sprayed CoO coatings and wear tracks after sliding tests at RT and HT with a VG ESCALAB 250 Xi (Thermo VG Scientific) Al K_α X-ray source set to 14 kV and 218 W. The coating's atomic concentration and chemical/oxidates states were evaluated with this XPS analysis.

5.3 Results

5.3.1 Coating characteristics

The XRD graph of CoO and NiO coatings is shown in **Figure 5. 1**. The diffraction peaks associated with 49.77° (200), 73.03° (220), 88.49° (311), 93.57° (222), and 114.6° (400) can be indexed to Powder Diffraction File (PDF) 04-004-8987 for CoO [**Figure 5. 1** (a)]. The NiO powder was partially reduced into metallic Ni for NiO coating [**Figure 5. 1** (b)]. The diffractions peaks (i.e., 43.54° (101), 50.72° (012), 74.53° (110), 90.50° (113), 95.90° (006)) for NiO and Ni (i.e., 52.18° (111), 61.02° (200), 91.76° (220), 114.69° (311) matched with PDF 00-044-1159, and PDF 00-004-0850, respectively. The reduction of the NiO into pure Ni could be due to the presence of hydrogen gas during spraying, which can be explained using the Ellingham diagram [37,38]. The different conditions/reasons for reducing NiO into metallic Ni have been previously described by co-authors elsewhere [33,39].

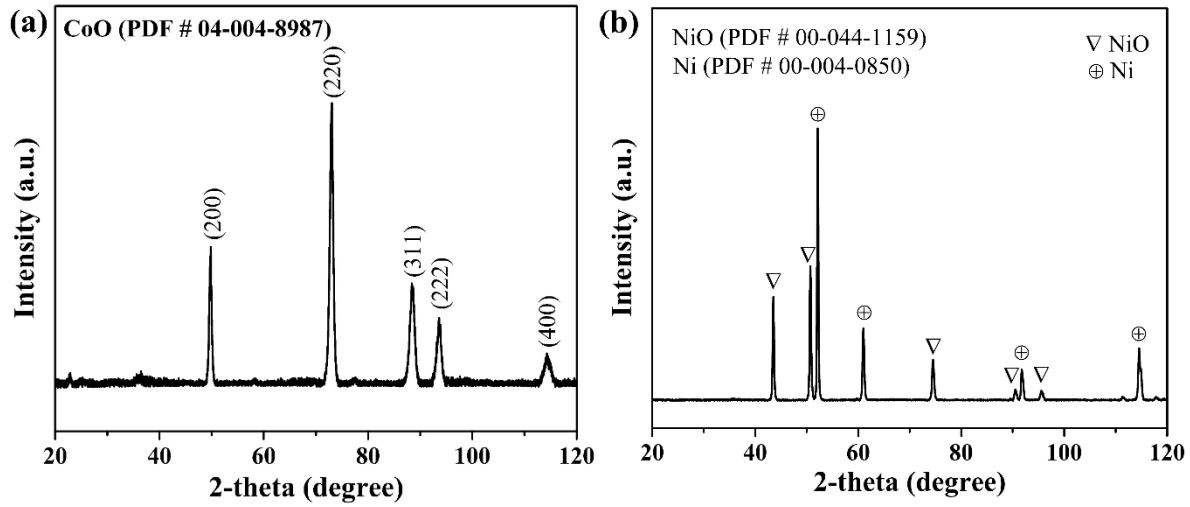

Figure 5. 1: XRD pattern of coatings prepared from (a) CoO and (b) NiO powder

SEM cross-sections of the CoO and NiO coatings are shown in **Figure 5. 2 (a)**, and **Figure 5. 2 (b),** respectively. The CoO coating revealed a denser microstructure which can possibly attributed to the high velocity of the in-flight particles of the HVOF process [30] [**Figure 5. 2 (a)**].

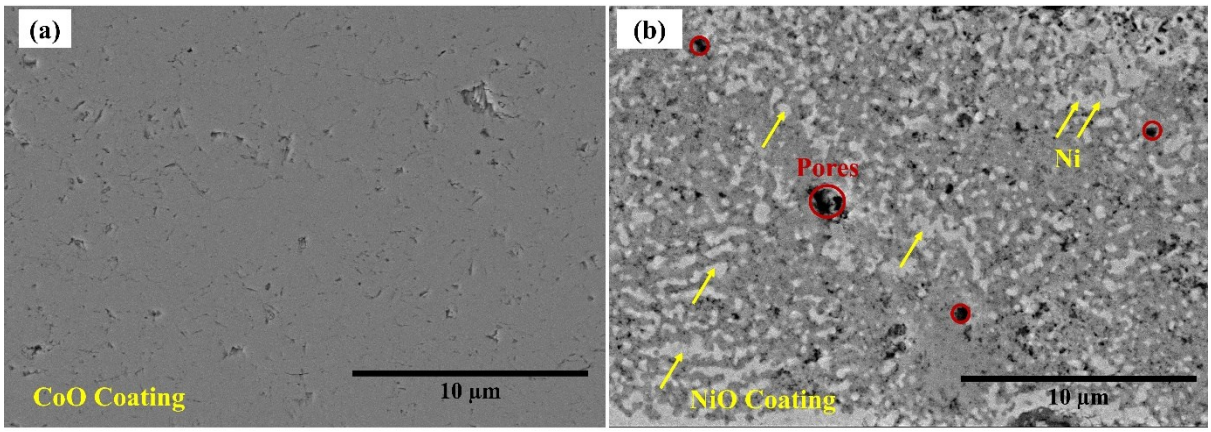

Figure 5. 2: SEM cross-section of (a) CoO and (b) NiO coating

On the other hand, an irregular surface with cauliflowers (not shown here) has been observed on the surface of the NiO coatings. The presence of pores (red circle) and metallic Ni (yellow arrows) in the NiO coatings is shown in [**Figure 5. 2 (b)**]. These results were further confirmed by the line scans on the coatings shown in **Figure 5. 3**. The high intensity on white zones indicated Ni, whereas the grey contrast showed the homogenous distribution of Ni and O, proving the NiO phase [**Figure 5. 3**]. The details of the coating's surface morphology and microstructures of CoO and NiO were described elsewhere [32,33].

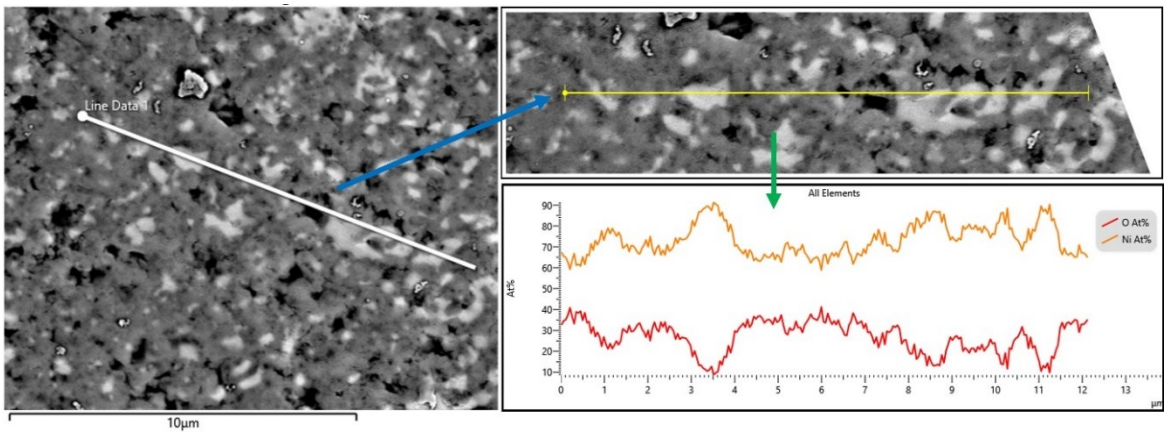

Figure 5. 3: Cross-sectional SEM line scan of NiO coating, showing the distribution of NiO and metallic Ni

5.3.2 Sliding wear behavior

5.3.2.1 Coefficient of friction and specific wear rate

The coefficient of friction vs number of cycles of CoO and NiO coatings is shown in **Figure 5. 4**. The coefficient of friction of the CoO and NiO coatings behaved quite differently at both, room temperature (RT) and high temperature (HT). At RT, the friction coefficient of the CoO and NiO was 0.63 and 0.45, respectively. On the other hand, at HT, the friction value of the CoO decreased to 0.5, whereas NiO friction coefficient increased (i.e., 0.7) up to 500 cycles and then dropped to 0.5. The sudden reduction of the friction coefficient of NiO at HT was due to the wear out of the coatings. In order to confirmed that further sliding wear testing was performed on NiO coating up to 500 and 1000 cycles at HT. It was found that the coatings worn out after 500 cycles which was verified by finding substrate elements (i.e., Fe, Cr, Mn, Si) using the SEM/EDS mapping on the worn surfaces [**Figure 5. 5**]. Furthermore, a small fraction of Al was found on the wear tracks which was from counterball Al_2O_3 [**Figure 5. 5**]. However, the friction coefficient of CoO and NiO at RT and CoO at HT maintained a steady state in all conditions except in the first few cycles, which could be due to the asperity polishing during sliding [40].

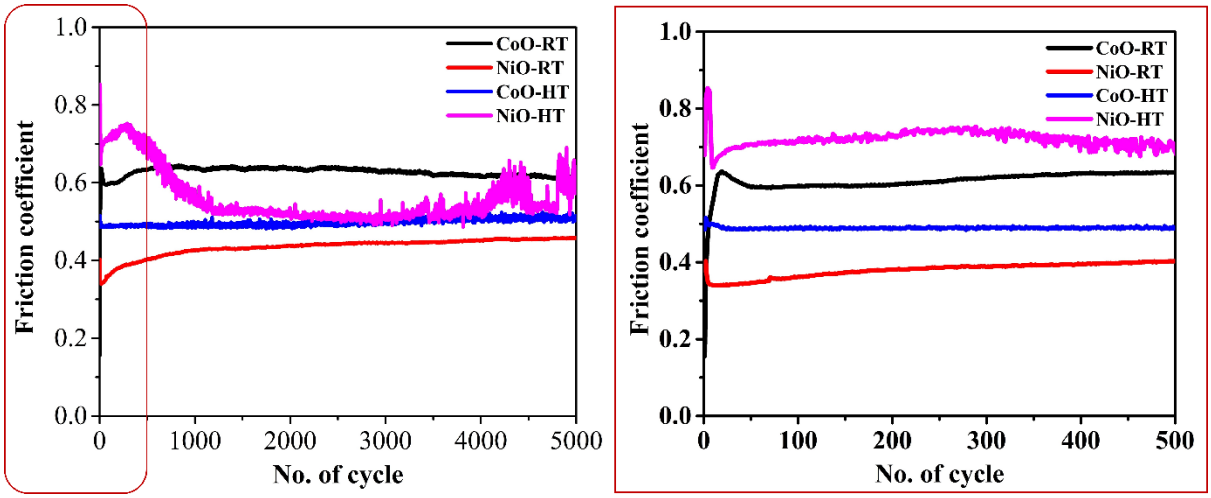

Figure 5. 4: Friction coefficient vs no. of cycle of CoO and NiO coatings at room (RT) and high temperature (HT)

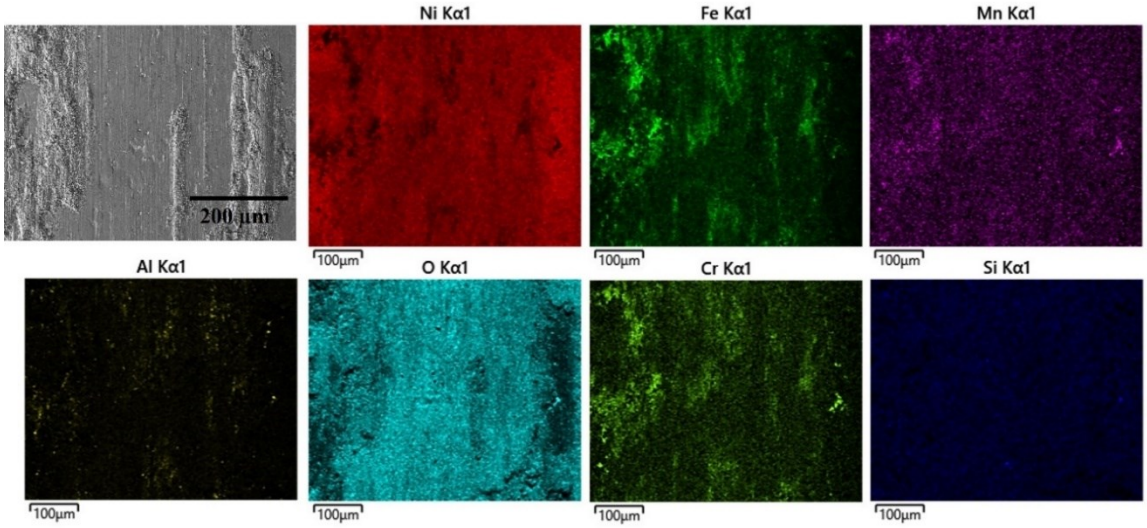

Figure 5. 5: SEM-EDS mapping of wear track after sliding 500 cycles at high temperature (HT) on the NiO coating

The specific wear rate of CoO and NiO coatings at RT and HT is shown in **Figure 5. 6**. The wear rate of the CoO at RT and HT was 22 ± 2.4 $\times 10^{-6}$ mm^3/Nm and 12 ± 2.0 $\times 10^{-6}$ mm^3/Nm, respectively. On the other hand, the NiO wear rate (42 ± 6.04 $\times 10^{-6}$ mm^3/Nm) was more than 45% higher than CoO at RT. The NiO coating has also worn out at high temperatures after the sliding test. Therefore, the wear rate at this temperature was relatively high and not depicted in **Figure 5. 6** but mentioned as 'coating worn out'.

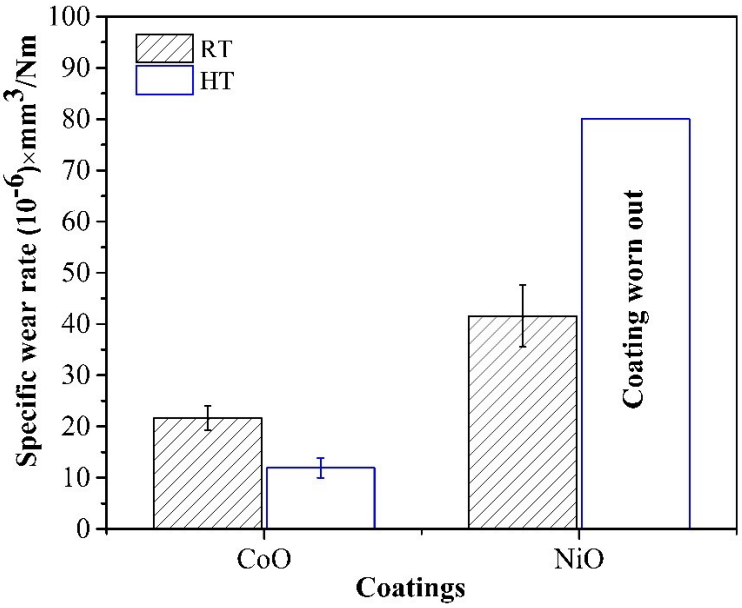

Figure 5. 6: Specific wear rate of CoO and NiO coatings at room (RT) and high temperature (HT)

5.3.2.2 Worn surface morphologies

Figure 5. 7 shows the SEM wear tracks of the CoO and NiO coatings after the dry sliding tests at RT and HT. **Figure 5. 7 (a)** shows the deep abrasive mark along the sliding direction with some grooves or grain pull out on the wear tracks. The grain pull-outs were mainly found in the ceramics where the boundaries of the surface grains were weaker and hence removed as the wear debris during sliding [41]. It should be noted that most of the wear debris are likely generated at the beginning of the testing due to the removal of the asperities. At HT. a comparatively smooth smeared surface with some shallow abrasive marks was observed on the worn surfaces [**Figure 5. 7 (b)**].

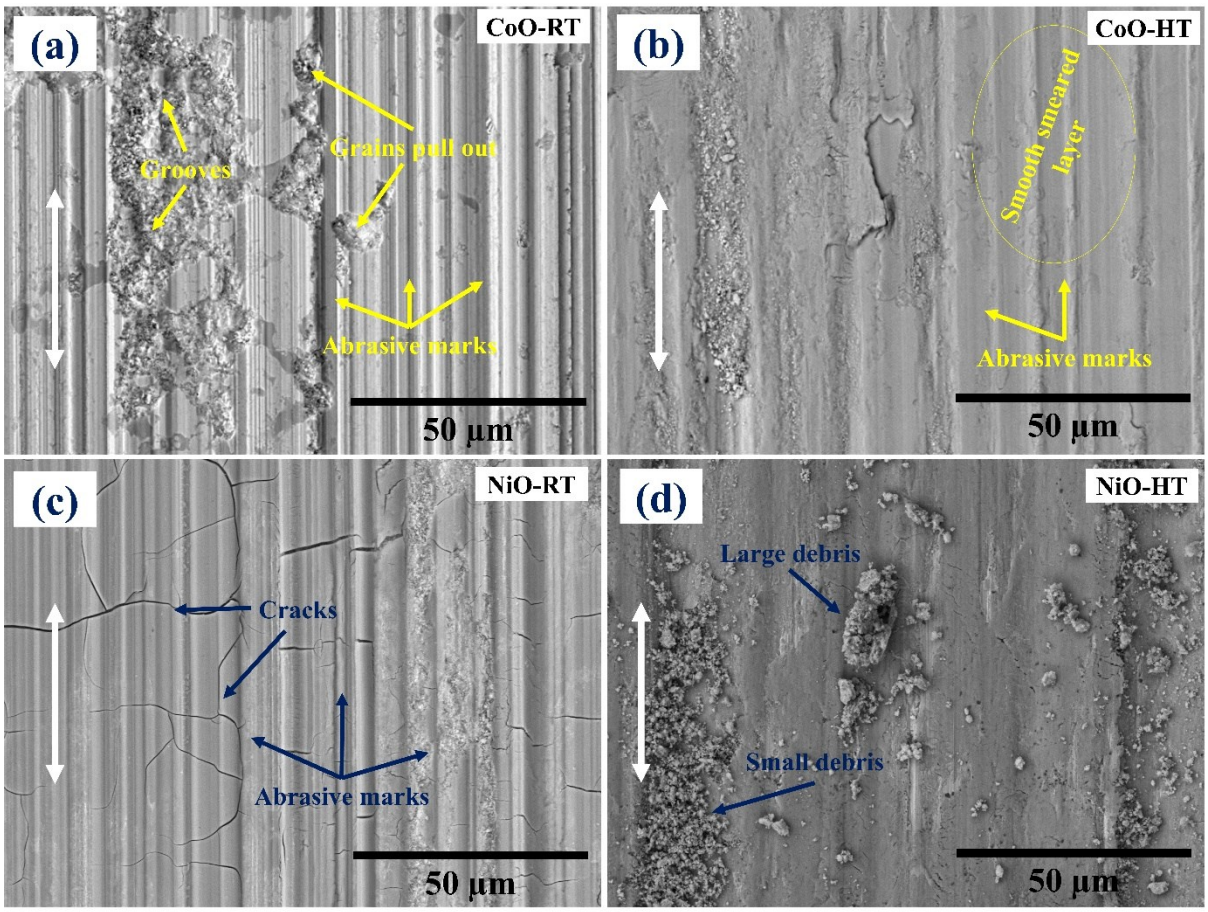

Figure 5. 7: SEM micrograph of the wear tracks after dry sliding test of (a) CoO at RT, (b) CoO at HT; (c) NiO at RT and (d) NiO at HT. ↕ indicate sliding directions

Abrasive lines/grooves parallel to the sliding direction for the NiO coatings was observed at RT [**Figure 5. 7 (c)**]. Additionally, fracture, and/or cracks propagated on the wear tracks perpendicular to the sliding direction or at a slight angle. On the contrary, the NiO coatings wore out after sliding at 5000 cycles at HT. The size of the debris particles varied between a few micrometers and the composition is a mixture between the substrate (i.e., steel) elements

and the coating (not shown here). This behavior indicated the low load-carrying capacity or poor wear resistance properties of NiO coatings at HT.

5.3.2.3 Raman analysis

Raman analysis was performed on the deposited coatings and worn surfaces (i.e., CoO and NiO) after sliding at RT and HT (except wear track of NiO at HT as it worn out) as shown in **Figure 5. 8**. The micro-Raman analysis on the CoO and NiO coatings correlated well with the XRD analysis [**Figure 5. 1**]. However, pure metallic Ni in the NiO coating [**Figure 5. 1 (b)**] was not detected with the Raman spectrum [**Figure 5. 8 (b)**] as it is not Raman active.

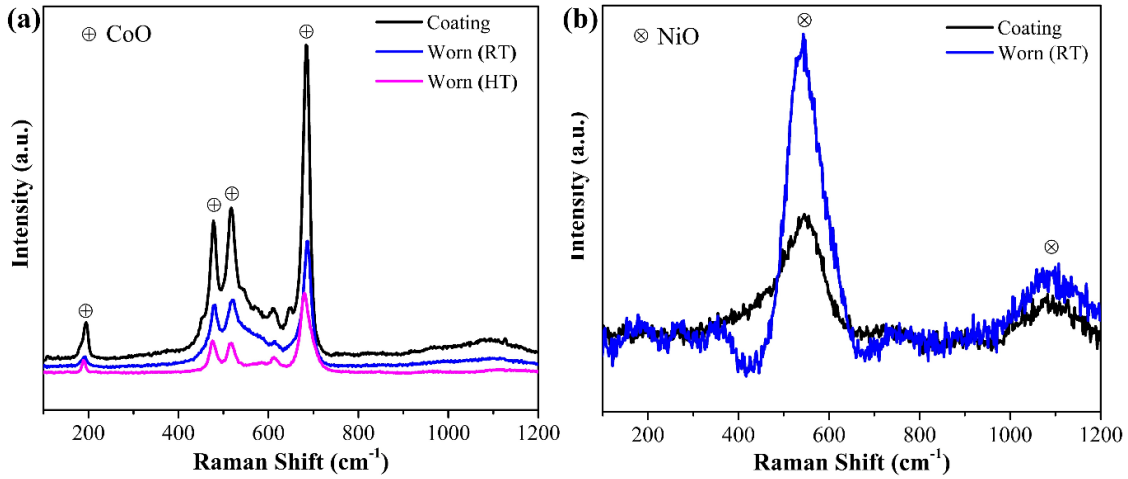

Figure 5. 8: Raman spectrum of unworn and worn coatings at (a) room temperature (RT) and (b) high temperature (HT)

The characteristic peaks at Raman shift 190 cm^{-1} ,477 cm^{-1}, 516 cm^{-1} and 680 cm^{-1} in the unworn, worn coatings at RT and HT corresponding to the CoO phase [**Figure 5. 8 (a)**] [42,43]. The peaks at Raman shift 545 cm^{-1} and 1080 cm^{-1} corresponds to NiO phase [**Figure 5. 8 (b)**] [42,44].

5.3.2.4 Counterface analysis

***Counterface against CoO coating*:** SEM images of the Al_2O_3 counterball running against CoO are shown in **Figure 5. 9** after sliding testing at RT and HT. The RT counterball shows material transfer on the center and periphery of the contact [**Figure 5. 9 (a)**]. In addition, the SEM image [**Figure 5. 9 (a, b)**] depicted severe abrasive marks in the sliding direction with materials island covering parts of the grooves. This severe abrasive behavior of the counterball is similar to that observed on the wear tracks at RT [**Figure 5. 7 (a)**]. A similar behavior was also observed on the for the HT counterball [**Figure 5. 9 (c-d)**]. However, the abrasive grooves were less evident, which correlates well with the wear tracks at HT **Figure 5. 7 (b)**. The wear

of the counterballs Al_2O_3 was observed after dry sliding at RT (i.e., $0.65 \pm 0.02 \times 10^{-6}$ mm^3/Nm) and HT (i.e., $0.67 \pm 0.002 \times 10^{-6}$ mm^3/Nm) was almost the same as illustrated in **Table 5. 2**.

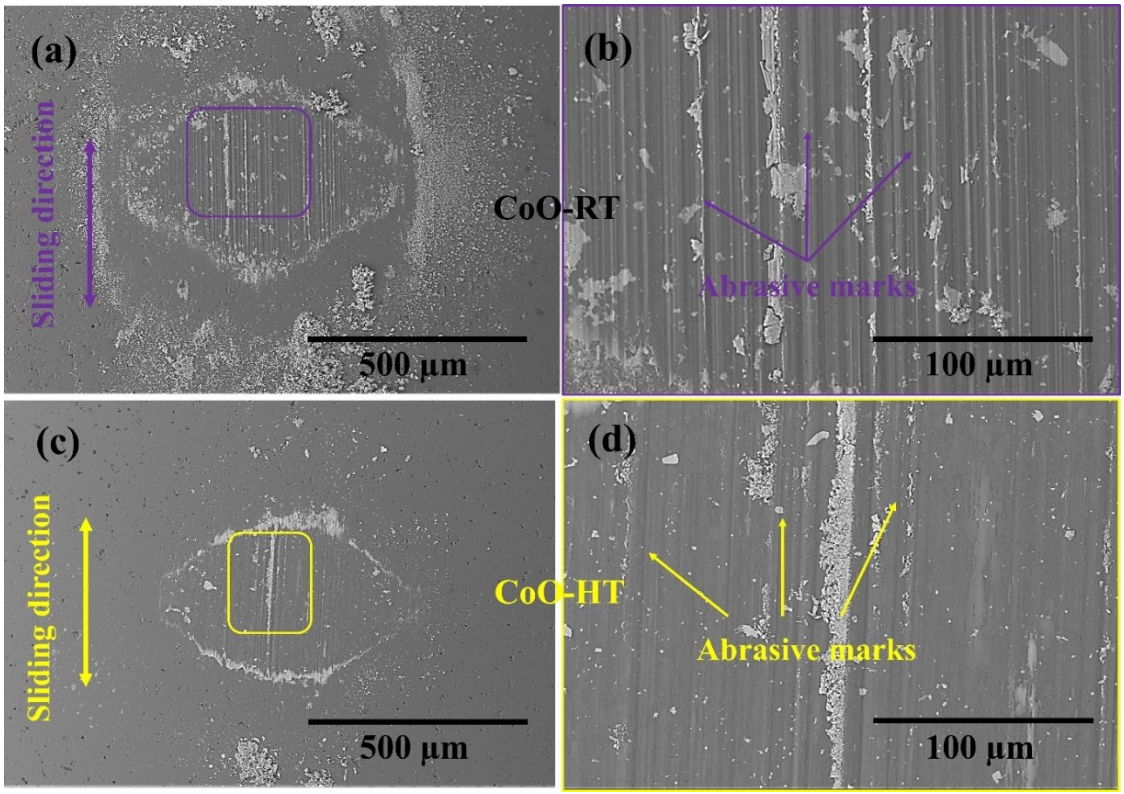

Figure 5. 9: SEM microstructures of Al_2O_3 counterfaces sliding against CoO coatings at (a-b) room temperature (RT), and (c-d) high temperature (HT)

Table 5. 2: Wear rate of Al_2O_3 counterface against CoO and NiO coatings at RT and HT after dry sliding wear testing.

Coating	Testing Condition	Counterface Wear Rate$\times 10^{-6}$ (mm^3/Nm)
CoO	RT	0.65 ± 0.02
	HT	0.67 ± 0.002
NiO	RT	1.20 ± 0.02
	HT	15.32 ± 0.6

***Counterface against NiO coating*:** The Al_2O_3 counterfaces sliding against the NiO coatings at RT and HT are shown in **Figure 5. 10**. Severe abrasive grooves with transferred material in the centre of the contact can be observed at RT counterfaces [**Figure 5. 10 (a-b)**]. The abrasive behavior could possibly be due to the abrasive nature of the NiO debris particles that formed on the wear tracks at RT [**Figure 5. 7 (c)**]. On the other hand, a vast and thick transfer film mixed with NiO and steel elements (not shown here) in the center and edges of the contact has

been observed at HT counterfaces [**Figure 5. 10 (c-d)**]. This thick transfer is likely due to the worn-out of the NiO coatings after the sliding test at HT [**Figure 5. 7 (d)**]. On the other hand, the wear on the alumina counterface at RT (i.e., 1.2 ± 0.02×10^{-6} mm^3/Nm) was low than HT but substantially higher than counterfaces sliding against CoO coatings [**Table 5. 2**].

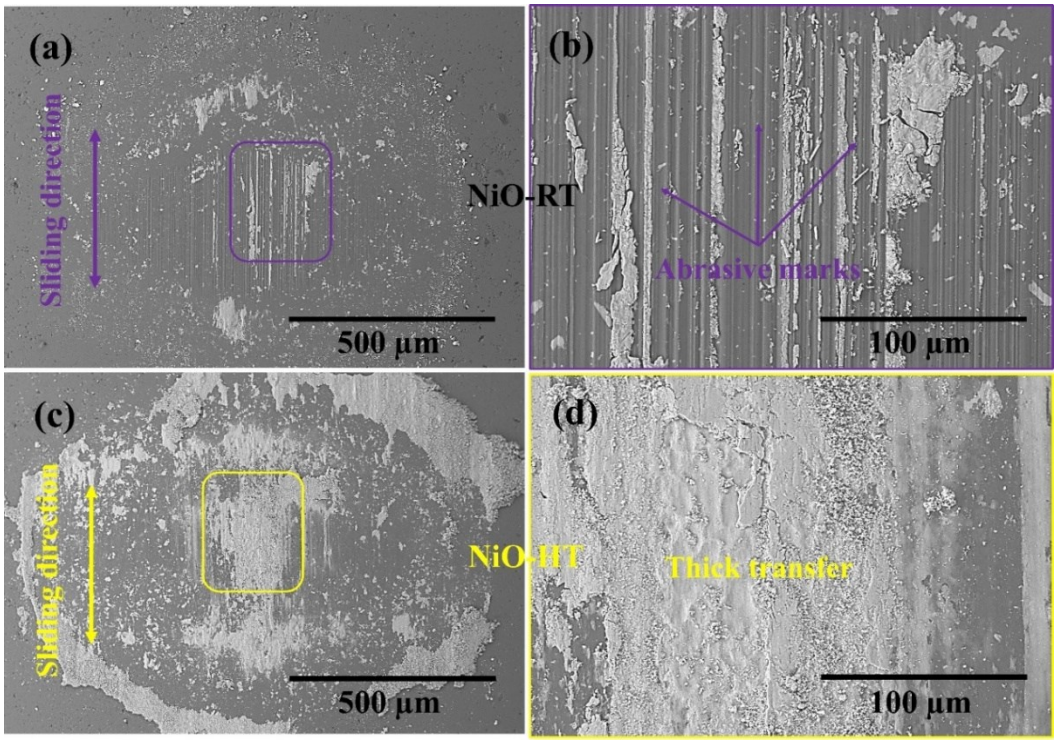

Figure 5. 10: SEM microstructures of Al_2O_3 counterfaces sliding against NiO coatings at (a-b) room temperature (RT), and (c-d) high temperature (HT)

5.3.2.5 Subsurface microstructure

***CoO subsurface analysis*:** The material's properties and microstructures in the subsurface (i.e., underneath the wear track) is generally modified during sliding in demanding conditions due to stress transfer or contact conditions during sliding, influencing the friction and wear mechanisms [20,45]. Thus, FIB/SEM analysis was performed on the wear tracks (preferably on the smoother zones) developed at RT and HT to characterize the subsurface microstructures. **Figure 5. 11** (a & d) shows the Focused Ion Beam (FIB)-SEM images in low magnification at RT and HT, respectively. The high-magnification ECCI images at RT are shown in **Figure 5. 11** (b & c), which clearly reveal submicrometric grains throughout the micrographs. No apparent tribofilm or grain refinement was observed near the contact interfaces. In addition, crack propagation and /or fractures appeared below the worn surface (i.e., closer to contact interfaces). Interestingly, three (I, II & III) distinct zones along with sintered or compacted

grains can be seen in the ECCI cross-section of the wear track at HT [**Figure 5. 11 (e-f)**]. Zone I is associated with the nanocrystalline/amorphous layer on the surface. Zone II is the nanocrystalline zone underneath and Zone III is the sub-micrometric zone.

EDS mapping and line analysis were performed on the CoO wear tracks to distinguish the variation of Co and O **[Figure 5. 12]**. Co and O were distributed homogeneously on the sub-surface without any variation. This was an initial indication that the only structural modifications (i.e., grain refinement) of the coatings in the sub-surface occurred during sliding at HT [**Figure 5. 11 (e-f)**].

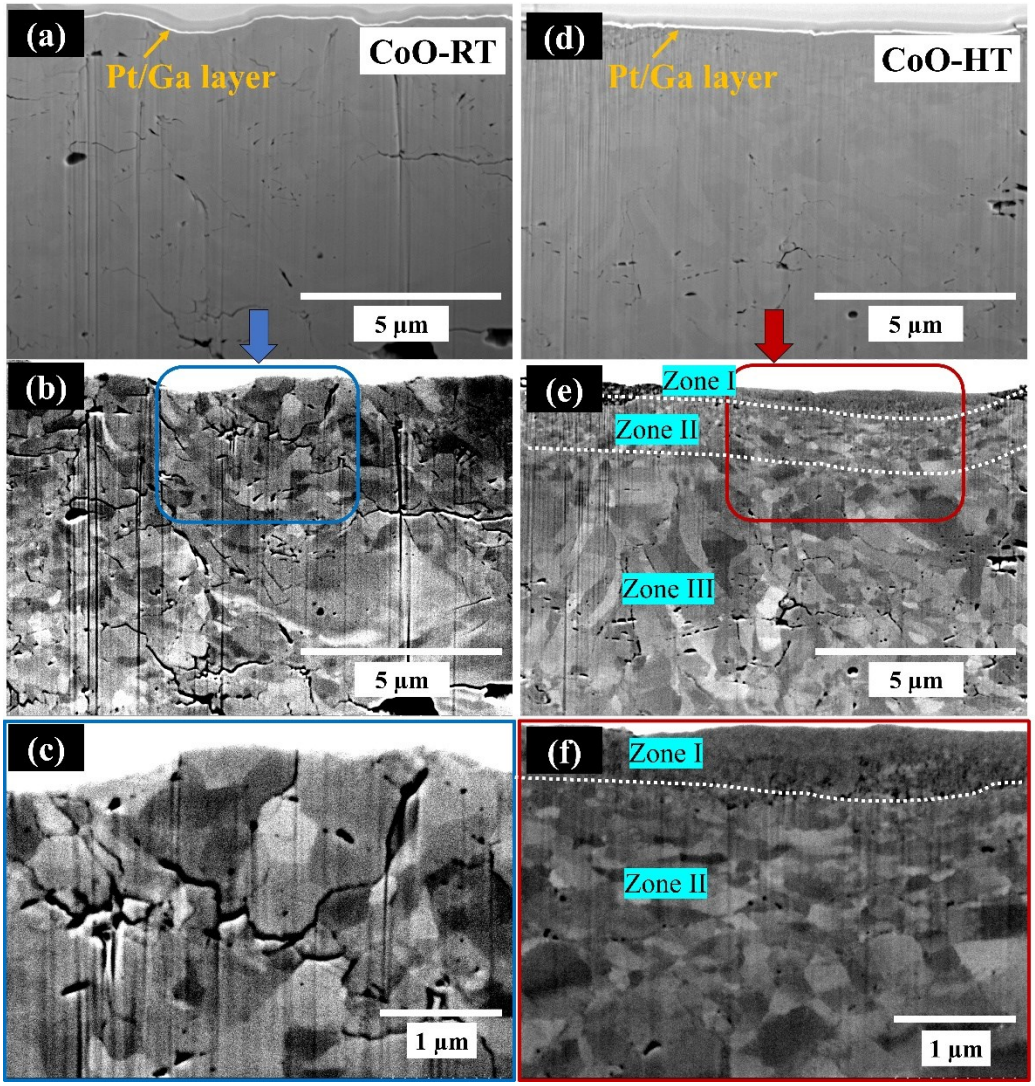

Figure 5. 11: SEM/FIB image of CoO coatings at (a) room temperature (RT) and (d) high temperature (HT). ECCI micrograph of this FIB cut of CoO wear track at (b-c) RT and (e-f) HT; **Zone I**: nanocrystalline/amorphous layer, **Zone II**: nanocrystalline zone, and **Zone III**: sub-micrometric zone.

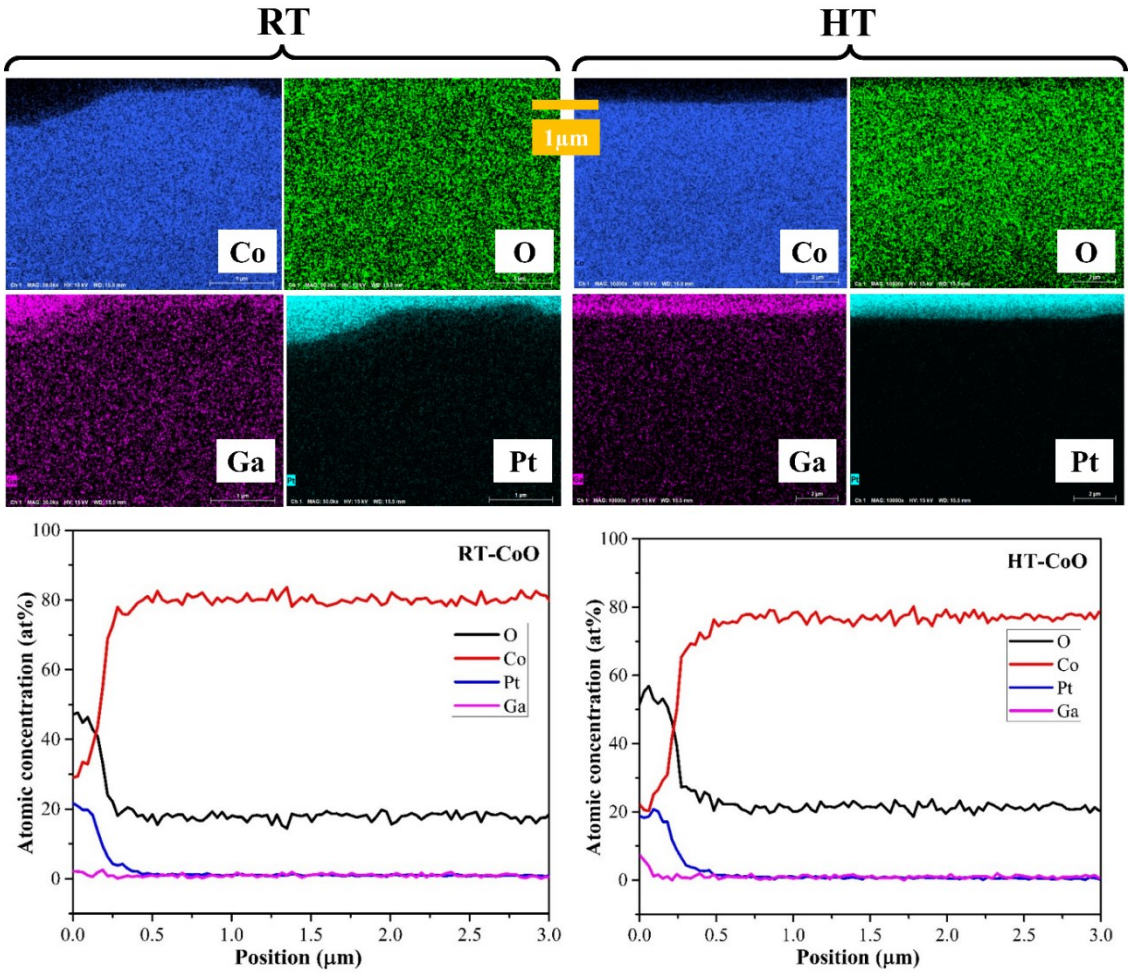

Figure 5. 12: EDS mapping and line analysis (i.e., top to bottom) of CoO at room temperature (RT) and high temperature (HT)

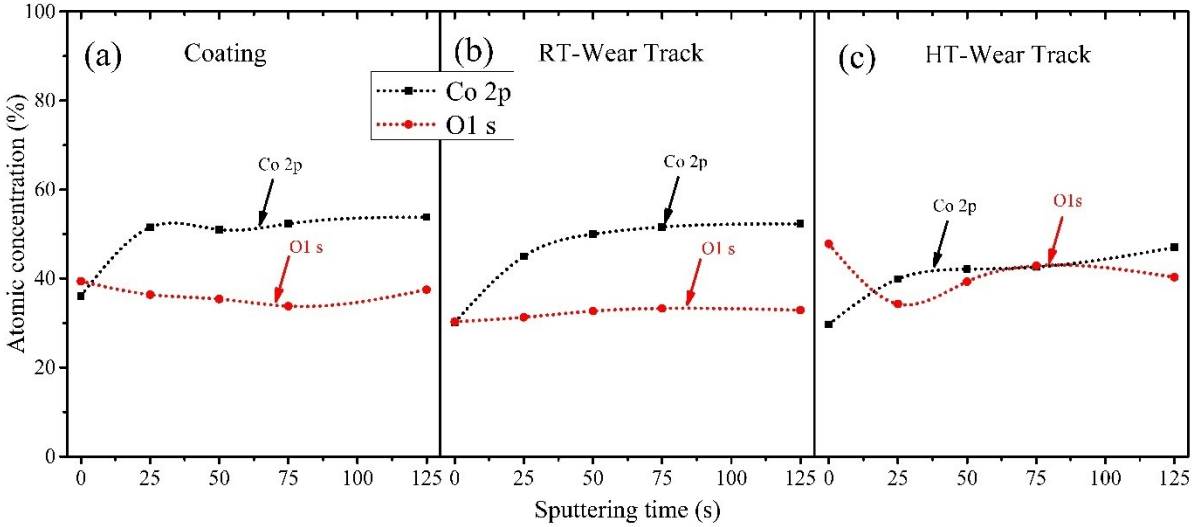

Figure 5. 13: XPS depth profiles of CoO (a) coating, (b) wear track at room temperature (RT), and (c) wear track at high temperature (HT)

The x-ray photoelectron spectroscopy (XPS) showed no significant variation of Co and O elements in the coatings and the wear tracks at RT [**Figure 5. 13 (a-b)**]. However, HT wear tracks showed a variation of Co and O on the surface and remained similar as a function of depth [**Figure 5. 13 (c)**]. The Co and O elements on the HT wear track could be associated with Co_3O_4.

***NiO subsurface analysis*:** The cross-section of the NiO coating after wear testing at RT is shown in **Figure 5. 14**. It should be noted that the cross-section of the NiO wear track at HT is not shown here since it was completely worn out after friction testing.

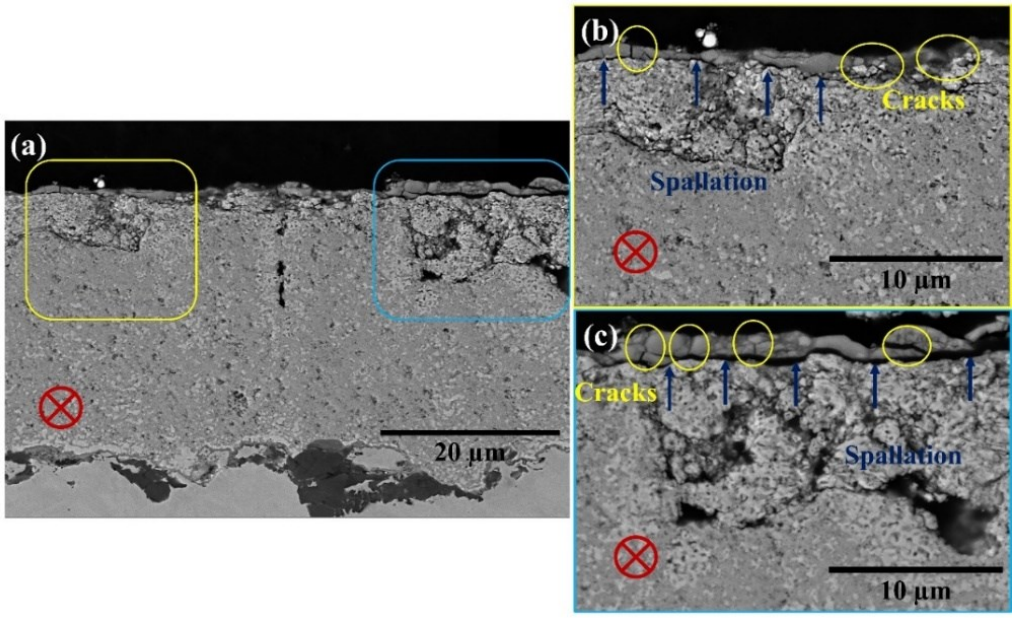

Figure 5. 14: SEM-cross-section of wear tracks of NiO coatings after tribotesting at room temperature (RT). Blue arrows and yellow circles showed spallation and cracks in the tribolayer. ⊗ indicate sliding direction.

A dense layer (i.e. tribofilm) at RT was formed on the wear tracks, as shown in **Figure 5. 14 (a)**, which can be associated with cracks, brittle fractures, and spallation from the coating [**Figure 5. 14 (b-c)**]. The cracks (i.e., yellow circles) within the tribolayer are consistent with the cracks observed on the surface of the wear tracks **Figure 5. 7 (c)**. These characteristics can be related to the hard and brittle behavior of the tribolayer [46–48].

5.4 Discussion

5.4.1 Friction and wear mechanisms of CoO coatings

In order to provide a better understanding on the friction and wear mechanisms of CoO coatings sliding at RT and HT, a schematic is shown in **Figure 5. 15** based on the *ex-situ*

analysis performed in this study. At room temperature, the governing wear mechanism is abrasion (i.e., possibly 2 or 3 body abrasions) with significant plastic flow of the asperities, which is indicated through the grooves in the parallel direction to the sliding, [**Figure 5. 7 (a)**] [49]. In addition, it is likely that localized shear deformation occurred due to the cyclic exposure of the wear track. The cyclic loading and frictional heating in the contact zone at RT were not sufficient to change any sub-surface grain refinement and thus, sub-micrometric grains were observed throughout the sub-surface [**Figure 5. 15 (a)**]. However, this cyclic loading led to the development of sub-surface cracks [**Figure 5. 11 (b-c)** and **Figure 5. 15 (a)**], detachment of materials from the worn surface, and formation of wear debris that accelerated severe abrasion, resulting in high friction and wear rates [**Figure 5. 4** and **Figure 5. 6**]. Crack formation and brittle behavior of ceramics at room temperature could accelerate detachment of wear fragments during sliding, generate high wear debris, and cause increased friction and wear [40]. A similar formation of brittle cracks on the wear tracks has been observed on the tribologically induced cobalt oxides for Co-based alloys, which were previously reported by Viat et al. [18], Korashy et al. [19] and Munagala et al. [20]. Also, Viat et al. [18] proved by micropillar compression testing that this oxides layer behaved as brittle behavior from room to 200°C, which resulted in relatively high friction and wear rates at room temperatures.

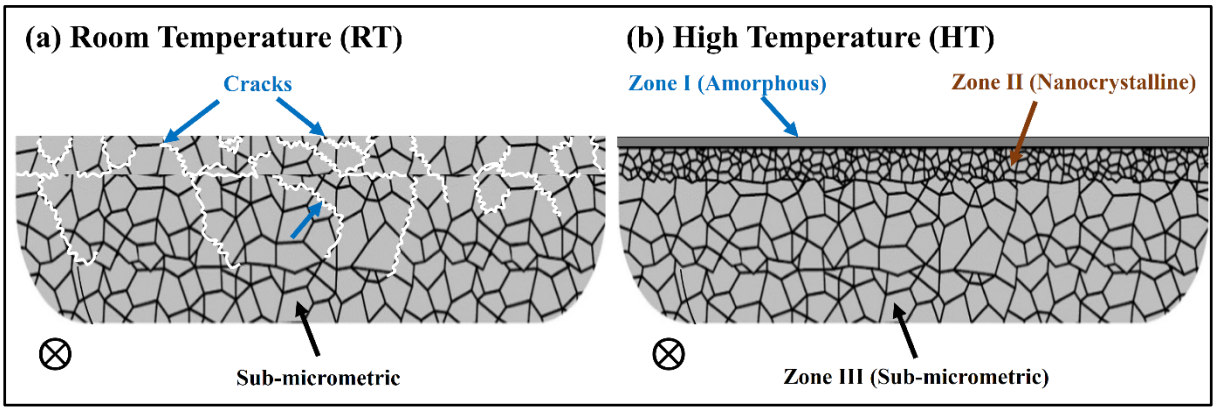

Figure 5. 15: Friction and wear mechanisms of CoO coatings after dry sliding at (a) room temperature (RT) and (b) high temperature (HT). ⊗ indicate sliding direction.

At high temperature, a comparatively smooth smeared surface with some shallow abrasive marks was observed on the wear tracks [**Figure 5. 7 (b)**]. The more ductile behavior in combination with the high frictional heating and reduced thermal conductivity (i.e., 9 W/m.K. at ~25°C) at high-temperature environment could promote the formation of such a smeared smooth surface on the wear tracks [50]. Consequently, this smeared tribofilm on the wear tracks will results in a low and stable friction coefficient and high wear resistance characteristics at HT compared to RT [**Figure 5. 4** and **Figure 5. 6**]. A similar observation of continuous smeared

tribofilm was observed by Roy et al. [35] for their plasma-sprayed tantalum oxide coatings at elevated temperatures, which reduced friction and wear. Additionally, Viat et al. [18] showed that the tribologically induced cobalt oxides undergo the brittle to ductile transition at above 300°C, which decreased friction and wear. This behavior could be responsible for changing the severe abrasive wear (RT) to mild abrasive wear at HT [**Figure 5. 7 (b)**].

Three distinctive zones (i.e., nanocrystalline amorphous, nanocrystalline, and sub-micrometric) were identified in the sub-surface of HT wear tracks, as explained in **section 5.3.2.5**. This is consistent with previous studies highlighting that the glaze layers closer to the interface were nanocrystalline with increased hardness for Co-based alloys, which ultimately decreased friction and wear [13,15,26,51]. This behavior has also been observed in other metallic alloys, forming lubricious oxide glazes on the wear tracks at high temperatures [20,52,53]. Some studies have even shown the presence of amorphous zones along with nanocrystalline grains in these cobalt oxide tribolayers [13,26,54]. In addition, Tang et al. [55] showed that the formation of CoO or Co_3O_4 oxides layer on the wear track at high temperatures can be explained by the greater diffusion of Co than Cr, which reduced the overall friction and wear for cobalt-based superalloys. The frictional heating at high temperatures could play a significant role for the formation of Co_3O_4 or remain CoO as per equation (5.1) [55]. However, further advanced characterization needs to be performed to fully understand the type or nature of the tribofilm closer to the contact interfaces.

$$CoO \xrightarrow[200\text{-}600°C]{\text{Oxidized}} Co_3O_4 \xrightarrow[850\text{-}1000°C\ (air)]{\text{Decomposed}} CoO \qquad (5.1)$$

5.4.2 Friction and wear mechanisms of NiO coatings

Similar to CoO, a schematic (**Figure 5. 15**) of the friction and wear mechanisms for the NiO coatings at RT and HT is shown based on the *ex-situ* analysis. The friction coefficient of NiO coatings was lower than the CoO coatings at RT [**Figure 5. 4**]. The low friction could be due to the high hardness of the NiO as compared to CoO coatings [56]. The effect of hardness on friction coefficient is described by the Archard [57]. Indeed, the high-hardness coatings can significantly reduce friction, as observed by researchers in their previously published literature [58–61]. However, due to the brittleness of the NiO, cracks were propagated on the wear track while two or three body abrasive wear mechanisms was dominant [**Figure 5. 7 (c)** and **Figure 5. 16 (a)**]. Evans et al. previously showed NiO is hard and brittle in atmospheric conditions [62]. Consequently, the formation of cracks and brittle natures of ceramics accelerated the removal of wear fragments during sliding, generating high wear debris, and consequently high

wear [40]. Goel et al. [45] and Mahade et al. [46] have observed a similar behavior in their plasma-sprayed alumina coatings at atmospheric sliding conditions.

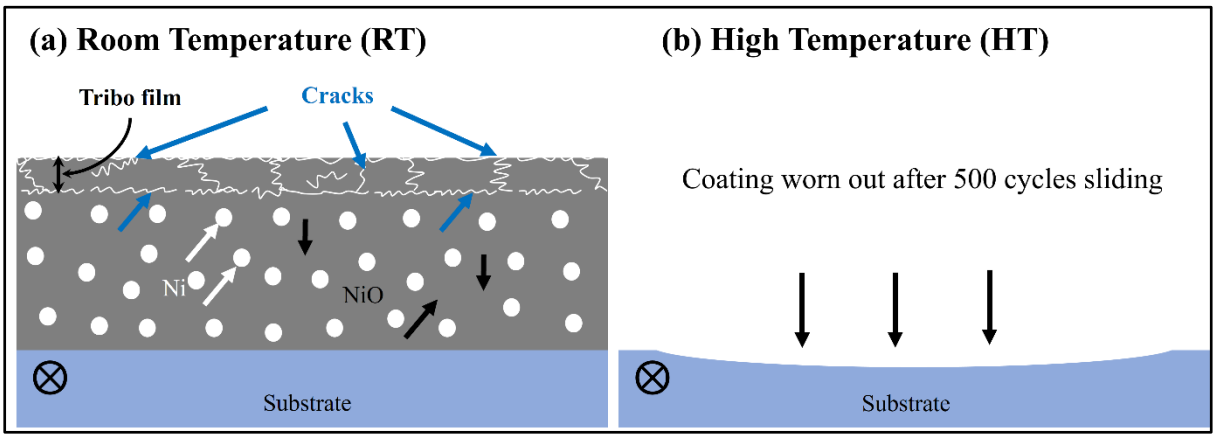

Figure 5. 16: Friction and wear mechanisms of NiO coatings after dry sliding at (a) room temperature (RT) and (b) high temperature (HT). ⊗ indicate sliding direction.

At high temperature, the friction coefficient of NiO coating was relatively high (~0.7) up to 500 cycles, which could possibly be due to the generation of hard particles (i.e., NiO) in the sliding process. A similar explanation for the high friction of NiAl coatings at high temperatures was made by Yao et al. [44]. Similarly to the friction coefficient, the wear rate of NiO coatings was relatively high and the coating was completely removed at the end of the test [**Figure 5. 6**; **Figure 5. 7 (d)**; **Figure 5. 16 (b)**]. Evans et al. showed that NiO employs is brittle in nature up to 500°C [62]. Therefore, in our study, it is likely that the NiO coating failed prematurely due to brittle fracture within the worn area.

In general, the lubricity of the CoO and NiO at high temperatures can be related to the polarizability approach or interaction parameter [63,64]. The interaction parameter of CoO and NiO are 0.059 and 0.083, respectively. Prakash et al. [64] found that with decreasing the interaction parameter the friction coefficient of the oxides decreased at high temperatures due to the weaker bond energy between anion and cation. In addition, the interaction parameter can be related to the activation energy for the improved lubricity. More specifically, the formation of vacancies and hopping of ions at the surface of an oxides becomes easier with lower the activation energy, and thus, increases the degree of freedom and mobility of ions. This increased mobility of ions at their surface is assumed to be at the basis of the low coefficient of friction of such oxides in sliding contacts [64].

5.5 Conclusions

The main purpose of this study was to critically evaluate the friction and wear behavior of the thermally sprayed CoO and NiO coatings at room temperature (RT) and high temperature (HT). In terms of wear characteristics, the CoO coatings outperform NiO in both states. The friction coefficient and specific wear rate of the CoO coatings decreased with increasing temperatures. *Ex-situ* analysis of the wear tracks after sliding at high temperatures revealed the formation of a thin, nanocrystalline amorphous tribofilm. At room temperature, brittle fractures, and sub-surface micro-cracks of CoO coating caused high friction and wear. At room temperature, NiO coating provided low friction and wear, which can possibly be attributed to the high hardness. At high temperature, on the other hand, the coating was utterly worn out and resulted in increased friction and wear due to its brittle nature [62].

5.6 References

[1] Wood PD. The effect of the counterface on the wear resistance of certain alloys at room temperature and 750° C. University of Northumbria at Newcastle (United Kingdom); 1997.

[2] Rose SR. Studies of the high temperature tribological behaviour of some superalloys. University of Northumbria at Newcastle (United Kingdom); 2000.

[3] Stott FH, Lin DS, Wood GC. The structure and mechanism of formation of the 'glaze'oxide layers produced on nickel-based alloys during wear at high temperatures. Corros Sci 1973;13:449–69.

[4] Ross E, Ignatov A, Stoyanov P. Tribological Characteristics of Manufactured Carbon Under Extreme Contact Conditions. Tribol Ind 2021;43.

[5] Stoyanov P, Harrington KM, Frye A. Insights into the tribological characteristic of Cu-based coatings under extreme contact conditions. JOM 2020;72:2191–7.

[6] Korashy A, Attia H, Thomson V, Oskooei S. Fretting wear behavior of cobalt-Based superalloys at high temperature–A comparative study. Tribol Int 2020;145:106155.

[7] Reed RC. The superalloys: fundamentals and applications. Cambridge university press; 2008.

[8] Stoyanov P, Dawag L, Goberman DG, Shah D. Friction and wear characteristics of single crystal Ni-based superalloys at elevated temperatures. Tribol Lett 2018;66:1–9.

[9] Pollock TM, Tin S. Nickel-based superalloys for advanced turbine engines: chemistry, microstructure and properties. J Propuls Power 2006;22:361–74.

[10] Stoyanov P, Dawag L, Joost WJ, Goberman DG, Ivory S. Insights into the static friction behavior of Ni-based superalloys. Surf Coatings Technol 2018;352:634–41.

[11] Inman IA, Datta S, Du HL, Burnell-Gray JS, Luo Q. Microscopy of glazed layers formed during high temperature sliding wear at 750° C. Wear 2003;254:461–7.

[12] Wood PD, Evans HE, Ponton CB. Investigation into the wear behaviour of Stellite 6 during rotation as an unlubricated bearing at 600 C. Tribol Int 2011;44:1589–97.

[13] Viat A, Bouchet M-IDB, Vacher B, Le Mogne T, Fouvry S, Henne J-F. Nanocrystalline glaze layer in ceramic-metallic interface under fretting wear. Surf Coatings Technol 2016;308:307–15.

[14] Viat A, Dreano A, Fouvry S, Bouchet M-IDB, Henne J-F. Fretting wear of pure cobalt chromium and nickel to identify the distinct roles of HS25 alloying elements in high temperature glaze layer formation. Wear 2017;376:1043–54.

[15] Viat A, Guillonneau G, Fouvry S, Kermouche G, Sao Joao S, Wehrs J, et al. Brittle to ductile transition of tribomaterial in relation to wear response at high temperatures. Wear 2017;392:60–8.

[16] DellaCorte C, Lukaszewicz V, Morris DE, Steinetz BM. Static and dynamic friction behavior of candidate high temperature airframe seal materials. 1994.

[17] Coskun MB, Aksoy S, Aksit MF. Friction and wear characteristics of Haynes 25, 188, and 214 superalloys against Hastelloy X up to 540° C. Tribol Lett 2012;45:497–503.

[18] Viat A, Guillonneau G, Fouvry S, Kermouche G, Sao Joao S, Wehrs J, et al. Brittle to ductile transition of tribomaterial in relation to wear response at high temperatures. Wear 2017;392–393:60–8. https://doi.org/10.1016/j.wear.2017.09.015.

[19] Korashy A, Attia H, Thomson V, Oskooei S. Characterization of fretting wear of cobalt-based superalloys at high temperature for aero-engine combustor components. Wear 2015;330:327–37.

[20] Munagala VNV, Alidokht SA, Sharifi N, Makowiec ME, Stoyanov P, Moreau C, et al. Room and elevated temperature sliding wear of high velocity oxy-fuel sprayed Diamalloy3001 coatings. Tribol Int 2022:108069.

[21] Scharf TW, Prasad S V, Kotula PG, Michael JR, Robino C V. Elevated temperature tribology of cobalt and tantalum-based alloys. Wear 2015;330:199–208.

[22] Harrington KM, Miller EC, Frye A, Stoyanov P. Tribological insights of Co-and Ni-based alloys in extreme conditions. Wear 2021;477:203827.

[23] Stott FH, Stevenson CW, Wood GC. Friction and wear properties of Stellite 31 at temperatures from 293 to 1073K. Met Technol 1977;4:66–74.

[24] Stoyanov P, Boyne A, Ignatov A. Tribological characteristics of Co-based plasma sprayed coating in extreme conditions. Results in Surfaces and Interfaces 2021;3:100007.

[25] Rynio C, Hattendorf H, Klöwer J, Eggeler G. On the physical nature of tribolayers and wear debris after sliding wear in a superalloy/steel tribosystem at 25 and 300 C. Wear 2014;317:26–38.

[26] Scharf TW, Prasad S V., Kotula PG, Michael JR, Robino C V. Elevated temperature tribology of cobalt and tantalum-based alloys. Wear 2015;330–331:199–208. https://doi.org/10.1016/j.wear.2014.12.051.

[27] Dreano A, Fouvry S, Sao-Joao S, Galipaud J, Guillonneau G. The formation of a cobalt-based glaze layer at high temperature: A layered structure. Wear 2019;440–441:203101. https://doi.org/10.1016/j.wear.2019.203101.

[28] Laskowski JA, DellaCorte C. Friction and wear characteristics of candidate foil bearing materials from

25° C to 800° C. National Aeronautics and Space Administration Washington, DC, USA; 1996.
[29] Peterson MB, Florek JJ, Lee RE. Sliding characteristics of metals at high temperatures. ASLE Trans 1960;3:101–9.
[30] Patel P, Alidokht SA, Sharifi N, Roy A, Harrington K, Stoyanov P, et al. Microstructural and Tribological Behavior of Thermal Spray CrMnFeCoNi High Entropy Alloy Coatings. J Therm Spray Technol 2022:1–17.
[31] Darut G, Ben-Ettouil F, Denoirjean A, Montavon G, Ageorges H, Fauchais P. Dry sliding behavior of sub-micrometer-sized suspension plasma sprayed ceramic oxide coatings. J Therm Spray Technol 2010;19:275–85. https://doi.org/10.1007/s11666-009-9415-1.
[32] Mohammadkhani S, Jalilvand V, Davis B, Gauthier GH, Dolatabadi A, Moreau C, et al. High-temperature behaviour of HVOF (Co,Ni)O coated Cu-Ni-Fe anodes. Corros Sci 2021;189:109563. https://doi.org/10.1016/j.corsci.2021.109563.
[33] Mohammadkhani S, Jalilvand V, Davis B, Ettouil F Ben, Dolatabadi A, Roué L, et al. Suspension plasma spray deposition of CoxNi1-xO coatings. Surf Coatings Technol 2020;399:126168. https://doi.org/10.1016/j.surfcoat.2020.126168.
[34] Tarasi F, Medraj M, Dolatabadi A, Oberste-Berghaus J, Moreau C. Enhancement of amorphous phase formation in alumina–YSZ coatings deposited by suspension plasma spray process. Surf Coatings Technol 2013;220:191–8.
[35] Roy A, Munagala VN V, Patel P, Sharifi N, Alidokht SA, Makowiec M, et al. Friction and wear behavior of suspension plasma sprayed tantalum oxide coatings at elevated temperatures. Surf Coatings Technol 2022:129097.
[36] Küçük Y. Effect of counterbody on the dry sliding wear performance of plasma sprayed calcia-stabilized zirconia coating. Int J Refract Met Hard Mater 2020;92. https://doi.org/10.1016/j.ijrmhm.2020.105284.
[37] Sabat KC. Production of nickel by cold hydrogen plasma. Plasma Chem Plasma Process 2021;41:1329–45.
[38] Sabat KC, Murphy AB. Hydrogen plasma processing of iron ore. Metall Mater Trans B 2017;48:1561–94.
[39] Jalilvand V, Mohammadkhani S, Ettouil F Ben, Roué L, Guay D, Dolatabadi A, et al. Study on the Formation of (Co, Ni) O Solid Solution and Metallic Ni Phases During Suspension Plasma Spraying of CoO and NiO Powders. J Therm Spray Technol 2022:1–15.
[40] Alidokht SA, Manimunda P, Vo P, Yue S, Chromik RR. Cold spray deposition of a Ni-WC composite coating and its dry sliding wear behavior. Surf Coatings Technol 2016;308:424–34.
[41] Swain M V. Microscopic observations of abrasive wear of polycrystalline alumina. Wear 1975;35:185–9.
[42] Roro KT, Mwakikunga B, Tile N, Yalisi B, Forbes A. Effect of accelerated thermal ageing on the selective solar thermal harvesting properties of multiwall carbon nanotube/nickel oxide nanocomposite coatings. Int J Photoenergy 2012;2012.
[43] Korashy A, Attia H, Thomson V, Oskooei S. Characterization of fretting wear of cobalt-based superalloys at high temperature for aero-engine combustor components. Wear 2015;330–331:327–37. https://doi.org/10.1016/j.wear.2014.11.027.
[44] Yao Q, Jia J, Chen T, Xin H, Shi Y, He N, et al. High temperature tribological behaviors and wear mechanisms of NiAl-MoO3/CuO composite coatings. Surf Coatings Technol 2020;395:125910.
[45] Chromik RR, Zhang Y. Nanomechanical testing of third bodies. Curr Opin Solid State Mater Sci 2018;22:142–55.
[46] Goel S, Björklund S, Curry N, Wiklund U, Joshi S V. Axial suspension plasma spraying of Al2O3 coatings for superior tribological properties. Surf Coatings Technol 2017;315:80–7. https://doi.org/10.1016/j.surfcoat.2017.02.025.
[47] Mahade S, Mulone A, Björklund S, Klement U, Joshi S. Incorporation of graphene nano platelets in suspension plasma sprayed alumina coatings for improved tribological properties. Appl Surf Sci 2021;570:151227.
[48] Erickson LC, Blomberg A, Hogmark S, Bratthäll J. Tribological characterization of alumina and silicon carbide under lubricated sliding. Tribol Int 1993;26:83–92.
[49] Stachowiak GW, Batchelor AW. Engineering tribology. Butterworth-heinemann; 2013.
[50] Watanabe H. Thermal constants for Ni, NiO, MgO, MnO and CoO at low temperatures. Thermochim Acta 1993;218:365–72.
[51] Rynio C, Hattendorf H, Klöwer J, Eggeler G. The evolution of tribolayers during high temperature sliding wear. Wear 2014;315:1–10.
[52] Shakhvorostov D, Gleising B, Büscher R, Dudzinski W, Fischer A, Scherge M. Microstructure of tribologically induced nanolayers produced at ultra-low wear rates. Wear 2007;263:1259–65.
[53] Greiner C, Liu Z, Strassberger L, Gumbsch P. Sequence of stages in the microstructure evolution in copper

under mild reciprocating tribological loading. ACS Appl Mater Interfaces 2016;8:15809–19.
[54] Bowden FP, Bowden FP, Tabor D. The friction and lubrication of solids. vol. 1. Oxford university press; 2001.
[55] Tang C-W, Wang C-B, Chien S-H. Characterization of cobalt oxides studied by FT-IR, Raman, TPR and TG-MS. Thermochim Acta 2008;473:68–73.
[56] Nicholls JR, Hall DJ, Tortorelli PF. Hardness and modulus measurements on oxide scales. Mater High Temp 1994;12:141–50.
[57] Archard J. Contact and rubbing of flat surfaces. J Appl Phys 1953;24:981–8.
[58] Muratore C, Voevodin AA. Chameleon coatings: adaptive surfaces to reduce friction and wear in extreme environments. Annu Rev Mater Res 2009;39:297–324.
[59] Mokhtar MOA. The effect of hardness on the frictional behaviour of metals. Wear 1982;78:297–304.
[60] Schulz H, Dörr J, Rass IJ, Schulze M, Leyendecker T, Erkens G. Performance of oxide PVD-coatings in dry cutting operations. Surf Coatings Technol 2001;146:480–5.
[61] Moore AJW, Tegart WJM. Relation between friction and hardness. Proc R Soc London Ser A Math Phys Sci 1952;212:452–8.
[62] Evans AG, Rajdev D, Douglass DL. The mechanical properties of nickel oxide and their relationship to the morphology of thick oxide scales formed on nickel. Oxid Met 1972;4:151–70.
[63] Dimitrov V, Komatsu T. Classification of simple oxides: a polarizability approach. J Solid State Chem 2002;163:100–12.
[64] Prakash B, Celis JP. The lubricity of oxides revised based on a polarisability approach. Tribol Lett 2007;27:105–12. https://doi.org/10.1007/s11249-007-9223-z.

Chapter 6

Microstructural and Tribological Characteristics of Thermally Sprayed Co-Ni-O Ternary Oxide Coatings[5]

Abstract

Due to their high thermal and chemical stability, ternary oxide coatings have been extensively investigated as potential solutions for high-temperature solid lubrication. In this study, the tribological behavior of the thermally sprayed $Co_{0.75}Ni_{0.25}O$ and $Co_{0.5}Ni_{0.5}O$ oxide coatings was investigated. The dry sliding reciprocating friction tests were performed against an Al_2O_3 counterface at room and elevated temperatures using a ball-on-flat tribometer. The results indicated that the friction and wear of $Co_{0.75}Ni_{0.25}O$ oxide coatings did not change significantly at atmospheric and elevated temperature conditions, whereas the friction and wear of the $Co_{0.5}Ni_{0.5}O$ increased at elevated temperatures. The correlations between the worn surface morphologies, the subsurface microstructure induced by wear, and the wear behavior of the coatings were discussed based on the characterizations, (i.e., microhardness, scanning electron microscopy (SEM), and electron channeling contrast imaging (ECCI)).

Keywords: *$Co_{0.75}Ni_{0.25}O$, $Co_{0.5}Ni_{0.5}O$, ternary oxides, HVOF, tribology, elevated temperatures*

[5] This chapter is ready to submit as a research article to *Tribology International*. **A. Roy**, V. Jalilvand, S. Mohammadkhani, P. Patel, A. Dolatabadi, L. Roue, D. Guay, R. R. Chromik, C. Moreau, P. Stoyanov. "Microstructural and tribological characteristics of thermally sprayed Co-Ni-O ternary oxide coatings." is ready to submit *"Tribology International"*.

6.1 Introduction

Co and Ni-based superalloys are widely used in high-temperature applications due to their excellent strength, creep, and fatigue resistance at high temperatures [1,2]. In some instances, these alloys are also employed in contacting surfaces, where two surfaces continuously slide or rub against each other. This includes aerospace, bearings, gas turbines, high-speed machine tools, etc. [3–5]. At elevated temperature, the wear resistance of Co and Ni-based superalloys can be attributed to the formation of oxide or glaze layer on the worn surfaces. More specifically, the layer is generated on the wear track due to the sintering or consolidation of the wear debris or fractured particles produced during sliding in harsh conditions [6–8]. However, it is important to note that the formation of the oxide layer is influenced by various factors such as temperature, sliding speed, applied load, surrounding environment, and the chemical nature of the surfaces, and thus can lead to variations in the friction and wear [9–11]. Coskun et al. [12], showed that Co-based superalloys (i.e., Haynes 25, Haynes 188, Haynes 214) form ternary oxides (i.e., Co oxide layer together with Ni, Cr, and W oxides) against Hastelloy X at 540°C in the sliding process. In addition, Inman et al. [7,8] found the formation of wear resistant nano-structured Co/Cr/Ni oxide layer in the contact interfaces for Nimonic 80A against Stellite 6 at 750°C and low sliding speed (i.e., 0.314 m/s). Similar to the Co-based alloys, for the nickel-based superalloys (i.e., Nimonic 75, Nimonic C263, Nimonic 108, and Incoloy 601), the binary and ternary oxides (i.e., NiO, CoO, FeO, Cr_2O_3, $NiCr_2O_4$) were formed on the wear track due to the sintering effect from 200°C to 800°C, which ultimately contributed to the friction reduction [6]. Laskowski et al. [13] showed the lowest pin wear (i.e., 2.84×10^{-6} mm^3/N-m) at 500°C due to the formation of a lubricious oxide (i.e., Ni-Cr oxide) film on the wear tracks for the Inconel X-750 vs Inconel 909. Thus, the formation of binary and ternary oxides in the contact interfaces of the cobalt and nickel-based superalloys has been shown to reduce friction and wear at elevated temperatures with the ternary oxide being dominant in reducing friction compared to the binary oxide at high temperatures [14–16]. However, the formation of lubricious ternary oxides (i.e., causing steady state friction coefficient) in the contact interfaces requires a long breaking period with high friction and wear [17]. Indeed, several studies have shown that long breaking periods prior to the formation of lubricious oxides (i.e., mainly ternary oxides) or steady state conditions are largely responsible for high friction and wear [18–21]. Thus, in order to reduce the break-in period, and consequently the overall wear rate, the authors developed nickel oxide and cobalt oxide coatings in a prior study and investigated their friction and wear behavior [22]. The nickel oxide was shown to have low

friction compared to cobalt oxide under atmospheric conditions. Therefore, a coating composed of cobalt and nickel oxide in their ternary solid solution may be capable of maintain low friction and wear at room and elevated temperature.

Thermal spraying techniques are coating deposition processes in which the heated or molten materials are accelerated at high velocity onto the substrate and form a coating [23]. The feedstock or powder materials are heated by electrical (i.e., plasma or arc) or chemical means, i.e., combustion flame [24]. Additionally, this process offers advantages such as lower cost, lower complexity, atmospheric deposition conditions, ease of application to large surfaces, and high deposition efficiency compared to the thin film process [25]. These advantages make it easier to apply coatings to large and wide surfaces on any machine component using the thermal spray process. The primary classification of the thermal spray processes is atmospheric plasma spraying (APS), high-velocity oxy-fuel (HVOF), high-velocity air-fuel (HVOF), flame spraying, detonation gun spraying, arc spraying, and suspension plasma spraying (SPS) [26]. In particular, high-velocity oxy-fuel (HVOF) has recently received more attention for the production of ceramic/oxide coatings [26–28]. Compared to APS and other thermal spray processes, the HVOF method can deposit particles at a higher velocity and at a lower process temperature, allowing for the formation of a dense coating with limited porosity [29]. The dense, low-porosity microstructures produced by the HVOF process are best suited for producing high-quality wear-resistant coatings [27,28].

In this article, ternary solid solution Co-Ni-O powders (i.e., $Co_{0.75}Ni_{0.25}O$ and $Co_{0.5}Ni_{0.5}O$) were used to deposit coatings by the HVOF process, and their tribological characteristics were evaluated under atmospheric and elevated temperature conditions. The ternary solid solution powders Co-Ni-O ($Co_{0.75}Ni_{0.25}O$ and $Co_{0.5}Ni_{0.5}O$) were prepared using solid state synthesis technique with different concentrations of NiO and CoO [26,30].

To the best of the author's knowledge, no data were available on the friction and wear behavior of Co-Ni-O coatings produced by the HVOF process. After dry sliding at ambient and elevated temperatures, the *ex-situ* analysis was performed on the wear tracks and counterballs to better understand the interfacial process.

6.2 Experimental

Co-Ni-O (i.e., $Co_{0.75}Ni_{0.25}O$ and $Co_{0.5}Ni_{0.5}O$) solid solution powders were prepared by solid-state synthesis technique. The details of the powder synthesis, morphology, particle size, and substrate preparation for depositing coatings were described in the previously published articles [26,30]. A Diamond Jet^{TM} 2700 High-Velocity Oxy-Fuel (HVOF) spray gun (Sulzer

Metco, USA) with a convergent-divergent nozzle was used to deposit the coatings. The powders were injected axially and carried by a nitrogen carrier gas, while propylene was used as the fuel gas for combustion. The in-flight particle temperature and velocity were measured by Accuraspray 4.0 (Tecnar, Canada). The details of the working principle of the HVOF can be found in the published literature by the co-authors [26,29,31]. The spraying parameters of $Co_{0.75}Ni_{0.25}O$ and $Co_{0.5}Ni_{0.5}O$ coatings are described in **Table 6. 1**. The X-ray diffraction of the starting powders and as-sprayed coatings was determined by X-ray diffraction (XRD) using a Bruker D8 diffractometer equipped with Cu Kα radiation [26,30].

Table 6. 1: HVOF spraying parameters used for depositing $Co_{0.75}Ni_{0.25}O$ and $Co_{0.5}Ni_{0.5}O$ coatings

Deposition parameters	$Co_{0.75}Ni_{0.25}O$	$Co_{0.5}Ni_{0.5}O$
Oxygen flow	217 lpm	217 lpm
Propylene flow	70 lpm	70 lpm
Air flow	167 lpm	167 lpm
N_2 carrier gas flow	15 lpm	15 lpm
Feed rate	10 g/min	10 g/min
Spray distance	180 mm	180 mm
Substrate temperature	~ 450°C	~ 450°C
Number of passes	45	55
In-flight particle temperature	~ 1840°C	~ 1920°C
In-flight particle velocity	~ 563 m/s	~ 575 m/s

To characterize the microstructure, the as-sprayed coatings were cold-mounted and polished to a final surface finish of 0.4 μm according to standard metallographic guidelines. The top surface and polished cross-section of the HVOF sprayed $Co_{0.75}Ni_{0.25}O$, and $Co_{0.5}Ni_{0.5}O$ coatings were analyzed using a field emission scanning electron microscope (FESEM; SU8010, Hitachi, Japan; equipped with an energy dispersive spectrometer). Likewise, the chemical elements mapping was determined by energy-dispersive X-ray spectroscopy (EDS). Moreover, to characterize the microstructure at much finer scales (i.e., grain, grain deformation and grain refinement etc.,) of the as sprayed coatings and after heating the coatings at 450°C in air (i.e., similar to elevated temperature tribotesting testing) were evaluated using Electron channeling contrast imaging (ECCI) (SU8230, Hitachi, Japan) using a photodiode backscattered electron (PDBSE) detector. The grains closer to the coating cross-section surface wear checked for better understanding its behavior before and after heating and ultimately

checked them with wear track samples. It should be mentioned that the samples which were tested for tribology testing was further observed their unworn surfaces under ECCI. The surface roughness and porosity of the coatings were analysed using optical profilometer (Zygo Corporation, USA) and ImageJ software (open source), respectively [32].

The Vickers micro-hardness of the coatings was performed on the top surface a load of 2 N ($HV_{0.2}$) at different temperatures using a Micro-Combi Tester (Anton Paar, Austra) according to the EN ISO 4516 standard [33]. For measuring the microhardness at elevated temperatures (HT), the sample was placed in the furnace at 450°C and then heated for around 25 to 30 minutes before microhardness testing. A similar approach was followed for performing an elevated temperature tribology test. The details of the Vickers hardness testing procedure were explained in a previously published article [32].

To evaluate the tribology of the deposited coatings, dry sliding reciprocating friction tests were performed on as sprayed coatings using a reciprocating ball-on-flat tribometer (Anton Paar, Austria). The wear testing parameters (i.e., load 5 N, track length 10 mm, and total sliding distance 100 m) were adopted based on the conditions of moving mechanical assemblies [22,29,31]. An Al_2O_3 (McMaster-Carr, USA) ball (Ø ~ 6.35 mm) was used as the counterface. The tribology testing procedure at different temperatures (i.e., room temperature (RT), and elevated temperature (HT)), and specific wear rate calculation using a non-contact optical profilometer (Zygo Corporation, USA) were explained in the previously published article [22,32]. It can be mentioned that for the elevated temperature (HT) wear tests, the furnace temperature was set at 450°C and the specimens were placed in the furnace. The surface of the coating was measured at around 300°C (i.e., using a thermocouple).

To characterize the phases after tribological testing, Raman analysis was performed using an InVia spectrometer (Renishaw, UK) on the unworn and worn coatings with an Ar^+ ion (λ = 514.5 nm) laser source. It can be mentioned that the Raman data of these $Co_{0.75}Ni_{0.25}O$ and $Co_{0.5}Ni_{0.5}O$ oxides are not available in the literature. Therefore, the deposited as-sprayed coatings were considered the baseline for the Raman shift to identify the phases of the wear tracks at RT and HT.

To understand the friction and wear mechanisms of the coatings at different temperatures, the wear tracks, and counter surfaces were observed under an SEM equipped with an EDS detector. Also, the sub-surface microstructure of the wear tracks was examined by cross sectioning the wear track perpendicular to the sliding direction. The samples with wear tracks were cold mounted first and then cut and polished to avoid the wear track's damage. Finally,

the sub-surface microstructures were observed under the SEM. Also, Electron Channeling Contrast Imaging (ECCI) (SU8230, Hitachi, Japan) was performed on the cross-sections of the coatings to reveal the sub-surface wear mechanisms.

6.3 Results

6.3.1 Coating analysis

Figure 6. 1 shows the XRD pattern of $Co_{0.75}Ni_{0.25}O$ and $Co_{0.5}Ni_{0.5}O$ powders and coatings. For the powders and coatings, only one set of peaks was observed, which was assigned to an *fcc* $Co_xNi_{1-x}O$ solid solution. This coating phase was similar to the powder phase, as highlighted in **Figure 6. 1 (a, b)**. Similar results with no phase change in HVOF-sprayed $Co_xNi_{1-x}O$ coatings were previously reported by Mohammadkhani et al. [26,30].

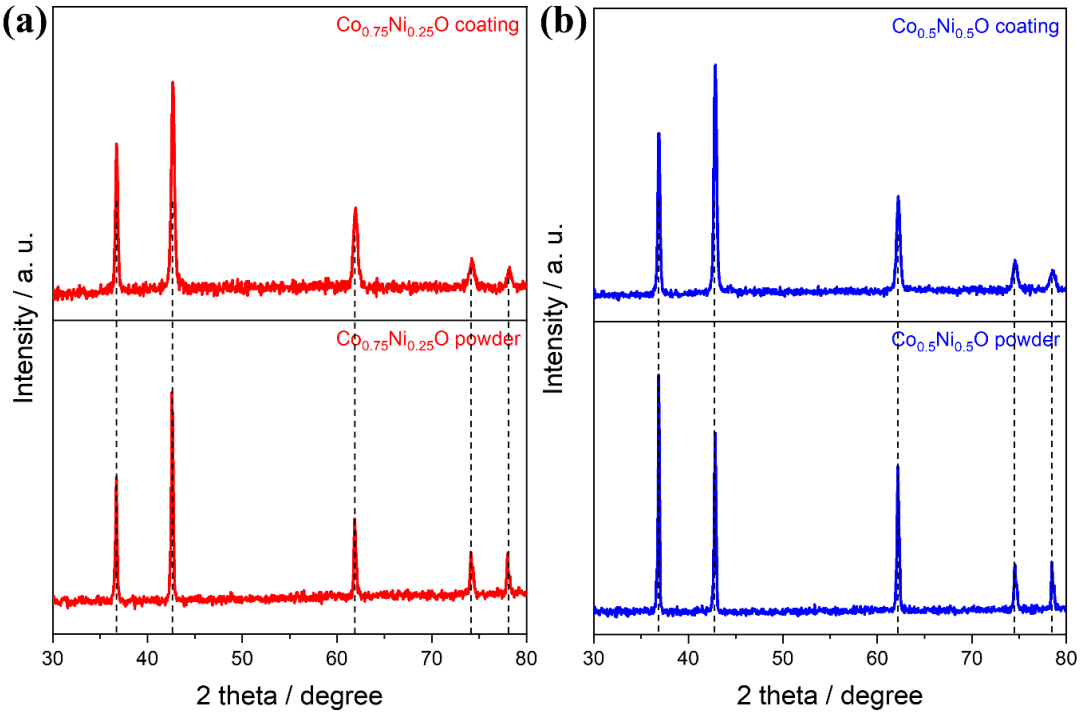

Figure 6. 1 : XRD pattern of (a) $Co_{0.75}Ni_{0.25}O$, and (b) $Co_{0.5}Ni_{0.5}O$ coatings prepared from the respective powders.

Low magnification BSE images of the $Co_{0.75}Ni_{0.25}O$ and $Co_{0.5}Ni_{0.5}O$ coatings with thicknesses of ~77 µm and ~165 µm, respectively, are shown in **Figure 6. 2**. The high magnification surface morphology and cross-section of the $Co_{0.75}Ni_{0.25}O$ coating are shown in **Figure 6. 3**. The EDS mapping of the corresponding surface and cross-section showed the homogeneous distribution of Co, Ni, and O elements [**Figure 6. 3 (a, b)**]. However, the distribution of the oxygen on the top surface was interrupted by the asperities (i.e., peaks and valleys). A similar observation was made for the $Co_{0.5}Ni_{0.5}O$ coating [**Figure 6. 3 (a, b)**]. The

homogeneous distribution of Co, Ni, and O indicated the solid solution phase of $Co_{0.75}Ni_{0.25}O$ and $Co_{0.5}Ni_{0.5}O$ coatings, which correlated well with the XRD results [**Figure 6. 1 (a, b)**]. The topography of both coatings was almost the same, i.e., fully molten, flattened splats with some angular particles on top. The detailed characteristics of the $Co_xNi_{1-x}O$ coatings (i.e., $Co_{0.75}Ni_{0.25}O$ and $Co_{0.5}Ni_{0.5}O$) are shown in **Table 6. 2**.

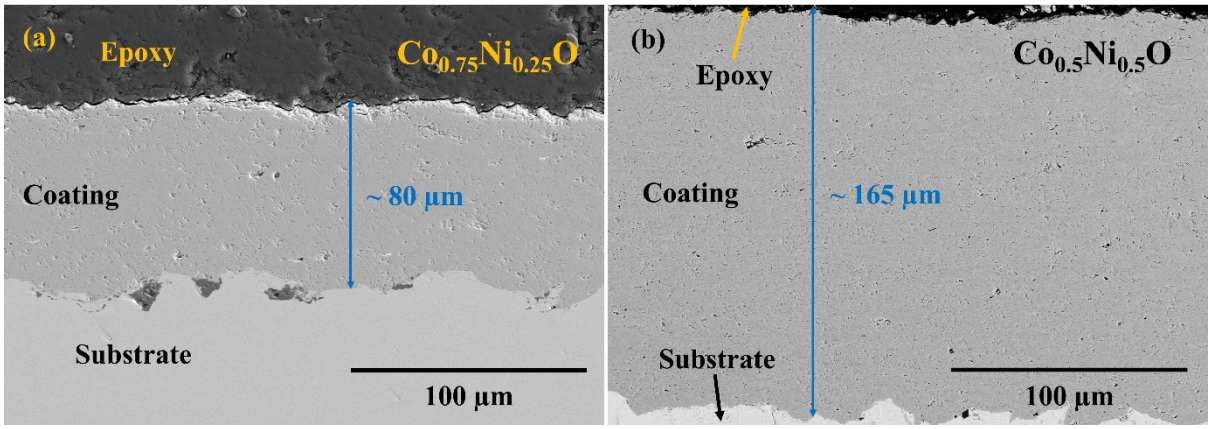

Figure 6. 2: SEM cross-section of (a) $Co_{0.75}Ni_{0.25}O$ and (b) $Co_{0.5}Ni_{0.5}O$

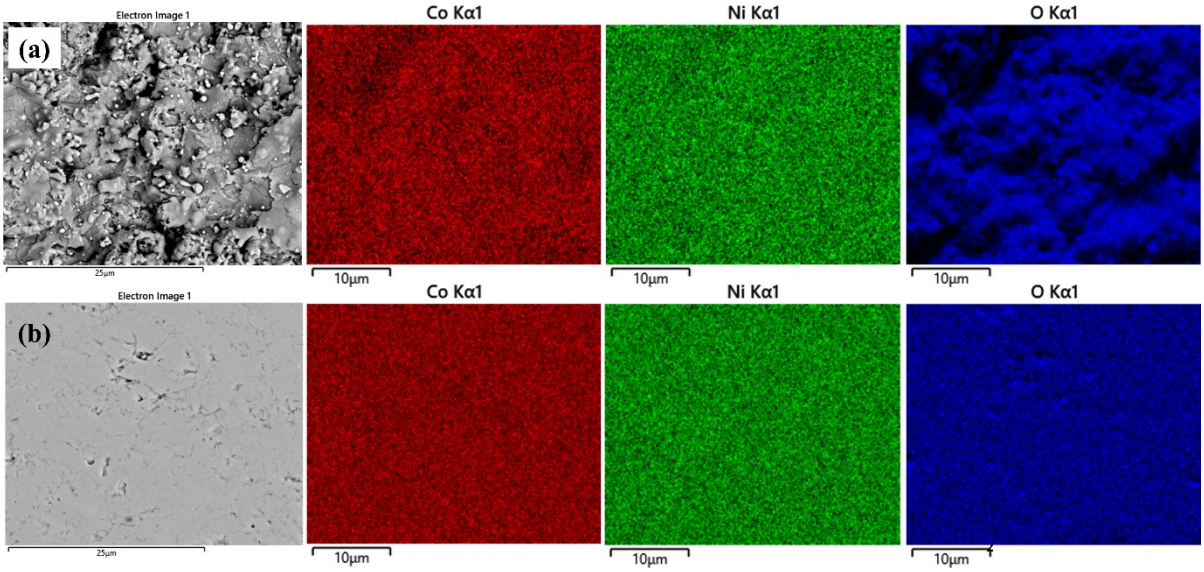

Figure 6. 3: SEM EDS color map of $Co_{0.75s}Ni_{0.25}O$ coating (a) top surface, (b) cross-section

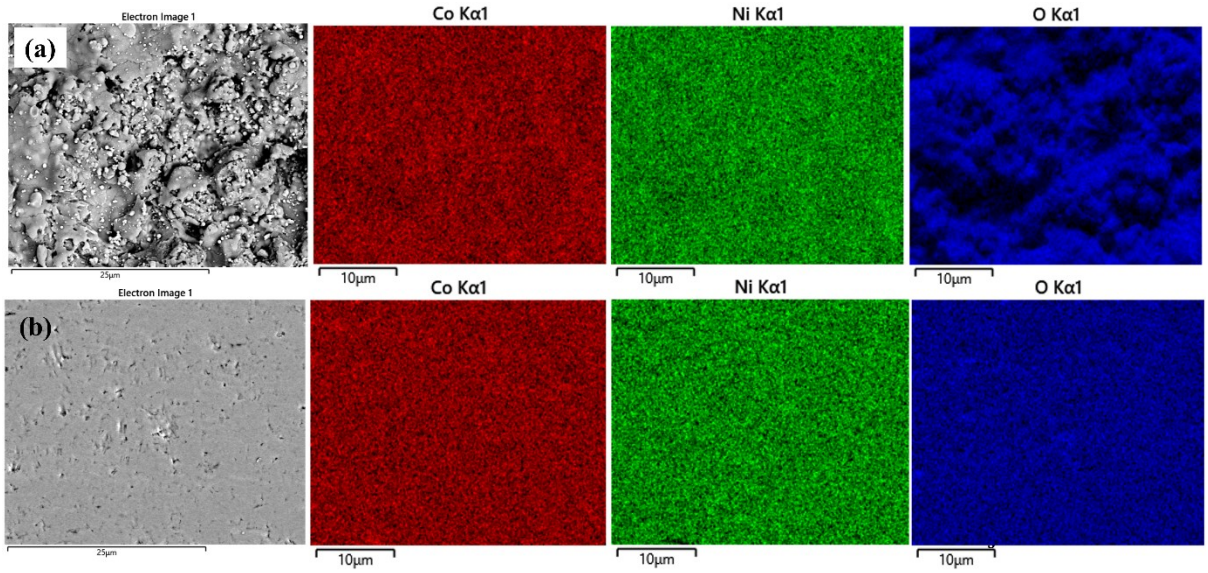

Figure 6. 4: SEM EDS color map of $Co_{0.5}Ni_{0.5}O$ coating (a) top surface, (b) cross-section

Table 6. 2: Characteristics of HVOF sprayed Co-Ni-O coatings

Coating	Thickness (µm)	Surface roughness (Sa)	Porosity (%)	Microhardness ($HV_{0.2}$)
$Co_{0.75}Ni_{0.25}O$	~ 80	~ 2.5 µm	< 2.0	~ 685 (RT)
				~ 594 (HT)
$Co_{0.5}Ni_{0.5}O$	~ 165	~ 2.5 µm	< 4.0	~ 764 (RT)
				~ 535 (HT)

To determine the grain size and grain orientation of the as-sprayed coatings and after exposure at 450°C, ECCI was performed on the $Co_{0.75}Ni_{0.25}O$ coating cross-sections near to the surface [**Figure 6. 5 (a-b); (c-d)**]. In general, all the particles were completely melted and there were no residues of unmelted particles, indicating sufficient velocity and temperatures of the in-flight particles. Also, some of the cracks were seen between the splat, indicating the poor cohesion between the grains. The authors believed that the grain sizes and distribution of the grains in the coatings were the same before and after heating at 450°C. However, some of the changes of the grains could be seen in two different conditions, however; this could be due to the variation of the selected area closer to the coating surfaces.

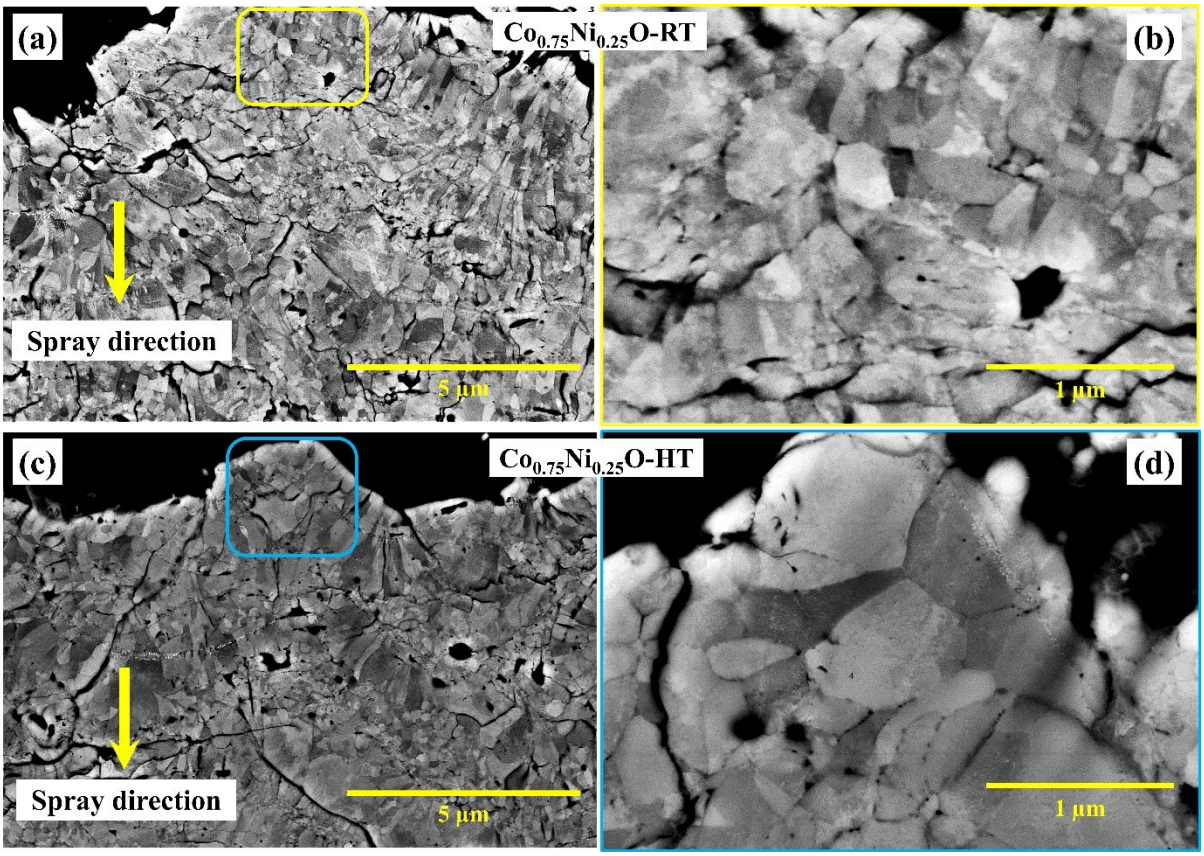

Figure 6. 5: Electron Channeling Contrast Imaging (ECCI) of the cross-section of $Co_{0.75}Ni_{0.25}O$ at RT (a-b) and after heating at 450°C (c-d)

The grain size and orientation of the $Co_{0.5}Ni_{0.5}O$ coatings before and after heating at 450°C are shown in **Figure 6. 6**. It can be seen that the grains were vertically oriented and had a lamellar structure with limited interfacial bonding. The authors believed that the grain size and orientation of the $Co_{0.5}Ni_{0.5}O$ coating after exposure to 450°C were the same as at RT [**Figure 6. 6 (a-b)**, and **Figure 6. 6 (c-d)**]. A wide distribution of microcracks, pores and limited compacted grains were visible on the coatings. The vertically oriented grains were not clearly visible due to the presence of lamellar porous structures. Also, some of white areas or spots were found on the grains or in the coating as a lamellar structure [**Figure 6. 6 (a-b)**, and **Figure 6. 6 (c-d)**]. An EDS mapping of these spots or zones showed the presence of Si, which came from the colloidal silica suspension (i.e., 0.4 µm) during polishing. The silica flowed or was trapped in the pores of the coatings due to the comparatively high porosity of $Co_{0.5}Ni_{0.5}O$ than $Co_{0.75}Ni_{0.25}O$ [**Table 6. 2**].

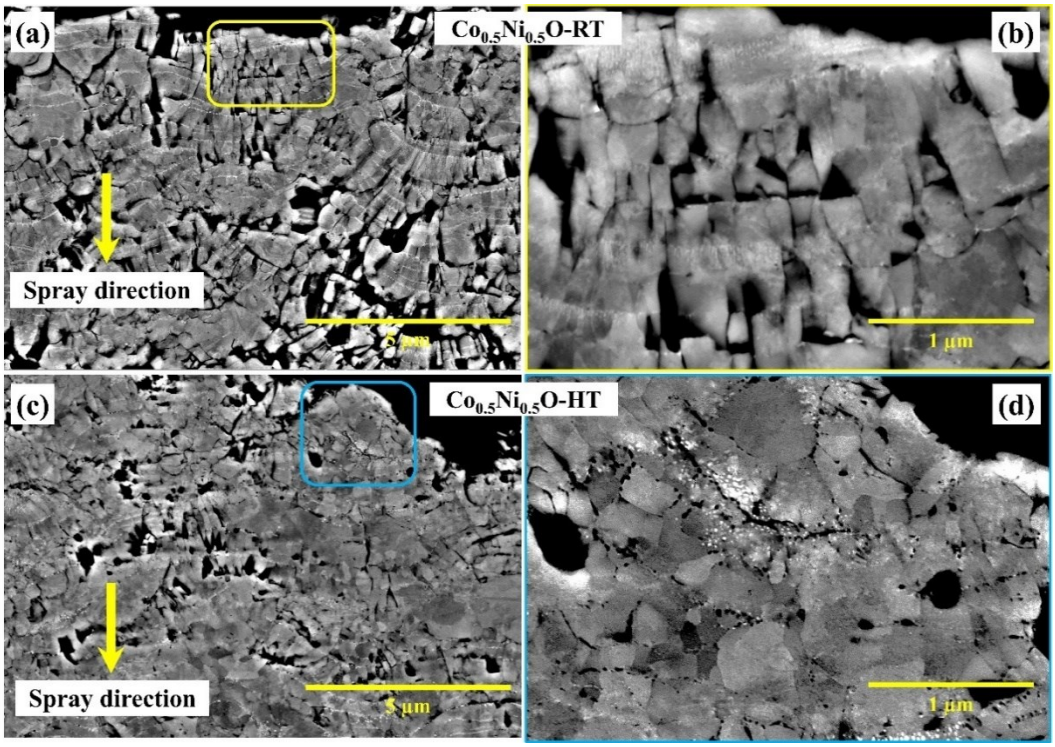

Figure 6. 6: Electron Channeling Contrast Imaging (ECCI) of the cross-section of $Co_{0.5}Ni_{0.5}O$ at RT (a-b) and after heating at 450°C (c-d)

The micro-hardness of the coatings performed at RT and HT is shown in **Figure 6. 7**. The hardness value of the $Co_{0.75}Ni_{0.25}O$ and $Co_{0.5}Ni_{0.5}O$ coating at RT and HT were 685 $HV_{0.2}$, ~594 $HV_{0.2}$, and ~764 $HV_{0.2}$, ~535 $HV_{0.2}$, respectively. No visible cracks were observed on the coatings during the microhardness experiment.

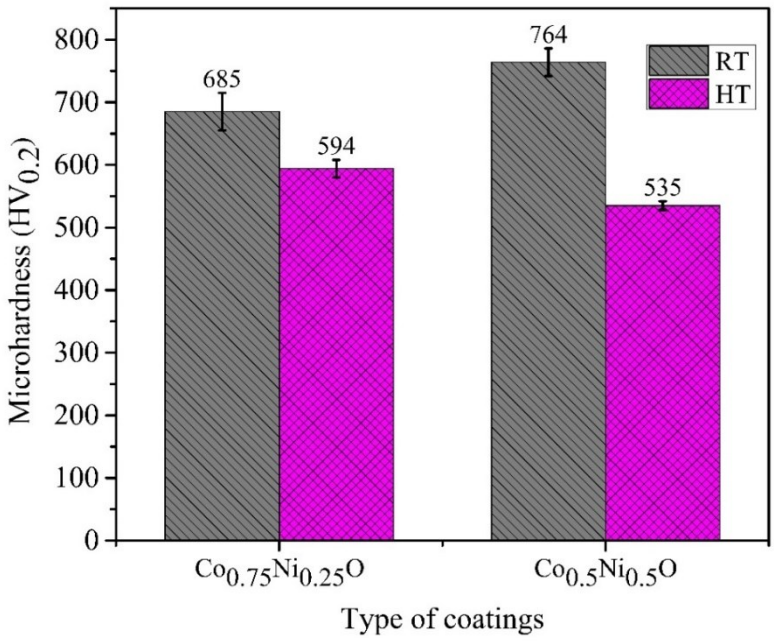

Figure 6. 7: Microhardness of $Co_{0.75}Ni_{0.25}O$ and $Co_{0.5}Ni_{0.5}O$ coatings at different temperatures

6.3.2 Sliding wear behavior

6.3.2.1 Coefficient of friction and specific wear rate

The friction coefficient vs number of cycles of Co-Ni-O coatings is shown in **Figure 6. 8**. At RT, the friction coefficient of $Co_{0.75}Ni_{0.25}O$ coating was above 0.4 upon initial sliding and then increased to approximately 0.61. On the other hand, at HT, $Co_{0.75}Ni_{0.25}O$ showed a stable friction coefficient from the beginning of the test and maintained the constant value of 0.6 throughout the end of the test. The trend of the $Co_{0.5}Ni_{0.5}O$ friction behavior was similar to that of $Co_{0.75}Ni_{0.25}O$ coating at RT but showed a shorter running-in period and maintained low and stable friction coefficient of 0.49 until the end of sliding. Meanwhile, $Co_{0.5}Ni_{0.5}O$ coating exhibited higher friction coefficient (i.e., 0.68) with large fluctuations at HT.

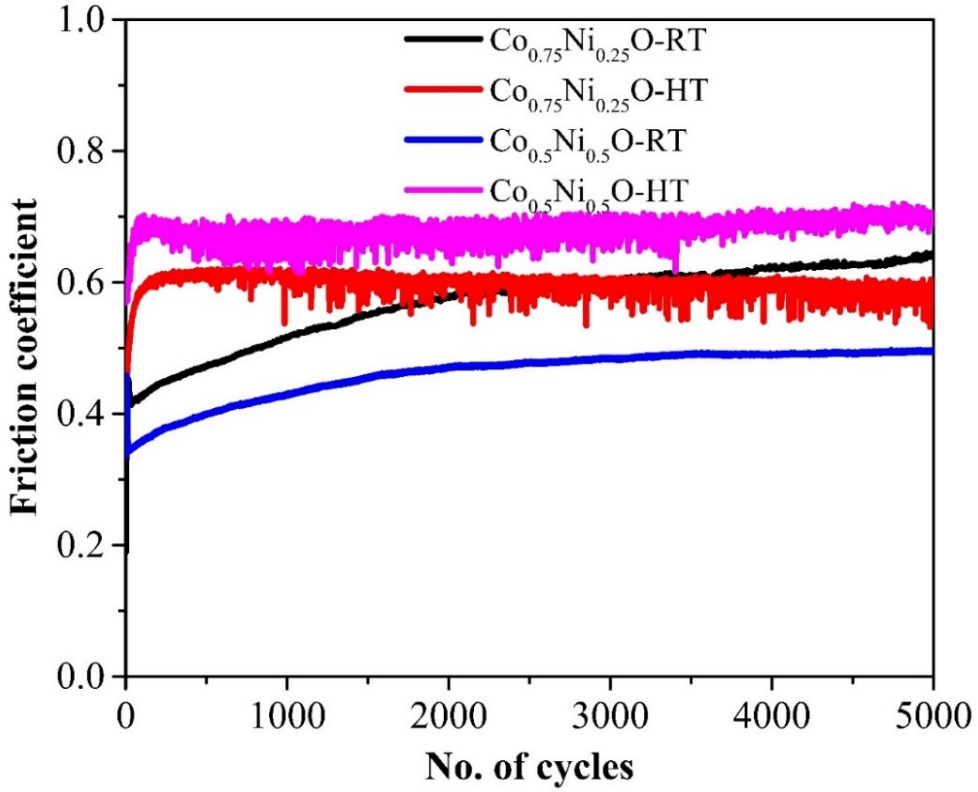

Figure 6. 8: Friction coefficient vs no. of cycles of Co-Ni-O coatings at different temperatures

The specific wear rate of $Co_{0.75}Ni_{0.25}O$ and $Co_{0.5}Ni_{0.5}O$ coatings at RT and HT is shown in **Figure 6. 9**. The wear rate of the $Co_{0.75}Ni_{0.25}O$ at RT and HT was ~ 26 ± 4.00 $\times 10^{-6}$ mm^3/Nm and ~ 24 ± 3.30 $\times 10^{-6}$ mm^3/Nm, respectively. On the other hand, the wear rate of $Co_{0.5}Ni_{0.5}O$ was 8.3 ± 3.3 $\times 10^{-6}$ mm^3/Nm and 888 ± 10.6 $\times 10^{-6}$ mm^3/Nm at RT and HT, respectively. The wear rate of the $Co_{0.5}Ni_{0.5}O$ coating was much higher at HT than at RT. Similarly, the $Co_{0.5}Ni_{0.5}O$ coating at HT, showed significantly lower wear resistance than $Co_{0.75}Ni_{0.25}O$ (i.e.,

RT and HT). The friction coefficient and wear rate of the $Co_{0.75}Ni_{0.25}O$ and $Co_{0.5}Ni_{0.5}O$ coatings at RT and HT summarized in **Table 6. 3**.

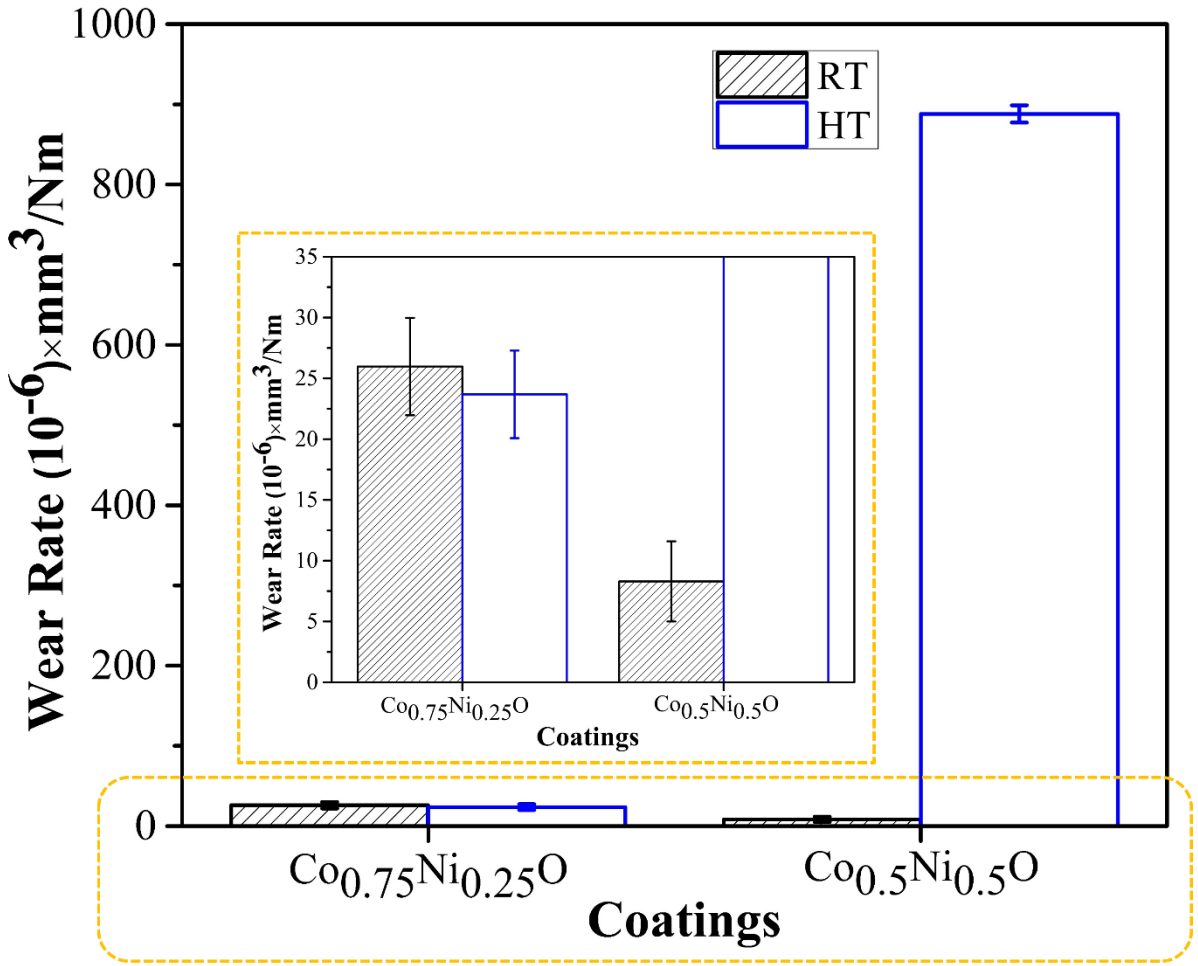

Figure 6. 9: Specific wear rate of Co-Ni-O coatings at RT and HT

Table 6. 3: Average coefficient of friction and specific wear rate

Coating	Testing condition	Friction coefficient	Specific wear rate (10^{-6} mm^3/Nm)
$Co_{0.75}Ni_{0.25}O$	RT	0.61 ± 0.02	25.97 ± 4.00
	HT	0.60 ± 0.01	23.68 ± 3.60
$Co_{0.5}Ni_{0.5}O$	RT	0.49 ± 0.01	8.30 ± 3.30
	HT	0.68 ± 0.02	888 ± 10.66

6.3.2.2 Worn surface morphologies

Figure 6. 10 shows the SEM wear tracks of the $Co_{0.75}Ni_{0.25}O$ after dry sliding tests at RT and HT. **Figure 6. 10 (a-b)** shows the deep abrasive mark along the sliding direction with some grooves or grain pull out on the wear tracks. The grain pulls out were mainly found in the ceramics where the boundaries of the surface grains were weaker and hence removed as the wear debris during sliding [34]. Furthermore, this wear debris can also be produced at the beginning of the test cycles due to the removal of the asperities. A comparatively smooth smeared surface with some shallow abrasive marks was observed on the wear tracks of HT [**Figure 6. 10 (c-d)**]. An EDS elemental mapping showed the homogeneous distribution of Co, Ni and O on the wear tracks at both RT and HT.

Similarly, the SEM wear surface morphologies of the $Co_{0.5}Ni_{0.5}O$ coating at RT and HT are shown in **Figure 6. 11**. The abrasive grooves in the sliding direction were observed on the wear track at RT **[Figure 6. 11 (a)**]. Interestingly, the wear track width of this coating was much smaller at RT than at HT and even much smaller than the wear tracks of $Co_{0.75}Ni_{0.25}O$ (i.e., RT, and HT). The high magnification BSE image showed the smeared smooth surfaces, and its EDS elemental mapping revealed the homogeneous distribution of Co, Ni and O **[Figure 6. 11 (b)**]. On the other hand, the significant smeared zones were observed on the worn surfaces at HT **[Figure 6. 11 (c)**]. Moreover, the presence of smeared surface as well as larger number of small debris with brittle fractures was witnessed on the high magnification BSE image **[Figure 6. 11 (d)**]. Despite the change in wear mechanisms at HT, the same phase and homogeneous distribution of Co, Ni and O elements were still present.

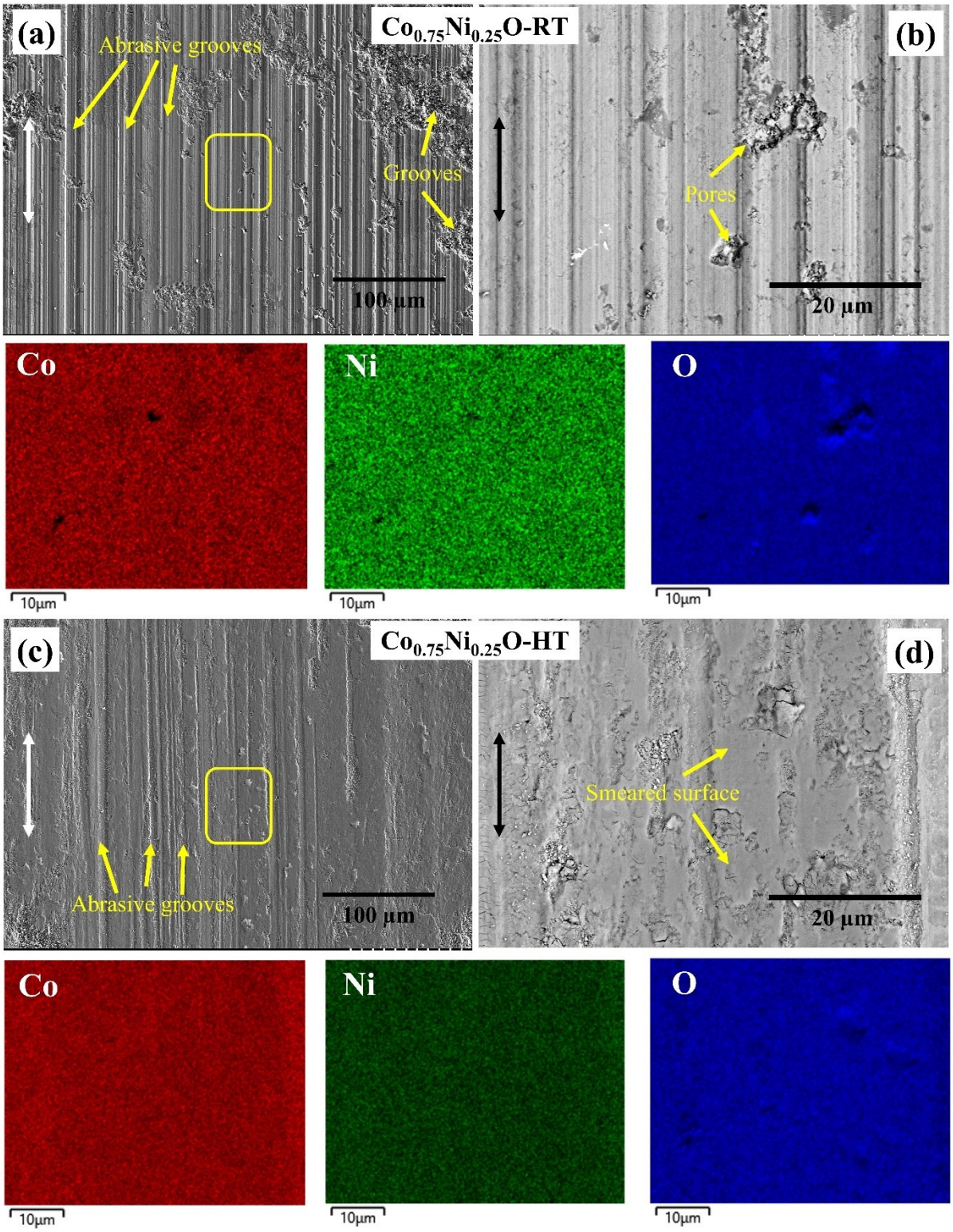

Figure 6. 10: (a-c) Secondary SEM, (b-d) BSE images and their corresponding EDS mapping of $Co_{0.75}Ni_{0.25}O$ at RT and HT. ↕ indicate sliding directions

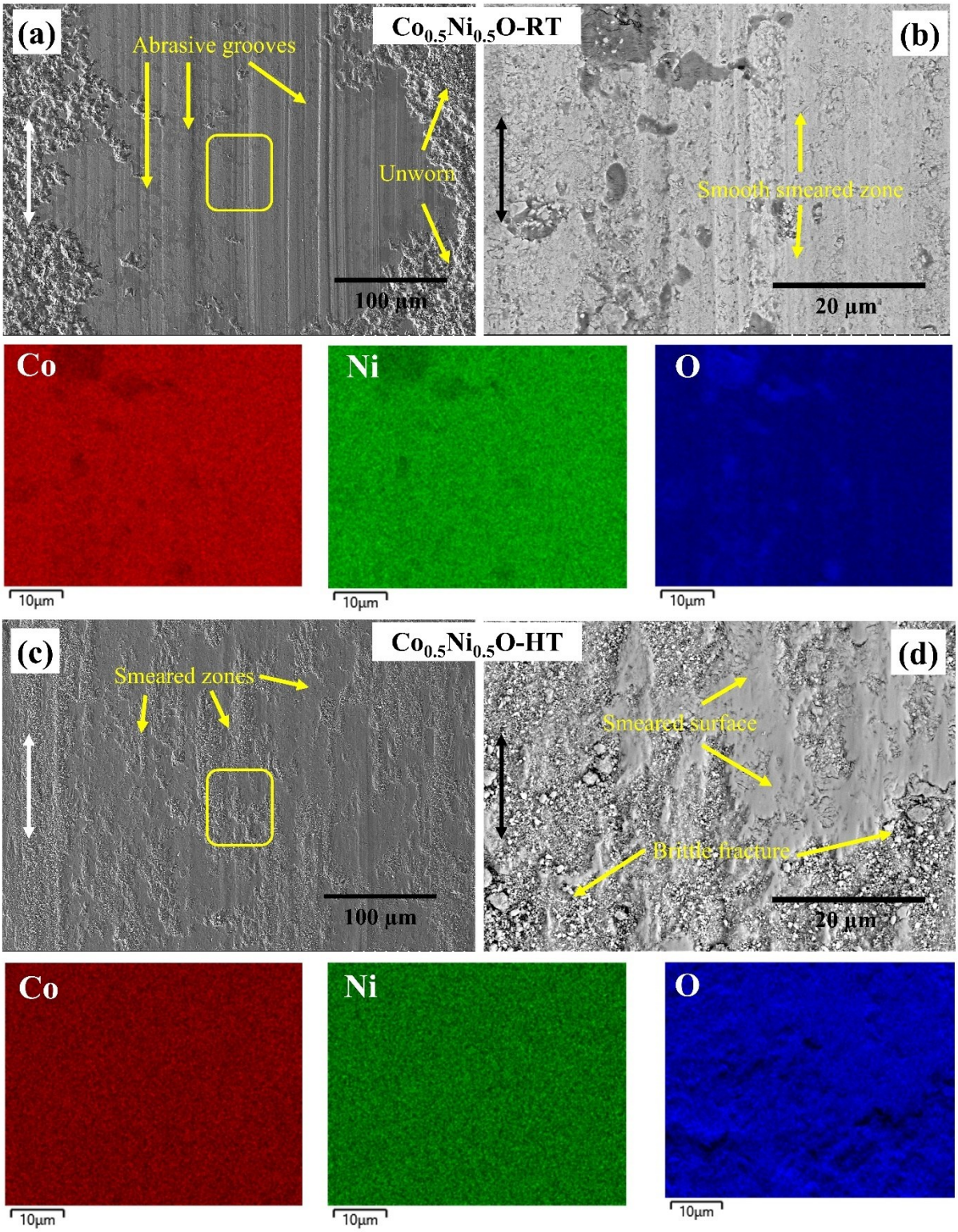

Figure 6. 11: (a-c) Secondary SEM, (b-d) BSE images and their corresponding EDS mapping of $Co_{0.5}Ni_{0.5}O$ at RT and HT. ↕ indicate sliding directions.

6.3.2.3 Subsurface analysis

$Co_{0.75}Ni_{0.25}O$ subsurface: The subsurface microstructures provide the information about the friction and wear behavior of the materials. The change in material properties and microstructure in the subsurface (i.e., underneath the wear track) could be altered or modified by the stress transfer or contact conditions during sliding, thus influencing the friction and wear mechanisms [31,35]. The ECCI of the cross-section of the wear tracks perpendicular to the sliding direction is shown in **Figure 6. 12 (a-d)**. The figure shows the delamination of the coating closer to the surface. Subsurface crack wear also propagated [**Figure 6. 12 (a-b)**]. The sub-micron elongated grain can be observed closer to the surface. These features were observed throughout the subsurface wear track. In addition, the mixed grains, (i.e., small, large, and deformed), were observed in the subsurface wear track. No significant variation of the grains was observed in the sub-surface. The EDS mapping of **Figure 6. 12 (a)**. showed no variation in the distribution of Co, Ni and O on the sub-surface wear tracks [**Figure 6. 12 (e)**]. On the other hand, the ECCI subsurface microstructures of the wear track after sliding at HT are shown in **Figure 6. 13 (a-d)**. The more refined grains were observed closer to the wear tracks at HT as compared to RT. All of the grains were in the ultra-nano or nano size range. However, the larger grains (i.e., nano, or sub-micron grains) were observed below the ultra-nano size grains [**Figure 6. 13 (d-e)**]. In general, the different color or contrast of the grains indicated the same phases but the different orientations in the lattice position. Additionally, the cracks were propagated horizontally below the compacted or sintered refined grains which was similar to the RT wear tracks subsurface [**Figure 6. 12 (a-b)**]. The EDS mapping of **Figure 6. 13 (a)** showed the homogeneous distribution of Co, Ni and O **Figure 6. 13 (e)**. However, the thin uniform distribution of Co and O was observed closer to the wear track surface which could related to the CoO phase as identified by the Raman analysis [**Figure 6. 16** (a)]. Moreover, the cracking, debris formation and detachment of the coating from the worn surface at HT [**Figure 6. 13 (a)**, and **(e)]**, was less than that at RT [**Figure 6. 12 (a)**, and **(e)**].

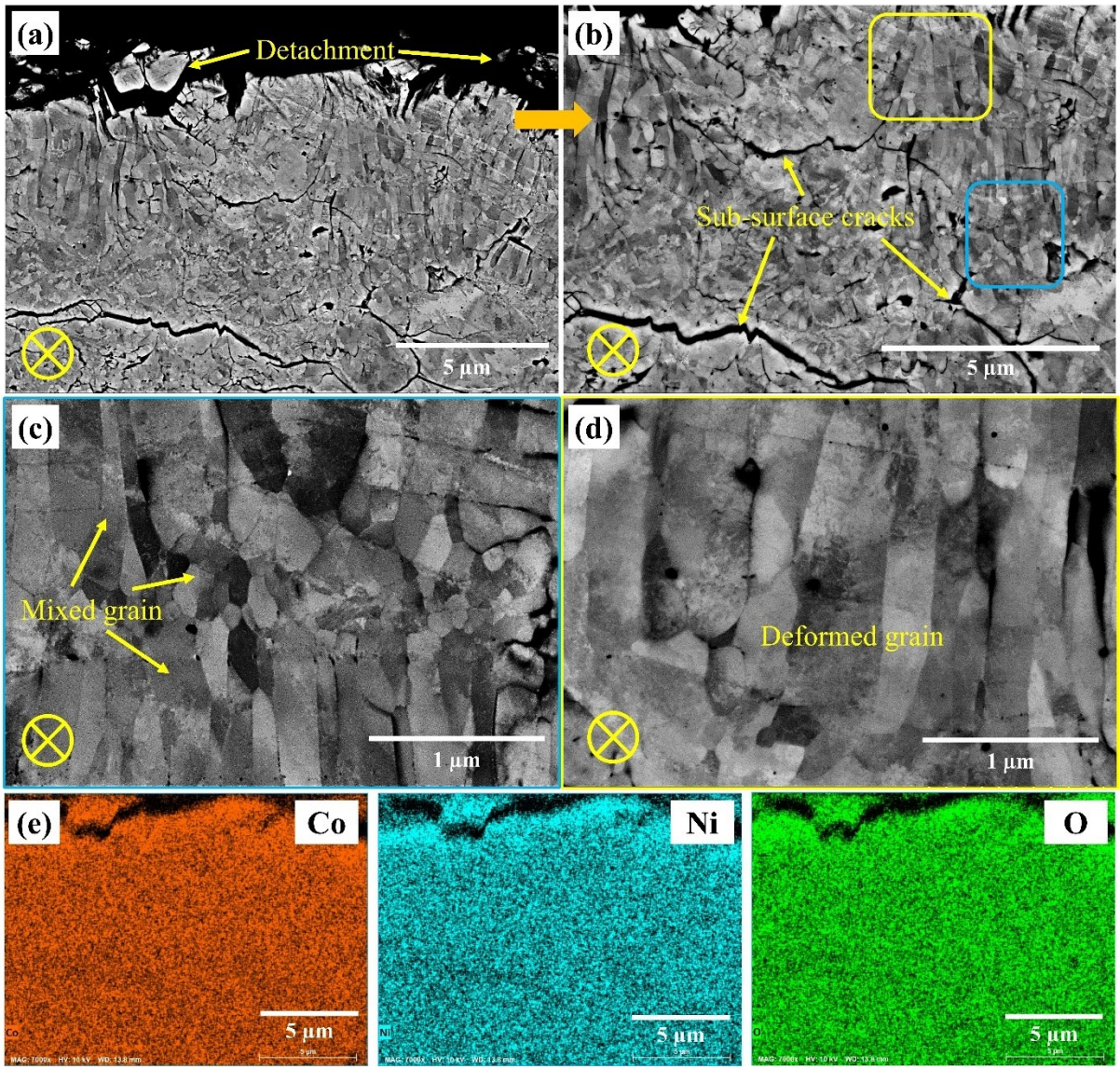

Figure 6. 12: ECCI image of $Co_{0.75}Ni_{0.25}O$ (a-d) worn subsurfaces and corresponding (e) SEM/EDS mapping of (a) at RT. ⊗ indicate sliding directions.

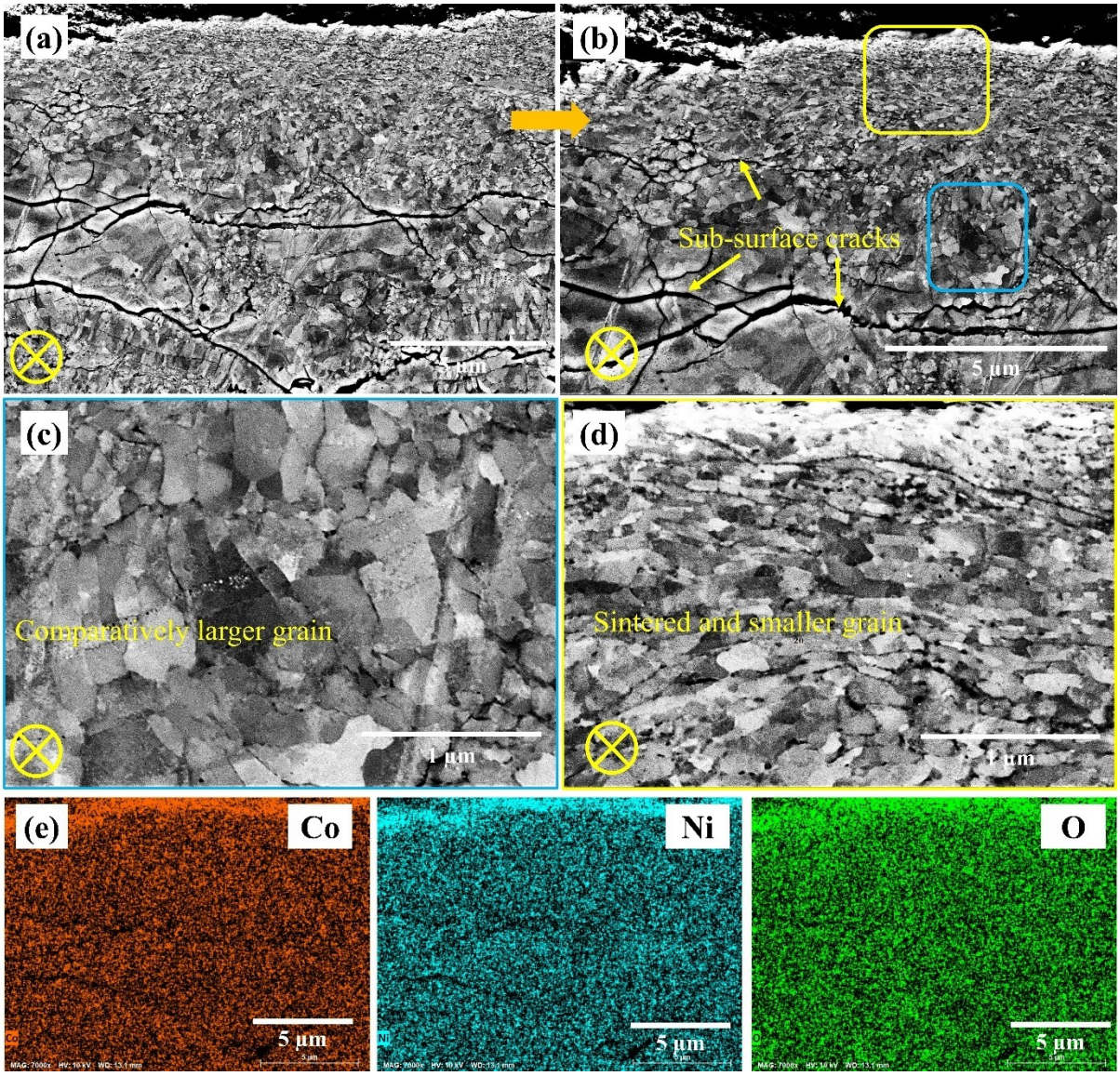

Figure 6. 13: ECCI image of $Co_{0.75}Ni_{0.25}O$ (a-d) worn subsurface and corresponding (e) SEM/EDS mapping of (a) at HT. ⊗ indicate sliding directions.

$Co_{0.5}Ni_{0.5}O$ subsurface: The subsurface wear track cross-section of the $Co_{0.5}Ni_{0.5}O$ coating at RT is shown in **Figure 6. 14 (a-b)**. A lamellar porous microstructure with similar grain sizes and orientations was noticed throughout the subsurface. The grains were clearly visible within the dense and compacted regions, indicating good sintering as compared to the porous zones **Figure 6. 14 (c-d)**. Some of the cracks were also observed between the grain boundaries. Based on the grain distribution and cohesion between the grains, it can be said that the wear mechanisms could be brittle fracture [36]. Additionally, the lamellar white dotted lines were observed in the subsurface wear tracks. Closer inspection or high magnification of these white zones showed the presence of Si (not shown here) as explained previously. Similarly, the EDS

mapping of **Figure 6. 14 (a)** showed the homogeneous distribution of Co, Ni, and O with no variation in at% for $Co_{0.5}Ni_{0.5}O$.

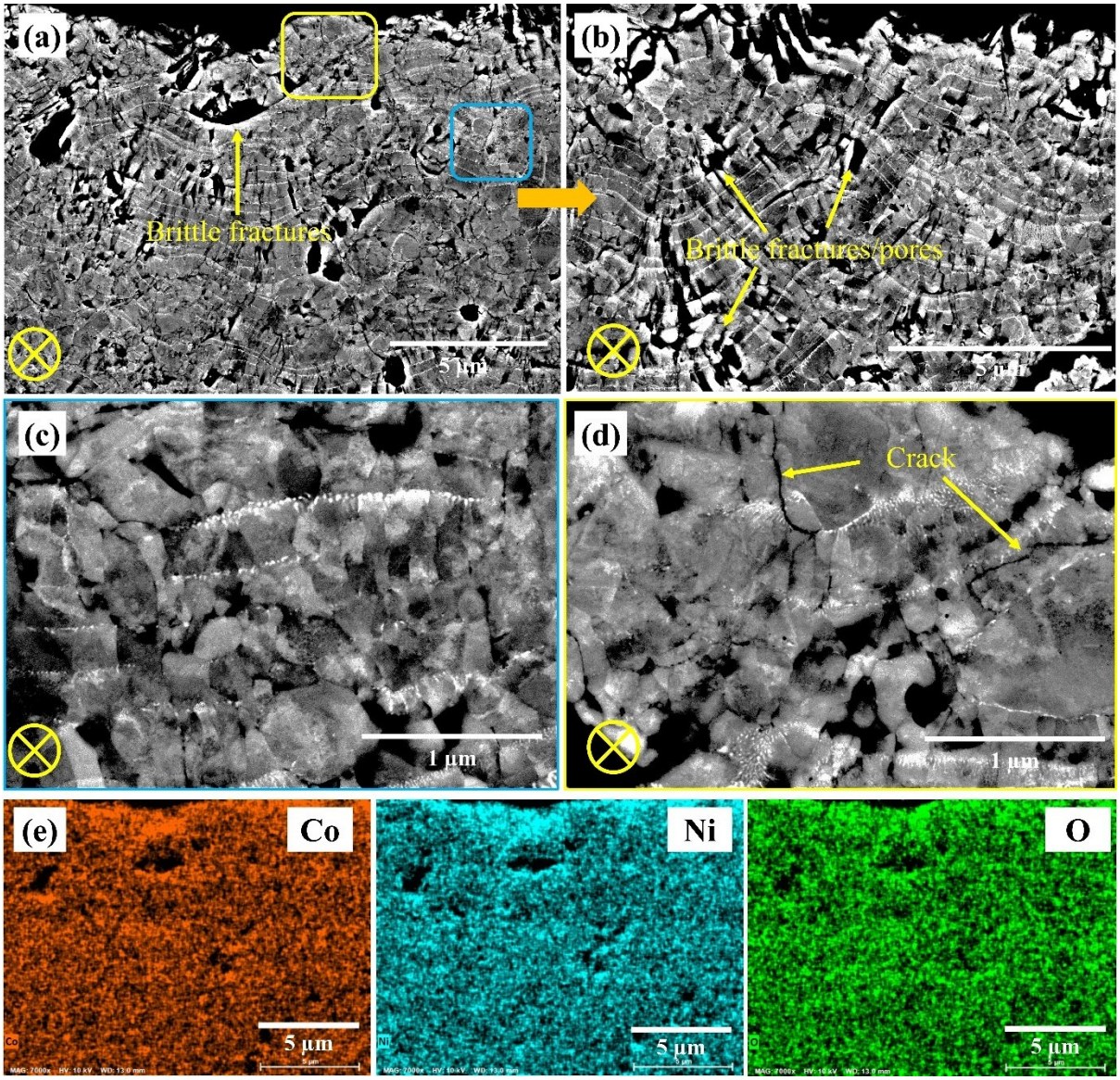

Figure 6. 14: ECCI image of $Co_{0.5}Ni_{0.5}O$ (a-d) worn subsurface and corresponding (e) SEM/EDS mapping of (a) at RT. ⊗ indicate sliding directions.

The wear track sub-surface of the $Co_{0.5}Ni_{0.5}O$ coating after 5000 cycles of dry sliding at HT is shown in **Figure 6. 15 (a-d)**. The detachment of the coatings closer to the wear tracks and a significant number of debris formation were observed on the coating cross-section. Additionally, the sintering or compaction of the grains was not homogeneously distributed closer to the wear tracks. Furthermore, the presence of the elongated pores with lamellar porous microstructures was observed in the subsurface. The high magnification ECCI images of the compacted zones closer to the wear tracks showed the larger grains with cracks within the grain boundaries [**Figure 6. 15 (c)**]. Nearly identical grain sizes with large pore distributions were

observed much deeper from the wear marks. No changes in the $Co_{0.5}Ni_{0.5}O$ solid solution were observed in the subsurface wear tracks [**Figure 6. 15 (e)**].

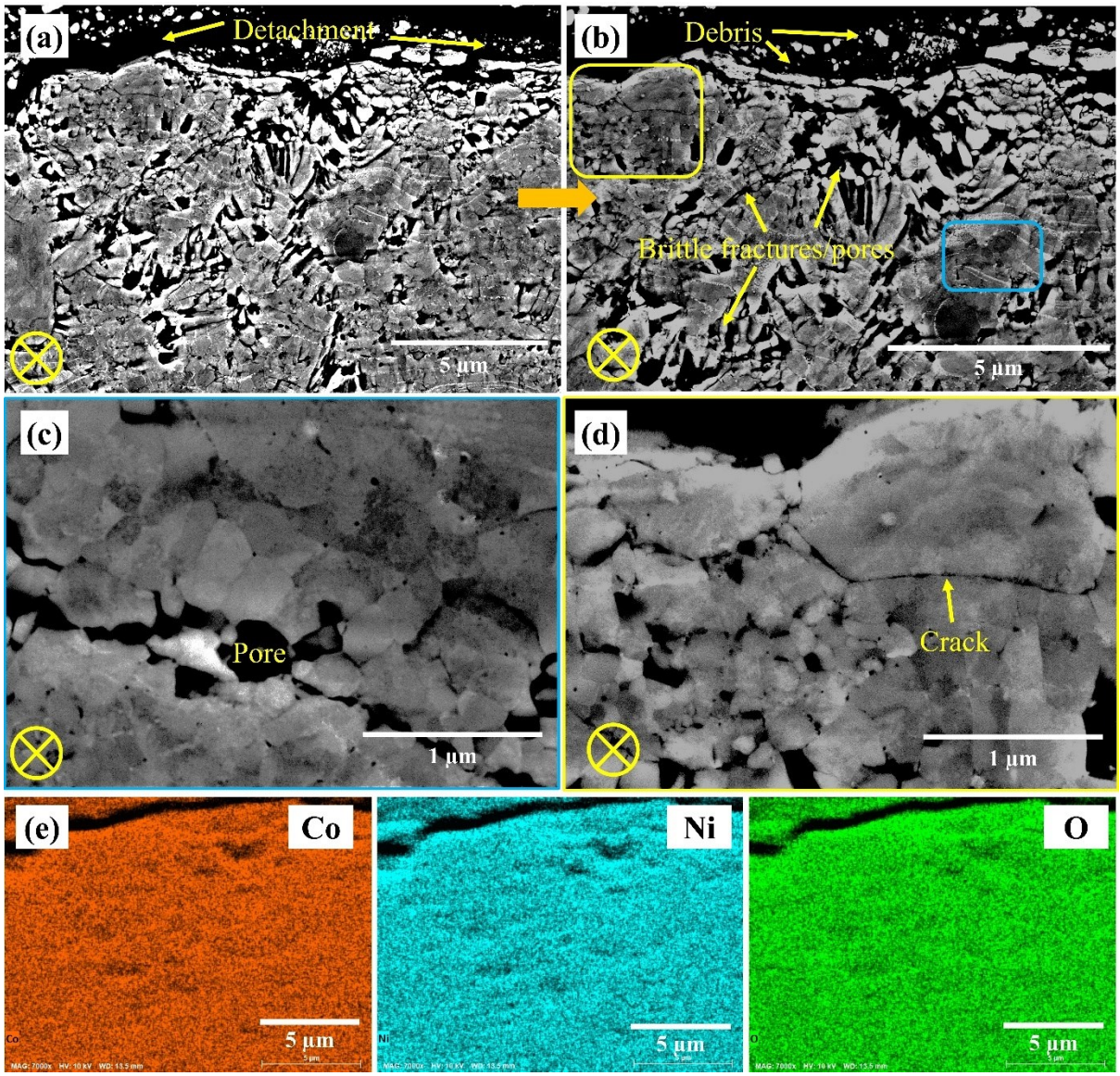

Figure 6. 15: ECCI image of $Co_{0.5}Ni_{0.5}O$ (a-d) worn subsurface and corresponding (e) SEM/EDS mapping of (a) at HT. ⊗ indicate sliding directions.

6.3.2.4 Raman analysis

A Raman analysis was performed on the deposited coatings and the worn surfaces (i.e., $Co_{0.75}Ni_{0.25}O$ and $Co_{0.5}Ni_{0.5}O$) after the RT and HT wear test, as shown in **Figure 6. 16**. The Raman analysis of the $Co_{0.75}Ni_{0.25}O$ and $Co_{0.5}Ni_{0.5}O$ coatings correlated well with the XRD analysis [**Figure 6. 1**]. It should be noted that the wavenumber or Raman shift for these $Co_{0.75}Ni_{0.25}O$ and $Co_{0.5}Ni_{0.5}O$ oxides is not available in the literature. Therefore, the Raman

shift (cm^{-1}) obtained from the deposited coatings was considered as the baseline since they did undergo any phase transformation from the powder particles [**Figure 6. 1**]. The characteristic peaks (Raman shifts) for the deposited $Co_{0.75}Ni_{0.25}O$ coatings were 530 cm^{-1}, 681 cm^{-1}, and 1080 cm^{-1} [**Figure 6. 16 (a)**]. Moreover, the characteristic peaks at Raman shift 180 cm^{-1} ,477 cm^{-1}, 516 cm^{-1}, 680 cm^{-1}, and 1080 cm^{-1} the worn coatings at HT corresponding to the CoO and NiO phase, respectively [**Figure 6. 16 (a)**] [14,37,38]. The presence of frequent Raman shifts of CoO at HT wear track could be related to the presence of thin CoO layer on the sub-surface wear track [**Figure 6. 13** (e)]. The peak at Raman shifts 534 cm^{-1} and 1056 cm^{-1} correspond to the $Co_{0.5}Ni_{0.5}O$ phase obtained on the coatings and after sliding at RT. An additional peak at Raman shift 545 cm^{-1} at HT could corresponds to NiO phase [**Figure 6. 16 (b)**]. It should be noted that more detailed analysis needs to be performed in order to fully understand the different phases presents.

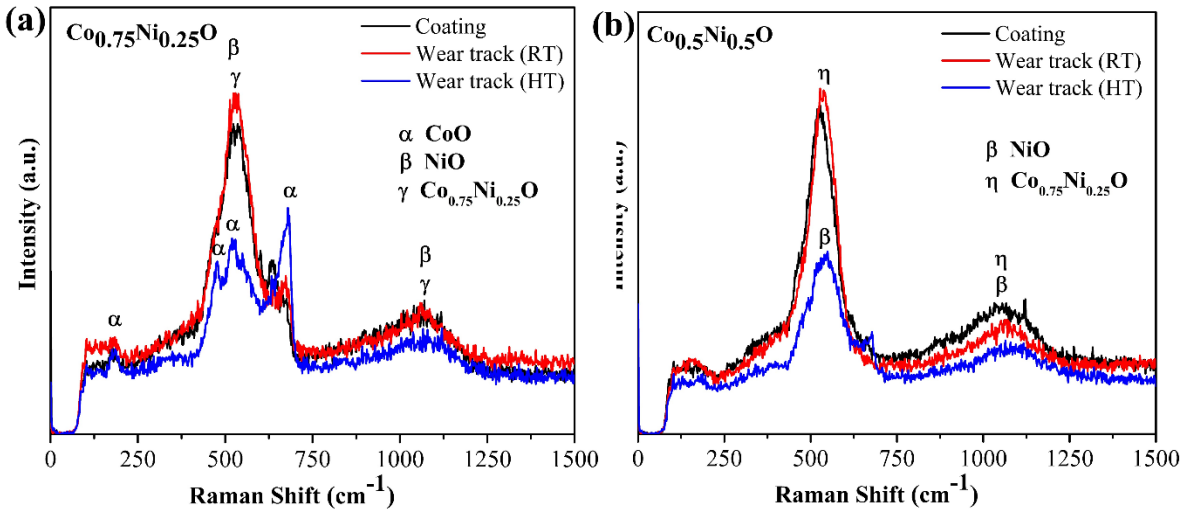

Figure 6. 16: Raman spectrum of unworn and worn coatings at (a) 25°C and (b) 300°C

6.3.2.5 Counterface analysis

$Co_{0.75}Ni_{0.25}O$ Counterface: SEM images of the Al_2O_3 counterballs at the end of 100 m dry sliding distance mated against the $Co_{0.75}Ni_{0.25}O$ coating at RT and HT are shown in **Figure 6. 17**. At RT, the shape of the counterface contact was elliptical and severe abrasive grooves were observed in the sliding direction. These grooves were mainly due to the abrasion and three-body wear caused by the entrapped wear debris during reciprocating sliding. Additionally, the transfer film was not homogeneous within the contact zone and few grooves were covered by the coating materials. Overall, the RT counterface was governed by abrasive wear mechanisms similar to worn surface mechanisms [**Figure 6. 10 (a-b)**]. The high magnification EDS layered

structure, and mapping showed the distribution of coating elements (i.e., Co, Ni, O) on the Al_2O_3 counterface contacts [**Figure 6. 17 (b)**]. It showed that the some of the abrasive grooves were filled with Co, Ni, and O (i.e., predominantly with Co and Ni oxides). In contrast, the HT counterface was circular in shape rather than elliptical as shown in [**Figure 6. 17 (c)**]. An adhesive transfer film along with abrasive grooves were observed on the contact surfaces. However, the counter surface was covered mainly with Co and O (i.e., cobalt oxides) [**Figure 6. 17 (d)**].

$Co_{0.5}Ni_{0.5}O$ Counterface: The counterface of the $Co_{0.5}Ni_{0.5}O$ coating at RT showed the abrasive behavior in the sliding direction as shown in **Figure 6. 18 (a)**. The EDS layer and elemental mapping showed the discrete distribution of the transferfilm [**Figure 6. 18 (b)**]. The uneven presence of the transferfilm elements (i.e., Co, Ni and O) caused the high wear of the counterballs at RT compared to the counterballs of $Co_{0.75}Ni_{0.25}O$ at RT and HT [**Table 6. 4**]. However, the contact area of the HT countersurface was comparatively larger than that of the RT counterface [**Figure 6. 18 (c) and inset]**. It was assumed that the counterballs were first worn-down during sliding and then filled with the coating materials. Mapping showed the thick coverage of the Ni, Co, and O on the counterball surface RT [**Figure 6. 18 (d)]**. Therefore, the wear rate of this counterball at HT was much higher than that at RT, as well as that of the $Co_{0.75}Ni_{0.25}O$ counterball [**Table 6. 4**].

Table 6. 4: Wear rate of counterface Al_2O_3 against $Co_{0.75}Ni_{0.25}O$ and $Co_{0.5}Ni_{0.5}O$ coatings at RT and HT after dry sliding wear testing.

Coating	Testing Condition	Counterface Wear Rate×10^{-6} (mm^3/Nm)
$Co_{0.75}Ni_{0.25}O$	RT	1.88 ± 0.12
	HT	1.56 ± 0.21
$Co_{0.5}Ni_{0.5}O$	RT	6.35 ± 0.25
	HT	21.2 ± 0.27

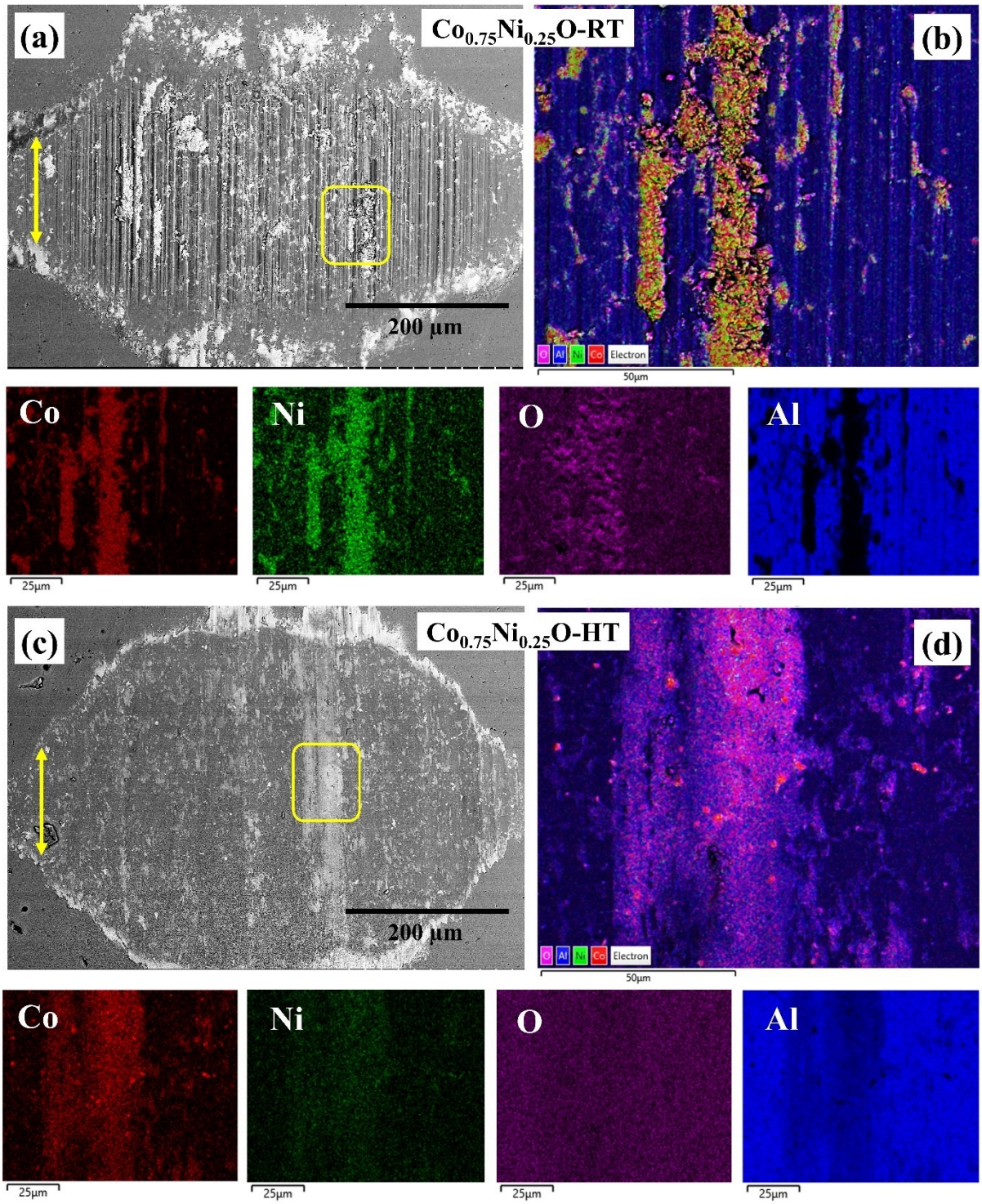

Figure 6. 17: (a-c) SEM image, and high magnification (b-d) EDS layered structures and corresponding elemental map distribution of alumina countersurfaces against $Co_{0.75}Ni_{0.25}O$ coating at RT and HT, respectively. ↕ indicate sliding directions.

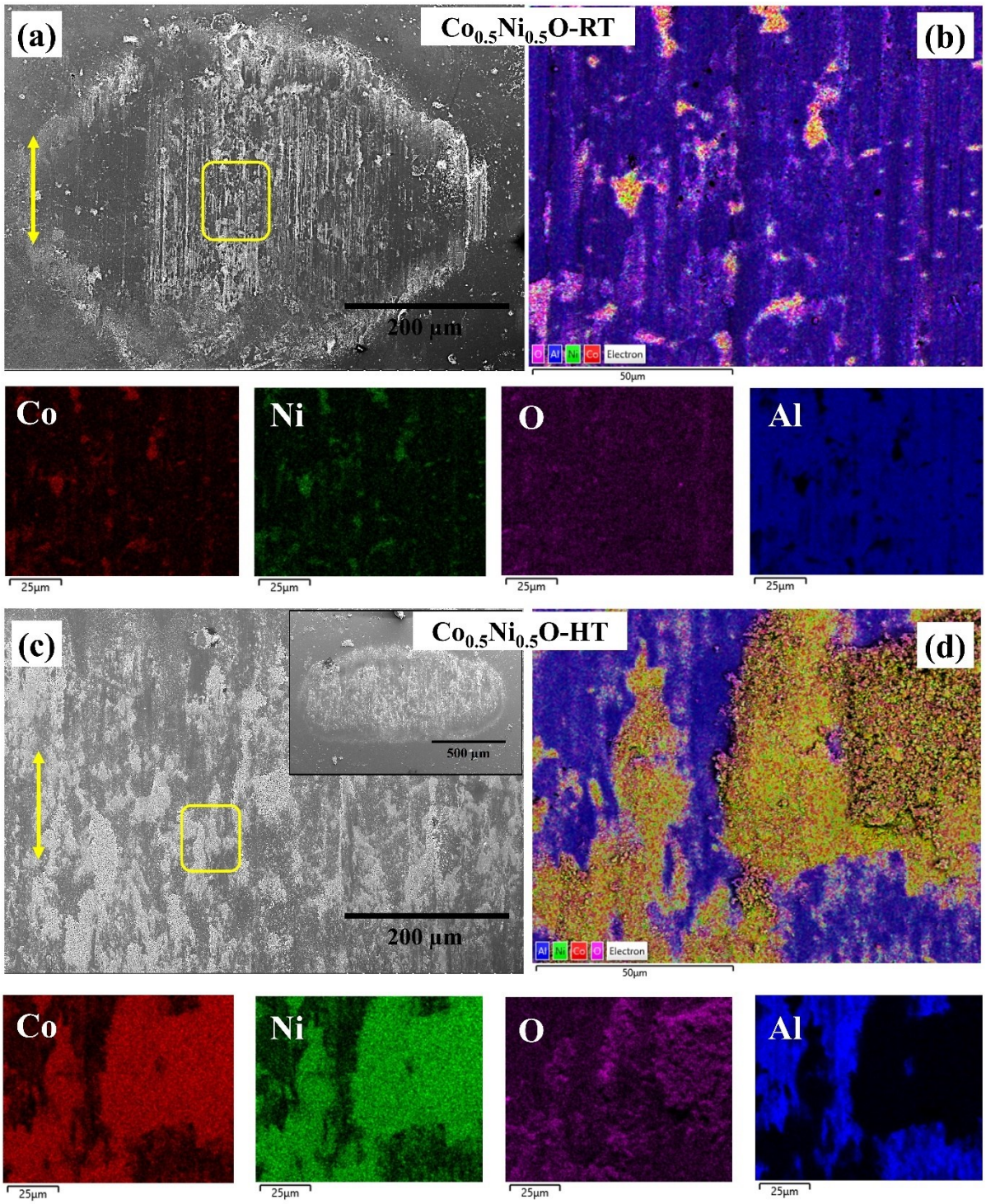

Figure 6. 18: (a-c) SEM image, and high magnification (b-d) EDS layered structures and corresponding elemental map distribution of alumina countersurfaces against $Co_{0.5}Ni_{0.5}O$ coating at RT and HT, respectively. ↕ indicate sliding directions.

s

6.4 Discussion

6.4.1 Coating characteristics

The presence of the fully molten, flattened splats with a continuous smooth top surface of the as-sprayed coatings and dense microstructure with limited porosity could be due to the high velocity and temperatures of the inflight particles [**Table 6. 2**] [26,29,30]. The visible pores [**Figure 6. 3 (b), Figure 6. 4 (b)**] on the coating cross-section could be caused by material shrinkage on cooling from the liquid state, shadowing effect, and poor wetting onto the adjacent surface of the droplets [39]. However, the porosity of the as-sprayed coatings was strongly influenced by the deformability, the wetting properties of the deposited particles, and flame chemistry [40]. Additionally, the surface roughness of the sprayed oxides was comparatively lower than that of other plasma sprayed processes due to the good spreading behavior of the particles in the HVOF process [28,41]. It should be noted that the roughness and porosity of the coatings can be significantly influenced by the degree of melting of the feedstock particles, spray parameters, substrate surface chemistry, and the nature of molten droplets on the substrate [36,42,43].

From the ECCI [**Figure 6. 5**], it can be seen that the micron-sized grains closer to the surface were oriented vertically inclined, which could be due to the impact of the particles perpendicular to the substrates during spraying [26,29,44]. A similar orientation and deformation of the grains was observed for $Co_{0.5}Ni_{0.5}O$ coatings in **Figure 6. 6**. However, the large pores and cracks made it difficult to clearly see the grain orientation and sizes. The large pores and cracks between splats or grains could be due to the sufficiently deposited molten particles. The researchers previously observed that the thermally sprayed ceramic coating usually has a lamellar porous structure, especially when the coating was mainly deposited by sufficiently molten spray particles [36]. This is true for HVOF sprayed coatings because the powder particles were ejected at an in-flight particle temperature of > 1900°C [**Table 6. 2**]. Moreover, three different types of pores (i.e., global pores, microcracks in individual splats, and unbonded splat interfaces) were observed by the researchers for a thermally sprayed oxide coating. Global pores were formed by shadowing effects and insufficient filling of voids on the splat during the propagation of the molten droplet, while microcracks were formed by quenching stress (i.e., rapid cooling after splat solidification) [36]. The unbonded intersplat interfaces was considered to be a special two-dimensional pores with an opening of about 100 nm [45]. All three pores and corresponding cracks were observed in the $Co_{0.5}Ni_{0.5}O$ coating;

thus, disrupting grain sizes and orientations. The low deformability and sintering may also be other reasons for the low cohesion between splats and grains for $Co_{0.5}Ni_{0.5}O$ coating.

The microhardness value of the $Co_{0.5}Ni_{0.5}O$ coating (~764 $HV_{0.2}$) was 10% higher than that of $Co_{0.75}Ni_{0.25}O$ (~685 $HV_{0.2}$) at RT [**Figure 6. 7**]. This may be due to the higher amount of NiO (50 mol%) in $Co_{0.5}Ni_{0.5}O$ than in $Co_{0.75}Ni_{0.25}O$ (i.e., 25 mol% NiO), as NiO was harder than CoO and ultimately contributed to increasing hardness [46]. At elevated temperatures, the hardness of both coatings decreased; $Co_{0.75}Ni_{0.25}O$ and $Co_{0.5}Ni_{0.5}O$ decreased by approximately 13% and 30%, respectively. The decrease in hardness of other oxides at high temperatures has also been observed previously, which may be due to the softening effect [32,47]. Additionally, the decrease in hardness of the $Co_{0.5}Ni_{0.5}O$ coating compared to $Co_{0.75}Ni_{0.25}O$ was higher, possibly due to the coating's high porosity, low sintering ability or low cohesion between the splats, as discussed in the previous paragraph [48].

6.4.2 Friction and Wear Mechanisms

The friction and wear resistance properties of the oxides are highly dependent on their chemical composition, hardness, ductility, adherence to the substrate, and substrate support [6,8,9]. In this study, HVOF sprayed Co-Ni-O (i.e., $Co_{0.75}Ni_{0.25}O$ and $Co_{0.5}Ni_{0.5}O$) coatings were investigated at room and elevated temperature conditions; their microstructural changes in the wear tracks subsurface and stability closer to the interfaces were also observed.

At room temperature (RT), the friction coefficient of the $Co_{0.75}Ni_{0.25}O$ (i.e., 0.61) was higher than that of $Co_{0.5}Ni_{0.5}O$ (i.e., 0.49) coatings at the end of the sliding distance. For both coatings at RT, the trend of the friction coefficient curve was almost the same except for the running-in period at the beginning of the test. The running-in period of $Co_{0.75}Ni_{0.25}O$ (i.e., ~ 2000 cycles) was longer than that of $Co_{0.5}Ni_{0.5}O$ (i.e., ~ 1500 cycles). In general, the low friction of $Co_{0.75}Ni_{0.25}O$ and $Co_{0.5}Ni_{0.5}O$ coatings at the beginning of the test may be due to the presence of surface contaminants and low amount of adhesion [49]. As a result, this layer was removed during further sliding and adhesion phenomenon increased, eventually reaching a stable and increased friction coefficient. A similar frictional behavior of plasma sprayed tantalum oxide and copper oxide coatings was observed in the author's previous work [32,50]. In general, the low friction coefficient of $Co_{0.5}Ni_{0.5}O$ could be due to its high hardness (i.e., ~764 $HV_{0.2}$) as compared to $Co_{0.75}Ni_{0.25}O$ (i.e., ~685 $HV_{0.2}$) at RT [**Figure 6. 7**]. The high hardness resulted low friction of various thermally sprayed oxides which has been observed by many researchers i.e., La_2O_3 [51], Al_2O_3 [52], Cr_2O_3 [53]. In addition, the small contact width of the wear tracks [**Figure 6. 11 (a)**] and counterface [**Figure 6. 18 (a)**] due to its high hardness

could be another reason for the lower friction of $Co_{0.5}Ni_{0.5}O$ coating than $Co_{0.75}Ni_{0.25}O$ at RT [**Figure 6. 8** and **Figure 6. 9**].

At elevated temperature, the friction coefficient of the $Co_{0.75}Ni_{0.25}O$ coating remained stable and constant from the beginning of the sliding test and reached a lower value at the end of the test. This comparatively low and stable friction coefficient (i.e., as compared to $Co_{0.5}Ni_{0.5}O$) could be attributed to the softening of the coating (i.e., from ~685 $HV_{0.2}$ to ~594 $HV_{0.2}$) [**Figure 6. 7**] as well as the presence of a relatively smooth smeared surface with some shallow abrasive marks on the wear tracks [**Figure 6. 10 (c-d)**] and the counterball [**Figure 6. 17 (c)**]. On the other hand, at elevated temperatures, the high friction coefficient of $Co_{0.5}Ni_{0.5}O$ coating caused by brittle fractures, grooves, and excessive generation of loose debris on the wear tracks [**Figure 6. 11 (c-d)**].

Based on the ***ex-situ*** **analysis**, a schematic of wear mechanisms of $Co_{0.75}Ni_{0.25}O$ and $Co_{0.5}Ni_{0.5}O$ coatings after sliding at different temperatures is shown in **Figure 6. 19**. For the $Co_{0.75}Ni_{0.25}O$ coating, during sliding at RT, the significant plastic flow of the asperities occurred, and evidence of grooves, as well as abrasive wear mechanisms (i.e., possibly 2 or 3 body abrasions) were observed on the wear track [**Figure 6. 10 (a-b)**] and counterface [**Figure 6. 17 (a-b)**] [54]. Furthermore, the cyclic loading caused the localized shear deformation on the wear track subsurface. This cyclic loading and frictional heating in the contact zone at RT caused the subsurface grain deformation, which was orientated vertically [**Figure 6. 12 (a-d)**]. The repeated sliding and loading also resulted in the development of subsurface cracks, delamination of the oxide layer from the worn surface [**Figure 6. 12 (a), Figure 6. 1 (a)**], and formation of wear debris that accelerated severe abrasion resulting in increased wear rates at the end of the test [**Figure 6. 8** and **Figure 6. 9**]. The wear debris ultimately transferred to the countersurface and formed a predominant NiO transfer film which acted as an abrasive media and further generated more debris, resulting in high wear [**Figure 6. 17**]. The generation of wear debris and subsurface crack formation during sliding and eventual generation of high wear has been previously observed for ceramics [55,56].Moreover, similar subsurface crack formation with brittle behavior on the wear tracks was observed on the tribologically induced cobalt oxides for Co-based alloys, which were previously reported by Viat et al. [57], Korashy et al. [58] and Munagala et al. [31]. Under atmospheric conditions, the dominant abrasive wear mechanisms have also been observed in plasma-sprayed alumina coatings [59,60].

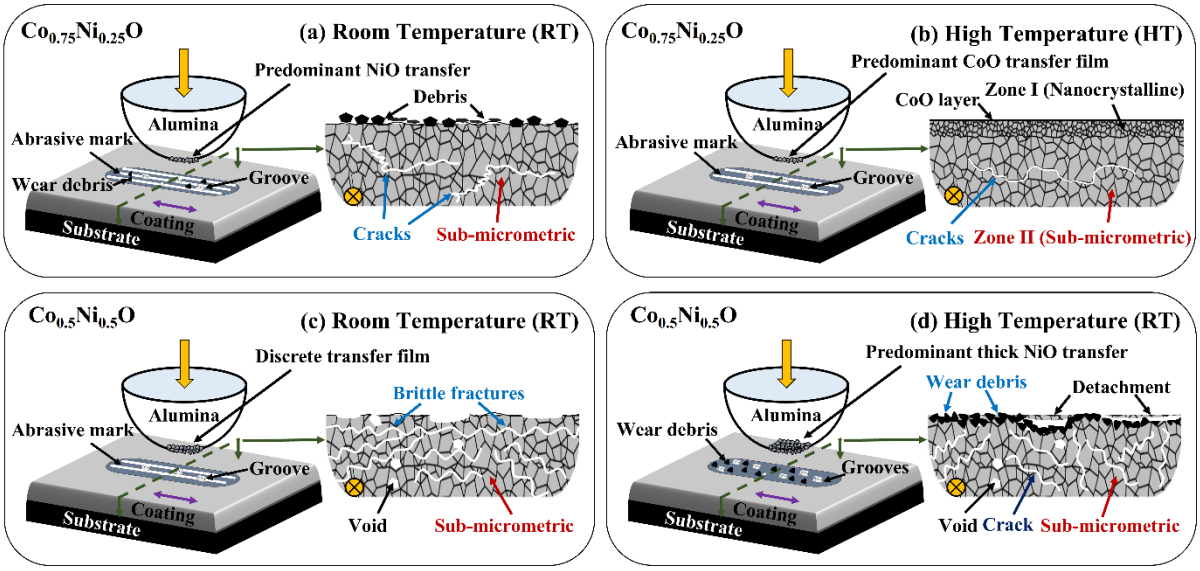

Figure 6. 19: Schematic of wear mechanisms of (a-b) $Co_{0.75}Ni_{0.25}O$ and (c-d) $Co_{0.5}Ni_{0.5}O$ at different temperatures.

Similar $Co_{0.75}Ni_{0.25}O$, the $Co_{0.5}Ni_{0.5}O$ coating at room temperatures showed also brittle behavior due to its high hardness [**Figure 6. 7**]. The high hardness contributed to enhanced wear resistant properties as compared to $Co_{0.75}Ni_{0.25}O$ coating. This low wear rate caused by the dominated abrasive wear mechanisms on the wear track over the adhesive or smeared smooth surface [**Figure 6. 11 (a-b)**]. Additionally, lamellar microcracks, or brittle fractures were propagated in the subsurface of the wear track due to the coating high hardness [**Figure 6. 14 (a-d); Figure 6. 19 (c)**] [36,55,57]. Furthermore, this high hardness led to the discrete distribution of transfer film on the counterface [**Figure 6. 18**].

At elevated temperatures $Co_{0.75}Ni_{0.25}O$ coating showed comparatively low wear than at RT which could be associated with the smeared smooth surface [**Figure 6. 10 (c-d)**] and softening of the coating (i.e., from ~685 $HV_{0.2}$ to ~594 $HV_{0.2}$) [**Figure 6. 7**]. This feature of the wear track may be related to the ductile behavior of the coatings as observed by the previous researchers [32,61,62]. At the elevated temperature test, high frictional heating and cyclic contact stress in the contact interfaces helped to promote two different zones in wear track subsurface i.e., Zone I: nanocrystalline or ultrafine grains (~ 3 μm thickness) along with thin uniform cobalt oxide layer closer to the wear track surface, and Zone II: sub-micrometric grain [**Figure 6. 19 (b)**] and reduce wear rate. In addition, a predominant cobalt oxide transfer film also developed on the countersurface. The cobalt oxide vs cobalt oxide combination contributed to reduce wear of the coatings. Furthermore, Jiang et al. [63] and Kato et al. [64] showed that the formation of the ultrafine grain closer to the wear track was enhanced at elevated temperatures due to the greater sintering or compacting ability of the oxide particles.

The subsurface grain refinement closer to the wear track was also observed by Stoyanov et al. [65] in their metal-ceramic sample, which ultimately helped to reduce wear. According to Viat et al. [10], the oxides with the highest auto-diffusion coefficient helped to promote the ultrafine grain or nanocrystalline grain at elevated temperatures. However, more research is needed to know the driving mechanisms for the grain refinement of the oxides closer to the wear track subsurface.

The specific wear rate of $Co_{0.5}Ni_{0.5}O$ coating after dry sliding for 100 m at elevated temperature was high compared to RT and much higher than $Co_{0.75}Ni_{0.25}O$ coating (both RT and HT) [**Figure 6. 8** and **Figure 6. 9**]. It was believed that the coating, due to its brittle behavior, produced a lot of wear debris during sliding, which led to the abrasive wear behavior at HT. The high debris generation created gouges and brittle fractures on the wear tracks [**Figure 6. 11 (c-d)**] and also caused the nickel oxide transfer film on the counterface, and ultimately increased wear [66]. Additionally, this third body or presence of high amount of abrasive nickel oxide caused the high wear on the counterfaces during sliding [**Figure 6. 18 (c), inset; Table 6. 4**]. The high atomic percentage of NiO (50 at%) in the Co-Ni-O coating made it brittle and its brittleness could be up to more than 500°C, similar to NiO [67]. Furthermore, the low sintering ability and high porosity of the coatings caused detachment of the tribolayers from the worn surface and continued to produce high wear debris [**Figure 6. 15 (a, b); Figure 6. 19 (d)**]. Also, crack formation and the brittle nature of the ceramics accelerated the removal of wear fragments during sliding, generated high wear debris, and caused high wear [55]. The similar wear behavior was observed by Goel et al. [45] and Mahade et al. [46] in their plasma-sprayed alumina coatings. It can be noted that the grain refinement or orientation was hindered due to the presence of pores and the brittle nature of the coatings at HT [**Figure 6. 15 (a-d)**]. Therefore, the authors believe that further research is needed to better understand the oxide diffusion and sintering mechanisms at different temperatures.

6.5 Conclusions

The solid-state synthesized ternary solid solution Co-Ni-O (i.e., $Co_{0.75}Ni_{0.25}O$ and $Co_{0.5}Ni_{0.5}O$) powder was deposited using the HVOF process. A dense coating with limited porosity and low surface roughness was obtained due to the impact of the impinging particles on the substrate at high velocity and sufficient temperature [26,29,30]. The hardness of the $Co_{0.5}Ni_{0.5}O$ coating increased due to the higher concentration of NiO compared to $Co_{0.75}Ni_{0.25}O$ [46]. In addition, the tribological behavior of these $Co_{0.75}Ni_{0.25}O$ and $Co_{0.5}Ni_{0.5}O$ coatings was

investigated by performing reciprocating sliding wear tests at room temperature (RT) and elevated temperature (HT).

- The frictional behavior of the $Co_{0.75}Ni_{0.25}O$ coating did not change significantly at RT and HT, but the wear rate was comparatively lower at HT than at RT. This low wear may be due to the grain refinement or greater sintering ability of the oxides in the wear track subsurface. On the other hand, the high wear rate at RT was due to high debris generation, tribolayer delamination, abrasive wear behavior, and brittle fracture behavior of the coating. In addition, the predominant presence of cobalt oxide transfer film at HT over nickel oxide transfer film at RT on the mating surfaces caused the low wear at HT.
- The significantly lower friction and wear behavior was observed for $Co_{0.5}Ni_{0.5}O$ coating during sliding at RT compared to $Co_{0.75}Ni_{0.25}O$ at RT and HT. The high hardness of the coating contributed to reducing the low friction and wear. On the other hand, the highest friction and wear were observed for this $Co_{0.5}Ni_{0.5}O$ coating at HT. The low tribological performance was due to the greater generation of wear debris, brittleness, crack propagation in the wear track subsurface and, most importantly, the low sintering or compaction of the oxides at HT.

6.6 References

[1] Korashy A, Attia H, Thomson V, Oskooei S. Fretting wear behavior of cobalt-Based superalloys at high temperature–A comparative study. Tribol Int 2020;145:106155.

[2] Reed RC. The superalloys: fundamentals and applications. Cambridge university press; 2008.

[3] Stoyanov P, Dawag L, Goberman DG, Shah D. Friction and wear characteristics of single crystal Ni-based superalloys at elevated temperatures. Tribol Lett 2018;66:1–9.

[4] Pollock TM, Tin S. Nickel-based superalloys for advanced turbine engines: chemistry, microstructure and properties. J Propuls Power 2006;22:361–74.

[5] Stoyanov P, Dawag L, Joost WJ, Goberman DG, Ivory S. Insights into the static friction behavior of Ni-based superalloys. Surf Coatings Technol 2018;352:634–41.

[6] Stott FH, Lin DS, Wood GC. The structure and mechanism of formation of the 'glaze'oxide layers produced on nickel-based alloys during wear at high temperatures. Corros Sci 1973;13:449–69.

[7] Inman IA, Datta S, Du HL, Burnell-Gray JS, Luo Q. Microscopy of glazed layers formed during high temperature sliding wear at 750° C. Wear 2003;254:461–7.

[8] Wood PD, Evans HE, Ponton CB. Investigation into the wear behaviour of Stellite 6 during rotation as an unlubricated bearing at 600 C. Tribol Int 2011;44:1589–97.

[9] Viat A, Bouchet M-IDB, Vacher B, Le Mogne T, Fouvry S, Henne J-F. Nanocrystalline glaze layer in ceramic-metallic interface under fretting wear. Surf Coatings Technol 2016;308:307–15.

[10] Viat A, Dreano A, Fouvry S, Bouchet M-IDB, Henne J-F. Fretting wear of pure cobalt chromium and nickel to identify the distinct roles of HS25 alloying elements in high temperature glaze layer formation. Wear 2017;376:1043–54.

[11] Viat A, Guillonneau G, Fouvry S, Kermouche G, Sao Joao S, Wehrs J, et al. Brittle to ductile transition of tribomaterial in relation to wear response at high temperatures. Wear 2017;392:60–8.

[12] Coskun MB, Aksoy S, Aksit MF. Friction and wear characteristics of Haynes 25, 188, and 214 superalloys against Hastelloy X up to 540° C. Tribol Lett 2012;45:497–503.

[13] Laskowski JA, DellaCorte C. Friction and wear characteristics of candidate foil bearing materials from 25° C to 800° C. National Aeronautics and Space Administration Washington, DC, USA; 1996.

[14] Yao Q, Jia J, Chen T, Xin H, Shi Y, He N, et al. High temperature tribological behaviors and wear mechanisms of NiAl-MoO3/CuO composite coatings. Surf Coatings Technol 2020;395:125910.

[15] Stone DS, Harbin S, Mohseni H, Mogonye JE, Scharf TW, Muratore C, et al. Lubricious silver tantalate films for extreme temperature applications. Surf Coatings Technol 2013;217:140–6. https://doi.org/10.1016/j.surfcoat.2012.12.004.

[16] Gao H, Otero-de-la-Roza A, Gu J, Stone D, Aouadi SM, Johnson ER, et al. (Ag, Cu)–Ta–O ternaries as high-temperature solid-lubricant coatings. ACS Appl Mater Interfaces 2015;7:15422–9.

[17] Yuan H, Song J. An Improved Calculation Model for the Prediction of the Wear of Coated Electrical Contacts. Technologies 2019;7:77.

[18] Zhu R, Zhang P, Yu Z, Yan H, Li S, Wu D, et al. Microstructure and wide temperature range self-lubricating properties of laser cladding NiCrAlY/Ag2O/Ta2O5 composite coating. Surf Coatings Technol 2020;383. https://doi.org/10.1016/j.surfcoat.2019.125248.

[19] Yao Q, Jia J, Chen T, Xin H, Shi Y, He N, et al. High temperature tribological behaviors and wear mechanisms of NiAl-MoO3/CuO composite coatings. Surf Coatings Technol 2020;395:125910. https://doi.org/10.1016/j.surfcoat.2020.125910.

[20] Viat A, Dreano A, Fouvry S, De Barros Bouchet MI, Henne JF. Fretting wear of pure cobalt chromium and nickel to identify the distinct roles of HS25 alloying elements in high temperature glaze layer formation. Wear 2017;376–377:1043–54. https://doi.org/10.1016/j.wear.2017.01.049.

[21] Dréano A, Fouvry S, Guillonneau G. A tribo-oxidation abrasive wear model to quantify the wear rate of a cobalt-based alloy subjected to fretting in low-to-medium temperature conditions.

Tribol Int 2018;125:128–40. https://doi.org/10.1016/j.triboint.2018.04.032.
[22] Roy A. Enhanced lubricating behavior of cobalt oxide over nickel oxide. Tribol Lett 2023.
[23] Fauchais PL, Heberlein JVR, Boulos MI. Thermal spray fundamentals: from powder to part. Springer Science & Business Media; 2014.
[24] Vardelle A, Moreau C, Akedo J, Ashrafizadeh H, Berndt CC, Berghaus JO, et al. The 2016 thermal spray roadmap. J Therm Spray Technol 2016;25:1376–440.
[25] Amin S, Panchal H. A review on thermal spray coating processes. Transfer 2016;2:556–63.
[26] Mohammadkhani S, Jalilvand V, Davis B, Gauthier GH, Dolatabadi A, Moreau C, et al. High-temperature behaviour of HVOF (Co,Ni)O coated Cu-Ni-Fe anodes. Corros Sci 2021;189:109563. https://doi.org/10.1016/j.corsci.2021.109563.
[27] Bolelli G, Cannillo V, Lusvarghi L, Manfredini T. Wear behaviour of thermally sprayed ceramic oxide coatings. Wear 2006;261:1298–315.
[28] Toma F-L, Stahr CC, Berger L-M, Saaro S, Herrmann M, Deska D, et al. Corrosion resistance of APS-and HVOF-sprayed coatings in the Al 2 O 3-TiO 2 system. J Therm Spray Technol 2010;19:137–47.
[29] Patel P, Alidokht SA, Sharifi N, Roy A, Harrington K, Stoyanov P, et al. Microstructural and Tribological Behavior of Thermal Spray CrMnFeCoNi High Entropy Alloy Coatings. J Therm Spray Technol 2022:1–17.
[30] Mohammadkhani S, Schaal E, Dolatabadi A, Moreau C, Davis B, Guay D, et al. Synthesis and thermal stability of (Co,Ni)O solid solutions. J Am Ceram Soc 2019;102:5063–70. https://doi.org/10.1111/jace.16397.
[31] Munagala VNV, Alidokht SA, Sharifi N, Makowiec ME, Stoyanov P, Moreau C, et al. Room and elevated temperature sliding wear of high velocity oxy-fuel sprayed Diamalloy3001 coatings. Tribol Int 2022:108069.
[32] Roy A, Munagala VNV, Patel P, Sharifi N, Alidokht SA, Makowiec M, et al. Friction and wear behavior of suspension plasma sprayed tantalum oxide coatings at elevated temperatures. Surf Coatings Technol 2023;452:129097.
[33] EN ISO 4516: 2002. Metallic and Other Inorganic Coatings - Vickers and Knoop Microhardness Tests. 2004.
[34] Swain M V. Microscopic observations of abrasive wear of polycrystalline alumina. Wear 1975;35:185–9.
[35] Chromik RR, Zhang Y. Nanomechanical testing of third bodies. Curr Opin Solid State Mater Sci 2018;22:142–55.
[36] Li C-J, Luo X-T, Yao S-W, Li G-R, Li C-X, Yang G-J. The bonding formation during thermal spraying of ceramic coatings: a review. J Therm Spray Technol 2022;31:780–817.
[37] Roro KT, Mwakikunga B, Tile N, Yalisi B, Forbes A. Effect of accelerated thermal ageing on the selective solar thermal harvesting properties of multiwall carbon nanotube/nickel oxide nanocomposite coatings. Int J Photoenergy 2012;2012.
[38] Korashy A, Attia H, Thomson V, Oskooei S. Characterization of fretting wear of cobalt-based superalloys at high temperature for aero-engine combustor components. Wear 2015;330–331:327–37. https://doi.org/10.1016/j.wear.2014.11.027.
[39] Davis JR. Handbook of thermal spray technology. ASM international; 2004.
[40] Cabral-Miramontes JA, Gaona-Tiburcio C, Almeraya-Calderón F, Estupiñan-Lopez FH, Pedraza-Basulto GK, Poblano-Salas CA. Parameter Studies on High-Velocity Oxy-Fuel Spraying of CoNiCrAlY Coatings Used in the Aeronautical Industry. Int J Corros 2014;2014:703806. https://doi.org/10.1155/2014/703806.
[41] Xiao JK, Tan H, Wu YQ, Chen J, Zhang C. Microstructure and wear behavior of FeCoNiCrMn high entropy alloy coating deposited by plasma spraying. Surf Coatings Technol 2020;385:125430. https://doi.org/10.1016/j.surfcoat.2020.125430.
[42] Richter A, Berger LM, Conze S, Sohn YJ, Vaßen R. Emergence and impact of Al2TiO5 in Al2O3-TiO2 APS coatings. IOP Conf Ser Mater Sci Eng 2019;480. https://doi.org/10.1088/1757-899X/480/1/012007.
[43] Zheng J, Wen K, Liu Y, Gao L, Ma Z, Diao X. Laser irradiation behavior of plasma-sprayed tantalum oxide coatings. Ceram Int 2020;46:3875–81. https://doi.org/10.1016/j.ceramint.2019.10.113.

[44] Zhang Y, Brodusch N, Descartes S, Chromik RR, Gauvin R. Microstructure refinement of cold-sprayed copper investigated by electron channeling contrast imaging. Microsc Microanal 2014;20:1499–506.
[45] Chang-Jiu LI, Wang W-Z. Quantitative characterization of lamellar microstructure of plasma-sprayed ceramic coatings through visualization of void distribution. Mater Sci Eng A 2004;386:10–9.
[46] Nicholls JR, Hall DJ, Tortorelli PF. Hardness and modulus measurements on oxide scales. Mater High Temp 1994;12:141–50.
[47] Amano T, Okazaki M, Takezawa Y, Shiino A, Takeda M, Onishi T, et al. Hardness of oxide scales on Fe-Si alloys at room-and high-temperatures. Mater. Sci. forum, vol. 522, Trans Tech Publ; 2006, p. 469–76.
[48] Picas JA, Menargues S, Martin E, Baile MT. Cobalt free metallic binders for HVOF thermal sprayed wear resistant coatings. Surf Coatings Technol 2023:129243.
[49] Waterhouse RB. The role of adhesion and delamination in the fretting wear of metallic materials. Wear 1977;45:355–64.
[50] Roy A, Sharifi N, Munagala VN V, Alidokht SA, Patel P, Makowiec M, et al. Microstructural evolution and tribological behavior of suspension plasma sprayed CuO as high-temperature lubricious coatings. Wear 2023:204874.
[51] Zhang Z, Wang Z, Liang B. Microstructure and dry-sliding wear behavior of thermal sprayed and fused Ni-based coatings with the addition of La 2 O 3. Tribol Lett 2010;37:141–8.
[52] Michalak M, Sokołowski P, Szala M, Walczak M, Łatka L, Toma F-L, et al. Wear behavior analysis of Al2O3 coatings manufactured by APS and HVOF spraying processes using powder and suspension feedstocks. Coatings 2021;11:879.
[53] Su W, Niu S, Huang Y, Wang C, Wen Y, Li X, et al. Friction and wear properties of plasma-sprayed Cr2O3–BaCrO4 coating at elevated temperatures. Ceram Int 2022;48:8696–705.
[54] Stachowiak GW, Batchelor AW. Engineering tribology. Butterworth-heinemann; 2013.
[55] Alidokht SA, Manimunda P, Vo P, Yue S, Chromik RR. Cold spray deposition of a Ni-WC composite coating and its dry sliding wear behavior. Surf Coatings Technol 2016;308:424–34.
[56] Hu H, Mao L, Yin S, Liao H, Zhang C. Wear-resistant ceramic coatings deposited by liquid thermal spraying. Ceram Int 2022.
[57] Viat A, Guillonneau G, Fouvry S, Kermouche G, Sao Joao S, Wehrs J, et al. Brittle to ductile transition of tribomaterial in relation to wear response at high temperatures. Wear 2017;392–393:60–8. https://doi.org/10.1016/j.wear.2017.09.015.
[58] Korashy A, Attia H, Thomson V, Oskooei S. Characterization of fretting wear of cobalt-based superalloys at high temperature for aero-engine combustor components. Wear 2015;330:327–37.
[59] Goel S, Björklund S, Curry N, Wiklund U, Joshi S V. Axial suspension plasma spraying of Al2O3 coatings for superior tribological properties. Surf Coatings Technol 2017;315:80–7. https://doi.org/10.1016/j.surfcoat.2017.02.025.
[60] Mahade S, Mulone A, Björklund S, Klement U, Joshi S. Incorporation of graphene nano platelets in suspension plasma sprayed alumina coatings for improved tribological properties. Appl Surf Sci 2021;570:151227.
[61] Erdemir A. A crystal chemical approach to the formulation of self-lubricating nanocomposite coatings. Surf Coatings Technol 2005;200:1792–6.
[62] Erdemir A. A crystal-chemical approach to lubrication by solid oxides. Tribol Lett 2000;8:97–102. https://doi.org/10.1023/a:1019183101329.
[63] Jiang J, Stott FH, Stack MM. The role of triboparticulates in dry sliding wear. Tribol Int 1998;31:245–56.
[64] Kato H, Komai K. Tribofilm formation and mild wear by tribo-sintering of nanometer-sized oxide particles on rubbing steel surfaces. Wear 2007;262:36–41.
[65] Stoyanov P, Merz R, Romero PA, Wählisch FC, Abad OT, Gralla R, et al. Surface softening in metal–ceramic sliding contacts: An experimental and numerical investigation. ACS Nano 2015;9:1478–91.
[66] Bagde P, Sapate SG, Khatirkar RK, Vashishtha N. Friction and abrasive wear behaviour of Al2O3-13TiO2 and Al2O3-13TiO2+ Ni Graphite coatings. Tribol Int 2018;121:353–72.

[67] Evans AG, Rajdev D, Douglass DL. The mechanical properties of nickel oxide and their relationship to the morphology of thick oxide scales formed on nickel. Oxid Met 1972;4:151–70.

Chapter 7

Influencing Factors on the Lubricity of Oxide Coatings[6]

Abstract

This article provides an insight into the factors that influence the lubricity of oxides or oxide coatings. Therefore, the dry sliding tests of thermally sprayed CuO, Ta_2O_5, CoO, NiO, $Co_{0.75}Ni_{0.25}O$, and $Co_{0.5}Ni_{0.5}O$ coatings were performed at room and high temperatures. It was found that a low interaction parameter of the oxides, regardless of the microstructure of the oxide coatings, led to the low friction. No such correlation was observed with the high interaction parameter and ionic potential. Furthermore, the high sintering ability or diffusion coefficient of the oxides played a role in reducing friction and wear at high temperatures.

Graphical Abstract

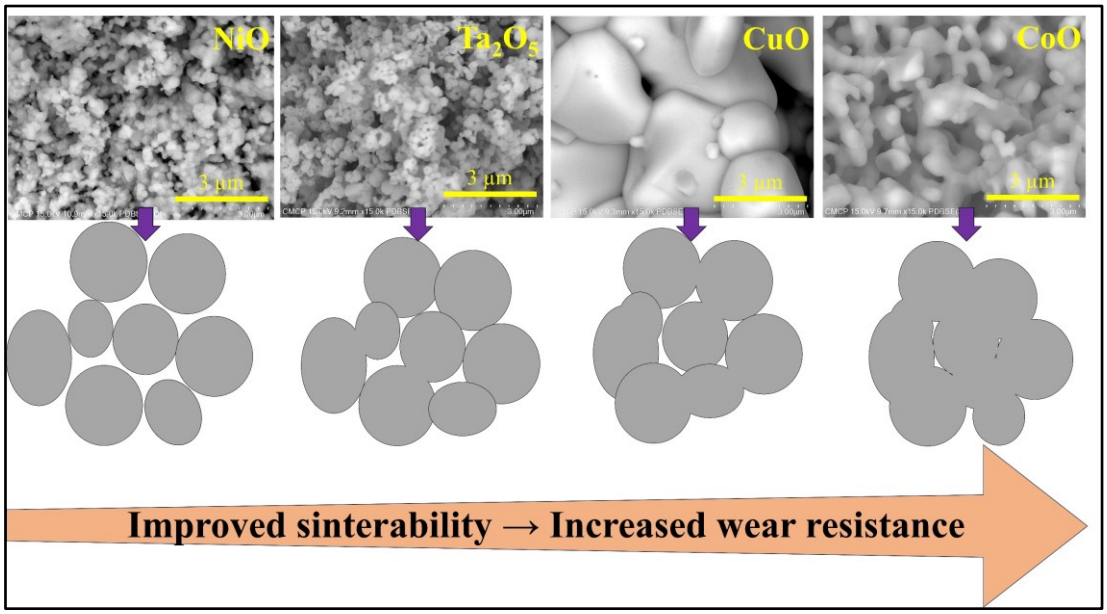

[6] This chapter is prepared as a communication article in order to submit to the *MRS Communication.* **A. Roy**, R. R. Chromik, C. Moreau, P. Stoyanov "Influencing factors on the lubricity of the oxide coatings." *Manuscript is ready to submit "MRS Communication".*

7.1 Introduction

Oxides or oxide coatings as a solid lubricant could be a potential solution for high temperature applications due to their chemical and thermal stability. In addition, oxides are obvious candidates for consideration where oxidation resistant compounds are required [1,2]. Also, such oxides could be potential replacements for traditional solid lubricants such as MoS_2, WS_2, graphite, etc., which rapidly oxidize or thermally degrade at elevated temperatures [3]. However, oxides possess strong covalent bonds in the plane, which contributes to the difficulty of shearing the surfaces [4]. As a result, many oxide ceramics can exhibit high coefficients of friction (i.e., greater than 0.8), high contact stresses, and produce surface cracks and wear debris under atmospheric conditions. Though, similar oxides have shown improved tribological properties at high temperatures due to the ductile behavior or low shear strength on the wear tracks [5–7]. Therefore, different researchers have correlated different factors or parameters to define the friction and wear mechanisms of oxides under different conditions.

Erdemir [8,9] proposed the crystal-chemical approach or ionic potential theory to indicate the oxides friction or lubricity at high temperatures. The ionic potential (φ) is the ratio between the cationic charge and the radius of the cation of the oxides. It was suggested that oxides with higher ionic potential exhibit low friction coefficient at high temperatures, which is mainly attributed to the greater screening of cations by surrounding anions. The surrounding anions make it difficult to interact with other cations and consequently, this results in low shear strength at high temperatures. Similarly, Dimitrov et al. [10] co-related the lubricating behavior of the solid oxides with polarizability or interaction parameters at elevated temperatures. With a low interaction parameter of the oxides, the bond energy between cation and anion weaken, which eventually decreases the friction and effectively improves the lubricity [10,11]. However, the wear characteristics of the oxides have not been correlated with this ionic potential or interaction parameters.

Hardness or Archard's wear equation could be another factor to define the oxide lubricity at room temperature, which helps to reduce wear but leads to high friction [12–14]. Though, the hardness or Archard's wear equation is sometimes not correlated especially at high temperatures due to the existence of different wear mechanisms other than abrasive at room temperature [14].

Deano et al. [15], and Viat et al. [16], showed that the formation of lubricious cobalt oxides close to the wear track during sliding at high-temperature in Co-based alloys, due to its greater

sintering or diffusion coefficient, resulted in reduced friction and wear. Additionally, a layered structure of lubricious oxides was formed on the wear track based on the diffusion behavior of oxides in Co-based alloys during high temperature sliding [17–19].

Bowden and Tabor [20] also formulated different combinations, such as hard counterface vs soft substrate, similar hardness of counterface vs substrate, and similar hardness of counterface & substrate separated by a soft layer deposited on the substrate surface, which showed different friction behavior. These combinations could be applicable to define the friction and wear behavior of oxides or oxide coatings at different temperatures.

It has been seen that different researchers have correlated different parameters such as ionic potential, interaction parameters, hardness, Bowden-Tabor theory, sintering or diffusion etc. There is no single parameter or factor that can indicate the lubricity of the oxide friction and wear under different conditions. Therefore, the authors tried to compare and correlate the different parameters to find the dominant one either for the friction and wear characteristics of the oxide coatings (i.e., CuO, Ta_2O_5, CoO, NiO, $Co_{0.75}Ni_{0.25}O$, and $Co_{0.5}Ni_{0.5}O$) studied here at room and elevated temperatures.

7.2 Materials and methods

The different oxide coatings such as CuO, Ta_2O_5, CoO, NiO, $Co_{0.75}Ni_{0.25}O$, and $Co_{0.5}Ni_{0.5}O$ were prepared by thermal spray process. The main difference was that the deposited coatings were obtained in two different thermal spray processes, (i.e., suspension plasma spray (SPS) and high velocity oxygen fuel (HVOF)). The details of the thermal spray process, coating deposition parameters, morphology and microstructure of the coatings can be found in previously published articles [5,6,21,22].

The Vickers micro-hardness of the coatings was performed on the top surface at a load of 2 N ($HV_{0.2}$) using a Micro-Combi Tester (Anton Paar, Austria) according to the EN ISO 4516 standard [23]. The details of the Vickers hardness testing procedure were explained in a previously published article [6,22].

Dry sliding wear tests were performed using a reciprocating ball on flat tribometer (Anton Paar TriTec SA, Switzerland) at room and elevated temperatures. The wear tests were performed on the as-sprayed coatings at two different temperatures: room or atmospheric temperature (RT), and high temperature (HT). For the high-temperature (HT) test, the samples (substrate/coating) were placed in the furnace, where they were heated to 450°C. The

temperature recorded at the surface of the coating was around 300°C (i.e., using a thermocouple). In this study, the atmospheric and high temperatures friction test conditions were referred to as RT and HT, respectively. The test conditions can be found elsewhere [5,6,21,22]. The steady state friction coefficient was taken into consideration for comparison.

The depth of the wear tracks after sliding tests was measured using a 3D optical surface profiler (Zygo Corporation, USA). The wear area (mm^2) was calculated by integrating the wear track profiles, and the wear area was multiplied by the track length (mm) to determine the wear volume (mm^3). The wear volume was normalized by dividing by the applied load (N) and the total sliding distance (m) to obtain the specific wear rate, k (mm^3/N.m.) [24].

The sintering of the CuO, CoO, Ta_2O_5, and NiO oxides powder were performed at 600°C and 1000°C for 1 hours 30 minutes in atmospheric conditions. The heating rate was 10°C/min and cooled down in the furnace. The average particles size of the powders was from 500 nm to 700 nm and a 1 gm of powders were put in Quartz crucible for sintering in a furnace (Thermo Scientific, Canada).

The morphology of the oxide powders and the sintered powders morphology were analyzed using a field emission scanning electron microscope (FESEM) (SU8010, Hitachi, Japan).

7.3 Results and discussion

The dry sliding tests of all the oxide coatings (i.e., CuO, Ta_2O_5, CoO, NiO, $Co_{0.75}Ni_{0.25}O$, and $Co_{0.5}Ni_{0.5}O$), studied here were performed using the same testing conditions. The lowest friction coefficient at room temperature was 0.45 for the NiO coating, while the lowest friction coefficient at elevated temperature (i.e., 450°C) was seen with the CuO (i.e., 0.46). In terms of the wear behavior, the $Co_{0.5}Ni_{0.5}O$ has the lowest wear rate of 0.83×10^{-5} mm^3/Nm at room temperature and CoO has the lowest wear rate of 1.2×10^{-5} mm^3/Nm at high temperature. In general, the CoO showed the best combination of friction and wear at high temperature compared to all the oxides (details are in **Table SS 1**)

As previously explained (**Introduction section**), a comparison of the ionic potential and interaction parameters was shown with the friction coefficient and specific wear rate of the oxide coatings at high temperatures was shown in **Figure 7. 1**. The ionic potential and interaction parameters are highlighted in the supplementary section (**Table SS 2**). As the ionic potential of the oxides increases, the friction coefficient also increases at high temperatures [**Figure 7. 1 (a)**]. Thus, the friction coefficient is not directly correlated with the proposed crystal chemical approach or the ionic potential theory [8,9]. Instead, the authors found the

opposite behavior. Similar suggestions have been made by Prakash et al. [10,11] and have highlighted some limitations of the ionic potential theory such as it does not consider the nature of interactions between anions and cations in oxides as well as oxides with ionic potential of 1-3. On the other hand, the friction coefficient of the oxide coatings increases with increasing interaction parameters. In other words, at low interaction parameters, the oxides have low coefficient of friction at high temperatures [**Figure 7. 1 (b)**]. In general, oxides with a low interaction parameter have a high density of free electrons. These electrons do not contribute to bonding and therefore an increase in the surface free energy is expected. An increase in the surface free energy could lead to a decrease in the activation energy for the formation of vacancies and for the hopping of ions causing surface diffusion, which can play a prominent role in reducing the coefficient of friction in sliding contacts [10,11].

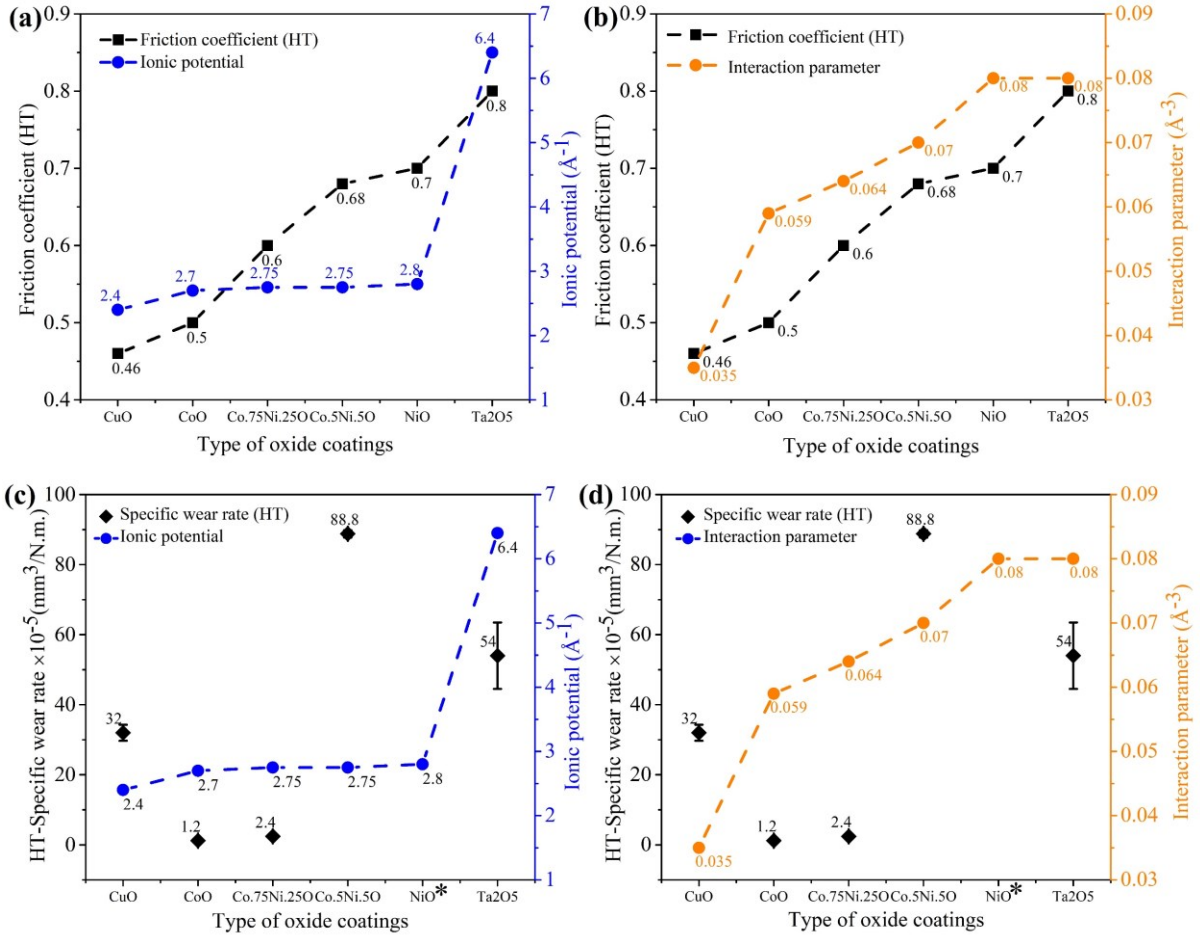

Figure 7. 1: High temperature friction coefficient and wear rate of different oxide coatings as a function of (a-c) ionic potential, and (b-d) interaction parameter. * NiO coating worn out after 500 cycles.

In addition, the mechanism of friction of oxides at different temperatures can be explained by considering the number of vacancies, N, at equilibrium given by

$$N = Ce^{\left(\frac{-Q}{kT}\right)} \qquad (\mathbf{7.1})$$

Where, Q the activation energy (J), T the temperature (°K), k the Boltzmann constant ($m^2kgs^{-2}\ K^{-1}$), and C a constant. Finally, the low interaction parameter can be correlated with the low activation energy, high vacancy formation, high diffusion, and greater sintering ability.

In the case of oxides with a high interaction parameter, the mobility of the ions decreases due to a lower number of vacancies available, and this may be the origin of a higher sensitivity to cracking [10,11]. This could be the reasons for the high friction and the delamination, cracking, lack of tribofilm on the wear tracks for NiO, Ta_2O_5, and $Co_{0.5}Ni_{0.5}O$ oxide coatings during sliding wear tests at high temperatures [**Table SS 3**]. However, it is believed that there is a lack of data for many oxides on the activation energy for anion vacancy, hence; a strong correlation between activation energy and interaction parameter is not noticeable. Therefore, additional research is needed to find the activation energy, diffusion coefficient of different oxides in order to correlate them with the friction behavior at high temperatures.

Similar to the friction coefficient, the specific wear rate of CuO, Ta_2O_5, CoO, NiO, $Co_{0.75}Ni_{0.25}O$, and $Co_{0.5}Ni_{0.5}O$ oxide coatings with ionic potential, and interaction parameter after dry sliding at high temperatures is shown in **Figure 7. 1 (c)** and **(d)**, respectively. The wear rate fluctuated with the increased of ionic potential [**Figure 7. 1 (c)**]. On the other hand, the wear rate of CuO, CoO, and $Co_{0.75}Ni_{0.25}O$ decreased with increasing interaction parameter. However, as the interaction parameter was further increased, the wear rate for $Co_{0.5}Ni_{0.5}O$, and NiO increased. The wear rate for Ta_2O_5 decreased with increasing interaction parameter. Thus, the wear rate of the oxides fluctuates with the variation or increase of the interaction parameters [**Figure 7. 1 (d)**]. Therefore, neither the ionic potential nor the interaction parameters satisfy the wear resistance characteristics of oxide coatings. The wear resistance of the oxides could be influenced by coating microstructures as well as different test parameters such as varying frequency, load, contact conditions, applied load, temperatures etc., as tribology is not a materials property but system response. Deano et al. [15] extensively studied the influence of temperature, sliding cycles on the formation of glaze layer for cobalt-based superalloy, which ultimately contributed to the reduction of wear. In addition, Viat et al. [16] showed that the

tribologically induced cobalt oxides from cobalt-based alloy undergo the brittle to ductile transition above 300°C, which reduced friction and wear. In addition, the formation of transfer film and tribofilm on the mating surface and wear track, respectively, contributed to the reduction of wear. In addition, the layered structure on the wear track, greater sintering ability or grain refinement during sliding also improves the wear resistance properties of the oxides at high temperatures [17,18].

Overall, at room temperature, the brittle fractures dominate, which could be due to the low frictional heating in the contact interfaces as well as the high hardness of the oxides, which ultimately produced a lot of debris and contributed to have high wear rate. This high hardness is sometimes helpful to reduce wear according to Archard's wear equation [12] [**Equation 7.2**].

$$Q = K\frac{WL}{H} \qquad (\mathbf{7.2})$$

Q is the total volume of wear debris produced
K is a dimensionless constant
W is the total normal load
L is the sliding distance
H is the hardness of the softest contacting surfaces

However, in most of the cases it could be opposite (i.e., increases the wear) as it increases the material brittleness (i.e., lack of ductility for increasing wear resistance). To elucidate this, the graph between the microhardness vs specific wear rate at room temperature is shown in **Figure 7. 2 (a)**. It is shown that with high hardness, $Co_{0.5}Ni_{0.5}O$ coating has low wear rate and extending this trend for $Co_{0.75}Ni_{0.25}O$ and CoO coatings. Also, the lowest hardness Ta_2O_5 coating led to the highest wear. However, it could be different for NiO coatings [**Figure 7. 2 (a)**]. On the other hand, the high temperature wear rate does not correlate with the coatings' microhardness [**Figure 7. 2 (b)**].

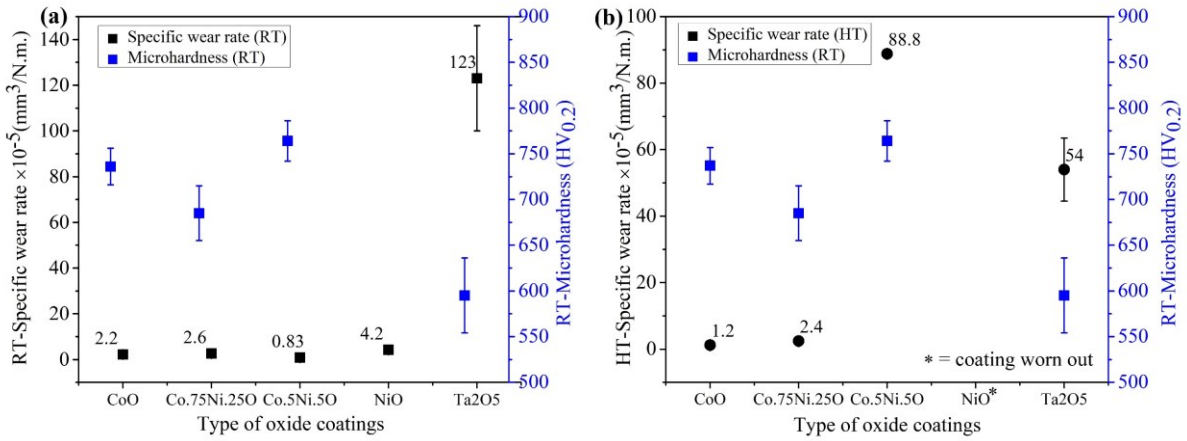

Figure 7. 2. The specific wear rate of oxide coatings as a function of microhardness at (a) Room and (b) high temperature

Therefore, it could be said that the wear rate for the oxides studied (i.e., Ta_2O_5, CoO, $Co_{0.75}Ni_{0.25}O$, and $Co_{0.5}Ni_{0.5}O$), correlated to some extent with the Archard equation or hardness value at room temperature, but not at high temperatures. The main reasons could be due to the abrasive nature of the coatings during sliding at atmospheric conditions. Whereas, at the high temperature sliding, the coatings phenomenon changed to smearing, ductility, adhesion, grain refinement, etc.

In addition, the thermal conductivity and melting point of the oxides did not correlate to the friction and wear behavior of the coatings [**Table SS 2**]. In short, it can be said that the wear behavior at high temperature can be influenced by other properties, such as the transition from brittle to ductile behavior, the formation of smeared smooth layer on the wear track, the smaller grain refinement, greater sintering ability of the oxides (i.e., leading to the formation of the glaze layer at the interface) or the oxide coatings studied here.

Thus, in order to elucidate the driving mechanisms behind the wear resistance at elevated temperatures, a sintering study at 600°C and 1000°C for 1 hour 30 minutes at the heating rate of 10°C/minutes in atmospheric conditions was conducted on CoO, CuO, Ta_2O_5, and NiO powders [**Figure 7. 3**]. It should be mentioned that NiO powders were initially more aggregated than other powders possibly due to high moisture absorption.

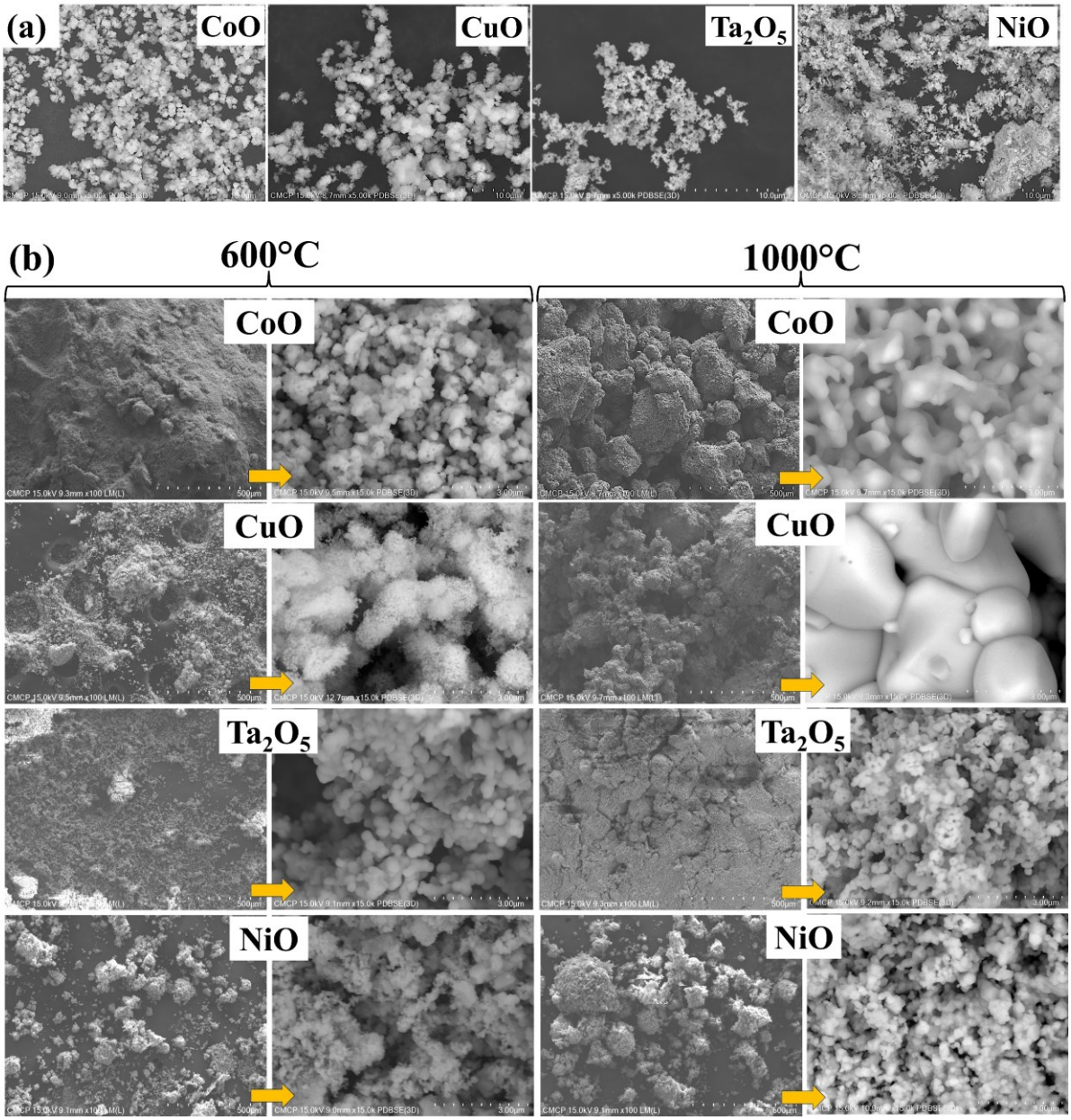

Figure 7. 3 a) Powder morphology of CoO, CuO, Ta_2O_5, and NiO; (b) The sintering behavior of CoO, CuO, Ta_2O_5, and NiO powders at different temperatures.

Interestingly, at 600°C, no possible/visible changes of the powders were observed, whereas at 1000°C, the sintering was noticeable [**Figure 7. 3**]. However, for CuO, the powders aggregated and agglomerated. Similarly, more aggregation and agglomeration were observed for CoO than CuO. The neck connection or diffusion was observed for CoO and CuO at 1000°C. No evident aggregation of powders was noticed for NiO. The powder moved easily in the crucible when it was shaken after removing from the furnace. On the other hand, Ta_2O_5 powders agglomerated little but more than NiO. The results indicated that CoO coating has lowest wear rate after dry sliding at high temperatures. Moreover, this trend followed like high

to low wear rate (i.e., NiO→Ta_2O_5→CuO→CoO) and correspondingly their rate of agglomeration increased. Therefore, sintering at 1000°C can be correlated with the sintering ability of different oxides during sliding at comparatively high temperatures, and consequently a comparable standard between sintering and friction and wear value can be obtained.

In addition to the sintering ability (i.e., formation of the glaze layer), the variation of friction and wear at high temperature could be explained by Bowden and Tabor theory [20]: (a) Hard counterface metal in contact with soft substrate metal (large contact area, *A* and small shear strength, *s*), (b) Similar hardness of counterface metal and substrate metal in contact with each other (small *A* and large *s*), (c) Similar hardness of counterface metal and substrate metal separated by a thin film of soft metal deposited on the substrate surface (both *A* and *s* are small) [**Figure SS 1**]. CuO, CoO, Ta_2O_5, and $Co_{0.75}Ni_{0.25}O$ exhibit relatively ductile behavior or low shear strength at high temperature than at room temperatures. Moreover, the CoO coatings formed soft amorphous layer closer to the wear track at elevated temperature [5,6,21,22]. Therefore, the decreased friction and wear rate at high temperatures of these oxides (i.e., CuO, CoO, Ta_2O_5, and $Co_{0.75}Ni_{0.25}O$) can be correlated with the soft on hard combination [**Figure SS 1 (c)**]. Similarly, for room temperature sliding conditions, CuO, CoO, Ta_2O_5, and $Co_{0.75}Ni_{0.25}O$ were comparatively hard or lack of ductility. This behavior can be correlated well with hard-on-hard combination where the coatings have high shear strength, leading more debris formation, and hence high friction and wear [**Figure SS 1 (b)**]. On the other hand, at room temperature, this hard-on-hard correlation did not work for NiO and $Co_{0.5}Ni_{0.5}O$ coatings still though they were hard and brittle in nature. In contrast, the NiO and $Co_{0.5}Ni_{0.5}O$ coatings remained in brittle phase during dry sliding at high temperature and correlated well with hard-on-hard combination where the coatings showed high friction and wear. So, the combination pattern of the mating surface and chemical behavior of the materials or coatings can vary the nature of the oxides layer in the contacting surface at high temperatures [25].

Finally, the lattice constant could be another parameter for governing the friction and wear behavior of the oxides at room and elevated temperatures. As lattice represents the distance between atoms in the crystal; thus, in general, a decrease in the lattice constant means that the electrons are more tightly bound to the atom and therefore require more energy to remove [26]. The details of the crystal structure of different oxides and their corresponding lattice constants can be found in **Table SS 4**.

Figure 7. 4 shows the room temperature friction coefficient of different oxide coatings as a function of lattice parameter. At atmospheric conditions, there seems to be a correlation,

where the friction coefficient decreased with decreasing the lattice parameter. The lower the lattice constant could imply the stronger bonding of the atoms in the oxides and hence, high hardness. The stronger bonding of the atoms normally difficult to shear which could lead to high friction [1,27]. However, the observed study for CoO, $Co_{0.75}Ni_{0.25}O$, $Co_{0.5}Ni_{0.5}O$, and NiO coatings decreased friction coefficient with decreasing the lattice parameter.

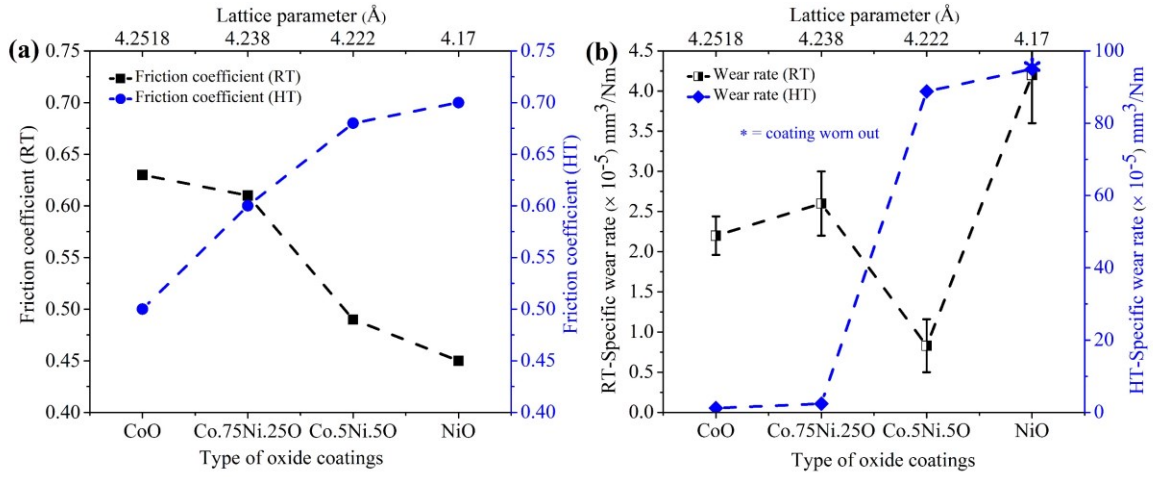

Figure 7. 4. Room and elevated temperatures (a) friction coefficient, and (b) specific wear rate of different oxide coatings as a function of lattice parameter.

Like friction value of different oxide coatings, the wear rate at room and elevated temperatures is shown in **Figure 7. 4 (b)**. At high temperature, the increase in lattice parameter decreased the specific wear rate of the oxides. This can be correlated with the low shear strength or relative ductile behavior of the coatings during sliding at high temperatures, which contributed to the decrease in wear rate. It is believed that during dry sliding at high temperatures for CoO coatings or cobalt-based alloys formed amorphous or soft Co_3O_4 layer (i.e., high lattice constant decreased bond strength between atoms), which caused to decrease friction and wear [16–18]. Therefore, CoO has comparatively lower wear rate than $Co_{0.75}Ni_{0.25}O$, $Co_{0.5}Ni_{0.5}O$, and NiO. On the contrary, at room temperature, the specific wear rate also decreased with increasing lattice constants except for $Co_{0.5}Ni_{0.5}O$.

However, the friction coefficients of the oxides with different crystal structures may not be generalized. Thus, it could be valid or comparable within the same crystal structures, such as rock salt (i.e., Co_3O_4, CoO, $Co_{0.75}Ni_{0.25}O$, $Co_{0.5}Ni_{0.5}O$, and NiO) of different oxides. Therefore, additional research is needed to study the crystal behavior during sliding at room and elevated temperatures at the nanoscale to confirm or determine the importance of lattice constants on the friction and wear value of different oxides.

7.4 Conclusions

The dry sliding wear tests of thermally sprayed CuO, Ta_2O_5, CoO, NiO, $Co_{0.75}Ni_{0.25}O$, and $Co_{0.5}Ni_{0.5}O$ coatings were carried out and their lubricity phenomenon was correlated with various factors such as ionic potential, interaction parameter, hardness, sintering behavior, and lattice constants. It was found that a low interaction parameter and high sintering behavior of the oxide coatings, regardless of the microstructure of the oxide coatings, led to the low friction and wear, respectively, at high temperatures.

Acknowledgments

The author gratefully acknowledges the research funding from the NSERC Discovery Grant-Pantcho Stoyanov for funding this work. The author also acknowledges the help of Camilo for assistance with the furnace experiment.

7.5 References

[1] Roy A, Patel P, Sharifi N, Chromik RR, Stoyanov P, Moreau C. Binary and ternary lubricious oxides for high temperature tribological applications: A review. Results in Surfaces and Interfaces 2023:100117.

[2] Stoyanov P, Harrington KM, Frye A. Insights into the tribological characteristic of Cu-based coatings under extreme contact conditions. JOM 2020;72:2191–7.

[3] Sliney HE. Solid lubricant materials for high temperatures-a review. Tribol Int 1982;15:303–15. https://doi.org/10.1016/0301-679X(82)90089-5.

[4] Muratore C, Voevodin AA. Chameleon Coatings: Adaptive Surfaces to Reduce Friction and Wear in Extreme Environments. Annu Rev Mater Res 2009;39:297–324. https://doi.org/10.1146/annurev-matsci-082908-145259.

[5] Roy A, Sharifi N, Munagala VN V, Alidokht SA, Patel P, Makowiec M, et al. Microstructural evolution and tribological behavior of suspension plasma sprayed CuO as high-temperature lubricious coatings. Wear 2023:204874.

[6] Roy A, Munagala VNV, Patel P, Sharifi N, Alidokht SA, Makowiec M, et al. Friction and wear behavior of suspension plasma sprayed tantalum oxide coatings at elevated temperatures. Surf Coatings Technol 2023;452:129097.

[7] Roy A, Jalilvand V, Mohammadkhani S, Patel P, Dolatabadi A, Roue L, et al. Enhanced Wear Resistance of Cobalt Oxide Over Nickel Oxide. Tribol Lett 2023;71:99.

[8] Erdemir A. A crystal-chemical approach to lubrication by solid oxides. Tribol Lett 2000;8:97–102. https://doi.org/10.1023/a:1019183101329.

[9] Erdemir A. A crystal chemical approach to the formulation of self-lubricating nanocomposite coatings. Surf Coatings Technol 2005;200:1792–6.

[10] Dimitrov V, Komatsu T. Classification of simple oxides: a polarizability approach. J Solid State Chem 2002;163:100–12.

[11] Prakash B, Celis J-P. The lubricity of oxides revised based on a polarisability approach. Tribol Lett 2007;27:105–12.

[12] Frérot L, Aghababaei R, Molinari J-F. A mechanistic understanding of the wear coefficient: From single to multiple asperities contact. J Mech Phys Solids 2018;114:172–84.

[13] Song EP, Ahn J, Lee S, Kim NJ. Microstructure and wear resistance of nanostructured Al2O3–8wt.% TiO2 coatings plasma-sprayed with nanopowders. Surf Coatings Technol 2006;201:1309–15.

[14] Leivo EM, Vippola MS, Sorsa PPA, Vuoristo PMJ, Mäntylä TA. Wear and corrosion properties of plasma sprayed AI 2 O 3 and Cr 2 O 3 coatings sealed by aluminum phosphates. J Therm Spray Technol 1997;6:205–10.

[15] Dreano A, Fouvry S, Guillonneau G. Understanding and formalization of the fretting-wear behavior of a cobalt-based alloy at high temperature. Wear 2020;452:203297.

[16] Viat A, Guillonneau G, Fouvry S, Kermouche G, Sao Joao S, Wehrs J, et al. Brittle to ductile transition of tribomaterial in relation to wear response at high temperatures. Wear 2017;392–393:60–8. https://doi.org/10.1016/j.wear.2017.09.015.

[17] Viat A, De Barros Bouchet MI, Vacher B, Le Mogne T, Fouvry S, Henne JF. Nanocrystalline glaze layer in ceramic-metallic interface under fretting wear. Surf Coatings Technol 2016;308:307–15. https://doi.org/10.1016/j.surfcoat.2016.07.100.

[18] Dreano A, Fouvry S, Sao-Joao S, Galipaud J, Guillonneau G. The formation of a cobalt-based glaze layer at high temperature: A layered structure. Wear 2019;440–441:203101. https://doi.org/10.1016/j.wear.2019.203101.

[19] Stoyanov P, Boyne A, Ignatov A. Tribological characteristics of Co-based plasma sprayed coating in extreme conditions. Results in Surfaces and Interfaces 2021;3:100007.

[20] Bowden FP, Bowden FP, Tabor D. The friction and lubrication of solids. vol. 1. Oxford university press; 2001.

[21] Roy A. Enhanced lubricating behavior of cobalt oxide over nickel oxide. Tribol Lett 2023.

[22] Amit Roy, Vahid Jalilvand, Saeed Mohammadkhani, Payank Patel, A. Dolatabadi, L. Roue, D. Guay, Richard R. Chromik, Pantcho Stoyanov CM. Microstructure and tribological characteristics of thermally sprayed Co-Ni-O ternary oxide coatings. Tribol Int n.d.

[23] EN ISO 4516: 2002. Metallic and Other Inorganic Coatings - Vickers and Knoop Microhardness Tests. 2004.

[24] Küçük Y. Effect of counterbody on the dry sliding wear performance of plasma sprayed calcia-stabilized zirconia coating. Int J Refract Met Hard Mater 2020;92. https://doi.org/10.1016/j.ijrmhm.2020.105284.

[25] Lugscheider E, Knotek O, Bärwulf S, Bobzin K %J S, Technology C. Characteristic curves of voltage and current, phase generation and properties of tungsten-and vanadium-oxides deposited by reactive dc-MSIP-

PVD-process for self-lubricating applications 2001;142:137–42.
[26] Caro Bayo MÁ. Theory of elasticity and electric polarization effects in the group-III nitrides 2013.
[27] Gao H, Otero-de-la-Roza A, Gu J, Stone D, Aouadi SM, Johnson ER, et al. (Ag, Cu)–Ta–O ternaries as high-temperature solid-lubricant coatings. ACS Appl Mater Interfaces 2015;7:15422–9.

Chapter 8

Conclusions and Recommendation

8.1 Summary and Conclusions

The main objective of this dissertation was to mimic the oxides or glaze layer normally formed during sliding of alloys or composites. The formation of these oxides on the wear tracks during sliding helped to improve the tribological behavior of the coatings. Consequently, the idea was to deposit these lubricious oxides instead of alloys or composites and to perform the dry sliding tests at different temperatures. In addition, the goal was to minimize the initial high run-in period and reduce friction and wear at high temperatures. Therefore, CuO, Ta_2O_5, CoO, NiO, $Co_{0.75}Ni_{0.25}O$, and $Co_{0.5}Ni_{0.5}O$ coatings were developed by using suspension plasma spray (SPS) and high velocity oxy-fuel (HVOF) processes.

1. The CuO coatings were developed by SPS using ethanol-based suspensions as feedstocks. The effects of spraying parameters such as nozzle size, spraying distance, plasma gas compositions and solid loading in the suspensions on the coating microstructures were investigated. The low melting (~1300°C), boiling (~2000°C) and decomposition (~1200°C) temperatures were identified for the porous microstructures of the CuO coatings. In addition, the high in-flight particle temperatures, and the plasma gas hydrogen (H_2) were considered as the influencing parameters for the reduction of CuO to Cu_2O and pure metallic Cu. The high solid loading (20 wt%) and short spraying distance (i.e., 30 mm) helped to densify the coating microstructures. Further sliding tests of the CuO coatings showed low friction and wear at high temperatures compared to atmospheric conditions. The presence of metallic Cu and Cu_2O in the coatings was converted to CuO on the wear tracks during sliding at room and elevated temperatures, as demonstrated by Raman analysis.
2. The SPS process was used to produce dense Ta_2O_5 coatings by optimizing the spray parameters such as nozzle size, spray distance, plasma gas compositions, and plasma power. The low friction and wear of the Ta_2O_5 at elevated temperature can be attributed to the ductile behavior of the coating. The relatively ductile behavior of the coating could be attributed to the higher frictional heating leading to the formation of a smeared or continuous smooth layer on the wear tracks with a stable transfer film on the

counterface. On the other hand, the opposite trend was observed at atmospheric temperature.

3. Dry sliding tests on the thermally sprayed CoO and NiO showed that the CoO coatings outperformed NiO at room and elevated temperature. *Ex-situ* analysis of CoO wear tracks after high temperature sliding showed that the formation of a thin nanocrystalline amorphous tribofilm resulted in low friction and wear. Whereas, at room temperature, subsurface microcracking of the CoO coating led to high friction and wear compared to elevated temperature. The nickel oxide coating, at room temperature, provided low friction, possibly due to its high hardness. At high temperature, however, the NiO coating was completely worn out and resulted in increased friction and wear due to its brittle nature.
4. Solid-state synthesized ternary Co-Ni-O (i.e., $Co_{0.75}Ni_{0.25}O$ and $Co_{0.5}Ni_{0.5}O$) powder was deposited using the HVOF process. A dense coating with limited porosity and low surface roughness was obtained due to the impact of the impinging particles on the substrate at high velocity and sufficient temperature. The hardness of the $Co_{0.5}Ni_{0.5}O$ coating increased due to the higher concentration of NiO compared to $Co_{0.75}Ni_{0.25}O$. The $Co_{0.5}Ni_{0.5}O$ coating showed poor tribological performance at high temperatures due to the higher concentration of NiO, which made the coating more brittle. However, at high temperatures, the low wear for the $Co_{0.75}Ni_{0.25}O$ coating is attributed to the grain refinement or greater sintering ability of the oxides in the wear track subsurface.
5. The oxides with low interaction parameter showed low friction at high temperature. As the interaction parameter decreased, the friction coefficient of the oxides at high temperature decreased due to the weaker binding energy between anion and cation. In addition, the interaction parameter can be related to the activation energy for the improved lubricity. More specifically, the formation of vacancies and hopping of ions at the surface of an oxide becomes easier with lower activation energy, thus increasing the degree of freedom and mobility of the ions. This increased mobility of ions at their surface is believed to be the basis for the low coefficient of friction of such oxides in sliding contacts.
6. The sintering of the oxides powder (i.e., CoO, CuO, Ta_2O_5, and NiO) at 1000°C for 1 hour 30 minutes in atmospheric conditions showed that the CoO aggregated and agglomerated more than any other oxides (i.e., CuO, Ta_2O_5, and NiO). Moreover, this trend followed a high to low wear rate (i.e., NiO→Ta_2O_5→CuO→CoO) and correspondingly their rate of agglomeration increased. Therefore, this agglomeration

ability of the powders at 1000°C can be correlated with the sintering ability of different oxides during sliding at comparatively high temperatures and hence, their friction and wear value.

8.2 Contributions to Original Knowledge

The main contributions of this dissertation can be summarized as follows:

1. For the first time, CuO, Ta_2O_5, CoO, NiO, $Co_{0.75}Ni_{0.25}O$, and $Co_{0.5}Ni_{0.5}O$ oxide coatings were developed by thermal spray process (i.e., SPS and HVOF) to mimic the *in-situ* oxides or lubricious glaze layer.
2. The influence of spray parameters on the coating microstructures of different oxides was investigated. Additionally, it was shown that the in-flight temperatures and the plasma gas composition play a significant role in the chemical reduction of CuO to Cu_2O and pure metallic Cu. Similar observations were made for NiO coatings.
3. For the first time, the sliding wear behavior of CuO, Ta_2O_5, CoO, NiO, $Co_{0.75}Ni_{0.25}O$, and $Co_{0.5}Ni_{0.5}O$ oxide coatings was studied at different temperatures.
4. It was found that the main wear mechanisms for having high friction or wear at room and low friction or wear at elevated temperature of different oxides were due to the brittle and ductile behavior of the coatings, respectively.
5. A potential tentative main parameter (i.e., sintering ability or interaction parameter or diffusion coefficient) for reducing the friction coefficient and specific wear rate of different oxides at high temperatures was recognized.

8.3 Suggestion for Future Work

1. The oxides such as CuO, Ta_2O_5, CoO, NiO, $Co_{0.75}Ni_{0.25}O$, and $Co_{0.5}Ni_{0.5}O$ coatings studied here were deposited by two different processes (i.e., SPS and HVOF). It would be interesting to try to deposit the coatings with a single spray process, either SPS or HVOF, and see their tribological behavior at different temperatures.
2. The challenges for the deposition of the CuO coatings can be minimized or the microstructure of the coatings can be improved by varying the plasma power, changing the secondary gas (H_2), and using He instead. In addition, HVOF could be a viable option to avoid reducing CuO particles in-flight or on the substrate, as it uses larger particles and lower flame temperatures than the SPS process. Further characterization

is also needed to investigate the mechanical performance (i.e., hardness, modulus, fracture toughness) of these coatings.

3. Different microstructures of Ta_2O_5 oxide coatings can be obtained by varying the spray parameters and thus checking their tribological performance under different test conditions. Further investigation is needed to verify their brittle and ductile wear mechanisms at room and elevated temperatures. In addition, Ta_2O_5 is the only oxide where the number of anions is not equal to the number of cations compared to the other oxides studied here. This variation of cations and anions could be considered to verify its tribological performance in the future.
4. The NiO coating sprayed by SPS process was reduced to pure metallic Ni and the coating microstructures were more like columnar. In addition, NiO coatings can be developed using the HVOF process to avoid or minimize the reduction to metallic Ni (i.e., coating microstructures) and to understand the tribological properties. This may be possible due to the much higher particle velocity and lower flame temperatures of the HVOF process. In addition, a systematic approach can be established by comparing the tribological performance of producing NiO and CoO coatings using the same spray process (i.e., either HVOF or SPS).
5. The oxides studied here should be evaluated in terms of their tribological behavior up to high temperatures above 750°C. In addition, the coatings should be critically evaluated using component level test in order to better understand their capability.
6. It was shown that the coefficient of friction and wear of CuO was lower than that of Ta_2O_5. On the other hand, the tantalum oxides have higher load carrying capacity due to their high hardness. Therefore, the influence of CuO or Ta_2O_5 in the composites of CuO + Ta_2O_5 in terms of their coating microstructures and wear resistance behavior at different temperatures needs to be further investigated. There may be a possibility of the formation of ternary oxides (i.e., $CuTa_2O_6$) on the coatings during spraying or on the wear tracks after the sliding test, which could improve the tribology of the coatings.
7. It has been shown that increasing the NiO content in the Co-Ni-O ternary solid solution (i.e., $Co_{0.5}Ni_{0.5}O$) decreases the wear resistance at high temperatures. It would be interesting to see the tribological behavior of these coatings at much higher temperatures. Also, it would be good to perform some advanced characterizations (i.e., FIB or TEM) to understand the dominant wear mechanisms of the Co-Ni-O (i.e., $Co_{0.75}Ni_{0.25}O$, and $Co_{0.5}Ni_{0.5}O$) coating.

8. In this dissertation, the tribological characteristics of different oxide (i.e., CuO, Ta_2O_5, CoO, NiO, $Co_{0.75}Ni_{0.25}O$, and $Co_{0.5}Ni_{0.5}O$) coatings were investigated under dry sliding conditions. It would be interesting to study the friction and wear behavior of the coatings under lubricated sliding conditions.
9. The third body approach to varying the tribology of the oxides studied here needs to be further understood at atmospheric and high temperatures. The physical, chemical, microstructural, and mechanical properties of the third body should be co-related to the observed changes in friction and wear mechanisms. Moreover, further advanced characterization such as TEM could be a viable option to identify the wear mechanisms in detail.
10. In addition, it is believed that additional research is needed to focus on the interaction parameter or sintering ability and diffusion coefficient, which could be the main driving mechanisms for reducing friction and wear of lubricious oxides. It would be interesting to summarize or list the chronological order of different oxide lubricity based on sintering ability or diffusion coefficient at high temperatures. Further studies related to sintering ability such as density measurement, preparation of green pellet and then sintering, etc. could be done to clearly understand their sinterability. A mathematical model could be developed instead of experimental tests to predict the friction and wear resistance behavior of different oxide coatings at different temperatures.

Appendix A

Supplementary section 1

Binary and Ternary Oxide for High Temperature Tribological Applications: A Review

Amit Roy[1, 2*], Payank Patel[1, 2], Navid Sharifi[1], Richard R. Chromik[2], Pantcho Stoyanov[3], Christian Moreau[1]

[1]Department of Mechanical, Industrial and Aerospace Engineering, Concordia University, 1455 de Maisonneuve Blvd. W, Montreal, Quebec H3G 1M8, Canada

[2]Department of Mining and Materials Engineering, McGill University, M.H. Wong Building, 3610 University Street, Montreal, QC H3A 0C5, Canada

[3]Department of Chemical and Materials Engineering, Concordia University, 1455 de Maisonneuve Blvd. W, Montreal, Quebec H3G 1M8, Canada

Nomenclatures

L	Applied load [N]	**W**	Wear rate [mm^3/N.m]
SV	Sliding speed or velocity [mm/s]	**RT**	Room temperature [°C]
SD	Sliding distance [m]	**k**	Radius of gyration [mm]
S	Stroke length [mm]	$\boldsymbol{A_r}$	Real area of contact [mm^2]
f	Frequency [Hz]	$\boldsymbol{\tau}$	Shear strength [N/mm^2]
T	Testing time or duration [s]	$\boldsymbol{\varphi}$	Ionic potential [$Å^{-1}$]
$\mathbf{P_H}$	Hertzian contact pressure [MPa]	**Z**	Cationic charge
μ	Coefficient of friction [COF]	**r**	Radius of the cation [Å]
MS	Magnetron sputtering	**PM**	Powder metallurgy
PLD	Pulse laser deposition	**TS**	Thermal spraying

Table S1: Tribological behavior of vanadium-based oxides

Author	Method	Material	Counter body	Load	Speed	Time/ Distance	Tribological Performance
Fateh et al. [1]	MS	VN	Al_2O_3	5 N	0.1 m/s	100 m	μ: 0.45 (RT); 0.48 (300°C); 0.47 (400°C); 0.4 (500°C); 0.36 (600°C); 0.25 (700°C)
Gassner et al. [2]	MS	VN	Al_2O_3	10 N	0.1 m/s	1000 m	**Combination with Al_2O_3 ball μ:** 0.55 (RT); 0.5 (500°C); 0.37 (700°C); **Combination with steel ball μ:** 1.35 (RT); 0.5 (500°C); 0.32 (700°C);
Ouyang et al. [3]	Ion platting	(V, Ti) N	Al_2O_3	10 N	--	60 min	**μ:** 0.81 (RT); 1.01 (200°C); 1.08 (300°C); 1.06 (400°C); 0.68 (500°C); 0.55 (600°C); 0.53 (650°C); 0.61 (700°C); **W:** $2.59 \times 10^{-7} mm^3/Nm$ (RT); $1.69 \times 10^{-7} mm^3/Nm$ (200°C); $4.38 \times 10^{-6} mm^3/Nm$ (400°C); $3.28\times 10^{-6} mm^3/Nm$ (500°C); $2.32 \times 10^{-6} mm^3/Nm$ (600°C); $1.31\times 10^{-5} mm^3/Nm$ (650°C);
Fateh et al. [4]	MS	V and VN	Al_2O_3	1-10 N	0.1 m/s	100 m	**V coating μ:** 1.05 (RT); 0.8 (300°C); 0.71 (400°C); 0.43(500°C); 0.42 (600°C); 0.27(700°C); **VN coating μ:** 0.45 (RT); 0.5 (300°C); 0.47 (400°C); 0.4 (500°C); 0.35 (600°C); 0.26 (700°C);
Fateh et al. [5]	MS	V_2O_5	Al_2O_3	1 N	0.1 m/s	50 m	μ: 0.55 (RT); 0.39 (300°C); 0.33 (400°C); 0.4 (500°C); 0.15 (600°C);
Mayrhofer et al. [6]	MS	TiAlN/VN	Al_2O_3	1 N	0.01 m/s	1000 m	**μ:** 0.55 (RT); 0.96 (500°C); 0.18 (700°C);
Kutschej et al. [7]	MS	Ti-Al-V-N	Al_2O_3	5 N	0.1 m/s	1000 m	**μ:** 0.95 (500°C); 0.7 (600°C); 0.55 (650°C); 0.27 (700°C)
Mu et al. [8]	Ion platting	VN and VCN	Al_2O_3	10 N	--	30 min	**VN coating μ:** 0.68 (RT); 0.46 (300°C); 0.36 (500°C); 0.56 (700°C); **W:** $2.987\times 10^{-6} mm^3/Nm$ (RT); $8.0 \times 10^{-6} mm^3/Nm$ (300°C); $8.732 \times 10^{-6} mm^3/Nm$ (500°C); **VCN coating μ:** 0.57 (RT); 0.39 (300°C); 0.30 (500°C); 0.54 (700°C); **W:** $0.836\times 10^{-6} mm^3/Nm$ (RT); $2.2 \times 10^{-6} mm^3/Nm$ (300°C); $5.736 \times 10^{-6} mm^3/Nm$ (500°C); At, 700°C the wear cannot be calculated due to excessive oxidation.

Table S2: Tribological behavior of molybdenum-based oxides

Author	Method	Material	Counter body	Load	Speed	Time/ Distance	Tribological Performance
Suszko T et al. [9]	MS	Mo_2N	Al_2O_3	1 N	0.3 m/s	2000 cycle	**μ:** 0.42 (RT); 0.7 (100°C); 0.55 (400°C);
Gassner, G., et al. [10]	MS	Mo-N	Al_2O_3	10 N	0.01 m/s	1000 m	**Combination with Al_2O_3 ball** **μ:** 0.38 (RT); 0.38 (500°C); 0.38 (700°C); **Combination with steel ball** **μ:** 0.62 (RT); 0.4 (500°C); 0.52 (700°C); **W:** $\sim 10^{-16} m^3/Nm$
Wang, Wenzhe, et al. [11]	MS	Mo-V-N	Al_2O_3	2 N	0.1 m/s	33 min	For optimized $Mo_{52}V_{22}N_{26}$ **μ:** 0.42 (RT); 0.27 (700°C); **W:** $6.5 \times 10^{-7} mm^3/Nm$ (RT); $19 \times 10^{-6} mm^3/Nm$ (700°C)
Liu, Chenkai, et al. [12]	MS	Mo_2N	Al_2O_3	5 N	--	30 min	**μ:** 0.3 (RT); 0.36 (100°C); 0.53 (200°C); 0.51 (300°C); 0.48 (400°C); 0.41 (500°C); 0.29 (550°C); **W:** $2.1 \times 10^{-6} mm^3/Nm$ (RT); $1.6 \times 10^{-6} mm^3/Nm$ (100°C); $5.3 \times 10^{-7} mm^3/Nm$ (200°C); $1.8 \times 10^{-6} mm^3/Nm$ (300°C); $1.9 \times 10^{-6} mm^3/Nm$ (400°C); $2.9\times 10^{-6} mm^3/Nm$ (500°C); $3.1 \times 10^{-5} mm^3/Nm$ (550°C);
Ghosh, Kunal, et al. [13]	PM	3Y-TZP + 0.5 wt % MgO + 0.5 wt% Mo	Al_2O_3	20 N	0.5 m/s	33 min	**μ:** 0.46 (RT); 0.21 (500°C); **W:** $3.04 \times 10^{-4} m^3/Nm$ (RT); $2.33 \times 10^{-4} m^3/Nm$ (500°C)
Qi, Y. E. [14]	PM	Al_2O_3-Mo	Al_2O_3	27 - 210 N	--	15 min	**f = 2 Hz and L = 70 N** **μ:** 0.9 (RT); 0.34 (800°C); **f = 2 Hz and L = 140 N** **μ:** 0.32 (800°C); **f = 2 Hz and L = 210 N** **μ:** 0.31 (800°C); **f = 5 Hz and L = 70 N;** **μ:** 0.25 (800°C);
M.E Cura et. al. [15]	PM	Al_2O_3-1-10 vol% Mo	Al_2O_3	5 N	0.5 m/s	1000 m	**μ:** 0.35-0.71 (RT); 0.27-0.36 (400°C);

Table S3: Tribological behavior of tungsten-based oxides

Author	Method	Material	Counter body	Load	Speed	Time/ Distance	Tribological Performance
Gassner et al. [10]	MS	W-N	Al_2O_3	10 N	0.01 m/s	1000 m	**Combination with Al_2O_3 ball** **μ:** 0.30 (RT); 0.50 (500°C); 0.45 (700°C); **Combination with steel ball** **μ:** 0.63 (RT); 0.7 (500°C); 0.57 (700°C); **W:** $\sim 10^{-16} m^3/Nm$

Polcar et. al. [16]	MS	W-N	Al_2O_3	5 N	--	--	**$W_{70}N_{30}$ Coating** **μ:** 0.44 (RT); 0.47 (100°C); 0.7 (200°C); 0.65 (300°C); 0.6 (400°C); 0.42 (500°C); **W** ($10^{-6}m^3/Nm$): 0.49 (RT); 0.02 (100°C); 0.02 (200°C); 0.75 (300°C); 2.6 (400°C); 5.8 (500°C); **$W_{53}N_{47}$ Coating** **μ:** 0.29 (RT); 0.6 (300°C); 0.59 (400°C); 0.67 (500°C); **W** ($10^{-6}m^3/Nm$): 0.25 (RT); 1.6 (300°C); 4.8 (500°C); **$W_{42}N_{58}$ Coating** **μ:** 0.25 (RT); 0.44 (100°C); 0.49 (200°C); 0.65 (300°C); 0.6 (400°C); 0.51(500°C); **W** ($10^{-6}m^3/Nm$): 0.01 (RT); 0.01 (100°C); 0.01 (200°C); 0.01 (300°C); 1.1 (400°C); 2.25 (500°C);
Yu et. al. [17]	MS	W-B-N	Al_2O_3	3 N	50 rpm	30 min	**μ:** 0.33 (RT); 0.65 (200°C); 0.56 (300°C); 0.55 (500°C); 0.52 (700°C); **W:** $2.1 \times 10^{-8}m^3/Nm$ (RT); $3.0 \times 10^{-8}m^3/Nm$ (200°C); $4.1 \times 10^{-8}m^3/Nm$ (300°C); $7.3 \times 10^{-8}m^3/Nm$ (500°C); $1.1 \times 10^{-7}m^3/Nm$ (700°C);
Ju et. al. [18]	MS	W-Si-N	Al_2O_3	3 N	50 rpm	30 min	**W_2N Coating** **μ:** 0.45 (RT); 0.51 (100°C); 0.62 (200°C); 0.72 (300°C); **W:** $0.9 \times 10^{-8}m^3/Nm$ (RT); $1.0 \times 10^{-6}m^3/Nm$ (100°C); $6.7 \times 10^{-6}m^3/Nm$ (200°C); $5.5 \times 10^{-5}m^3/Nm$ (300°C); **$W_{41}Si_{23.5}N_{34.5}$ Coating** **μ:** 0.3(RT); 0.68 (100°C); 0.79 (200°C); 0.75 (300°C);0.43 (400°C); 0.36 (600°C);
Yu et. al. [19]	MS	W_2N - Cu	Al_2O_3	3 N	50 rpm	30 min	**$W_{41}Cu_6N_{53}$ Coating** **μ:** 0.3 (RT); 0.39 (200°C); 0.34 (300°C); 0.32 (400°C);0.31 (500°C); 0.29 (600°C); **W:** $1.4 \times 10^{-8}m^3/Nm$ (RT); $8.1 \times 10^{-8}m^3/Nm$ (200°C); $9.0 \times 10^{-8}m^3/Nm$(300°C);$12 \times 10^{-8}m^3/Nm$ (400°C); $13 \times 10^{-8}m^3/Nm$ (500°C); $14 \times 10^{-8}m^3/Nm$ (600°C);

Table S4: Tribological behavior of copper-based oxides

Author	Method	Material	Counter body	Load	Speed	Time/ Distance	Tribological Performance
Valefi et al. [20]	PM	5CuO-3Y-TZP	Al_2O_3	1 N	0.05 m/s	1000 m	**μ:** 0.30 (RT); 0.8 (200°C); 0.70 (400°C); 0.35 (600°C); 0.38 (700°C); **W:** $0.4 \times 10^{-6} mm^3/Nm$ (595°C);
Kong et al. [21]	PM	CuO-3Y-TZP-Mo	Al_2O_3	10 N	0.2 m/s	30 min	**μ:** 0.2 (700°C); 0.18 (800°C); μ: 0.21 (900°C); 0.3 (1000°C); **W:** $3.67 \times 10^{-5} mm^3/Nm$ (700°C); $3.85 \times 10^{-5} mm^3/Nm$ (800°C); $2.22 \times 10^{-4} mm^3/Nm$ (900°C); $9.14 \times 10^{-4} mm^3/Nm$ (1000°C)
Zhu et al. [22]	PM	NiAl-Cr-Mo-CuO	Si_3N_4	10 N	0.19 m/s	60 min	**μ:** 0.9 (RT); 0.4 (600°C); μ: 0.2 (800°C); 0.2 (1000°C); **W:** $6 \times 10^{-5} mm^3/Nm$ (RT); $2.5 \times 10^{-4} mm^3/Nm$ (600°C); $2.0 \times 10^{-6} mm^3/Nm$ (800°C); $6.2 \times 10^{-6} mm^3/Nm$ (1000°C)
Cui et. al. [23]	PM	Fe21Cr-14Mo-10.5Ag-14CuO	Si_3N_4	10 N	0.19 m/s	60 min	**μ:** 0.64 (RT); 0.6 (200°C); 0.56 (400°C); 0.45 (600°C); 0.42 (800°C); **W:** $0.8 \times 10^{-5} mm^3/Nm$ (RT); $0.8 \times 10^{-5} mm^3/Nm$ (200°C); $0.8 \times 10^{-5} mm^3/Nm$ (400°C); $0.25 \times 10^{-5} mm^3/Nm$ (600°C); $0.15 \times 10^{-5} mm^3/Nm$ (800°C)
Pasaribu et. al. [24]	PM	CuO - Al_2O_3	Al_2O_3	5 N	0.1 m/s	1000 m	**μ:** 0.4 – 0.8 **W:** $< 10^{-7} mm^3/Nm$
Roy et. al. [25]	TS	CuO	Al_2O_3	5 N	0.0314 m/s	50 m	**μ:** 0.46 (RT); 0.6 (350°C); **W:** $68 \times 10^{-5} mm^3/Nm$ (RT); $32 \times 10^{-5} mm^3/Nm$ (350°C);

Table S5: Tribological behavior of vanadate-based oxides

Author	Method	Material	Counter body	Load	Speed	Time/ Distance	Tribological Performance
Aouadi et al. [26]; and Muratore et. al [27]	MS	VN/Ag	Si_3N_4	2 N	0.11 m/s	--	**μ**: 0.3 (RT); 0.30 (350°C); μ: 0.12 (700°C); 0.08 (900°C); 0.2 (1000°C)
Guo et al. [28,29]	PLD	VN/Ag	Al_2O_3	10 N	200 rpm	20 min	**μ**: 0.30 (RT); 0.20 (300°C); 0.18 (500°C); 0.10 (700°C); 0.08 (900°C);
Mu et al. [30]	Ion platting	VN-VN/Ag	Al_2O_3	10 N	200 rpm	30 min	**μ**: 0.44 (RT); 0.42 (300°C); 0.45 (500°C); 0.19 (700°C); W: $1.881 \times 10^{-6} mm^3/Nm$ (RT); $5.5 \times 10^{-5} mm^3/Nm$ (300°C); $6.107 \times 10^{-5} mm^3/Nm$ (500°C);

Luster et al. [31]	MS & Burnishing	VN-AgV_3O_4	Si_3N_4	2 N	200 rpm	10,000 cycles	**μ**: 0.90 (RT); μ: 0.20 (750°C);
Xin et al. [32]	Laser Cladding	NiCrAlY/ Cr_3C_2 (NiCr)/V_2O_5/Ag_2O	Si_3N_4	3 N	0.19 m/s	45 min	**μ**: 0.52 (RT); 0.49 (200°C); 0.35 (400°C); 0.26 (600°C); μ: 0.147 (800°C); **W**: $5.6 \times 10^{-5}\ mm^3/Nm$ (RT); $5 \times 10^{-5}\ mm^3/Nm$ (200°C); $6.8 \times 10^{-5}\ mm^3/Nm$ (400°C); $4.4 \times 10^{-5}\ mm^3/Nm$ (600°C); $2.86 \times 10^{-7}\ mm^3/Nm$ (800°C)
Liu et al. [33]	PM	NiAl/Ag V_3O_4	Inconel 718	2 N	300 rpm	60 min	**μ**: 0.31 (RT); 0.21 (300°C); 0.16 (500°C); 0.13 (700°C); 0.06 (900°C); **W**: $2.5 \times 10^{-5}\ mm^3/Nm$ (RT); $3.7 \times 10^{-5}\ mm^3/Nm$ (300°C); $4.8 \times 10^{-5}\ mm^3/Nm$ (500°C); $2.8 \times 10^{-5}\ mm^3/Nm$ (700°C); $1.08 \times 10^{-5}\ mm^3/Nm$ (900°C)
Liu et al. [34]	PM	NiAl-Mo-AgV_3O_4	Inconel 718	2 N	300 rpm	60 min	**μ**: 0.39 (RT); 0.36 (300°C); 0.26 (500°C); 0.2 (700°C); 0.16 (900°C); **W**: $1.9 \times 10^{-5}\ mm^3/Nm$ (RT); $1.3 \times 10^{-5}\ mm^3/Nm$ (300°C); $1.5 \times 10^{-5}\ mm^3/Nm$ (500°C); $1.1 \times 10^{-5}\ mm^3/Nm$ (700°C); $0.1 \times 10^{-5}\ mm^3/Nm$ (900°C)
Zhang et al. [35]	PM	NiCr/Ag V_3O_4	Si_3N_4	9.8 N	0.1884 m/s	20 min	**μ**: 0.73 (RT); 0.64 (200°C); 0.35 (400°C); 0.34 (600°C); 0.34 (800°C); **W**: $1.7 \times 10^{-4}\ mm^3/Nm$ (RT); $2.7 \times 10^{-4}\ mm^3/Nm$ (200°C); $2.6 \times 10^{-4}\ mm^3/Nm$ (400°C); $2.55 \times 10^{-4}\ mm^3/Nm$ (600°C); $2.1 \times 10^{-4}\ mm^3/Nm$ (800°C)
Du et al. [36]	APS	NiCoCrAlY-Cr_2O_3-$AgVO_3$	Si_3N_4	9.8 N	0.1884 m/s	20 min	**μ**: 0.48 (100°C); 0.5 (200°C); 0.45 (400°C); 0.24 (600°C); 0.22 (800°C); **W**: $2.8 \times 10^{-4}\ mm^3/Nm$ (RT); $6.9 \times 10^{-4}\ mm^3/Nm$ (200°C); $8 \times 10^{-4}\ mm^3/Nm$ (400°C); $5 \times 10^{-4}\ mm^3/Nm$ (600°C); $3.5 \times 10^{-4}\ mm^3/Nm$ (800°C)
Bondarev et al. [37,38]	MS	VCN-Ag	Al_2O_3	1 N	0.1 m/s	9000 cycle	**μ:** 0.48 (100°C); 0.55 (150°C); 0.52 (200°C); 0.35 (250°C); 0.35 (300°C); 0.38 (350°C); 0.5 (400°C); 0.7 (450°C); 0.65 (500°C); 0.55 (550°C); 0.5 (600°C); 0.3 (650°C); 0.18 (700°C); **W**: $2.5 \times 10^{-5}\ mm^3/Nm$ (RT); $3.7 \times 10^{-5}\ mm^3/Nm$ (300°C); $4.8 \times 10^{-5}\ mm^3/Nm$ (500°C); $2.8 \times 10^{-5}\ mm^3/Nm$ (700°C); $1.08 \times 10^{-5}\ mm^3/Nm$ (900°C)

Zhao et. al. [39]	Ion platting	VN/Ag	Al_2O_3	10 N	100 rpm	--	**μ**: 0.56-0.50 (RT); 0.44-0.57 (300°C); 0.45-0.46 (500°C); 0.22-0.30 (700°C);

Table S6: Tribological behavior of molybdate-based oxides

Author	Method	Material	Counter body	Load	Speed	Time/ Distance	Tribological Performance
Stone et al. [40]	RMS	$AgMoO_4$	Si_3N_4	1 N			**μ:** 0.37 (RT); 0.32 (300°C); 0.25 (450°C); 0.12 (600°C);
Li et al. [41]	PM	NiCrAlY-Mo-Ag	Si_3N_4	5 N	0.3 m/s	200 m	**μ:** 0.53 (RT); 0.40 (300°C); 0.41 (500°C); 0.28 (700°C); 0.23 (900°C); **W:** $7.35 \times 10^{-5}\ mm^3/Nm$ (RT); $2.9 \times 10^{-5}\ mm^3/Nm$ (300°C); $3.5 \times 10^{-5}\ mm^3/Nm$ (500°C); $2.3 \times 10^{-5}\ mm^3/Nm$ (700°C); $1.6 \times 10^{-5}\ mm^3/Nm$ (900°C)
Chen et al. [42]	APS	NiCrAlY-Mo-Ag	Si_3N_4	5 N	0.3 m/s	200 m	**μ:** 0.32 (RT); 0.31 (200°C); 0.4 (400°C); 0.32 (600°C); 0.28 (800°C); **W:** $6 \times 10^{-5}\ mm^3/Nm$ (RT); $6 \times 10^{-5}\ mm^3/Nm$ (200°C); $10 \times 10^{-5}\ mm^3/Nm$ (400°C); $5 \times 10^{-5}\ mm^3/Nm$ (600°C); $4 \times 10^{-5}\ mm^3/Nm$ (800°C)
Liu et al. [43]	PM	Ni-Cr_2O_3-Ag_2MoO_4	Inconel 718	2 N	0.287 m/s	30 min	**μ:** 0.94 (RT); 0.6 (300°C); 0.5 (500°C); 0.26 (700°C); **W:** $8 \times 10^{-5}\ mm^3/Nm$ (RT); $7 \times 10^{-5}\ mm^3/Nm$ (300°C); $3 \times 10^{-5}\ mm^3/Nm$ (500°C); $1.02 \times 10^{-5}\ mm^3/Nm$ (700°C);
Liu et al. [44]	PM	Ni-Cr_2O_3-$Ag_2Mo_2O_7$	Inconel 718	2 N	0.287 m/s	30 min	**μ:** 0.85 (RT); 0.8 (300°C); 0.4 (500°C); 0.33 (700°C); **W:** $92.03 \times 10^{-5}\ mm^3/Nm$ (RT); $88 \times 10^{-5}\ mm^3/Nm$ (300°C); $4.5 \times 10^{-5}\ mm^3/Nm$ (500°C); $1.51 \times 10^{-5}\ mm^3/Nm$ (700°C);
Zhang et al. [45]	PM	Ag-Mo	Si_3N_4	9.8 N	0.188 m/s	20 min	**μ:** 0.63 (RT); 0.65 (200°C); 0.75 (400°C); 0.18 (500°C); 0.18 (600°C); **W:** $5 \times 10^{-4}\ mm^3/Nm$ (RT); $6 \times 10^{-4}\ mm^3/Nm$ (200°C); $6.5 \times 10^{-4}\ mm^3/Nm$ (400°C); $2 \times 10^{-4}\ mm^3/Nm$ (600°C);
Muratore et al. [46]	MS & PLD	YSZ-Ag-Mo-MoS_2	Si_3N_4	1 N	0.2 m/s	--	**μ:** 0.2 (RT); 0.1 (300°C); 0.2 (500°C); 0.2 (700°C);
Hu et al. [47]	MS & PLD	YSZ-Ag-Mo	Si_3N_4	1 N	--	--	**μ:** 0.42 (RT); 0.30 (300°C); 0.40 (500°C); 0.39 (700°C);
Aouadi et al. [48]	UMS	Mo_2N-MoS_2-Ag	Si_3N_4	1 N	0.2 m/s	10, 000 cycles	**μ:** 0.42 (RT); 0.37 (350°C); 0.10 (600°C); **W:** $2 \times 10^{-4}\ mm^3/Nm$ (RT); $7 \times 10^{-5}\ mm^3/Nm$ (350°C); $1 \times 10^{-5}\ mm^3/Nm$ (600°C);
Aouadi et al. [49]	UMS	Mo_2N-MoS_2-Ag	Si_3N_4	1 N	0.11 m/s	300, 000 cycles	**μ:** 0.4 (RT); 0.3 (350°C); 0.1 (600°C); **W:** $2 \times 10^{-5}\ mm^3/Nm$ (RT); $6 \times 10^{-6}\ mm^3/Nm$ (350°C); $8 \times 10^{-7}\ mm^3/Nm$ (600°C);
Shtansky et al. [50]	MS	MoCN-Ag	Al_2O_3	1 N	0.1 m/s	300 m	**μ:** 0.27 (RT); 0.35 (100°C); 0.47 (150°C); 0.6 (200°C); 0.7 (250°C); 0.72 (300°C); 0.79 (350°C); 0.35 (400°C); 0.35 (450°C); 0.42 (500°C); 0.32 (550°C); 0.30 (600°C); 0.41 (650°C); 0.41 (700°C);
Wang et al. [51]	PM	NiCr-MoO_3-Ag	Al_2O_3	20 N	0.108 m/s	60 min	**μ:** 0.65 (RT); 0.45 (300°C); 0.3 (500°C); 0.2 (700°C); 0.19 (900°C); **W:** $15 \times 10^{-5}\ mm^3/Nm$ (RT); $10 \times 10^{-5}\ mm^3/Nm$ (300°C); $6.5 \times 10^{-5}\ mm^3/Nm$ (500°C); $2 \times 10^{-5}\ mm^3/Nm$ (700°C); $4.68 \times 10^{-6}\ mm^3/Nm$ (900°C)

Chen et al. [52]	HVOF	NiMoAl-Cr_3C_2-Ag	Si_3N_4	15 N	600 rpm	45 min	**μ:** 0.19 (RT); 0.26 (200°C); 0.32 (400°C); 0.28 (600°C); 0.25 (800°C); **W:** $1.2 \times 10^{-6}\, mm^3/Nm$ (RT); $6.0 \times 10^{-6}\, mm^3/Nm$ (200°C); $6.0 \times 10^{-5}\, mm^3/Nm$ (400°C); $9.0 \times 10^{-6}\, mm^3/Nm$ (600°C); $9.0 \times 10^{-6}\, mm^3/Nm$ (800°C)
Li et al. [53]	APS	NiCrAlY-Mo-Ag	Al_2O_3	10 N	0.3 m/s	60 min	**μ:** 0.55 (RT); 0.48 (300°C); 0.45 (500°C); 0.28 (700°C); 0.18 (900°C); **W:** $7.2 \times 10^{-5}\, mm^3/Nm$ (RT); $2 \times 10^{-5}\, mm^3/Nm$ (300°C); $3 \times 10^{-5}\, mm^3/Nm$ (500°C); $1.9 \times 10^{-5}\, mm^3/Nm$ (700°C); $3 \times 10^{-5}\, mm^3/Nm$ (900°C)
Lu et al. [54]	PLD	Mo-V-Ag-O	Al_2O_3	2 N	0.11 m/s	30 min	**μ:** 0.91 (RT); 0.8 (300°C); 0.6 (400°C); 0.24 (500°C);
Dai et al. [55]	MS	Ag-MoNbN	Al_2O_3	1 N	0.1 m/s	--	**μ:** 0.6 (RT); 0.45 (100°C); 0.35 (200°C); 0.31 (300°C); 0.29 (400°C); 0.31 (500°C); 0.18 (600°C); 0.09 (700°C); 0.1 (800°C);
Wang et al. [56]	RMS	MoVN-Ag	Al_2O_3	2 N	0.1 m/s	33 min	**μ:** 0.4 (RT); 0.6 (300°C); 0.19 (500°C); 0.28 (700°C); **W:** $4.4 \times 10^{-7}\, mm^3/Nm$ (RT); $3 \times 10^{-6}\, mm^3/Nm$ (300°C); $1.0 \times 10^{-7}\, mm^3/Nm$ (500°C); $4.6 \times 10^{-7}\, mm^3/Nm$ (700°C);
Takeichi et al. [57]	Burnishing	$Cu_3Mo_2O_9$; $CuMoO_4$	Steel	61.8 N	55 mm/s	30 min	**Friction coefficient of $Cu_3Mo_2O_9$;** **μ:** 0.70 (RT); 0. 58 (200°C); 0.58 (400°C); 0.50 (500°C); 0.42 (600°C); 0.35 (700°C); **Friction coefficient of $CuMoO_4$** **μ:** 0.65 (RT); 0. 60 (200°C); 0.55 (400°C); 0.49 (500°C); 0.40 (600°C); 0.42 (700°C);
Xin et al. [58]	Laser Cladding	NiCrAlY/Cr_3C_2(NiCr/Cu/MoO_3)	Si_3N_4	3 N	0.19 m/s	45 min	**μ:** 0.63 (RT); 0.76 (200°C); 0.48 (400°C); 0.36 (600°C); 0.34 (800°C); **W:** $6.05 \pm 0.38 \times 10^{-5}\, mm^3/Nm$ (RT); $7.7 \pm 0.75 \times 10^{-5}\, mm^3/Nm$ (200°C); $6.57 \pm 0.43 \times 10^{-5}\, mm^3/Nm$ (400°C); $2.90 \pm 0.32 \times 10^{-5}\, mm^3/Nm$ (600°C); $1.0 \pm 0.51 \times 10^{-5}\, mm^3/Nm$ (800°C)
Yao et al. [59]	APS	NiAl-MoO_3/CuO	Al_2O_3	10 N	0.1 m/s	60 min	**μ:** 0.60 (RT); 0.55 (200°C); 0.55 (400°C); 0.35 (600°C); 0.16 (800°C); **W:** $2.5 \times 10^{-5}\, mm^3/Nm$ (RT); $10 \times 10^{-5}\, mm^3/Nm$ (200°C); $19 \times 10^{-5}\, mm^3/Nm$ (400°C); $6 \times 10^{-5}\, mm^3/Nm$ (600°C); $3.7 \times 10^{-5}\, mm^3/Nm$ (800°C)
Kong et. al. [60]	PM	$ZrO_2(Y_2O_3)$-Ag-CaF_2-10Mo	Al_2O_3	10 N	0.2 m/s	30 min	**μ:** 0.65 (RT); 0.62 (200°C); 0.51 (400°C); 0.56 (600°C); 0.28 (800°C); 0.32 (1000°C); **W:** $2.5 \times 10^{-5}\, mm^3/Nm$ (RT); $2.4 \times 10^{-5}\, mm^3/Nm$ (200°C); $6.5 \times 10^{-5}\, mm^3/Nm$ (400°C); $3.0 \times 10^{-5}\, mm^3/Nm$ (600°C); $2.5 \times 10^{-5}\, mm^3/Nm$ (800°C); $13 \times 10^{-5}\, mm^3/Nm$ (1000°C)
Ouyang et al. [61]	PM	NiCr-$BaMoO_4$	Si_3N_4	5 N	--	60 min	**μ:** 0.60 (RT); 0.26-0.29 (400°C); 0.31-0.40 (600°C); **W:** $0.65 \times 10^{-5} \sim 9 \times 10^{-5}\, mm^3/Nm$ (RT); $1.06 \times 10^{-5} \sim 2.15 \times 10^{-5}\, mm^3/Nm$ (400°C); $3.43 \times 10^{-5} \sim 4.25 \times 10^{-6}\, mm^3/Nm$ (600°C);
Xiao et. al. [62]	SPS	TZ3Y20A-$SrMoO_4$	Al_2O_3	4.9 N	200 rpm	60 min	**μ:** 0.28 (RT); 0.23 (200°C); 0.54 (400°C); 0.55 (600°C); 0.41 (800°C); **W:** At RT and 200°C, the wear rates are in the range of $10^{-7}\, mm^3/Nm$ while for 400°C to 800°C is $10^{-5} \sim 10^{-4}\, mm^3/Nm$

Table S7: Tribological behavior of tantalate-based oxides

Author	Method	Material	Counter body	Load	Speed	Time/ Distance	Tribological Performance
Zhu et al. [63]	Laser Cladding	NiCrAlY/ Ag_2O/Ta_2O_5	Si_3N_4	30 N	300 rpm	60 min	**μ:** 0.45 (RT); 0.43 (350°C); 0.26 (550°C); 0.13 (750°C); **W:** $307.5 \times 10^{-6}\ mm^3/Nm$ (RT); $130.3 \times 10^{-6}\ mm^3/Nm$ (350°C); $78.6 \times 10^{-6}\ mm^3/Nm$ (550°C); $32.1 \times 10^{-6}\ mm^3/Nm$ (750°C).
Stone et al. [64]	Burnishing	$AgTaO_3$	Si_3N_4	2 N	0.11 m/s	10 m	**μ:** 0.43 (RT); 0.32 (350°C); 0.23 (500°C); μ: 0.18 (750°C);
	MS	Ag-Ta					**μ:** 0.59 (RT); 0.43 (350°C); 0.25 (500°C); μ: 0.06 (750°C);
	MS	TaN/Ag					**μ:** 0.39 (RT); 0.36 (350°C); 0.30 (500°C); 0.23 (750°C);
Wang et al. [65]	MS	Ta-Ag	Si_3N_4	1.5 N	300 rpm	141 m	**μ:** 0.7 (RT); 0.5 (400°C); 0.4 (600°C); 0.32 (700°C); **W:** $1.6 \times 10^{-5}\ mm^3/Nm$ (700°C);
Gao et al. [66]	MS	(Ag, Cu)-Ta-O	Si_3N_4	2 N	0.11 m/s	10 m	**μ:** 0.58 (RT); 0.42 (350°C); 0.30 (500°C); 0.25 (750°C); **At 750°C:** **W:** $0.52 \times 10^{-7}\ mm^3/Nm$ ($CuTa_2O_6$)

Table S8: Tribological behavior of niobate-based oxides

Author	Method	Material	Counter body	Load	Speed	Time/ Distance	Tribological Performance
Stone et al. [67]	MS	NbN-Ag	Si_3N_4	1 N	90 mm/s	--	**μ:** 0.35 (RT); 0.30 (350°C); 0.27 (750°C); 0.33 (1000°C);
Shirani et al. [68]	PM	Ag_2O, Nb_2O_5	Si_3N_4	1 N	2.5 cm/s	--	**μ:** 0.8 (RT); 0.24 (600°C);
Feng et al. [69]	PM	NiAl-NbC-Ag	Al_2O_3	20 N	10.5 cm/s	60 min	**μ:** 0.58 (RT); 0.53 (300°C); 0.45 (500°C); 0.48 (700°C); 0.26 (900°C); **W:** $1 \times 10^{-5}\ mm^3/Nm$ (RT); $7.5 \times 10^{-5}\ mm^3/Nm$ (300°C); $24 \times 10^{-5}\ mm^3/Nm$ (500°C); $24.8 \times 10^{-5}\ mm^3/Nm$ (700°C); $1.5 \times 10^{-5}\ mm^3/Nm$ (900°C)
Feng et al. [70]	PM	NiAl-$AgNbO_3$	Al_2O_3	10 N	10.5 cm/s	60 min	**μ:** 0.48 (RT); 0.50 (200°C); 0.46 (400°C); 0.41 (600°C); 0.3 (800°C); **W:** $5.1 \times 10^{-5}\ mm^3/Nm$ (RT); $10 \times 10^{-5}\ mm^3/Nm$ (200°C); $18.5 \times 10^{-5}\ mm^3/Nm$ (400°C); $8.5 \times 10^{-5}\ mm^3/Nm$ (600°C); $3.5 \times 10^{-5}\ mm^3/Nm$ (800°C)

Wu et al. [71]	MS	NbCN-Ag	Al_2O_3	3 N	50 rpm	30 min	**μ:** 0.30 (RT); 0.39 (200°C); 0.45 (300°C); 0.41 (400°C); 0.35 (500°C); **W:** $0.4 \times 10^{-7}\ mm^3/Nm$ (RT); $0.8 \times 10^{-7}\ mm^3/Nm$ (200°C); $2.7 \times 10^{-8}\ mm^3/Nm$ (300°C); $3.2 \times 10^{-7}\ mm^3/Nm$ (400°C); $6.7 \times 10^{-7}\ mm^3/Nm$ (500°C)

Table S9: Tribological behavior of tungstate-based oxides

Author	Method	Material	Counter body	Load	Speed	Time/ Distance	Tribological Performance
Stone et al. [40]	MS	Ag_2WO_4	Si_3N_4	1 N	--	--	**μ:** 0.56 (RT); 0.53 (300°C); 0.48 (450°C); 0.43 (600°C);
Zhu et al. [72]	PM	Ni_3Al-Ag-BaF_2/CaF_2-W	Si_3N_4	10 N	0.19 m/s	60 min	**μ:** 0.32 (RT); 0.3 (200°C); 0.3 (400°C); 0.42 (600°C); 0.35 (800°C); **W:** $0.2 \times 10^{-4}\ mm^3/Nm$ (RT); $0.25 \times 10^{-4}\ mm^3/Nm$ (200°C); $1.8 \times 10^{-4}\ mm^3/Nm$ (400°C); $6.2 \times 10^{-4}\ mm^3/Nm$ (600°C); $1.1 \times 10^{-4}\ mm^3/Nm$ (800°C)
Feng et. al. [73]	PM	NiCr-Ti_3SiC_2-$Ag_2W_2O_7$	Si_3N_4	10 N	0.2 m/s	60 min	**μ:** 0.49 (RT); 0.46 (200°C); 0.44 (400°C); 0.33 (600°C); **W:** $8 \times 10^{-5}\ mm^3/Nm$ (RT); $7 \times 10^{-5}\ mm^3/Nm$ (200°C); $9 \times 10^{-5}\ mm^3/Nm$ (400°C); $5.5 \times 10^{-5}\ mm^3/Nm$ (600°C);
Xue [74]	PM	Ni-Cr-W-Al-Ti-MoS_2	Al_2O_3	100 N	0.8 m/s	1500 m	**μ:** 0.5 (200°C); 0.30 (400°C); 0.18 (600°C); **W:** $1.8 \times 10^{-5}\ mm^3/Nm$ (RT); $1.5 \times 10^{-5}\ mm^3/Nm$ (200°C); $1.2 \times 10^{-5}\ mm^3/Nm$ (400°C); $2.4 \times 10^{-5}\ mm^3/Nm$ (600°C);
Huang et al. [75]	PM	W-Cu	Cast iron	50 N & 20 N	--	38 min	**W70-Cu30** (900°C) **μ:** 0.5 (5 N); 0.35 (20 N). **W80-Cu20** (900°C) **μ:** 0.53 (5 N); 0.46 (20 N);
Prasad et al. [76]	Burnishing	ZnO-WS_2	Steel	1 N	200 rpm	--	**μ:** 0.02 (300°C); 0.22 (500°C);

References

[1] Fateh N, Fontalvo GA, Gassner G, Mitterer C. Influence of high-temperature oxide formation on the tribological behaviour of TiN and VN coatings. Wear 2007;262:1152–8.

[2] Gassner G, Mayrhofer PH, Kutschej K, Mitterer C, Kathrein M. A new low friction concept for high temperatures: lubricious oxide formation on sputtered VN coatings. Tribol Lett 2004;17:751–6.

[3] Ouyang JH, Murakami T, Sasaki S. High-temperature tribological properties of a cathodic arc ion-plated (V, Ti) N coating. Wear 2007;263:1347–53.

[4] Fateh N, Fontalvo GA, Gassner G, Mitterer C %J T letters. The beneficial effect of high-temperature oxidation on the tribological behaviour of V and VN coatings 2007;28:1–7.

[5] Fateh N, Fontalvo GA, Mitterer C. Tribological Properties of reactive magnetron sputtered V 2 O 5 and VN–V 2 O 5 coatings. Tribol Lett 2008;30:21–6.

[6] Mayrhofer PH, Hovsepian PE, Mitterer C, Münz W-D. Calorimetric evidence for frictional self-adaptation of TiAlN/VN superlattice coatings. Surf Coatings Technol 2004;177:341–7.

[7] Kutschej K, Mayrhofer PH, Kathrein M, Polcik P, Mitterer C. Influence of oxide phase formation on the tribological behaviour of Ti–Al–V–N coatings. Surf Coatings Technol 2005;200:1731–7.

[8] Mu Y, Liu M, Zhao Y. Carbon doping to improve the high temperature tribological properties of VN coating. Tribol Int 2016;97:327–36.

[9] Suszko T, Gulbiński W, Jagielski J. The role of surface oxidation in friction processes on molybdenum nitride thin films. Surf Coatings Technol 2005;194:319–24.

[10] Gassner G, Mayrhofer PH, Kutschej K, Mitterer C, Kathrein M. Magnéli phase formation of PVD Mo–N and W–N coatings. Surf Coatings Technol 2006;201:3335–41.

[11] Wang W, Zheng S, Pu J, Cai Z, Wang H, Wang L, et al. Microstructure, mechanical and tribological properties of Mo-VN films by reactive magnetron sputtering. Surf Coatings Technol 2020:125532.

[12] Liu C, Ju H, Yu L, Xu J, Geng Y, He W, et al. Tribological properties of Mo2N films at elevated temperature. Coatings 2019;9:734.

[13] Ghosh K, Mazumder S, Kumar Singh B, Hirani H, Roy P, Mandal N. Tribological Property Investigation of Self-Lubricating Molybdenum-Based Zirconia Ceramic Composite Operational at Elevated Temperature. J Tribol 2020;142.

[14] Qi Y, Zhang Y-S, Hu L-T. High-temperature self-lubricated properties of Al2O3/Mo laminated composites. Wear 2012;280:1–4.

[15] Cura ME, Liu XW, Kanerva U, Varjus S, Kivioja A, Söderberg O, et al. Friction behavior of alumina/molybdenum composites and formation of MoO3− x phase at 400 C. Tribol Int 2015;87:23–31.

[16] Polcar T, Parreira NMG, Cavaleiro A %J W. Structural and tribological characterization of tungsten nitride coatings at elevated temperature 2008;265:319–26.

[17] Yu L, Zhao H, Xu J %J A surface science. Mechanical, tribological and corrosion performance of WBN composite films deposited by reactive magnetron sputtering 2014;315:380–6.

[18] Ju H, He X, Yu L, Xu J %J S, Technology C. The microstructure and tribological properties at elevated temperatures of tungsten silicon nitride films 2017;326:255–63.

[19] Yu L, Zhao H, Ju H, Xu J %J TSF. Influence of Cu content on the structure, mechanical and tribological properties of W2N-Cu films 2017;624:144–51.

[20] CuO_2011_High-Temperature Tribological and Self-Lubricating Behavior of Copper Oxide-Doped Y-TZP Composite Sliding Against Alumina.pdf n.d.

[21] Kong L, Bi Q, Zhu S, Qiao Z, Yang J, Liu W. Effect of CuO on self-lubricating properties of ZrO2 (Y2O3)–Mo composites at high temperatures. J Eur Ceram Soc 2014;34:1289–96.

[22] Zhu S, Cheng J, Qiao Z, Tian Y, Yang J. High temperature lubricating behavior of NiAl matrix composites with addition of CuO. J Tribol 2016;138.

[23] Cui G, Liu Y, Gao G, Liu H, Kou Z %J M. Microstructure and high-temperature wear performance of FeCr matrix self-lubricating composites from room temperature to 800 C 2020;13:51.

[24] Pasaribu HR, Reuver KM, Schipper DJ, Ran S, Wiratha KW, Winnubst AJA, et al. Environmental effects on friction and wear of dry sliding zirconia and alumina ceramics doped with copper oxide. Int J Refract Met Hard Mater 2005;23:386–90.

[25] Roy A, Sharifi N, Munagala VN V, Alidokht SA, Patel P, Makowiec M, et al. Microstructural evolution and tribological behavior of suspension plasma sprayed CuO as high-temperature lubricious coatings. Wear 2023:204874.

[26] Aouadi SM, Singh DP, Stone DS, Polychronopoulou K, Nahif F, Rebholz C, et al. Adaptive VN/Ag nanocomposite coatings with lubricious behavior from 25 to 1000° C. Acta Mater 2010;58:5326–31.

[27] Muratore C, Bultman JE, Aouadi SM, Voevodin AA. In situ Raman spectroscopy for examination of high temperature tribological processes. Wear 2011;270:140–5.

[28] Guo H, Han M, Chen W, Lu C, Li B, Wang W, et al. Microstructure and properties of VN/Ag composite

films with various silver content. Vacuum 2017;137:97–103.
[29] Guo H, Lu C, Zhang Z, Liang B, Jia J. Comparison of microstructures and properties of VN and VN/Ag nanocomposite films fabricated by pulsed laser deposition. Appl Phys A 2018;124:694.
[30] Mu Y, Liu M, Wang Y, Liu E. PVD multilayer VN–VN/Ag composite coating with adaptive lubricious behavior from 25 to 700 C. RSC Adv 2016;6:53043–53.
[31] Luster B, Stone D, Singh DP, to Baben M, Schneider JM, Polychronopoulou K, et al. Textured VN coatings with Ag3VO4 solid lubricant reservoirs. Surf Coatings Technol 2011;206:1932–5.
[32] Xin B, Yu Y, Zhou J, Wang L, Ren S, Li Z. Effect of silver vanadate on the lubricating properties of NiCrAlY laser cladding coating at elevated temperatures. Surf Coatings Technol 2016;307:136–45.
[33] Liu E, Bai Y, Gao Y, Yi G, Jia J. Tribological properties of NiAl-based composites containing Ag3VO4 nanoparticles at elevated temperatures. Tribol Int 2014;80:25–33.
[34] Liu E, Gao Y, Bai Y, Yi G, Wang W, Zeng Z, et al. Tribological properties of self-lubricating NiAl/Mo-based composites containing AgVO3 nanowires. Mater Charact 2014;97:116–24.
[35] Zhang W, Du L, Lan H, Huang C, Zhang W. Wear behavior of a NiCr/AgVO 3 self-lubricating composite. Acta Metall Sin (English Lett 2013;26:435–40.
[36] Du L, Zhang W, Zhang W, Zhang T, Lan H, Huang C. Tribological and oxidation behaviors of the plasma sprayed NiCoCrAlY-Cr2O3-AgVO3 coating. Surf Coatings Technol 2016;298:7–14.
[37] Bondarev A V, Kvashnin DG, Shchetinin I V, Shtansky D V. Temperature-dependent structural transformation and friction behavior of nanocomposite VCN-(Ag) coatings. Mater Des 2018;160:964–73.
[38] Bondarev A V, Golizadeh M, Shvyndina N V, Shchetinin I V, Shtansky D V. Microstructure, mechanical, and tribological properties of Ag-free and Ag-doped VCN coatings. Surf Coatings Technol 2017;331:77–84.
[39] Zhao Y, Mu Y, Ming LIU. Mechanical properties and friction− wear characteristics of VN/Ag multilayer coatings with heterogeneous and transition interfaces. Trans Nonferrous Met Soc China 2020;30:472–83.
[40] Stone D, Liu J, Singh DP, Muratore C, Voevodin AA, Mishra S, et al. Layered atomic structures of double oxides for low shear strength at high temperatures. Scr Mater 2010;62:735–8.
[41] Li B, Gao Y, Han M, Guo H, Wang W, Jia J. Microstructure and tribological properties of NiCrAlY-Mo-Ag composite by vacuum hot-press sintering. Vacuum 2017;143:1–6.
[42] Chen J, An Y, Yang J, Zhao X, Yan F, Zhou H, et al. Tribological properties of adaptive NiCrAlY–Ag–Mo coatings prepared by atmospheric plasma spraying. Surf Coatings Technol 2013;235:521–8.
[43] Liu E, Wang W-Z, Gao Y, Jia J-H. Tribological properties of adaptive Ni-based composites with addition of lubricious Ag 2 MoO 4 at elevated temperatures. Tribol Lett 2012;47:21–30.
[44] Liu E-Y, Gao Y-M, Wang W-Z, Zhang X-L, Wang X, Yi G-W, et al. Effect of Ag2Mo2O7 incorporation on the tribological characteristics of adaptive Ni-based composite at elevated temperatures. Tribol Trans 2013;56:469–79.
[45] Zhang T, Huang C, Lan H, Du L, Zhang W. Tribological properties and lubrication mechanisms of a Ag–Mo composite. Lubr Sci 2016;28:141–56.
[46] Muratore C, Voevodin AA. Molybdenum disulfide as a lubricant and catalyst in adaptive nanocomposite coatings. Surf Coatings Technol 2006;201:4125–30.
[47] Hu JJ, Muratore C, Voevodin AA. Silver diffusion and high-temperature lubrication mechanisms of YSZ–Ag–Mo based nanocomposite coatings. Compos Sci Technol 2007;67:336–47.
[48] Aouadi SM, Paudel Y, Luster B, Stadler S, Kohli P, Muratore C, et al. Adaptive Mo 2N/MoS 2/Ag tribological nanocomposite coatings for aerospace applications. Tribol Lett 2008;29:95–103. https://doi.org/10.1007/s11249-007-9286-x.
[49] Aouadi SM, Paudel Y, Simonson WJ, Ge Q, Kohli P, Muratore C, et al. Tribological investigation of adaptive Mo2N/MoS2/Ag coatings with high sulfur content. Surf Coatings Technol 2009;203:1304–9.
[50] Shtansky D V, Bondarev A V, Kiryukhantsev-Korneev P V, Rojas TC, Godinho V, Fernández A. Structure and tribological properties of MoCN-Ag coatings in the temperature range of 25–700° C. Appl Surf Sci 2013;273:408–14.
[51] Wang J-Y, Shan Y, Guo H, Li B, Wang W, Jia J. Friction and Wear Characteristics of Hot-Pressed NiCr–Mo/MoO 3/Ag Self-Lubrication Composites at Elevated Temperatures up to 900 C. Tribol Lett 2015;59:48.
[52] Chen J, Zhao X, Zhou H, Chen J, An Y, Yan F. Microstructure and tribological property of HVOF-sprayed adaptive NiMoAl–Cr3C2–Ag composite coating from 20° C to 800° C. Surf Coatings Technol 2014;258:1183–90.
[53] Li B, Gao Y, Jia J, Han M, Guo H, Wang W. Influence of heat treatments on the microstructure as well as mechanical and tribological properties of NiCrAlY-Mo-Ag coatings. J Alloys Compd 2016;686:503–10.
[54] Lu C, Fu Y, Jia J, Yi G, Xie E, Guo H. Effect of substrate temperatures on the properties of PLD Mo–V–Ag–O nanocomposite thin films. Vacuum 2019;167:357–63.
[55] Dai X, Wen M, Wang J, Cui X, Wang X, Zhang K. The tribological performance at elevated temperatures

of MoNbN-Ag coatings. Appl Surf Sci 2020;509:145372.
[56] Wang W, Pu J, Cai Z, Zheng S, Wei Y. Insights into friction properties and mechanism of self-lubricating MoVN-Ag films at high temperature. Vacuum 2020:109332.
[57] Takeichi Y, Inada M, Minami K, Kawamura M, Dzimko M. Tribological properties of copper molybdate powder solid lubricants under high temperature conditions. Tribol Online 2015;10:127–37.
[58] Xin B, Yu Y, Zhou J, Wang L, Ren S. Effect of copper molybdate on the lubricating properties of NiCrAlY laser clad coating at elevated temperatures. Surf Coatings Technol 2017;313:328–36.
[59] Yao Q, Jia J, Chen T, Xin H, Shi Y, He N, et al. High temperature tribological behaviors and wear mechanisms of NiAl-MoO3/CuO composite coatings. Surf Coatings Technol 2020;395:125910. https://doi.org/10.1016/j.surfcoat.2020.125910.
[60] Kong L, Zhu S, Qiao Z, Yang J, Bi Q, Liu W. Effect of Mo and Ag on the friction and wear behavior of ZrO2 (Y2O3)–Ag–CaF2–Mo composites from 20° C to 1000° C. Tribol Int 2014;78:7–13.
[61] Ouyang J-H, Shi C-C, Liu Z-G, Wang Y-M, Wang Y-J. Fabrication and high-temperature tribological properties of self-lubricating NiCr–BaMoO4 composites. Wear 2015;330:272–9.
[62] Li X bing, Li YF. Tribological Properties of Spark Plasma Sintering TZ3Y20A–SrMoO4 Composites at Elevated Temperature. Tribol Lett 2017;65:1–10. https://doi.org/10.1007/s11249-017-0905-x.
[63] Zhu R, Zhang P, Yu Z, Yan H, Li S, Wu D, et al. Microstructure and wide temperature range self-lubricating properties of laser cladding NiCrAlY/Ag2O/Ta2O5 composite coating. Surf Coatings Technol 2020;383:125248.
[64] Stone DS, Harbin S, Mohseni H, Mogonye J-E, Scharf TW, Muratore C, et al. Lubricious silver tantalate films for extreme temperature applications. Surf Coatings Technol 2013;217:140–6.
[65] Wang J, Li J, Li H, Zhang X, Huang J, Xiong D. Friction and wear properties of amorphous and nanocrystalline Ta-Ag films at elevated temperatures as function of working pressure. Surf Coatings Technol 2018;353:135–47.
[66] Gao H, Otero-de-la-Roza A, Gu J, Stone D, Aouadi SM, Johnson ER, et al. (Ag, Cu)–Ta–O ternaries as high-temperature solid-lubricant coatings. ACS Appl Mater Interfaces 2015;7:15422–9.
[67] Stone DS, Migas J, Martini A, Smith T, Muratore C, Voevodin AA, et al. Adaptive NbN/Ag coatings for high temperature tribological applications. Surf Coatings Technol 2012;206:4316–21.
[68] Shirani A, Gu J, Wei B, Lee J, Aouadi SM, Berman D. Tribologically enhanced self-healing of niobium oxide surfaces. Surf Coatings Technol 2019;364:273–8.
[69] Feng X, Jia J, Wang W, Shan Y. Mechanical and tribological properties of NiAl–NbC–Ag composites prepared by hot-pressing sintering. J Mater Res 2017;32:2361–72.
[70] Feng X, Lu C, Jia J, Xue J, Wang Q, Sun Y, et al. High temperature tribological behaviors and wear mechanisms of NiAl–NbC–Ag composites formed by in-situ decomposition of AgNbO3. Tribol Int 2020;141:105898.
[71] Wu F, Yu L, Ju H, Asempah I, Xu J. Structural, mechanical and tribological properties of NbCN-Ag nanocomposite films deposited by reactive magnetron sputtering. Coatings 2018;8:50.
[72] Zhu S, Bi Q, Yang J, Liu W. Ni 3 Al matrix composite with lubricious tungstate at high temperatures. Tribol Lett 2012;45:251–5.
[73] Feng S, Zhou X, Zhang Q. Tribological Behavior of Ni-based Self-lubricating Composites with the Addition of Ti 3 SiC 2 and Ag 2 W 2 O 7. J Wuhan Univ Technol Sci Ed 2019;34:698–706.
[74] Xue M. High temperature oxidation and wear behaviour of powder metallurgically developed Ni-Cr-W-Al-Ti-MoS2 composite. Indian J Eng Mater Sci 2009;16:111–5.
[75] Huang Y, Zhou X, Hua N, Que W, Chen W. High temperature friction and wear behavior of tungsten–copper alloys. Int J Refract Met Hard Mater 2018;77:105–12.
[76] Prasad S V, McDevitt NT, Zabinski JS. Tribology of tungsten disulfide–nanocrystalline zinc oxide adaptive lubricant films from ambient to 500 C. Wear 2000;237:186–96.

Appendix B

Supplementary section 2

Influencing Factors on the Lubricity of Oxide Coatings

Amit Roy, Department of Mechanical, Industrial and Aerospace Engineering, Concordia University, Montreal, QC H3G 1M8, Canada
Richard R. Chromik, Department of Mining and Materials Engineering, McGill University, Montréal, QC H3A 0C5, Canada
Christian Moreau, Department of Mechanical, Industrial and Aerospace Engineering, Concordia University, Montreal, QC H3G 1M8, Canada
Pantcho Stoyanov, Department of Chemical and Materials Engineering, Concordia University, Montreal, QC H3G 1M8, Canada

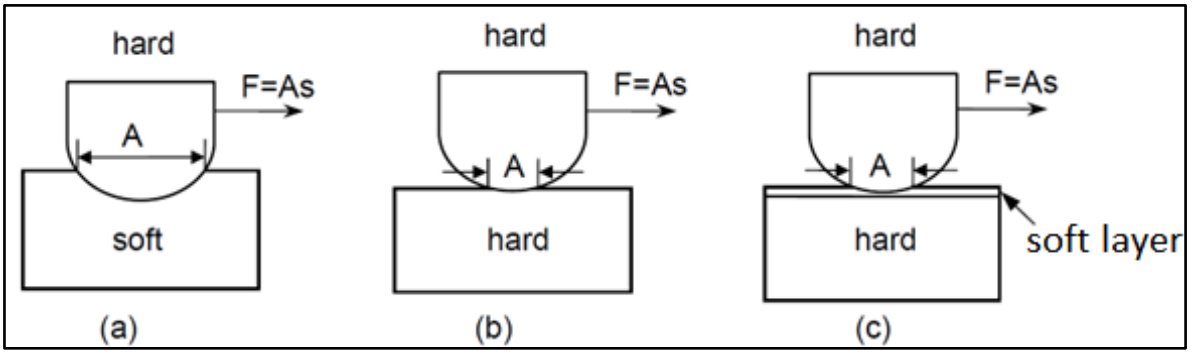

Figure SS 1. Relation of friction coefficient to substrate material hardness. (a) Hard counterface metal in contact with soft substrate metal (large *A* and small *s*), (b) Similar hardness of counterface metal and substrate metal in contact with each other (small *A* and large *s*), (c) Similar hardness of counterface metal and substrate metal separated by a thin film of soft metal deposited on the substrate surface (both *A* and *s* are small) [1].

Table SS 1: Steady state friction coefficient of different oxides after dry sliding test at room and at high temperatures

Type of oxides	Friction coefficient (μ)		Specific wear rate $\times 10^{-5}$ (mm^3/N.m.)	
	RT	HT	RT	HT
CuO	0.7*	0.46	68	32
CoO	0.63	0.5	2.2	1.2
NiO	0.45	0.7	4.2	‡
Ta_2O_5	0.9	0.8	123	54
$Co_{0.75}Ni_{0.25}O$	0.61	0.6	2.6	2.4
$Co_{0.5}Ni_{0.5}O$	0.49	0.68	0.83	88.8

* The friction coefficient continuously increased and no steady state behavior was observed. The value highlighted here was the maximum friction coefficient at the end of the test.

‡ Coating worn out after 500 cycles

Table SS 2: The ionic potential, interaction parameter, thermal conductivity, and melting point of different oxides studied here [2–5]

Type of oxides	Ionic potential ($Å^{-1}$)	Interaction parameter ($Å^{-3}$)	Thermal conductivity, k (W/m.k.)	Melting point (°C)
CuO	2.4	0.035	33	1326
CoO	2.7	0.059	9	1935
NiO	2.8	0.08	35	1955
Ta_2O_5	6.4	0.08	5	1872
$Co_{0.75}Ni_{0.25}O$	2.75	0.06	---	---
$Co_{0.5}Ni_{0.5}O$	2.75	0.07⁑	---	---

⁑ The interaction parameter was calculated according to the equation (**2.1**) mentioned in **chapter 2**.

$$A = X_1A_1 + X_2A_2 \qquad (2.1)$$

Where, X_i and A_i are the mol% of the individual oxides and the interaction parameters of the respective oxides, respectively [4,5].

Table SS 3: The summary of wear track phenomenon based on the surface and sub-surface analysis [6–9]

Type of oxides	Wear mechanisms and interfacial processes (surface and sub-surface)	
	RT	HT
CuO	Adhesive wear, greater transfer film formation on the counterface	Abrasive wear, thin transfer film formation on the counterface
CoO	Severe abrasive, sub-surface crack propagation	Smooth smeared layer, ductile, greater sintering ability or grain refinement, thin amorphous layer formation closer to the wear track
NiO	Brittle fractures, cracking, spallation of tribofilm	Coating worn out, brittle fractures
Ta_2O_5	Brittle fractures, cracking	Ductile behavior, smeared layer
$Co_{0.75}Ni_{0.25}O$	Sub-surface cracking, deformed long grain	Greater sintering ability or grain refinement
$Co_{0.5}Ni_{0.5}O$	Brittle fractures, cracking	Detachment of tribofilm, cracking, brittle fractures

Table SS 4: The summary of crystal structure and their corresponding lattice constants [6,10–13]

Type of oxides	Crystal structure	Lattice constant (Å)
Co_3O_4	Spinel	8.067 (a=b=c)
CoO	Rock salt	4.2518 (a=b=c)
$Co_{0.75}Ni_{0.25}O$	Rock salt	4.238 (a=b=c)
$Co_{0.5}Ni_{0.5}O$	Rock salt	4.222 (a=b=c)
NiO	Rock salt	4.17 (a=b=c)
CuO	Monoclinic	a = 4.6837, b = 3.4226, and c = 5.1288
Ta_2O_5	Orthorhombic	a = 6.198, b = 40.29 and c = 3.888

References

[1] Bowden FP, Bowden FP, Tabor D. The friction and lubrication of solids. vol. 1. Oxford university press; 2001.

[2] Erdemir A. A crystal-chemical approach to lubrication by solid oxides. Tribol Lett 2000;8:97–102. https://doi.org/10.1023/a:1019183101329.

[3] Erdemir A. A crystal chemical approach to the formulation of self-lubricating nanocomposite coatings. Surf Coatings Technol 2005;200:1792–6.

[4] Dimitrov V, Komatsu T. Classification of simple oxides: a polarizability approach. J Solid State Chem 2002;163:100–12.

[5] Prakash B, Celis J-P. The lubricity of oxides revised based on a polarisability approach. Tribol Lett 2007;27:105–12.

[6] Roy A, Sharifi N, Munagala VN V, Alidokht SA, Patel P, Makowiec M, et al. Microstructural evolution and tribological behavior of suspension plasma sprayed CuO as high-temperature lubricious coatings. Wear 2023:204874.

[7] Roy A, Munagala VNV, Patel P, Sharifi N, Alidokht SA, Makowiec M, et al. Friction and wear behavior of suspension plasma sprayed tantalum oxide coatings at elevated temperatures. Surf Coatings Technol 2023;452:129097.

[8] Roy A. Enhanced lubricating behavior of cobalt oxide over nickel oxide. Tribol Lett 2023.

[9] Amit Roy, Vahid Jalilvand, Saeed Mohammadkhani, Payank Patel, A. Dolatabadi, L. Roue, D. Guay, Richard R. Chromik, Pantcho Stoyanov CM. Microstructure and tribological characteristics of thermally sprayed Co-Ni-O ternary oxide coatings. Tribol Int n.d.

[10] Mohammadkhani S, Jalilvand V, Davis B, Gauthier GH, Dolatabadi A, Moreau C, et al. High-temperature behaviour of HVOF (Co,Ni)O coated Cu-Ni-Fe anodes. Corros Sci 2021;189:109563. https://doi.org/10.1016/j.corsci.2021.109563.

[11] Mohammadkhani S, Schaal E, Dolatabadi A, Moreau C, Davis B, Guay D, et al. Synthesis and thermal stability of (Co,Ni)O solid solutions. J Am Ceram Soc 2019;102:5063–70. https://doi.org/10.1111/jace.16397.

[12] Roy A, Munagala VN V, Patel P, Sharifi N, Alidokht SA, Makowiec M, et al. Friction and wear behavior of suspension plasma sprayed tantalum oxide coatings at elevated temperatures. Surf Coatings Technol 2022:129097.

[13] Cardenas-Flechas LJ, Barba-Ortega JJ, Joya MR. Analysis and evaluation of structural properties of Co 3 O 4 microparticles obtained at low temperature. Cerâmica 2022;68:52–9.